

Dissertation

Fabrication of Polarized Emissive Light-Emitting Diodes Based  
on CdSe/CdS Quantum Rods Synthesized in a Continuous  
Flow Reactor

Dissertation zur Erlangung des Doktorgrades an der Fakultät  
für Mathematik, Informatik und Naturwissenschaften in  
Kooperation mit dem Fraunhofer IAP-CAN

Fachbereich Chemie Universität Hamburg

vorgelegt von

Christian Castillo Delgadillo

aus Mexiko-Stadt

2022



The experimental part of this work was performed between February 2019 and March 2022 at Fraunhofer CAN and at the Institute of Physical Chemistry at the University of Hamburg under the supervision of Dr. Jan Steffen Niehaus and Prof. Dr. Alf Mews.

1. Supervisor: Dr. Jan Steffen Niehaus
2. Supervisor: Prof. Dr. Alf Mews

Date of the thesis defense: July 15th, 2022



*Our knowledge is a receding mirage in an expanding desert of ignorance.*

– Will Durant



## I Publications

Staechlin, Y. U., Deffner, M., Krohn, S., Castillo Delgadillo, C., Niehaus, J. S., Lange, H.  
Carrier localization in zero-dimensional and one-dimensional CdSe-CdS heterostructures.  
*J. Chem. Phys.* **2022**, 156

## List of Abbreviations

|      |  |
|------|--|
| AC   | Alternating current                    |
| AFM  | Atomic force microscopy                |
| AO   | Atomic orbital                         |
| AR   | Aspect ratio                           |
| CB   | Conduction band                        |
| CBP  | 4,4'-Bis(N-carbazolyl)-1,1-biphenyl    |
| CIE  | Comission International de l'Eclairage |
| C/S  | Core/Shell                             |
| CSTR | Continuous flow stirred tank reactor   |
| DC   | Direct current                         |
| DOP  | Degree of polarization                 |
| EL   | Electroluminescence                    |
| EML  | Emitting layer                         |
| EQE  | External quantum efficiency            |
| ETL  | Electron transport layer               |
| FFE  | Fringe-field electrode                 |
| FRET | Förster resonance energy transfer      |
| FWHM | Full width at half maximum             |
| HDA  | Hexadecylamine                         |
| HH   | Heavy hole                             |
| HIL  | Hole injection layer                   |
| HOMO | Highest occupied molecular orbital     |
| HPA  | <i>n</i> -Hexylphosphonic acid         |
| HTL  | Hole transport layer                   |
| HWHM | Half-width-half-maximum                |
| IDE  | Interdigitated electrode               |
| ITO  | Indium tin oxide                       |
| LC   | Liquid crystal                         |
| LCD  | Liquid crystal display                 |
| LED  | Light-emitting diode                   |



|           |   |
|-----------|---|
| LH        | Light hole  |
| LUMO      | Lowest unoccupied molecular orbital                               |
| MO        | Molecular orbital   |
| ODPA      | Octadecylphosphonic acid  |
| PBD       | 2-Biphenyl-4-yl-5-(4-tert-butylphenyl)- 1,3,4-oxadiazole          |
| PDMS      | Polydimethylsiloxan   |
| PEB       | Post-exposure bake  |
| PEDOT:PSS | Poly(3,4-ethylenedioxythiophene)–poly(styrenesulfonate)           |
| PEQLED    | Polarized emissive quantum-rod based light-emitting diode         |
| PFR       | Piston flow reactor   |
| PVD       | Physical vapor deposition   |
| PVK       | Poly vinyl(N-carbazole)   |
| QCM       | Quartz crystal microbalance                                       |
| QD        | Quantum dot   |
| QLED      | Quantum-dot based light-emitting diode                            |
| QR        | Quantum rod   |
| QY        | Quantum yield   |
| RCA       | Radio Corporation of America                                      |
| RGB       | Red, green, blue  |
| SEM       | Scanning electron microscopy                                      |
| TCTA      | tris(4-carbazoyl-9-ylphenyl)amine                                 |
| TEM       | Transmission electron miscroscopy                                 |
| TFB       | Poly(9,9–dioctylfluorene-alt-N-(4–sec-butylphenyl)-diphenylamine) |
| TGA       | Thermogravimetric analysis  |
| TMAH      | Tetramethylammonium hydroxide pentahydrate                        |
| TMSS      | Bis(trimethylsilyl)sulfide  |
| TOP       | Trioctylphosphine   |
| TOPO      | Trioctylphosphine oxide   |
| TPBi      | 2,2',2''-(1,3,5-Benzinetriyl)-tris(1-phenyl-1-H-benzimidazole)    |
| TPD       | Poly(N,N'-bis(4-butylphenyl)-N,N'-bis(phenyl)benzidine)           |

|        |                     |
|--------|---------------------|
| UV     | Ultraviolet         |
| UV-vis | Ultraviolet-visible |
| VB     | Valence band        |
| WB     | Wide Band           |
| XRD    | X-ray diffraction   |

## List of Symbols

|                |   |
|----------------|---|
| $\chi$         | Spin-allowed optical transition rate            |
| $\Delta_{cr}$  | Crystal field splitting                         |
| $\Delta_{so}$  | Split-off spin-orbit splitting                  |
| $\epsilon$     | Attenuation coefficient                         |
| $\epsilon$     | Dielectric constant                             |
| $\epsilon_0$   | Permittivity constant                           |
| $\eta_{ext}$   | External quantum efficiency                     |
| $\eta_{int}$   | Internal quantum efficiency                     |
| $\eta_L$       | (Luminous) current efficiency                   |
| $\eta_{oc}$    | Light out-coupling efficiency                   |
| $\eta_P$       | Luminosity, luminous (power) efficiency         |
| $\gamma$       | Charge carrier balance factor                   |
| $\hbar$        | Reduced Planck constant                         |
| $\lambda$      | Wavelength of incident (and scattered) light    |
| $\mu$          | Effective mass                                  |
| $\omega$       | Frequency                                       |
| $\phi_0$       | Peak photopic response of the eye               |
| $\Phi_{lum}$   | Luminous flux                                   |
| $\psi$         | Wavefunction                                    |
| $\tau$         | Residence time                                  |
| $\theta$       | Scattering angle                                |
| $\theta_{QR}$  | Angle of a single QR relative to electric field |
| $\varphi_{QY}$ | Internal luminescent quantum yield              |
| $A$            | Absorbance                                      |

|              |   |
|--------------|---|
| $A$          | Area  |
| $a_0$        | Exciton Bohr radius                                 |
| $b$          | Optical pathway                                     |
| $c$          | Concentration                                       |
| $c$          | Speed of light in vacuum                            |
| $D$          | Diameter  |
| $d$          | Interplanar distance                                |
| $\vec{E}$    | Electric field vector                               |
| $e$          | Elemental charge                                    |
| $E_g$        | Band gap energy                                     |
| $f$          | Frequency   |
| $g(\lambda)$ | Photopic response shape function                    |
| $h$          | Planck's constant                                   |
| $I$          | Intensity   |
| $I$          | Current, photocurrent                               |
| $J$          | Current density                                     |
| $k$          | Wave vector   |
| $L$          | Luminance   |
| $P$          | Degree of polarization                              |
| $p$          | Momentum  |
| $P_{QLED}$   | Power   |
| $p_{vap}$    | Vapor pressure                                      |
| $q$          | Electronic charge                                   |
| $R(\lambda)$ | Photodiode responsivity over a wavelength $\lambda$ |
| $r$          | Radius  |
| $r_A$        | Rate of reaction "A"                                |
| $S$          | Degree of alignment                                 |
| $t$          | Time  |
| $T_G$        | Growth temperature                                  |
| $T_N$        | Nucleation temperature                              |
| $U^*$        | Accelerated voltage                                 |

|           |                      |
|-----------|----------------------|
| $\dot{V}$ | Volumetric flow      |
| $V$       | Voltage              |
| $V_{th}$  | Threshold voltage    |
| $V_{tot}$ | Total reactor volume |

## Contents

|          |  |          |
|----------|--|----------|
| <b>I</b> | <b>Publications</b>  | <b>I</b> |
| <b>1</b> | <b>Abstract / Kurzfassung</b>  | <b>1</b> |
| 1.1      | English . . . . .  | 1        |
| 1.2      | Deutsch . . . . .  | 1        |
| <b>2</b> | <b>Introduction</b>  | <b>2</b> |
| <b>3</b> | <b>Theoretical Background</b>  | <b>4</b> |
| 3.1      | Properties and Composition of Semiconductor Nanomaterials . . . . .                        | 4        |
| 3.1.1    | Quantum Size Effect . . . . .  | 6        |
| 3.1.2    | Core/Shell Semiconductor Nanoparticles . . . . .   | 8        |
| 3.2      | Anisotropic Nanomaterials . . . . .  | 11       |
| 3.2.1    | Alignment of Quantum Rods . . . . .  | 15       |
| 3.3      | Synthesis of Nanomaterials . . . . .   | 17       |
| 3.3.1    | Synthesis of Elongated CdSe/CdS Quantum Rods . . . . .                                     | 18       |
| 3.3.2    | Reaction Mechanism for CdSe/CdS Quantum Rods . . . . .                                     | 19       |
| 3.3.3    | Considerations and Principles for the Use of a Reactor In Nanoparticle Syntheses . . . . . | 21       |
| 3.3.4    | Reactor at Fraunhofer CAN . . . . .  | 23       |
| 3.4      | Quantum Dot-based Light-Emitting Diodes . . . . .  | 25       |
| 3.4.1    | Mechanisms for Efficient Quantum dot-based Light-Emitting Diodes                           | 30       |
| 3.4.2    | Polarized Emissive Quantum Rod-based Light-Emitting Diodes . .                             | 32       |
| 3.5      | Photolithography . . . . .   | 34       |
| 3.6      | Physical Vapor Deposition . . . . .  | 36       |
| 3.7      | Analytical Methods . . . . .   | 38       |
| 3.7.1    | UV-vis Spectroscopy . . . . .  | 38       |
| 3.7.2    | Emission Spectroscopy . . . . .  | 40       |
| 3.7.3    | Measuring Linearly Polarized Emission . . . . .  | 41       |
| 3.7.4    | Measuring the Efficiency of Light-emitting Diodes . . . . .                                | 42       |
| 3.7.5    | Transmission Electron Microscopy . . . . .   | 45       |

---

|          |   |           |
|----------|---|-----------|
| 3.7.6    | Atomic Force Microscopy . . . . .   | 45        |
| 3.7.7    | X-ray Diffractometry . . . . .  | 46        |
| <b>4</b> | <b>Objective</b>  | <b>48</b> |
| <b>5</b> | <b>Results and Discussion</b>   | <b>49</b> |
| 5.1      | Fabrication of CdSe Cores . . . . .   | 49        |
| 5.1.1    | Influence of Nucleation and Growth Temperature . . . . .  | 49        |
| 5.1.2    | Influence of Selenium to Cadmium Ratio . . . . .  | 55        |
| 5.1.3    | Size Control of CdSe Cores . . . . .  | 57        |
| 5.1.4    | Summary . . . . .   | 63        |
| 5.2      | Fabrication of CdSe/CdS Quantum Rods . . . . .  | 65        |
| 5.2.1    | Influence of Growth Temperature . . . . .   | 65        |
| 5.2.2    | Adjusting the Quantum Rod Size with Volumetric Flow Rates . . . . .                             | 69        |
| 5.2.3    | Design of Different Quantum Rod Species . . . . .   | 73        |
| 5.2.4    | Summary . . . . .   | 80        |
| 5.3      | Alignment of Quantum Rods with an Electrostatic Field Using Interdigitated Electrodes . . . . . | 81        |
| 5.3.1    | Alignment on Interdigitated Electrodes by Drop-casting . . . . .                                | 81        |
| 5.3.2    | Frequency Dependence on Interdigitated Electrodes . . . . .                                     | 83        |
| 5.4      | Alignment of Quantum Rods with an Electrostatic Field Using Fringe-Field Electrodes . . . . .   | 87        |
| 5.4.1    | Variation of the Electrode Width and Interdistance . . . . .                                    | 88        |
| 5.4.2    | Influence of the Quantum Rod Solvent . . . . .  | 97        |
| 5.4.3    | Influence of Organic Additives . . . . .  | 102       |
| 5.4.4    | Influence of Frequency and Voltage . . . . .  | 108       |
| 5.4.5    | Influence of the Quantum Rod Sample . . . . .   | 115       |
| 5.4.6    | Summary . . . . .   | 117       |
| 5.5      | Fabrication of PEQLEDs . . . . .  | 118       |
| 5.5.1    | Synthesis of ZnO Nanoparticles . . . . .  | 118       |
| 5.5.2    | Transfer of Aligned Quantum Rod Films to LED Substrates . . . . .                               | 122       |
| 5.5.3    | PEQLEDs with Conventional Stack . . . . .   | 123       |
| 5.5.4    | PEQLEDs with Inverted Stack . . . . .   | 132       |

---

|          |  |            |
|----------|--|------------|
| 5.5.5    | Summary . . . . .  | 143        |
| <b>6</b> | <b>Outlook</b>   | <b>144</b> |
| <b>7</b> | <b>Summary</b>   | <b>146</b> |
| 7.1      | English . . . . .  | 146        |
| 7.2      | Deutsch . . . . .  | 147        |
| <b>8</b> | <b>Experimental</b>  | <b>149</b> |
| 8.1      | Preparation of Precursors for the Reactor . . . . .  | 149        |
| 8.1.1    | Preparation of the Selenium Precursor . . . . .  | 149        |
| 8.1.2    | Preparation of the Cadmium Precursor for the Cores . . . . .                                       | 149        |
| 8.1.3    | Preparation of the Sulfur Precursor . . . . .  | 150        |
| 8.1.4    | Preparation of the Cadmium Precursor for the Quantum Rods . . .                                    | 151        |
| 8.2      | General Synthesis of CdSe Cores and CdSe/CdS Core/Shell Nanoparticles<br>Using a Reactor . . . . . | 152        |
| 8.3      | Fabrication of Substrates via Photolithography . . . . .   | 154        |
| 8.3.1    | Fabrication of a Chromium Mask . . . . .   | 154        |
| 8.3.2    | Preparation of Substrates for Photolithography . . . . .   | 155        |
| 8.3.3    | Fabrication of Interdigitated Electrodes . . . . .   | 155        |
| 8.3.4    | Fabrication of Fringe-Field Electrodes . . . . .   | 156        |
| 8.3.5    | Fabrication of Structured Indium-tin Oxide Substrates . . . . .                                    | 157        |
| 8.4      | Alignment of Quantum Rods . . . . .  | 158        |
| 8.5      | Fabrication of Polarized Emissive Light-emitting Diodes . . . . .                                  | 159        |
| 8.5.1    | Synthesis of ZnO Nanoparticles for the ETL . . . . .   | 159        |
| 8.5.2    | Fabrication of the Light-emitting Diodes . . . . .   | 160        |
| <b>9</b> | <b>Acknowledgments</b>   | <b>163</b> |
|          | <b>References</b>  | <b>165</b> |
| <b>A</b> | <b>Appendices</b>  | <b>177</b> |
| A.1      | Safety . . . . .   | 177        |
| A.1.1    | Chemicals Used . . . . .   | 177        |

|                                |     |
|--------------------------------|-----|
| A.1.2 KMR Substances . . . . . | 184 |
| A.2 Curriculum Vitae . . . . . | 186 |
| A.3 Erklärung . . . . .        | 189 |



# 1 Abstract / Kurzfassung

## 1.1 English

In this thesis, a successful fabrication route for polarized emissive quantum rod based light-emitting diodes (PEQLEDs) emitting red light in the visible spectrum was established and analyzed. The PEQLEDs were developed using a conventional and inverted stack and exhibit high degrees of polarization. The high degree of polarization is possible due to the optimized alignment method, which is based on an electrostatic alignment using fringe-field electrodes. The factors and parameters that allow for a successful alignment were investigated and optimized. The polarized emission is possible due to the anisotropy of the used material: CdSe/CdS quantum rods. These were synthesized in a two step procedure using a continuous flow reactor. This allowed for a fast screening of reaction parameters and a high throughput of the synthesized material. The main focus of this work was the integration of CdSe/CdS QRs into novel opto-electronic devices (PEQLEDs) to deliver polarized emission in ensemble with high degrees of polarization.

## 1.2 Deutsch

Im Rahmen dieser Arbeit wurde erfolgreich eine Herstellungsmethode für polarisiert emittierende Leuchtdioden basierend auf Nanostäbchen, die rotes Licht emittieren, entwickelt und analysiert. Die PEQLEDs wurden auf einem konventionellen und inversen *stack* entwickelt und zeigen hohe Polarisationsgrade. Die hohe Polarisation wurde mit Hilfe einer optimierten Ausrichtungsmethode ermöglicht. Diese basiert auf einer elektrostatischen Ausrichtung mit *fringe-field* Elektroden. Die Einflussfaktoren und Parameter, die eine erfolgreiche Ausrichtung ermöglichen, wurden untersucht. Die polarisierte Emission ist möglich anhand der Eigenschaften der eingesetzten CdSe/CdS Nanostäbchen. Diese wurden in einer Zwei-Schritt-Prozedur in einem kontinuierlichen Flussreaktor synthetisiert. Dies ermöglicht die Untersuchung der Reaktionsparameter und eine hohe Produktionsrate von dem synthetisierten Material. Der Fokus dieser Arbeit lag in der Integration von CdSe/CdS Nanostäbchen in neuartigen Leuchtdioden (PEQLEDs), welche hohe Polarisationsgrade im Ensemble zeigen.

## 2 Introduction

Throughout the last decades, the exponential development of technologies in several application fields has led to the emergence of new sciences. Among these, nano sciences have grown from just a keyword in some investigative groups to a broad field where chemistry, physics and materials science merge. The research on materials in the nano-scale have led to impactful discoveries like the quantum confinement,<sup>[1,2]</sup> which have led to the development of novel and enhanced materials. Due to their exceptional optical properties, semiconductor nanocrystals, also known as quantum dots, found application in several technical fields such as lighting and display technologies,<sup>[3–8]</sup> photovoltaics,<sup>[9–11]</sup> biology and bionanomedicine.<sup>[5,12]</sup> Due to the tunability of semiconductor nanoparticles in prospect of their emission color through precise control of their size, the focus on these materials is of great consideration. Several semiconductor materials and their expected emission range in the visible spectrum are shown in figure 1. Their unique emissive properties fulfill requirements of color purity, gamut, stability and efficiency.<sup>[4,13,14]</sup> All these properties are of main relevance in the development of displays and novel opto-electronic devices.

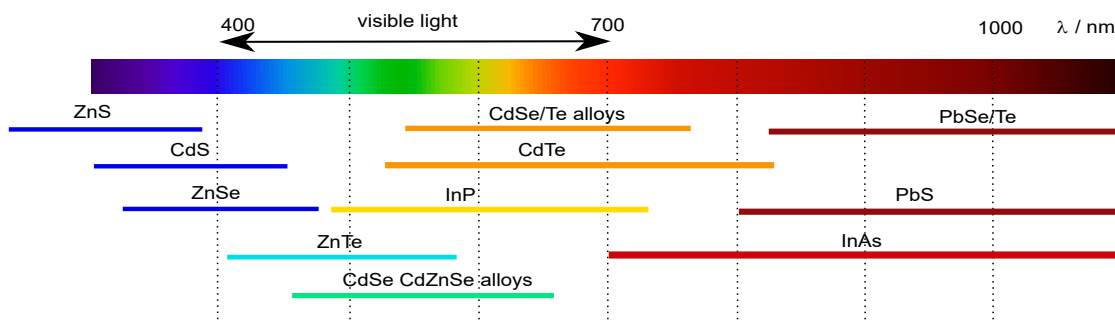


**Figure 1:** Overview of the expected spectral ranges of emission for some semiconductor quantum dots.

To this day, quantum dots are the main emission source in some commercial televisions, such as the QLED Television from Samsung,<sup>[15]</sup> the C63 series of TCL,<sup>[16]</sup> among others. While their concurrence, organic light-emitting diodes (OLED) still offer an enhanced quality concerning black and dark colors, quantum dots remain critical materials for display fabrication due to their better gamut.<sup>[17]</sup> Thus, new developments in display fabrication in spite of the color quality involve the combination of organic light emitters and quantum dots in so called Q-OLED televisions.<sup>[18]</sup>

Today's focus on emitters for display applications relies mostly on cadmium-free alternatives. For instance, Samsung's QLED televisions all contain cadmium-free materials such as InP/ZnSe/ZnS and ZnS/ZnTeSe/ZnS.<sup>[19,20]</sup> However, the development of new technologies such as 3D-holograms, head-up displays and enhanced liquid crystal displays (LCD) also require components that exhibit additional properties.<sup>[21,22]</sup> Here, CdSe/CdS quantum rods offer benefits concerning their opto-electronic properties compared to spherical cadmium-based and cadmium-free materials. For instance, quantum rods exhibit a high quantum yield and polarized emission.<sup>[23]</sup> It is the polarized emission that attracts a high interest due to their possible use in 3D technologies, head-up displays and LCDs with an improved energy efficient generation of light.<sup>[22,24–28]</sup> While much development has been made on highly efficient electroluminescent quantum dot-based light-emitting diodes (QLED), less is true for devices exhibiting polarized emission. Main issues revolve around the polarization and efficiency of the fabricated devices.<sup>[24,26]</sup>

In this work, a fabrication route for polarized emissive light-emitting diodes based on CdSe/CdS quantum rods was analyzed and developed. For this, the production of CdSe/CdS quantum rods using a continuous flow reactor, developed at Fraunhofer IAP-CAN, was used. This offers the advantage of a high throughput and screening of the produced materials, which are needed for the fabrication of the device. Furthermore, the alignment of QRs using an optimized method will be discussed. This step is of great relevance, since the polarization properties of the fabricated QR film should be transferred to the opto-electronic device. The polarized emissive QLEDs were analyzed and characterized for its polarization and performance with the aim of achieving devices with higher polarization than those reported in the literature.

### 3 Theoretical Background

The following sections offer a detailed theoretical background of the three main topics this thesis is divided into.

First, the properties and composition of semiconductor nanoparticles, with focus on anisotropic nanomaterials, will be discussed. The synthetic methods using a continuous flow reactor and the anisotropic properties, such as polarized emission will be discussed in detail. Next, the several approaches to exploit the anisotropic properties of one-dimensional nanomaterials will be explained, focusing on the alignment of these materials using several established methods. Last, the principles of light-emitting diodes (LED) and the fabrication of quantum-dot based LEDs will be further explained. The advantages and challenges of using anisotropic materials and will also be briefly discussed.

#### 3.1 Properties and Composition of Semiconductor Nanomaterials

Nanoscale materials exhibit physical properties which differ from those of their macroscopic counterpart. The properties of semiconductor crystalline structures can be explained with the help of the energy band model. Thus their electronic structure can be highlighted and distinguished among other materials such as metallic conductors and insulators.<sup>[6,29]</sup>

In principle, the basic building blocks of matter are atomic nuclei and electrons. Following the rules of quantum mechanics, electrons can be ascribed to an individual discrete energy level, also called an atomic orbital (AO). Depending on their angular momentum, AOs can have different geometries delivering s-, p-, d- and f-orbitals. When building a molecule, electrons orbiting AOs are shared between two atoms, forming a covalent bond and thus a molecular orbital (MO).<sup>[6,29,30]</sup> Mathematically, this is described by the linear combination of the AOs, resulting in a bonding ( $\sigma$ ) and an anti-bonding ( $\sigma^*$ ) molecular orbital, respectively. MOs exhibit discrete energy levels and are occupied following Pauli's rule, mainly starting at the orbitals with the lowest energy (bonding orbitals). By using this scheme, it is possible to derive the electronic structure of more complex systems up to polyatomic materials.<sup>[29]</sup>

In the case of macroscopic solids, atoms and their respective AOs build so called energy bands, which result from the interaction between AOs with the same energy within the crystal. The calculation of these electronic structures is possible by simplifying the system, which is a periodic, infinite crystal. By using Bloch-functions (detailed derivations can be found in further literature), which describe the periodic combination of AOs, electrons are described as a superposition of plane waves extended throughout the solid.<sup>[31]</sup> Thus, the energy structure in a solid does not exhibit discrete energy levels, but a broad energy band. Each energy band is characteristic for each crystalline solid material and defines their physical behavior. Such is the case in metallic compounds, where the linear combination of each orbital within the metal delivers a tight succession of several MOs (see figure 2).<sup>[32]</sup> Metallic compounds exhibit bands which span over the whole crystal, which result in delocalized electrons throughout both bands. These materials merge the energy bands corresponding to the orbitals with the valence electrons (valence band, VB) with the proximate band with higher energy level, the conduction band (CB).<sup>[32]</sup> Since the electrons can freely move between the VB and the CB, metals exhibit outstanding electrical conductivity.

On the other hand, semiconductors exhibit an energetic separation between their VB and CB, the band gap (see figure 2, middle). Their narrow band gap allows electrons to land into the conduction band through energy supply. After kinetic stimulation it is possible to adjust the Fermi energy, in which case the electrons can freely move through the CB, thus, exhibiting electrical conductivity at higher temperatures (above 0 K). After an electron ( $e^-$ ) reaches the CB it leaves a positive hole ( $h^+$ ) in the valence band (in other words, a valence to conduction band transition). The formed quasi particle – electron-hole pair – is known as an exciton.<sup>[32]</sup>

Opposite to metals, insulators have an empty CB and their VB is separated by a wide band gap. Thus, it is not possible for electrons to reach the CB and makes electric conduction impossible.<sup>[32]</sup>

Figure 2 depicts the band alignment for metals, semiconductors and insulators. It is to be noted, that Fermi level is dependent on the kinetic state of the system. Thus, electric conduction can be achieved for semiconductors after kinetic stimulation.<sup>[30,32,33]</sup>

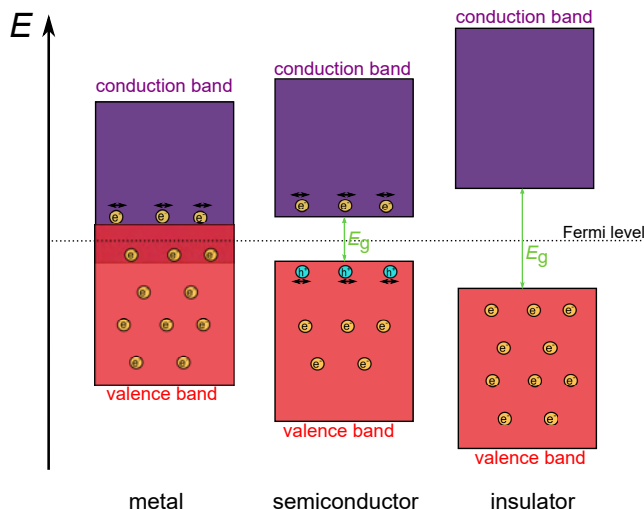


**Figure 2:** Schematic illustration of the band alignments for metals, semiconductors and insulators. The Fermi energy is depicted as the energy at the middle of the band gap. Left: electrons are delocalized in both valence and conduction band for metallic compounds. Middle: Semiconductors exhibit a small band gap, whereas after kinetic stimulation, electrons can move to the conduction band. This leaves a hole at the valence band. Right: the band gap in insulators is too big to allow valence to conduction band transitions.

Nanoscale materials can be classified as materials between molecular and macroscopic matter. They frequently exhibit behavior which is intermediate between macroscopic crystalline solids and that of a molecular system. In the case of semiconductor nanomaterials, their opto-electronic properties can be described using quantum mechanical approximations. For instance, the subsequent addition of atomic orbitals (in this case: the highest occupied molecular orbitals: HOMO, and the lowest unoccupied molecular orbitals: LUMO) leads to a progressive formation of discrete energy levels, which consequently merge into energy bands. Thus, the HOMO and LUMO lead to the formation of the valence and conduction band, respectively.<sup>[30,32,33]</sup>

### 3.1.1 Quantum Size Effect

For semiconductor nanoparticles, the shift of the electronic levels with sinking particle size has an important influence on their opto-electronic properties. This is exemplified in figure 3. This comes due to the confinement of excitons in solids. To describe this, the relevant length scale needed is the exciton Bohr radius  $a_0$  of the bulk material (e.g.  $a_0 = 1.74$  eV for CdSe).<sup>[6,10,30,34]</sup> This describes the spatial extension of excitons in solids

and can be described by the following equation 1 with the effective mass approximation.

$$a_0 = \frac{\epsilon \hbar^2}{\mu_{e,h} e^2} \quad (\text{where : } \mu_{e,h} = \frac{m_e m_h}{m_e + m_h}) \quad (1)$$

Here,  $\epsilon$  is the dielectric constant of the specific material,  $\hbar$  the reduced Planck constant,  $e$  the elemental charge and  $\mu$  the effective mass for the electron (e) and hole (h). As the nanocrystal size reaches  $a_0$ , confinement begins to affect the exciton wave function, inducing changes in the density of electronic states and in the energy level separation. Thus, the bandgap increases for smaller nanoparticles (e.g. when the radius  $r \ll a_0$ ).<sup>[10,34]</sup>

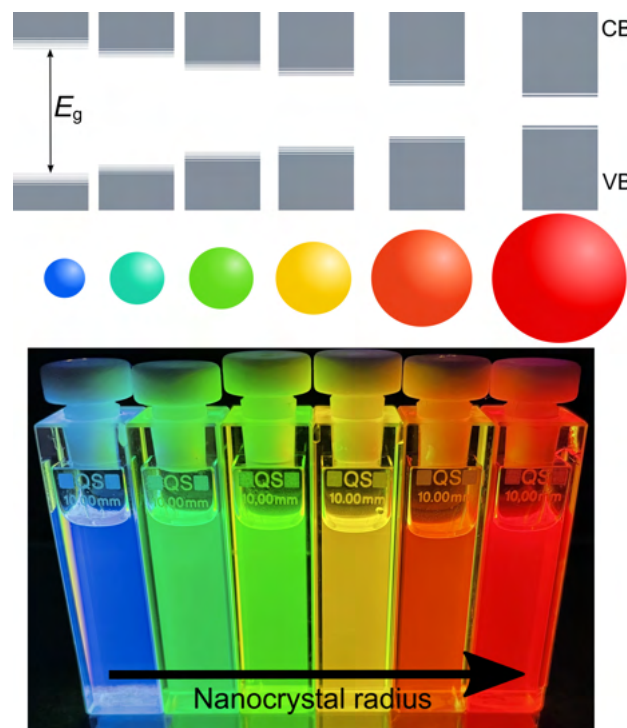


**Figure 3:** Schematic illustration of the quantum confinement effect on the energy level structure of semiconductor nanoparticles. As seen here, smaller nanoparticles (blue) have a bigger band gap, corresponding to energies of shorter wavelengths, thus higher energies. The lower panel shows colloidal suspensions of CdSe/CdS nanoparticles synthesized for this work of different sizes under UV excitation.

The effect of quantum confinement and its impact on the band gap energies for semiconductor nanoparticles can be described with the following equation 2.

$$E_g(\text{dot}) = E_g(\text{bulk}) + \frac{\hbar^2 \pi^2}{2\mu_{e,h} r^2} - \frac{1.8e^2}{4\pi\epsilon\epsilon_0 r} \quad (2)$$

Here,  $\epsilon_0$  is the permittivity constant of the bulk material. This equation, as defined by Brus *et al.*, is calculated by the addition of two terms: the Coulomb energy and its kinetic term. As seen in the equation, the nanoparticle's size has a strong effect on the energy of its band gap ( $E_g$ ), which shows a  $1/r^2$  dependence in the kinetic term of the wave function and a  $1/r$  dependence in the Coulomb interaction.<sup>[29,34,35]</sup>

These effects have a direct influence in the opto-electronic properties of the semiconductor nanomaterial, which exhibit unique properties compared to the bulk material such as broad absorption spectra, narrow and symmetric photoluminescence and slow exciton decay rates. These properties can be fine tuned after passivating the nanoparticle's surface with a second semiconductor material, thus inducing changes in the electronic structure of the wave functions.<sup>[3,29]</sup>

### 3.1.2 Core/Shell Semiconductor Nanoparticles

Nanoparticles consisting of the semiconductor core, passivated with an organic ligand, often exhibit low quantum-yields (QY).<sup>[36]</sup> The quantum yield defines the ratio of emitted photons to the number of absorbed photons from a material, in this case emissive nanoparticles.<sup>[37,38]</sup> The low QY comes due to the surface-related trap states which lead to non-radiative de-excitation of charge carriers.

An essential strategy to improve the opto-electronic properties of nanoparticles is the passivation of the semiconductor core with a shell of a second semiconductor. These systems are known as core/shell (C/S) nanoparticles. The growth of a semiconductor shell not only improves the photoluminescence properties, but also improves the stability of the material over photo-oxidation.<sup>[3,36]</sup> Furthermore, by choosing specific ligands which may block some crystall orientations in the core material, 1-dimensional nanostructures, such as elongated quantum rods may be synthesized. These materials exhibit properties dependent on their shape, thus being classified as anisotropic nanomaterials.<sup>[39]</sup> A detailed theoretical background for anisotropic nanomaterials will be shown in further chapters. Core/shell systems are classified according to the bandgap and its relative position of the energy levels of the semiconductors of choice. Hence, C/S systems can be distinguished into: type-I, type-II and quasi type-II.<sup>[3]</sup>



Type-I systems are characterized by a shell band gap which is larger than that of the core. Therefore, the core is electronically passivated and both the electron and hole are confined within the core material (see figure 4). Moreover, the shell passivates the surface and reduces the trap states, thus resulting in higher QY and improved stability.<sup>[3]</sup>

On the other hand, type-II systems are characterized by band edges corresponding to the valence and conduction band of the core that are energetically lower or higher than those of the shell. Depending on the selected materials, either the hole or the electron are mostly confined to the core or the shell (see figure 4). This results in a red-shift of the first excitonic transition relative to the band gap of either semiconductor. Depending on the shell thickness, it is possible to tune the emission wavelengths of the C/S material into spectral ranges that would be difficult to achieve with only a single component.<sup>[3,36]</sup>

In quasi type-II systems, either the valence- or conduction-band edge of the shell material is located in the band gap of the core. This results that one charge carrier is confined in the core, while the other is delocalized over the core and the shell. Thus, its wave function spreads over both the core and the shell. Since the band gap offset of either the conduction or valence band is small, this system can be tuned through the shell thickness and shows a visible red-shift.<sup>[3,40]</sup> As an example, in CdSe/CdS the hole is confined in the core material, and the electron is delocalized throughout the shell, resulting in a visible red-shift.<sup>[3]</sup> These C/S systems are schematically illustrated in the following figure 4. Here, the three types of C/S systems are represented by their different band alignment. The electron and wave functions are also depicted in order to represent the relevant confinement.

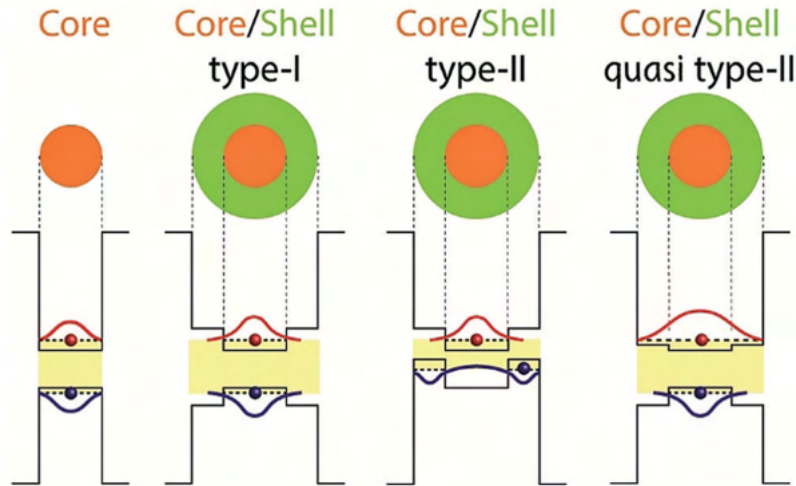


**Figure 4:** Schematic illustration of the different band alignments for core/shell nanomaterials: type-I, type-II and quasi type-II. The electron (red) and hole (blue) wave functions are shown and compared with the isolated core system.<sup>[3]</sup>

The synthesis of core/shell systems requires not only the appropriate band alignment, but also a minimal lattice mismatch between both of the semiconductor materials. Hence, an epitaxial type shell-growth is required. Here, the lattice mismatch and the same crystallization structure are kept into consideration. A high lattice mismatch results in structural deficiencies at the core-shell interface which lead to the formation of trap states.<sup>[36,41–43]</sup> The lattice parameters of some relevant semiconductors and their crystallization structure, as well as the corresponding band gap are summarized in the following table 1.

**Table 1:** Material parameters for some selected bulk semiconductors: crystallization structure, band gap and lattice parameter.<sup>[36,44]</sup>

| Material | Structure<br>(300 K) | $E_g$ /<br>eV | Lattice parameter /<br>Å |
|----------|----------------------|---------------|--------------------------|
| CdS      | Wurtzite             | 2.49          | 4.136/6.714              |
| CdSe     | Wurtzite             | 1.74          | 4.3/7.01                 |
| CdTe     | Zinc blende          | 1.43          | 6.482                    |
| ZnS      | Zinc blende          | 3.61          | 5.41                     |
| ZnSe     | Zinc blende          | 2.69          | 5.668                    |
| ZnTe     | Zinc blende          | 2.39          | 6.104                    |

An interesting way to reduce the strain arising from lattice mismatch is the use of an alloy or graded shell, which works as a mediating layer. This technique leads to high QY and offers a strategy to engineer different shells with dissimilar lattice parameters and therethrough influence the emission properties and its QY.<sup>[3]</sup>

The application of quantum dots for solid-state lighting, illumination and displays has to fulfill important criteria. The nanoparticles must exhibit high particle uniformity, high photoluminescence QYs, narrow and symmetric emission spectra, and minimized single-quantum dot blinking.<sup>[17,22,45,46]</sup> Although much progress has been made towards size uniformity and high QYs with narrow emission spectra, preventing "blinking" has proved to be rather challenging. The blinking process directly affects continuous photoluminescence, in which single quantum dots exhibit "on" and "off" states under continuous excitation. This limits the use of the nanoparticles in several applications.<sup>[45]</sup>

An approach towards improving the emissive properties and the quenching of blinking processes is the growth of a thick inorganic shell ( $>5$  nm) on the quantum dot in order to fully isolate the excited charge carriers from the semiconductor's surface and its environment. This process has proved to be relatively successful and accounts for suppressed blinking in several systems.<sup>[45,47,48]</sup> Here, the wave function of the nanocrystal core is isolated from the surface and its surrounding environment. Thus, the nanoparticle favors an epitaxial growth in which the optical properties remain stable and blinking is substantially suppressed.<sup>[48]</sup>

On the other hand, properties emerging from the shape control of the nanomaterial allow further engineering of photoluminescence (or electroluminescence) polarization and alignability.<sup>[39]</sup> For this, C/S (anisotropic) nanomaterials are of most interest. These properties in scope of their application in novel emitting devices will be discussed in the following chapter.

## 3.2 Anisotropic Nanomaterials

Anisotropic nanomaterials exhibit unique properties directly dependent on one physical direction. For instance, quantum rods show direction-dependent optical properties due to their elongated shape. Quantum rods (QR) exhibit linearly polarized emission which is dependant on the rod's length. This is exemplified in figure 5. Hu *et al.* reported linearly polarized emission on CdSe quantum rods along the long axis.<sup>[49]</sup> Single-molecule luminescence spectroscopy measurements confirm the transition from nonpolarized emission on spherical nanocrystals to purely linearly polarized emission on quantum rods with an

aspect ratio of 2.<sup>[49,50]</sup> Linearly polarized emission can also be observed on CdSe/CdS heterostructures.<sup>[39,51,52]</sup>

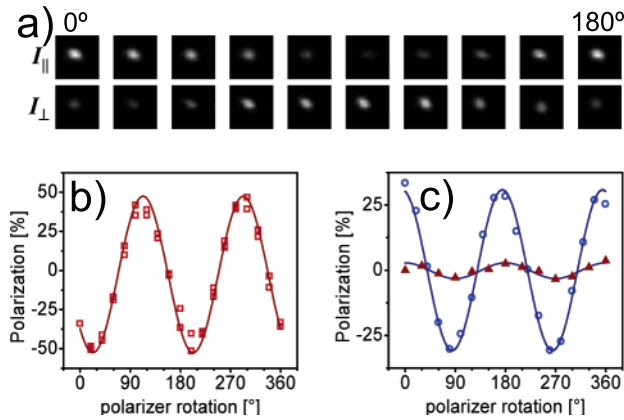


**Figure 5:** Captures of the photoluminescence of single CdSe/CdS quantum rods recorded simultaneously through a polarizer in two perpendicular directions. The detection angle was varied from  $0^\circ$  to  $180^\circ$  as seen in a). b) Photoluminescence intensity  $((I_{\parallel} - I_{\perp}) / (I_{\parallel} + I_{\perp}))$  ratios against the polarizer rotation angles of a single CdSe/CdS quantum rod with an aspect ratio of 1:4. c) Photoluminescence intensity ratios of a CdSe/CdS QR ensemble (aspect ratio 2.8:1) in a polymer matrix and of CdSe spherical cores (black triangles). Adapted with permission from D. V. Talapin, *et al. Nano Lett.* **2003**, *3*, 1677–1681. Copyright © 2003 American Chemical Society.<sup>[39]</sup>

QRs, such as CdSe QRs and CdSe/CdS QRs both exhibit linearly polarized band edge absorption and emission. Furthermore, QRs have been shown to exhibit a permanent dipole. Due to their permanent dipole and the induced dipole through excitation, QRs emit linearly polarized light.<sup>[53]</sup> The origin of this behavior and their relation to the increasing rod length has been ascribed to the electronic levels and their change due to the shear strain in one of the QR axis. Thus, in the excited state, the electron wavefunction ( $\psi_e$ ) from the CdSe core is able to extend into the conduction band of the CdS shell and into the shell volume to create polarized emission. The band edge electronic structure of the quantum rods and the change of this due to the elongated shell can be observed in the following figure 6.<sup>[23,51,54]</sup> This feature is of main interest for several applications requiring charge carrier separation and extraction and several reports have been accounted for this phenomenon. Not only does the carrier separation and shear strain induce polarized emission, but it also affects photoconductivity which is required for applications such as photocatalysis.<sup>[55]</sup>

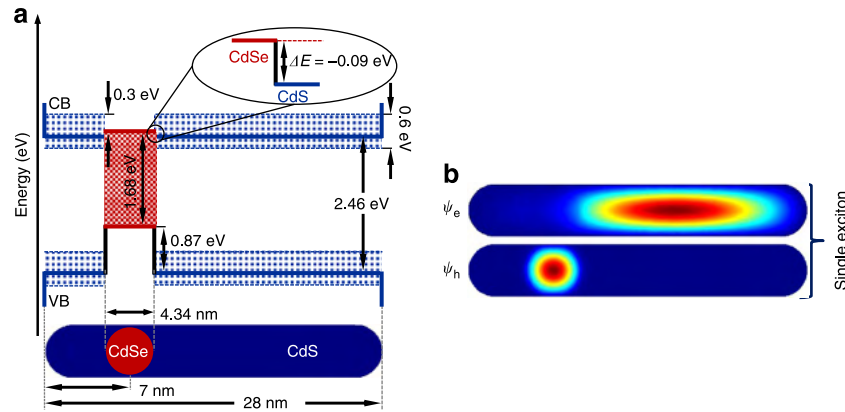


**Figure 6:** Electronic structure and calculated wavefunctions for CdSe/CdS quantum rods. a) Schematic of a CdSe/CdS quantum rod with their interfacial band alignment for both materials. For the calculations a core diameter of 4.34 nm and a total rod length of 28 nm were used. The calculated values are also shown in the graphic. b) Calculated wavefunctions for the electrons ( $\psi_e$ ) and holes ( $\psi_h$ ) in the single-exciton, which exhibits a mixed carrier dimensionality and a small overlap.<sup>[54]</sup>

In detail, the relationship of emission polarization to the NR geometry is typically explained by the exciton fine structure. In the case of CdSe, the valence band is made of 3 sub-bands: the heavy-hole (HH), the light-hole (LH) and the split-off sub-bands. The energy that separates the HH and LH sub-bands at  $k = 0$  is the crystal field splitting  $\Delta_{cr}$  (or net-splitting  $\Delta$ ) and the split-off spin-orbit splitting  $\Delta_{so}$ . Thus, the band-edge exciton fine structure for CdSe nanocrystals is consisted of eight states defined numerically by the total angular momentum of the exciton, as depicted in the following figure 7:  $|\pm 2\rangle$ ,  $|\pm 1^L\rangle$ ,  $|\pm 1^U\rangle$ ,  $|0^L\rangle$  and  $|0^U\rangle$ . The lower and upper sublevels (defined with the L and U superscripts, respectively) differ from each other by having a different total angular momentum and the + and - indicate spin handedness. The  $|\pm 2\rangle$  states are optically forbidden and  $|0^L\rangle$  has no oscillator strength and is therefore optically inactive too (this is exemplified in figure 7 with the dashed lines). For spherical CdSe nanocrystals the L states have lower energy than the U states. This changes if the crystal exhibits an elongated geometry, thus CdSe QRs exhibit a level swapping of the fine structure, which is dependant on the aspect ratio of the nanorod.<sup>[23,56]</sup>

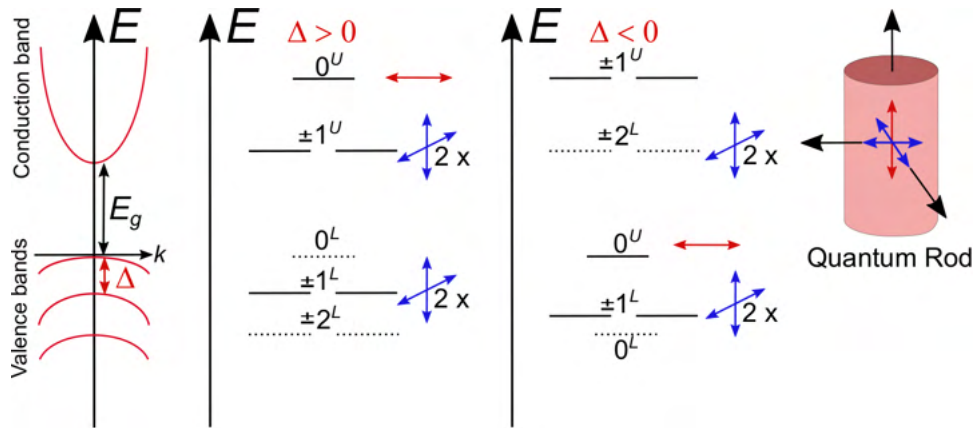


**Figure 7:** Schematic picture of the band structure for CdSe nanocrystals. It shows the conduction band and valence band with the heavy-hole, light-hole and split-off sub-bands, as well as the crystal field splitting  $\Delta$  at  $k = 0$ . The middle energy diagram shows the band-edge exciton fine structure for a positive net-splitting (in the case of spherical components). The optical inactive states are represented with dashed lines. Double degenerate 2D dipole emission is symbolized with the double blue arrows, while the 1D dipole emission is represented with a red arrow. The right energy diagram exhibits the change of energy levels for elongated QRs, meaning a negative net-splitting  $\Delta$ . On the right is a schematic geometrical representation of a quantum rod with arrows representing the 1D and 2D dipole contributions.

Photoluminescence occurs after radiative relaxation from the excited states of the exciton fine structure to the ground states. Thus, emission arises from the mixture of recombinations from the  $|0^U\rangle$  and the degenerated  $|\pm 1^U\rangle$  and  $|\pm 1^L\rangle$  states. The  $|0^U\rangle$  state is associated with a linear 1D dipole that oscillates along the  $c$ -axis, which emits linearly polarized photons along the wurtzite axis (this is represented in figure 7 with the red arrow). The  $\pm 1$  states, on the other hand, are two dimensional dipoles with photons circularly polarized in the inside plane (blue arrows in figure 7). In the case of CdSe QRs, the emission polarized along the  $c$ -axis is predominant for the  $\pm 1$  transitions, whereas in spherical CdSe QRs the opposite would be true.<sup>[23,56–58]</sup>

There are several factors to be considered in order to determine the probability of linearly polarized transitions in the QRs. As previously mentioned, the polarized emission on CdSe QRs arises from the dipole along the wurtzite  $c$ -axis. In the case of CdSe/CdS heterostructures, the emission derives from the radiative recombination inside the CdSe core. Thus, the polarization properties for the CdSe/CdS heterostructures strongly depend on the form and size of the CdSe cores and the CdS shell. As an example, an elongated core with an elongated shell will induce a greater strain in the core, which leads to a stronger separation of the energetic levels in the exciton fine structure, as described previously.<sup>[23,39,51,52,59,60]</sup>

### 3.2.1 Alignment of Quantum Rods

For the use as emitters with polarized light, colloidal quantum rod ensembles can be aligned using different methods. Some of the techniques used to achieve this purpose are: evaporation-mediated assembly, template-assisted assembly,<sup>[61]</sup> liquid-crystal (LC) self-alignment,<sup>[62]</sup> electrospinning<sup>[63]</sup> and electric field-assisted assembly.<sup>[64,65]</sup> The latter will be the main focus of this chapter and is the main method used in this work.

Due to their permanent and induced dipole, quantum rods can be aligned in the direction of an electrically induced electric field to create a superlattice. One way to achieve this is by applying a DC current in a setup using a plate capacitor. The quantum rods are then placed between the electrodes and are aligned along the electric field.<sup>[65]</sup> Another way of achieving an aligned superlattice but on a flat substrate was first reported by the group of Drndic for CdSe and CdTe quantum rods.<sup>[64]</sup> Here, an interdigitated electrode (IDE) on a ca. 100 nm thick silicon nitride was used to hold the suspended membranes. The set-up for this procedure is shown in figure 8. The colloidal QR solutions (in a hexane/octane solution) were drop-casted onto the device while applying a voltage to the electrodes. The alignment of the QRs can be confirmed by using transmission electron microscopy (TEM) and atomic force microscopy (AFM), as seen in figure 8 d) and e), where e) depicts a TEM image of the QRs (marked in red) after applying an electric field.<sup>[64]</sup> The degree of alignment  $S$  was calculated by using a nematic order parameter for the aligned substrates with the following equation 3:

$$S = \langle 2 \cos^2 \theta_{QR} - 1 \rangle_{\theta} \quad (3)$$

Here, is  $S$  the degree of alignment and  $\theta_{QR}$  the angle of a single QR relative to the direction of the electric field. The obtained parameters for the alignment were  $S = 0.8$ , which are much higher than those where no electric field was applied (with  $S = 0.1$ ).<sup>[64]</sup>

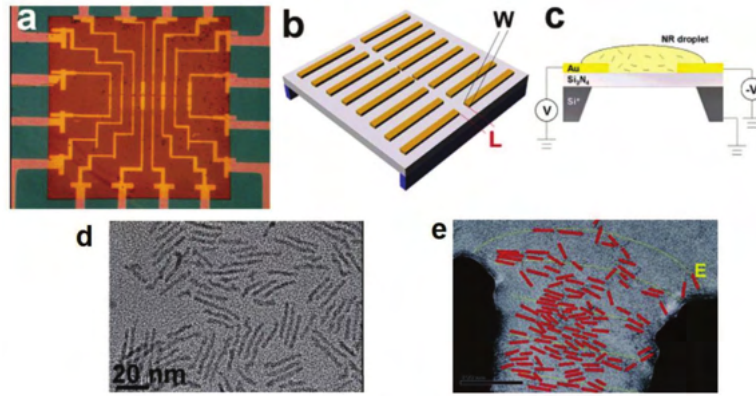


**Figure 8:** a) Optical image of the IDE used for the alignment procedure. b) Schematic illustration of a device with a suspended membrane containing eight patterned electrode pairs with different gap widths  $W$  and lengths  $L$ . c) Schematic illustration of the alignment procedure while applying a voltage to a drop-casted QR solution. d) TEM image of the QRs used for the experiment with a random orientation. e) TEM image of the aligned QRs after the alignment procedure. The QRs are highlighted red, while the theoretical direction of the electric field is highlighted in yellow. Adapted with permission from Z. Hu, *et al. Nano Lett.* **2006**, *6*, 2585-2591. Copyright © 2006 American Chemical Society.<sup>[64,66]</sup>

Alternatively to the use of a DC field, an AC field is also possible by using IDEs and varying frequencies as demonstrated by different research groups.<sup>[67,68]</sup> The use of an AC field prevents the QRs from drifting to the electrodes and creating an inhomogeneous film. Among other ways of improving the alignment of the QR film include the adjustment of the QR concentration, the ligands binding to the nanoparticle and the solution environment (e.g. using polymers such as PMMA or PEO).<sup>[69]</sup> These factors are though less published in the literature and depend on the end goal of the alignment. For instance, the use of polymers as reported by Lee *et al.*<sup>[70]</sup> and Russell *et al.*<sup>[69]</sup> which lead to high degrees of alignment, contain polymeric impurities that cannot be used for the fabrication of electroluminescent polarized emissive quantum-rod based light-emitting diodes (PEQLEDs).

For this work, the alignment using an electrostatic field was used on two different electrode structures: IDEs and fringe-field electrodes (FFE). The use of FFE is known in the LC technologies to switch the LCs in the desired direction. Their advantages include electrodes separated by an insulating layer, which prevents the substrates from any short circuit.<sup>[71,72]</sup> By designing the electrodes in a proper way, the electric fields can be used to align larger areas in comparison to IDEs. The increasing amount of defects by increasing the size of the electrodes on IDEs depends on the lithography process. Therefore, FFEs



are an interesting alternative to analyze and optimize the alignment procedure. The geometries and the equipotential lines these electrodes can generate are shown in figure 9.

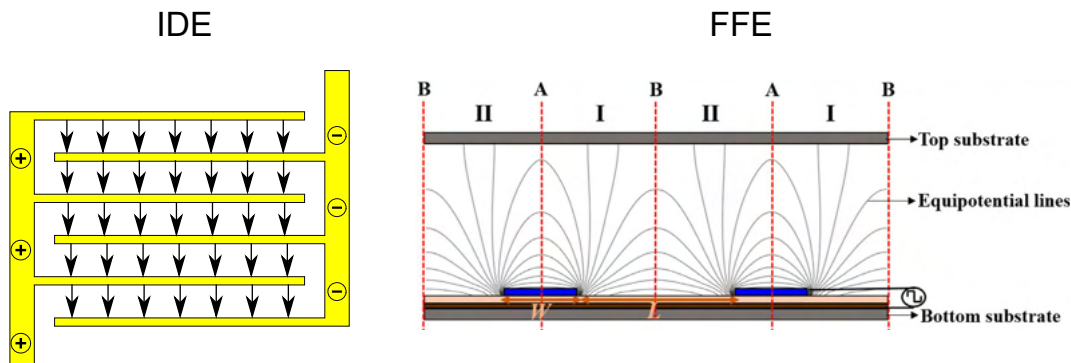


**Figure 9:** Left: Schematic illustration of an IDE with the equipotential lines as arrows. Right: Schematic illustration of the working principle of FFE for the use in liquid crystal displays. The equipotential lines are also illustrated.<sup>[72]</sup>

As seen, both structures offer the possibility to align QRs along their electric fields. These will be analyzed to thoroughly throughout this work.

### 3.3 Synthesis of Nanomaterials

The general synthesis of nanocrystals relies on chemical methods such as the "hot-injection". This is based on the separation of two main processes, mainly the nucleation of the nanocrystal monomers and their subsequent growth. By separating both steps, monodisperse samples (this means colloidal solutions with nanoparticles with a very similar size) can be achieved. Usually, a cold precursor solution containing an organometallic compound and chalcogenide precursors (in the case of metal chalcogenides such as cadmium chalcogenides) are quickly injected into a hot trioctylphosphine oxide (TOPO) solution at high temperatures (usually between 240 °C - 300 °C). Upon addition of a bonding ligand in the reaction solution – e.g. octadecylphosphonic acid (ODPA) – a colloidal solution of synthesized nanoparticles can be obtained.<sup>[3,4,73,74]</sup>

The synthesized nanocrystals are characterized by their unique composition, illustrated in the following figure 10. Here, a typical spherical nanoparticle (figure 10a), surrounded by a bonding ligand, can be observed. Moreover, a core/shell nanoparticle (figure 10b), depicting the core and the shell materials, can be seen.<sup>[10,36,75]</sup>

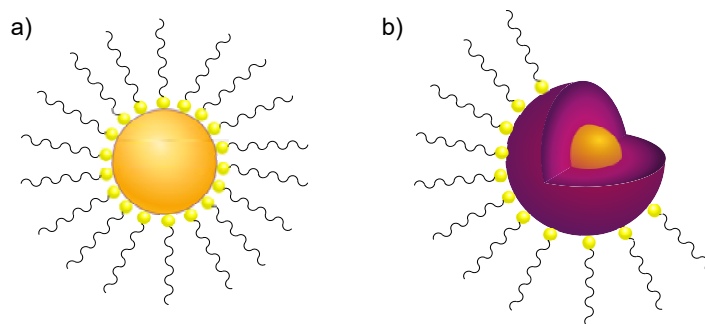


**Figure 10:** Schematic illustration of a nanoparticle and a core/shell nanoparticle. These are stabilized with organic ligands which bond to the surface of the particle.

Nanocrystals are composed mainly of an inorganic core, e.g. CdSe, and an organic ligand, which not only stabilizes the material but also protects it from oxidization, among other processes that can damage the nanoparticle.<sup>[6,33,73,75]</sup> Moreover, by addition of the organic ligand, it is possible to disperse the nanocrystals in organic solvents, enabling their usage in further systems, as well as reducing the crystal defects that could occur after synthesis.<sup>[73]</sup>

The theoretical and physical background on the processes of nucleation and growth can be found in the general literature and won't be discussed here in detail. The general synthesis for elongated CdSe/CdS heterostructures will be discussed briefly in the next chapter. Moreover, the considerations for using a reactor for the synthesis of nanomaterials will also be addressed.

### 3.3.1 Synthesis of Elongated CdSe/CdS Quantum Rods

Synthesis of CdSe/CdS quantum rods was reported by the Weller group in 2003.<sup>[39]</sup> The QRs exhibited high quantum yields (QY = 70 %) and aspect ratios (AR) of up to 5. The reaction involved the use of dimethylcadmium and bis(trimethylsilyl)sulfide (TMSS) as cadmium and sulfur precursors, respectively. The CdS deposition used a solution of the cadmium and sulfur precursors diluted with the CdSe cores in a mixture of hexadecylamine (HDA), TOPO and TOP. Since the use of highly toxic and pyrophoric precursors such as dimethylcadmium is usually avoided, the synthesis was later optimized with different precursors. For this end, the group of Manna reported a synthesis involving a cadmium oxide (CdO) precursor and tri-*n*-octylphosphine selenide (TOPSe)<sup>[76]</sup> This synthesis consisted of a seeded-type growth in which the previously synthesized CdSe cores are used as the so called "seeds" in a hot solution with the mixture of necessary surfac-

tants for the elongated growth. QRs with high ARs and good opto-electronic properties can be synthesized this way. A relationship between QY and AR has been reported by several groups. High QYs can be achieved with AR between 4-5 (QY = 70 %, <sup>[76]</sup> or QY = 90 % with a second CdS shell<sup>[77]</sup>) since many trap states and defects on the CdSe shell can be passivated. However, increasing the amount of CdS to achieve a QR with an increased length (and therefore a higher AR) also induces an increased amount of trap states in the CdS shell, therefore decreasing the QY. This relationship between length and width with the QY has been analyzed by several research groups. Accordingly, the change in absorption and emission in QRs originates mainly from the growth in thickness. Moreover, the drop in QY for longer QRs originates from the probability of exciton recombination decreasing when the excitation occurs at spots which are further away from the core.<sup>[77,78]</sup> The detailed synthesis and mechanism involving the growth of an elongated CdS shell on CdSe cores will be described in the following sections.

### 3.3.2 Reaction Mechanism for CdSe/CdS Quantum Rods

The growth of an elongated CdS shell on CdSe cores follows the principles of a heterogeneous growth. Detailed information about the growth mechanisms (heterogeneous and homogeneous) for nanoparticles can be found in the literature. In the case of CdSe/CdS QRs, the purified CdSe cores are used as seeds for the growth of the second semiconductor material. These are dissolved in a solution including the ligands. The cadmium and sulfur precursors are then injected to the solution at high temperatures, inducing the growth of the CdS shell. Thus, CdS ions bind on the surface of the CdSe seeds. There are several factors which lead to the growth of an elongated shell. First, the crystal structure of the CdSe cores is of main interest. For the successful growth of an elongated shell, CdSe cores crystallizing in the wurtzite structure should be used.<sup>[36,39,76,79]</sup> This is exemplified in the following figure 11.

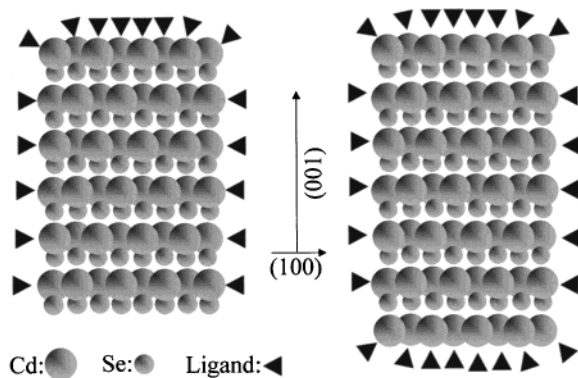


**Figure 11:** Schematic illustration of the CdSe crystal structure exhibiting the growth direction for the wurtzite crystal structure. As can be seen the  $(00\bar{1})$  facet terminates with Selenium atoms without any blocking ligands (triangles), enhancing the growth in this direction. Reprinted with permission from Z. A. Peng, X. Peng, *J. Am. Chem. Soc.* **2001**, *123*, 1389-1395. Copyright © 2001 American Chemical Society.<sup>[79]</sup>

As seen in figure 11 the wurtzite crystal structure of CdSe exhibits two facets of interest, mainly the negatively charged Se atoms in the  $(00\bar{1})$  facet and the positively charged Cd atoms in the  $(001)$  facet. These facets along the  $c$ -axis have only one dangling bond without surface reconstruction. Since the ligands used for the reaction are electron-donating species, these tend to bind only to the cationic species, mainly the Cd ions in the  $(001)$  facet. Therefore, any growth will preferentially happen on the uncoated  $(00\bar{1})$  facet, as seen in figure 11, left. After growing a single Cd monolayer on the  $(00\bar{1})$  facet (figure 11, right), the facet is still active due to the three dangling bonds it possesses.<sup>[79]</sup>

In order to increase the reactivity and enhance the growth in one specific facete, ligands such as phosphonic acids can be added to the reaction solution. Phosphonic acids have a preferred bond to the  $(001)$  facet, which allows the shell growth to be exclusively on the  $(00\bar{1})$  facet. These techniques not only allow the synthesis of elongated CdSe/CdS QRs but also for other 1D and 2D heterostructures.<sup>[80]</sup> Therefore, an exact analysis of the reactive chemistry should always be taken into account. For this end, the reproducibility and optimization for this reaction is performed by adapting the synthesis from a batch procedure (e.g. hot-injection) to a continuous flow microreactor. This will be presented in the following section.

### 3.3.3 Considerations and Principles for the Use of a Reactor In Nanoparticle Syntheses

Nanoparticle syntheses are based on batch processes such as the hot-injection method. This offer a simple and effective approach to synthesize materials and examine their properties. Less is true for the reproduction of these. Due to various factors such as equipment, temperature control and the chemicals itself, reproducibility is one of the main issues in batch syntheses for numerous materials. Furthermore, in spite of the interest these materials offer in various industry sectors, a scale-up of the synthesis comes also into consideration. This is also problematic for nanoparticle syntheses since many reaction parameters tend to change when changing the reaction volume. These problems can be targeted and solved by using a microfluidic reactor. A microreactor itself can be considered as a micro vessel designed to contain and effectively perform a chemical reaction.<sup>[81–83]</sup>

Microfluidic technology offers the advantage of fast screening of different reactions, while precisely controlling its reaction parameters. Flow-based set-ups can improve mass and heat transfer, which makes this technique ideal for medium to large-scale nanomaterial synthesis. Furthermore, by integrating special sensors, it is possible to characterize the materials *in situ*.<sup>[81,84]</sup> This technology has been applied and investigated for the synthesis of various nanomaterials such as CdSe, InP and their CS systems. Although some of their properties still exhibit some potential for improvement, much success has been achieved for their precise parameter control.<sup>[83,85–88]</sup>

In order to precisely adapt batch syntheses into a microfluidic reactor, some of the principles into reactor chemistry will be shortly presented.

Chemical reactors are built around the chemical reaction they must process. In the case of ideal, isothermal reactors there are four kinds:<sup>[89]</sup>

1. The batch reactor
2. The piston flow reactor, or plug flow reactor (PFR)
3. The perfectly mixed, continuous-flow reactor, or continuous-flow stirr tank reactor (CSTR)

#### 4. The completely segregated, continuous-flow stirred tank reactor

The ideal batch reactor is a classic reactor used mainly for organic syntheses. Reactions are carried out inside a glass flask with a reaction volume of few hundred milliliters. The precursors are charged to the system and rapidly mixed and heated. These reactors are mainly used for small volumes. Some of its limitations reside on the heat and mass transfer, which usually emerges after scaling-up the reaction. Moreover, a batch reactor has no input or output of mass during the reaction, unless it is due to the change of the components from a reactive perspective.<sup>[89]</sup>

Aiming at high-volume production, continuous flow reactors are the preferred choice. Since they offer an easier way to scale-up and are easier to monitor during the reaction, they offer a more uniform and cost-effective product. The two most important types of ideal, continuous flow reactors are: the piston flow reactor (PFR) and the continuous-flow stirred tank reactor (CSTR). The completely segregated, continuous-flow tank reactor, although with very interesting theoretical aspects, offers limited practical importance and shall not be further discussed. The PFR behaves like a batch reactor and is usually illustrated as a long tube as in figure 12 (right).<sup>[89,90]</sup>

Here, the reactant enters the reactor at a time  $t = 0$  and flows from the inlet to the outlet without any axial mixing. The reactant reacts as it flows down the tube, thus the tube can be tuned to adjust the reaction (e.g. reaction time) as needed.<sup>[89]</sup>

In contrast to the PFR, the CSTR offers a well mixed volume while maintaining the same concentration, temperature and pressure throughout the system. To guarantee this, the mixing should be sufficiently fast, so that the entering feed is quickly dispersed. Thus, the reaction rate at any point will be approximately the same. Moreover, the outlet concentration will be identical to the internal composition. A schematic illustration of a CSTR and a PFR is shown in figure 12.<sup>[89,90]</sup>

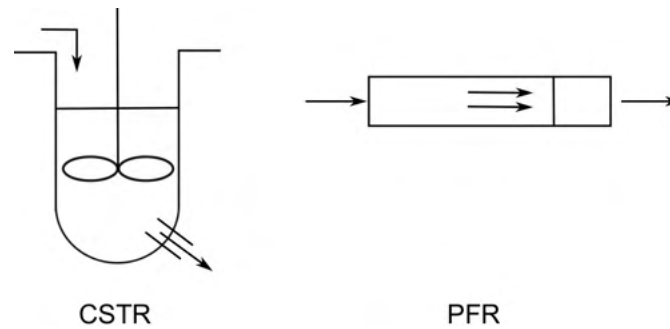


**Figure 12:** Schematic illustration of the two ideal continuous flow reactor types of interest: the CSTR (left) and the PFR (right). As seen in the picture, the CSTR has an inlet which allows the continuous insert of reactans, while the reactor posses a mixer to enable a homogenous reaction. The outlet allows the flow of the reactans. The PFR shows the ideal tubular piston, which enables a continuous flow of the reactants throughout the reactor.

### 3.3.4 Reactor at Fraunhofer CAN

The reactor set-up at Fraunhofer CAN was designed, optimized and patented throughout several works by Dr. Jan Niehaus,<sup>[91]</sup> Dr. Daniel Ness<sup>[92]</sup> and Dr. Tobias Jochum.<sup>[93]</sup> As previously described, this continuous flow reactor is based on a PFR which by adapting the flow rates should ideally exhibit no laminar flow. The reactor is schematically shown in the following figure 13.

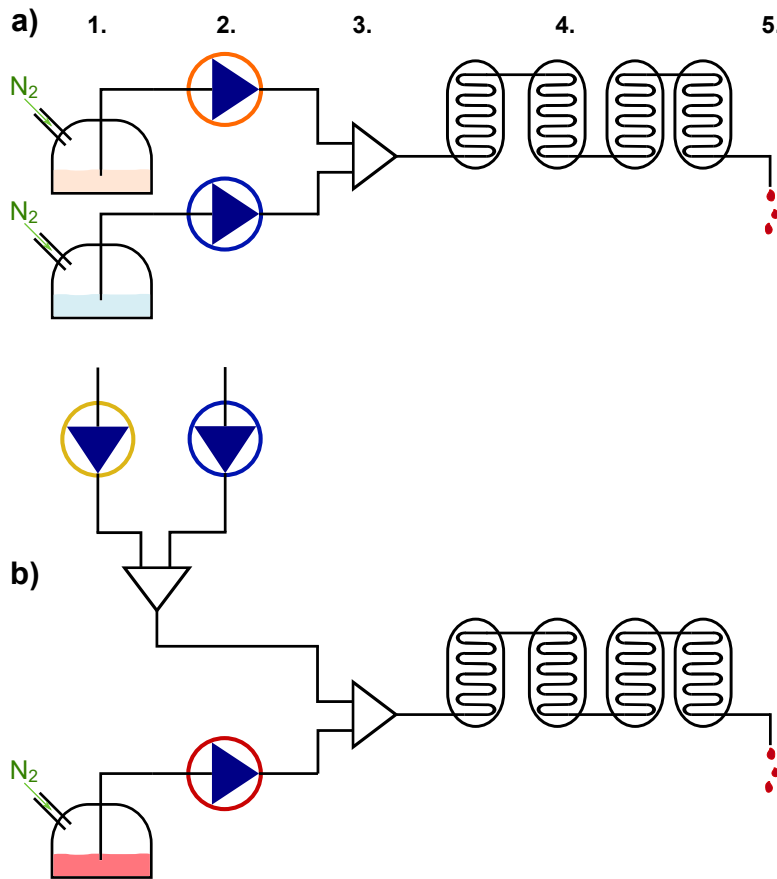


**Figure 13:** Schematic illustration of the reactor set-up at Fraunhofer CAN. **a)** For the synthesis of CdSe cores the reactor consists of the 1. liquid precursors with the selenium source (orange) and the cadmium source (blue). 2. The pump system which adjusts the flow rates of the solutions. 3. The mixing chamber that allows the homogeneous mixture of both precursors and heats the solution to the desired nucleation temperature. 4. The ovens for the growth of the nanocrystals. 5. An outlet to collect the product. **b)** For the synthesis of the elongated CdSe/CdS QRs. The only change are the source of the precursors, where the sulfur (yellow) and cadmium (blue) precursors are mixed first and then mixed with the CdSe cores (red).

As seen in figure 13 the reactor slightly differentiates itself for the synthesis of either a) CdSe cores or b) CdSe/CdS QRs. In detail, the synthesis of CdSe cores requires two precursors which must be in the liquid phase and should not be viscous. The cadmium precursor (either synthesized from CdO or cadmium acetate, see chapter 8.1.2) is represented in blue and is kept under a nitrogen atmosphere to avoid oxidation. The selenium precursor (orange), as well as the cadmium precursor, is pumped via a HPLC pump (figure 13 2.), where the flow rates for the solutions can be measured and adjusted. The pressure can also be controlled in order to identify irregularities which could lead to false results. Next, the solutions are mixed in a mixing chamber (figure 13), this is encased in a heater to allow the heating of the solutions while being mixed. As can be noticed, this step allows the reaction to start, hence the nucleation takes place in this section.



Depending on the reaction, an optional cooler can be added, but for the reactions in this work it was not needed. The solution then flows to the ovens (figure 13 4.) which can be added as needed in order to assure the desired reaction time. Last, the product is collected at the outlet (figure 13 5.).

The synthesis of the CdSe/CdS QRs uses the same equipment, the only difference is that the sulfur (yellow) and cadmium precursors are mixed beforehand at room temperature, while the CdSe cores (red) used for the reaction are mixed afterwards at a second mixing chamber.

As noticed before, the synthesis of the nanoparticles not only have a precise control through the flow rates and temperature in the mixing chambers and ovens, but allows a geometrical separation of the two main steps in nanoparticle syntheses: the nucleation and growth. While the nucleation takes place in the mixing chamber, the growth occurs in the ovens, which are separated themselves. To assure a precise control of the parameters, some considerations must be taken into account. For instance, the flow rates and the reaction time depend on the volumes of the apparatus and the residence time. For this reactor this can be represented with the following equation 4:

$$\tau = \frac{C_{in} - C_{out}}{-r_A} = \frac{V_{tot}}{\dot{V}} \quad (4)$$

Assuming the volumetric flow is constant at the inlet and the outlet, then the residence time ( $\tau$ ) can be calculated with the ratio of the overall reactor volume  $V_{tot}$  and the volumetric flow ( $\dot{V}$ ), the latter which can be calculated by adding the flow rates of the overall solutions. Indeed, the reaction rate  $r_A$  of e.g. reaction "A" is simplified in a PFR since the volumetric flow rate equals the rate of the reaction.<sup>[94,95]</sup>

### 3.4 Quantum Dot-based Light-Emitting Diodes

Colloidal semiconductor nanocrystals exhibit unique properties, which can be easily tuned with their size. Their emission in the visible and near infra-red spectrum makes these materials interesting for several applications in the display technology. Due to their tunable and pure colors emerging from the quantum size effect (see chapter 3.1.1), semiconductor nanoparticles (also called quantum dots: QDs) offer a distinguished advantage over

organic dyes. This is mainly characterized by their narrow emission (with the full-width half-maximum – FWHM of around 30 nm for CdSe), which is much sharper compared to inorganic phosphores (FWHM  $\sim$  50-100 nm).<sup>[14,22,96]</sup> This property together with their high stability make them enhanced luminescent sources of emission color, gamut and brightness. The color quality of emitters can be quantified with the help of the chromaticity diagram set by the Commission International de l'Éclairage (CIE), as seen in figure 14. Here, the colors that are visible to the human eye in terms of hue and saturated color are mapped; hence different possible combinations are illustrated. Typically, combining the emission of three light sources (or "colors") such as red, green and blue (thus the acronym "RGB", see figure 14 b) as an emissive display pixel, a broad amount of colors enclosed in a triangle on the CIE diagram can be generated. As seen in figure 14, using QDs as the sources for RGB emission generate an enhanced color gamut (depicted with the dotted line) in comparison to other standard light sources. Furthermore, the spectral tunability of QDs allows them to be used for the generation of white light, which compared to conventional LEDs, exhibit better properties while maintaining very high efficiencies.<sup>[97]</sup>

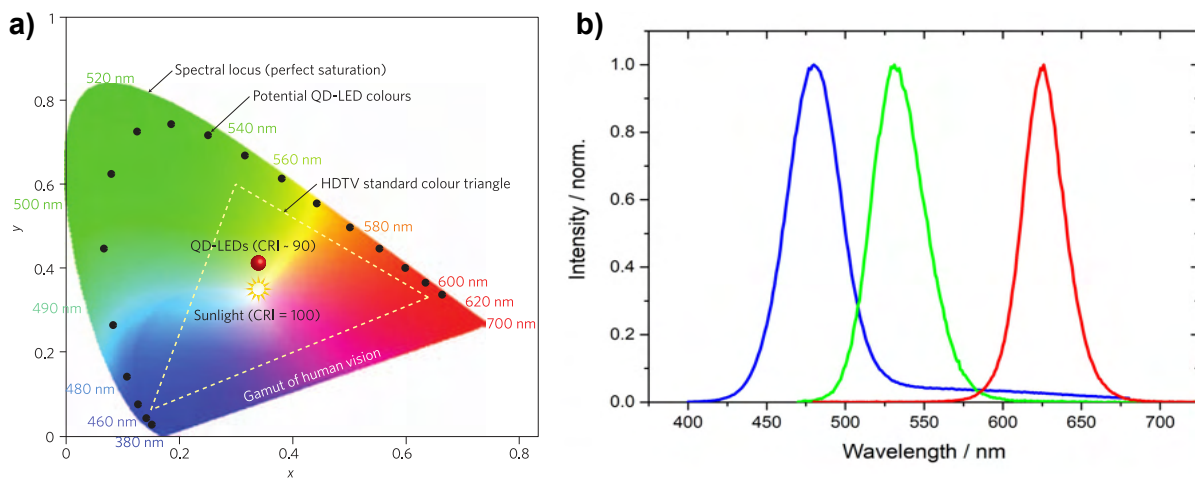


**Figure 14:** Optical properties of QDs for display technologies. a) CIE chromaticity diagram showing the QD gamut inside the dotted triangle. In comparison to high-definition television standard, the gamut emerging from QDs is much better. Reprinted by permission from Springer Nature: Springer Nature Photonics Y. Shirasaki, *et al.*, *Nat. Photonics* **2013**, *7*, 13-23, Copyright © 2013.<sup>[14,97]</sup> b) Sharp band-edge emission from CdSe/CdS heterostructures produced in this work which exhibit the possibility of producing the RGB colors for pixel generation. Combining the RGB emission produces white light.

These properties and advantages added to the high stability of QDs over longer period of time and their enhanced brightness make them unique candidates for the production of QD based emission sources such as: color converters (for the production of liquid crystal

displays: LCDs) and electroluminescent QD based light-emitting diodes.<sup>[14,66,98]</sup> In order to understand the advantages and limitations of QD-based LEDs, their mechanisms for emitting light will be discussed here briefly.

Quantum dot-based light-emitting diodes (QLED) operate in the same way as a conventional LED. In principle, an LED consists of a p-doped (p for positive) anode and an n-doped (n for negative) cathode. By applying a forward bias, holes from the p-doped area can recombine in the emitting layer (EML) under emission of a photon, whose energy corresponds to that of the semiconductor's band gap.<sup>[99]</sup>

In the case of a QLED, the EML consists of the semiconductor nanoparticle, whereas the process involved is called electroluminescence. In principle, electroluminescence describes the effect of light emission from a material excited by electric current as opposed to excitation by light (photoluminescence). This is achieved through radiative recombination of charge carriers, which are injected into the emissive layer. In detail, a QLED consists of several layers which facilitate the charge carrier mobility: the hole injection layer (HIL), the hole transport layer (HTL), the EML and the electron transport layer (ETL).<sup>[3,13]</sup> These can be organic or inorganic compounds and are schematically shown in the following figure 15.

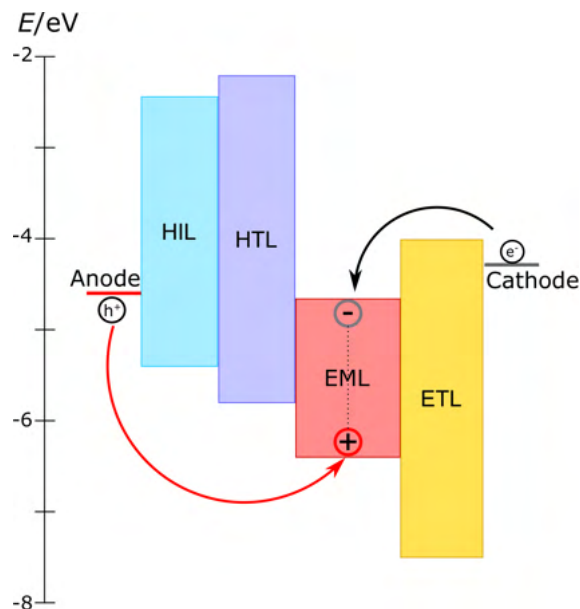


**Figure 15:** Schematic illustration of the band gap alignment for a quantum dot-based LED. By applying a forward bias, holes from the anode and electrons from the cathode are transported through the different layers (HIL, HTL and ETL) to the quantum-dot layer, which acts as the EML. After recombination of both charge carriers, a photon with the energy of the QD band-gap is emitted.

As seen in figure 15 the (QD) layer is embedded between the anode and cathode in order to induce hole and electron injection to the valence band maximum and conduction band minimum of the QD, respectively. This can only be achieved by exact alignment of the band gap edges and enhancement through the HIL, HTL and ETL. These layers facilitate the transport by enhancing the energy offsets considering the mobility, band alignment and charge carrier block properties of the materials.<sup>[14,100]</sup>

There are two possible ways of stacking QLEDs with their different transport layers. The band-edge alignment for these are schematically illustrated in figure 16. Typically, a conventional QLED stack consists of a transparent anode, usually of indium tin oxide (ITO), which allows the trespassing of photons through the material, enabling the emission of these. Due to its low electrical resistivity ( $2\text{-}4\cdot 10^{-4}\ \Omega\text{cm}$ ) caused by oxygen vacancies and substitutional tin dopants, and its high work function, ITO is an ideal material for the use as an electrode.<sup>[101]</sup> In order to enhance the injection of holes and adjust the wide band gap of ITO to the band edges of the EML, a HIL followed by a HTL is deposited into the stack. This not only serves as an enhancer for hole transport, but avoids electrons in the EML to penetrate into the HTL and HIL. Typical HIL include polymers such as poly(3,4-ethylenedioxythiophene)-poly(styrenesulfonate) (PEDOT:PSS) and poly(9,9-dioctylfluorene-*alt*-*N*-(4-*sec*-butylphenyl)-diphenylamine) (TFB) since their HOMO level is between the work function of the ITO and HOMO level of the HTL, which reduces the energy barrier for the injected holes. Some polymeric HTL are poly vinyl(*N*-carbazole) (PVK), 2-biphenyl-4-yl-5-(4-*tert*-butylphenyl)-1,3,4-oxadiazole (PBD) and poly(*N,N'*-bis(4-butylphenyl)-*N,N'*-bis(phenyl)benzidine) (poly-TPD). The injection of electrons into the LUMO level of the ETL (usually ZnO nanoparticles for QLEDs) occurs thanks to the low work function of materials such as magnesium, silver and aluminum.<sup>[3,100,102-106]</sup> Though this stack allows fast processing via spin-coating (usually spin-coating of the polymeric materials in an adequate solvent), the efficiency of this conventional stacking is still very low.

An alternative using mainly inorganic charge transport materials is the use of an inverted stack. Inverted QLEDs (this stacking will be abbreviated with *i*-QLED to facilitate its differentiation) offer more potential for high-performance devices based on their band alignment in multi-layered structures. Inorganic materials used in *i*-QLEDs as HTL have

more feasibility since they align better to the band edges of Cd-based devices. The materials can also be easily deposited via thermal evaporation (with a method called physical vapor deposition – PVD, see chapter 3.6) which allows a controlled and homogeneous deposition of the material. A typical i-QLED uses ITO as the cathode, followed by a layer of inorganic ZnO nanoparticles, which allows for the enhanced transport of electrons as reported by several working groups.<sup>[107–111]</sup> The EML is then embedded between the ZnO nanoparticles and the HTL/HIL. For the HIL some polymeric compounds like 4,4'-Bis(N-carbazolyl)-1,1'-biphenyl (CBP) and tris(4-carbazoyl-9-ylphenyl)amine (TCTA) can be used, which highly enhance the performance of the device.<sup>[103,112–115]</sup> Molybdenum trioxide (MoO<sub>3</sub>) is then used as an inorganic HIL. It can also be doped with magnesium or manganese to enhance performance and stability as reported in the literature.<sup>[116–119]</sup> Finally, silver or aluminum can be used as the anode. Both stacks and their band alignment using typical materials are shown in the following figure 16.

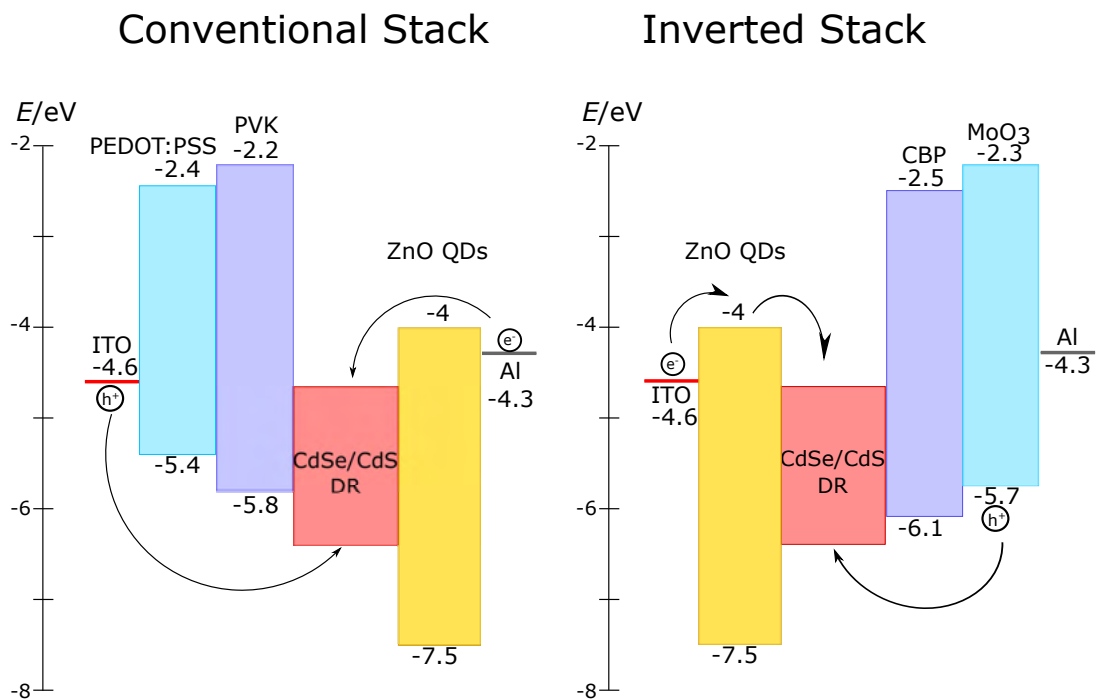


**Figure 16:** Schematic illustration of the band gap alignment for a quantum dot-based LED. By applying a forward bias, holes from the anode and electrons from the cathode are transported through the different layers (HIL, HTL and ETL) to the quantum-dot layer, which acts as the EML. After recombination of both charge carriers, a photon with the energy of the QD band-gap is emitted. Left: band-gap alignment of typical materials used for the fabrication of QLEDs with a conventional stack (band gap energies can be found in the literature).<sup>[3,100,102–106]</sup> Right: band-gap alignment of typical materials used for the fabrication of QLEDs with an inverted stack (band gap energies can be found in the literature).<sup>[103,112–117]</sup>

### 3.4.1 Mechanisms for Efficient Quantum dot-based Light-Emitting Diodes

Emission from QLEDs has its origin from several mechanisms. These are summarized in the following figure 17. Similar to photoluminescence, excitons can be formed in a QLED by absorption of high-energy photons, which after recombination emit a photon with the energy of the QD band gap. Typically for an electroluminescent QLED, excitons originate through either charge carrier injection (figure 17 b) or energy transfer (figure 17 c). While the first one involves a direct transfer of the charge carriers by applying a forward bias, the latter is an indirect injection by other species in the device. This effect is called Förster resonance energy transfer (FRET). Here, the generated exciton energy on the luminescent species is non-radiatively transferred to the EML by dipole-dipole coupling. This is only a viable mechanism if the device contains materials such as emissive polymers, small molecule organics or inorganic semiconductors, which are in close proximity of the QD layer. Since QLED designs mostly include such emissive materials for the charge transport layers, FRET is a dominant process that accounts to substantial exciton losses by the reduced energy transfer from each layer. Last, excitons can be generated by ionization through an electric field (figure 17 d). The electric field in the EML ionizes an electron from one QD to another, thereby generating a hole. Both charge carriers then meet inside the QD film to form an exciton.<sup>[14]</sup>

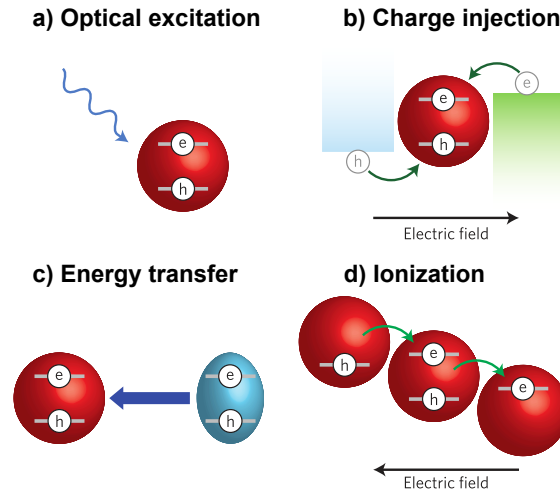


**Figure 17:** Schematic illustration of the different mechanisms to produce excitons in QLEDs. a) Optical excitation after absorbing a photon with high-energy. b) By applying a forward bias, the charge carriers are injected into the EML, forming an exciton in the QD-layer. c) An exciton is transferred via FRET from a nearby donor molecule, such as polymeric materials used as the HTL or ETL. d) By applying an electric field, electrons can be ionized from one nanoparticle to the other forming excitons in the EML. Reprinted by permission from Springer Nature: Springer Nature Nature Photonics Y. Shirasaki, *et al.*, *Nat. Photonics* **2013**, *7*, 13-23, Copyright © 2013.<sup>[14]</sup>

While QY from colloidal nanoparticle solutions can achieve almost unity,<sup>[48]</sup> the performance of QLEDs from a device efficiency perspective is still very low. Several processes contribute to the decrease in QLED performance such as QD photoluminescence quenching, poor photon outcoupling emerging from the unbalanced charge injection and a limited understanding of the operating mechanisms that lead to photon generation inside the device.<sup>[14]</sup> Furthermore, while ligands are optimized for photoluminescence performance, their properties tend to inhibit the proper charge carrier injection inside the EML.<sup>[120]</sup> In order to characterize the performance of a QLED, the efficiency of these will be briefly described.

The efficiency of QLEDs is evaluated in terms of the external quantum efficiency (EQE defined as  $\eta_{ext}$ ). This is defined as the ratio of the number of photons emitted by the QLED into the viewing direction to the number of electrons injected. This can be described with the following equation 5.

$$\eta_{ext} = \eta_{int} \cdot \eta_{oc} = \eta_{oc} \cdot \gamma \cdot \chi \cdot \varphi_{QY} \quad (5)$$

Here,  $\eta_{int}$  is the internal quantum efficiency, which describes the efficiency of the charge recombination process independent of  $\eta_{oc}$ , whereas  $\eta_{oc}$  is fraction of emitted photons

that are coupled out of the device (light out-coupling factor).  $\gamma$  is the charge carrier balance factor,  $\chi$  the spin-allowed optical transition rate and  $\varphi_{QY}$  the internal luminescent QY.<sup>[14,22]</sup> For CdSe species and generally all QDs,  $\chi$  is assumed to be 1, which is identical to the value of most efficient organic phosphors used in organic light-emitting devices (OLEDs).<sup>[121]</sup> Since  $\eta_{oc}$  has typically a value of 20 % in planar devices,<sup>[122]</sup> the parameters that induce the most efficiency degeneration are the charge carrier balance factor ( $\chi$ ) and the internal luminescent QY. This validates the assumptions mentioned before. For instance, photoluminescence quenching is strongly related to the  $\varphi_{QY}$ . While using metal oxides as charge transport layers often increase stability and brightness, these tend to increase the non radiative energy transfer inside the device layers due to the increased charged defect states. Furthermore, by applying a forward bias, the  $\varphi_{QY}$  can be reduced due to an increased in Auger recombination and exciton dissociation.<sup>[14,97,123,124]</sup>

Moreover, the out-coupling efficiency is strongly dependent on the orientation of the emitting dipoles in the QLED.<sup>[22]</sup> Anisotropic geometries such as in QRs can enhance the out-coupling factor and increase the EQE of the device. Suppression of the non-radiative Auger recombination, which is a major hindrance for high EQE values, comes from the delocalization of charge carries along the long axis in QRs. This decreases the Coulomb coupling of excitons, therefore suppressing Auger recombination.<sup>[22]</sup> Added to their polarized emission, which finds further applications in display technologies, these materials offer a novel form of systems that can be used in several different application fields.

### 3.4.2 Polarized Emissive Quantum Rod-based Light-Emitting Diodes

While extensive work has been done for the development of efficient QLEDs based on spherical nanoparticles, less is true for QLEDs based on anisotropic nanocrystals. Due to their usually lower QY<sup>[76-78]</sup> (see chapter 3.3.1), most of the development has been focused on spherical QDs and their integration in high-performance devices. However, due to their elongated structure, these materials offer unique properties that can find application in several fields in the display technology. Due to their polarized emission, QRs are potential candidates for the fabrication of head-up displays and LCDs.<sup>[26-28,66]</sup> For instance, the contrast generation in LCDs is mainly achieved by switching polarized light using liquid



crystals. Since the device includes a back-light unit (usually blue light) and a polarizer, the brightness and energy-efficiency of the device can be severely hindered. Moreover, for further applications like head-up displays or emerging fields like 3D-technologies, the generation of energy-efficient polarized light is of great importance. To this end, polarized light is usually generated by emission of unpolarized light by a conventional LED with the addition of subsequent polarizers. This procedure, as mentioned before, greatly reduces the energy efficiency and overall brightness of the device. By using electroluminescent QLEDs based on anisotropic materials, several points can be targeted. As mentioned in the previous chapters, nanomaterials offer a high color gamut, brightness and stability. This, added to the unique property of generating linearly polarized light, make the fabrication of polarized emissive quantum rod-based light-emitting diodes (PEQLEDs) a novel and interesting procedure for display technologies.

Fabrication of QLEDs based on QRs usually focuses on the enhancement of their performance in terms of EQE (by suppressing Auger recombination),<sup>[125–128]</sup> achieving values of up to EQE = 15 %.<sup>[128]</sup> Less is true for PEQLEDs focusing on their polarized emission. This comes due to the difficult alignment procedures and the implementation of the aligned QRs in a suitable QLED substrate. Hikmet *et al.* reported back in 2005 the fabrication of PEQLEDs by spin-coating a solution of QRs in a polymer solution on to a PVK layer (as the HTL, see chapter 3.4) and rubbing this film uniaxially to achieve oriented QRs. The stack was completed with a 2,2',2''-(1,3,5-benzinetriyl)-tris(1-phenyl-1-H-benzimidazole) (TPBi) layer and barium and aluminum to create the cathode.<sup>[24]</sup> The fabricated PEQLEDs exhibited polarized emission, which can be quantified with the degree of polarization (DOP) in the following equation 6.

$$\text{DOP} = P = \frac{I_{\parallel} - I_{\perp}}{I_{\parallel} + I_{\perp}} \quad (6)$$

Here,  $P$  describes the degree of polarization,  $I$  the intensities of light passing parallel (index  $\parallel$ ) or perpendicular (index  $\perp$ ) to the polarization filter in the measurement (about the measurement see chapter 3.7.3). As can be extracted from the equation, the degree of polarization shows an excess of polarized light in the desired direction.<sup>[129]</sup>

While the PEQLEDs fabricated by Hikmet *et al.* exhibit rather low DOPs with  $P = 0.2$ ,<sup>[24]</sup> increasing the polarization on QLED substrates has not made much progress. The

group of Rizzo *et al.* reported DOPs of around 0.23 by self-assembling QRs dissolved in an organic solvent and adding them on a water surface. This way, the QRs laying on the surface could be transferred with a polydimethylsiloxan (PDMS) stamp onto the QLED stack.<sup>[130]</sup> Newer procedures on producing PEQLEDs with higher EQEs include the Langmuir-Blodgett technique. As reported by the group of Roh *et al.*, using the Langmuir-Blodgett technique to deposit the QRs on an i-QLED stack allows for aligned substrates and efficient PEQLEDs exhibiting EQEs of 10 %. While the photoluminescence from this substrates show DOP of up to 0.21 (in comparison a spin-coated QR-based QLED shows a DOP of 0), the electroluminescence is still very low.<sup>[26]</sup>

For this end, the further optimization of alignment processes which are compatible to the fabrication of suitable electroluminescent QLEDs with polarized emission remains a challenge.

### 3.5 Photolithography

The fabrication of micro-structures is among the most important processes in the semiconductor industry. For the fabrication of electrodes (IDEs, FFEs), diodes, transistors and integrated circuits, photolithography offers the established way to efficiently produce these.<sup>[131–135]</sup> Lithography is the procedure used to transfer a computer-generated pattern onto a substrate (metals, ceramic, organic materials or semiconductors) by the use of photosensitive layers. The generated pattern can then be used to etch the underlying thin film (oxide, nitride, etc.) for various purposes. In detail, photolithography is the lithography art using ultraviolet (UV) light as the exposing source, which passes through a master image (the mask) to the wafers.<sup>[133,136]</sup>

Photolithography as used in this work is divided into the following steps and can be repeated as many times as required to generate the desired structure,<sup>[134,136]</sup> a schematic of the steps is also shown in figure 18.

1. **Pre-treating of the substrate:** To ensure the adhesion of the photoresist, silicon (or silicon dioxide) wafers are dehydrated to remove surface water. In the case of glass substrates, these are cleansed (e.g. using RCA, see chapter 8.3.2) and dehydrated.

2. **Photoresist coat:** Photoresists are usually organic polymers diluted in an organic solvent. These are coated onto the wafer via spin coating to achieve the desired thickness. The thickness can be tuned by varying the spin speed, ramp, viscosity or the temperature.
3. **Soft bake:** Photoresists contain a high amount of solvent even after spin-coating for a certain time. In order to process these, the remaining solvent is evaporated at high temperatures in the step called soft-bake or pre-bake. This stabilizes the photoresists and allows for a proper exposure in the following step.
4. **Exposure:** The substrate can subsequently be aligned in a mask aligner (or a micro writer) so that the desired layer can be properly exposed. Since photoresists are materials that undergo photochemical reactions, a light source (usually UV light) is used to induce the desired reaction. Depending on the type of photoresist, the area exposed to light after passing through a patterned mask will be soluble or insoluble to developers. Positive resists are typically insoluble in the developers, but are soluble after being exposed to light. In contrast, negative resists are soluble in developers and after exposure insoluble. Selective exposure can be achieved by using pre-patterned masks. Masks are usually sheets of glass, partially covered by an opaque material (e.g. chromium) that can be removed according to the desired pattern. A detailed schematic of this step can be seen in figure 18.
5. **Post-exposure bake:** This baking step (some times optional) allows additional chemical reactions or the diffusion of components within the resist film to further stabilize the layer. Additionally, this step fixes the standing wave effect. This effect originates from the exposure light that is reflected by the structure and the mask, which interferes with the incoming light. As a result, the sidewalls of the pattern tend to exhibit a wavelike form. Moreover, post-exposure bake (PEB) enhances the cross-linking during the polymerization while using negative photoresists, therefore improving the stability of the layer.
6. **Development:** During this step the pattern is created by removing and dissolving the either exposed or unexposed photoresist (depending on the photoresist).
7. **Hard bake:** This optional step usually involves the substrate to undergo very high temperatures. Since wafers with photoresist patterns usually go into etch or

ion implantation following the lithography process, this step allows volatile organic materials to leave the substrate.

8. **Etching:** By using wet-etching, the unprotected surface on the surface is prone to other chemicals, which in turn can dissolve the metallic layer and leaving a pattern from the protected area. Ideally, vertical sidewalls are etched due to the different etching rates from horizontal and vertical sidewalls.
9. **Removal:** The last step is the removal of the photoresist to expose the protected pattern. For this end, the photoresist is removed by using wet stripping or plasma stripping techniques. Wet stripping uses organic solvents to dissolve the remaining photoresist. However, the use of organic solvents may leave dirt on the surface of the structure. Therefore, adding a plasma stripping to remove this dirt is always recommended.

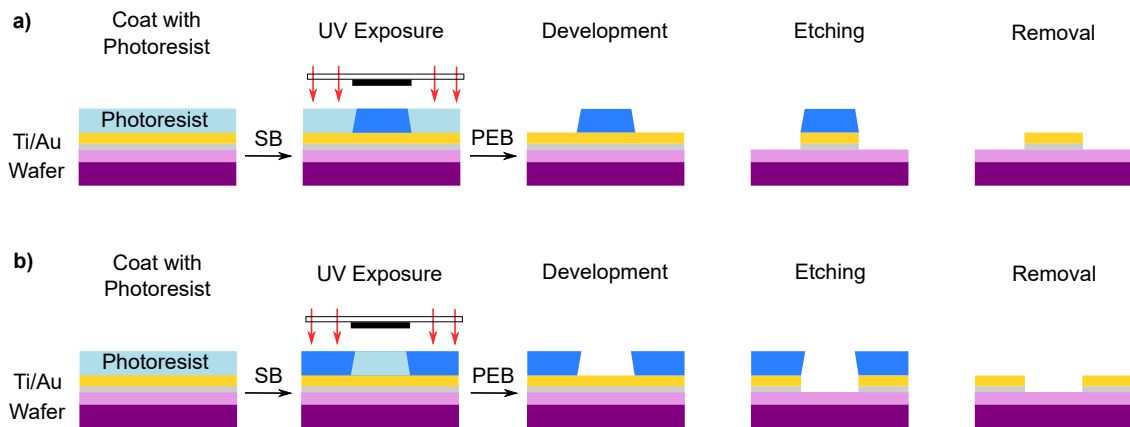


**Figure 18:** Photolithography process for a) Positive photoresist. After coating the substrate (usually a wafer, coated with 10 nm titanium and 40 nm gold) the substrate is exposed to UV light. After the post-exposure bake, the substrate is developed in order to wash away the exposed areas. The Ti/Au layer can then be etched and washed. Last, the photoresist is removed. b) Negative photoresist. The steps are the same, however, the unexposed areas are removed with the developer instead.

Due to the several steps in photolithography, it is always necessary to analyze the substrate's surface (e.g. with light microscopy) in order to find any irregularities such as: over-exposing, under-exposing, dirt or defects in the desired structure.

### 3.6 Physical Vapor Deposition

Physical vapor deposition (PVD) is a process in which materials are vaporized from a solid or liquid state and transported in the form of vapor through high vacuum to a

substrate where it condenses (or sublimates). This way, thin films in the range of few to hundred nanometers can be achieved in a very precise and homogenous way. The coated substrates can be varied in size and composition, moreover, they can include cavities or free-standing membranes, making this process a very attractive way to coat and fabricate devices.<sup>[137,138]</sup>

Advantages of PVD among other coating methods include the variety of materials it can use as a source. These include elements as well as organic compounds and compounds that react during the deposition (e.g. for the deposition of ITO). For instance, metals such as aluminum, silver, titanium and gold are among the typical materials which can be deposited using PVD. For the fabrication of QLEDs, organic compounds such as TCTA or CBP can be deposited in a controlled matter to the LED substrate. Furthermore, reactive deposition processes occur when the depositing material reacts with the ambient gas such as nitrogen or oxygen (as in the case for indium-tin oxide: ITO).<sup>[137,138]</sup>

PVD usually requires the use of high vacuum in a range of  $10^{-5}$  to  $10^{-9}$  mbar, depending on the material being deposited. This is strongly related to the gaseous contamination that is allowed and the densities of the materials being deposited. To this end, the thermal vaporization rate can be very high and the material that is vaporized has a composition which is in proportion to the relative vapor pressures of the material in the molten source. To achieve this, the heated source is usually a tungsten boat, which are resistant to very high temperatures. In order to prevent decomposition or vaporization of the substrate, the substrate which is to be coated is mounted at an appreciable distance from the source.<sup>[137]</sup>

In figure 19, is a picture of the PVD equipment from Fraunhofer CAN used in this work. The chamber includes two sources, where metals can be automatically evaporated using a source controller. The equipment also includes a source for organic compounds. In order to measure the deposited films a quartz crystal microbalance (QCM) is used as a sensor which tracks the amount of material that arrives to the substrate.



**Figure 19:** Equipment at Fraunhofer CAN for the PVD. The vacuum chamber is connected to a turbo pump, which allows the extraction of gas molecules in order to achieve high-vacuum. The chamber has also two inlets, allowing the insertion of materials from the outside as well from inside a glove box.

### 3.7 Analytical Methods

The study of nanocrystals requires the use of several analytical procedures. Among these, absorption and emission spectroscopy, transmission electron microscopy (TEM) and X-ray diffraction (XRD) offer great possibilities to analyze the opto-electronic behaviors, the nanoparticles morphology and size, their elemental composition and their crystallographic data, respectively. Furthermore, the polarization properties of anisotropic nanomaterials require specific methods in order to evaluate values such as the DOP. For their integration in efficient devices, some theoretical backgrounds are also required. These methods are briefly summarized in the following sections.

#### 3.7.1 UV-vis Spectroscopy

UV-vis absorption spectroscopy is a widely used analytical method, commonly used to observe electronic transitions and to determine the concentration of solutions. The basic

principle of this method relies on the absorption of light in the ultraviolet-visible (UV-vis) spectral region that leads to electronic excitation.

UV-vis measurements are operated by a spectrophotometer (figure 20) which measures the transmission, i.e. the intensity  $I$  of monochromatic light after passing through the sample with a defined optical pathway  $b$  in relation to the intensity  $I_0$  of light before passing it. The absorbance  $A_\lambda$  is then defined through equation 7. This relation is known as Lambert-Beer law and puts the absorbance in relation with the concentration  $c$  of a species with a (substance) attenuation coefficient  $\epsilon_\lambda$  in a solution, allowing for quantitative measurements.<sup>[139]</sup>

$$A_\lambda = \lg \left( \frac{I_0}{I} \right) = \epsilon_\lambda cb \quad (7)$$

For the measurements using a spectrophotometer, a reference sample is needed in order to extract the background noise and the solvent, as shown in the following figure 20.

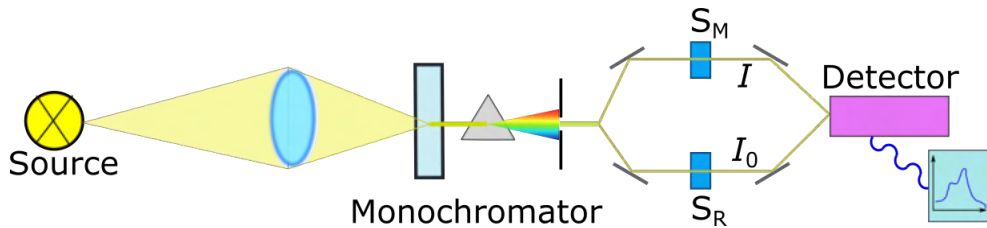


**Figure 20:** Schematic illustration of a spectrophotometer. This includes a light source, a lens to focus the light bundle, a monochromator, the measuring sample of interest ( $S_M$ ), a reference sample which includes the solvent ( $S_R$ ) and a detector. A computer then produces the desired absorbance spectrum.

The concentration and size of nanoparticle solutions, specifically CdSe cores, can also be calculated with UV-vis spectroscopy. For this, the group of Peng *et al.* correlated particle size for CdSe, CdS and CdTe nanocrystals and their absorbance maxima. Thus, the correlation via an empirical fitting function of the curves is shown in the following equation 8:<sup>[140]</sup>

$$D(\text{CdSe}) = (1.6122 \cdot 10^{-9})\lambda^4 - (2.6575 \cdot 10^{-6})\lambda^3 + (1.6242 \cdot 10^{-3})\lambda^2 - (0.4277)\lambda + (41.57) \quad (8)$$

Here is  $D$  the diameter of the CdSe nanocrystal and  $\lambda$  the wavelength of the first excitonic absorption peak of the analyzed sample.

Moreover, it is also possible to determine the attenuation coefficient  $\epsilon$  of the sample through the absorption spectra. For this, the formula designed by Peng *et al.* was further optimized by the group of Jasieniak *et al.*<sup>[141]</sup> Their group correlated absorption properties to simple 0D confinement models in order to generate a formula for  $\epsilon$ , which is shown in the following equation 9.

$$\epsilon_{1S} = 155507 + 6.67054 \cdot 10^{13} \cdot \exp\left(-\frac{E_{1S}}{0.10551}\right) \quad (9)$$

Here, is  $\epsilon_{1S}$  the attenuation coefficient of the CdSe nanocrystals at their 1S transition, hence their first excitonic transition (the unit of interest is  $M^{-1}cm^{-1}$ ). With the energy of the exciton transition  $E_{1S}$  it is possible to transform the equation in order to calculate the concentration  $c$  of the solution. For this, the half-width-half-maximum (HWHM) on the first absorption peak on the low energy side ( $\Delta E_{1S,HWHM}$ ) must be measured. By using Lambert-Beer's law (see equation 7) and rescaling the concentration from the nominal distribution width, the following equation 10 can be obtained:<sup>[141]</sup>

$$c(\text{CdSe}) = \frac{A_\lambda}{b \cdot \epsilon_{1S}} \cdot \frac{\Delta E_{1S,HWHM}}{0.06} \quad (10)$$

### 3.7.2 Emission Spectroscopy

Emission spectroscopy is a sensitive and versatile analytical method typically used for the detection of chemical species and their opto-electronic properties. Measurements are usually performed with a spectrofluorimeter. This instrument uses a single-beam in which the measured luminescence is expressed on a relative scale. Therefore, measurements can be affected by sample properties and instrumental factors such as the intensity of the exciting source, the instrument optics and the signal amplification.<sup>[142–144]</sup>

Spectrofluorimeters are usually composed of a light source, typically a xenon arc lamp with a continuous spectrum between 250 and 1000 nm. Next, an excitation monochromator, followed by the sample, and an emission monochromator are placed in order to select the wavelength of excitation and emitted light, respectively, to be observed by the detector.<sup>[142,143]</sup>



Acquired emission spectra provide relevant information about the nature and energy of the emitting excited state of the probe. In order to record an emission spectrum, data about the absorption must be known beforehand. Thus, the excitation monochromator is set to a wavelength value within the absorption spectrum of the sample. Typically in the last absorption band.<sup>[142,143]</sup>

### 3.7.3 Measuring Linearly Polarized Emission

The emission of aligned QR films, either on an electrode substrate or originated from electroluminescent QLEDs, should be linearly polarized. Linearly polarized light can be mathematically described by its electric field vector  $\vec{E}$ , which oscillates alternatively in the same positive and negative direction.<sup>[145]</sup> This is described with the following equations 11 and 12, where both components of the wave oscillate in phase:

$$\vec{E}_x = E_{0x} \cdot \cos(\omega t - kz) \quad (11)$$

$$\vec{E}_y = E_{0y} \cdot \cos(\omega t - kz) \quad (12)$$

Here,  $E_{0x}$  and  $E_{0y}$  are the amplitudes of the waves in  $x$  or  $y$  direction,  $t$  is the time,  $k$  the wave vector and  $\omega$  the frequency.<sup>[145]</sup>

The quantity of interest for polarization measurements is the intensity of polarized light  $I_0$ , which should be proportional to the electric field vector  $\vec{E}_0^2$ . To analyze the intensity a polarizer and an analyzer (e.g. a CCD camera) are used, whereas the measured intensity is described by Malus' law in equation 13.

$$I(\theta) = I_0 \cdot \cos^2(\theta) \quad (13)$$

Here,  $\theta$  is the angle between the transmission axis of the polarizer and the analyzer. Furthermore, the excess of linearly polarized light, can be described with the degree of polarization as previously described in equation 6 (see chapter 3.4.2), whereas  $P$  represents the amount of light linearly polarized in the desired direction.<sup>[129,145]</sup>

In praxis, the measurement of the DOP on aligned films (such as on electrodes or in PEQLEDs) consists of the following set-up which is shown in figure 21.

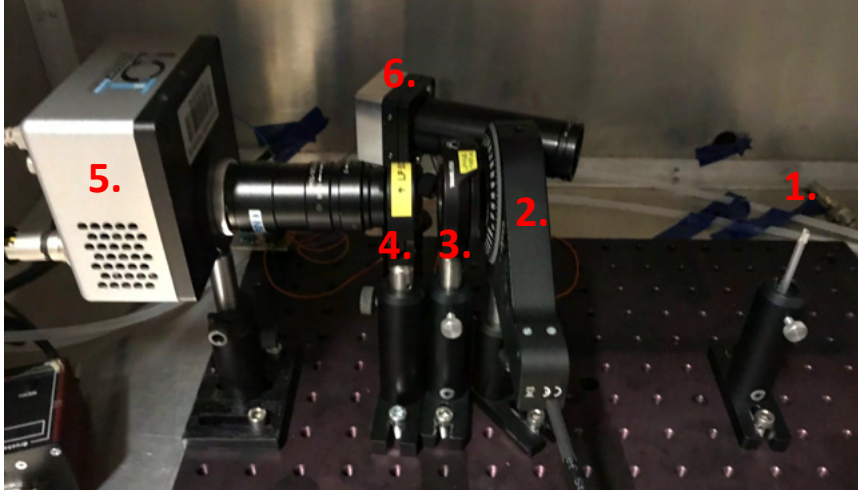


**Figure 21:** Set-up for the measurement of DOP used in this work. It consists of: 1. A sample holder, 2. a half-wave plate, 3. a polarizer, 4. a longpass filter, 5. a CCD camera and 6. a blue LED (with a wavelength of 451 nm).

The sample (figure 21 1.) is fixed and excited with a 451 nm blue LED. In the case of PEQLEDs, the excitation is not needed. The partially linearly polarized light is screened through a polarizer (figure 21 3.) and the excess of blue light is filtered with a longpass filter (figure 21 4.). A CCD camera (figure 21 5.) is then used to analyze the whole picture and scales the brightness of the scan linearly with the intensity changes by rotating the polarizer. Due to changes in the sensitivities of the detection system by rotating the polarizer (in order to achieve a full measurement through all degrees), which are determined by a G factor, a set-up involving a rotating polarizer is usually avoided. To fix it, a turnable half-waveplate is added to the measurement (figure 21 2.) between the sample and the fixed polarizer. Thus, the detector receives light of a constant polarization and the G factor can be neglected.<sup>[129,145]</sup>

### 3.7.4 Measuring the Efficiency of Light-emitting Diodes

Measuring the efficiency of QLEDs can be performed based on an established method reported by Forrest *et al.*<sup>[146]</sup> One of the main aspects to take into account while measuring the efficiency of a QLED is the eye response, described by the photopic<sup>a</sup> luminous efficacy. Thus, the eye response-weighted equivalents of the radiometric quantities of radiance, radiant efficiency and power are the luminance  $L$  (in candelas per meter squared:  $\text{cd}/\text{m}^2$ ),

<sup>a</sup>This is the light-adapted sensitivity of the standard human eye towards light

luminous current efficiency (cd/A) and luminous power efficiency (lm/W). These are important quantities used to describe the properties of a display and are therefore the quantities of main interest while optimizing a QLED device.<sup>[146]</sup>

In detail, to describe the efficiencies of QLEDs and evaluating the fundamental emission properties of these, the external and internal quantum efficiencies must be properly defined. Their dependence is shown in equation 5 (see chapter 3.4.1). In order to measure this, the responsivity of the photodetector as a function of wavelength must be taken into account. This is in order to avoid large errors arising from the slightly broad emission spectra of quantum dots (in comparison to a laser). Taking this into account, the photodiode responsivity  $R(\lambda)$  between wavelengths ( $\lambda$ ) can be defined with the following equation 14.

$$R(\lambda) = \frac{I_{det}(\lambda)}{f(\lambda)P_{QLED}(\lambda)} \quad (14)$$

Here is  $I_{det}(\lambda)$  the incremental photocurrent generated in the photodetector by the QLED's power  $P_{QLED}(\lambda)$  and  $f(\lambda) < 1$  is the fraction of light emitted to that coupled into the detector. With these assumptions, the EQE of the QLED can be calculated with the following equation 15

$$\eta_{ext} = \frac{q \int \lambda I_{det}(\lambda) d\lambda}{hc f I_{QLED} \int R(\lambda) d\lambda} \quad (15)$$

Here, is  $I_{QLED}$  the QLED's measured current,  $h$  Planck's constant,  $q$  the electronic charge and  $c$  the speed of light in vacuum. As mentioned before, in terms of display applications, the luminous current efficiency  $\eta_L$  in candelas per ampere is the proper term to use. The (luminous) current efficiency is equivalent to the external quantum efficiency  $\eta_{ext}$  while also weighting all the incident photons according to the photopic response of the eye. Thus, the luminous efficiency can be expressed with the following equation 16

$$\eta_L = \frac{AL}{I_{QLED}} \quad (16)$$

It is important to note that  $A$  is the device active area, which is not equal to the area of light emission. This is due to the effects of reflection and emission on the side of

the device, which do not contribute to the overall luminous efficiency. The (luminous) current efficiency is an important parameter for device characterization since it contains the sensitivity of a human eye specific to a wavelength. Another way to calculate it is in dependence of the current density  $J$  as in the following equation 17.

$$\text{Current efficiency : } \eta_L = \frac{L}{J} = \frac{(\Phi_{lum} \cdot \pi)/A}{J} \quad (17)$$

Here,  $J$  is the current density (in mA/cm<sup>2</sup>). Lumen and candela are related by 1 cd = 1 lm/sr, therefore for a Lambertian source emitting into the half plane: 1 lm =  $\pi \cdot 1$  cd, as in equation 17.<sup>[146]</sup>

Further, the luminous power efficiency, or luminosity  $\eta_P$  is the ratio of luminous power emitted in the forward direction  $L_p$  to the total electrical power necessary to drive the QLED at a particular voltage  $V$ . Thus, the luminosity can be calculated with the following equation 18:

$$\eta_P = \frac{\phi_0 \int g(\lambda) I_{det}(\lambda)/R(\lambda) d\lambda}{f I_{QLED} V} = f \cdot \frac{\Phi_{lum}}{I_{QLED} V} \quad (18)$$

Here, the luminous flux  $\Phi_{lum}$  is divided by the input of electrical unit power, thus the luminosity (or luminous power efficiency) will be given in lm/W. In order to calculate the luminosity, the normalized photopic response is described by a spectral shape  $g(\lambda)$  with a peak value  $\phi_0 = 683$  lm/W at  $\lambda = 555$  nm with  $g(\lambda = 555 \text{ nm}) = 1$ . This is standardized as the CIE 1931 luminous efficiency function or eye sensitivity function (also found as  $V(\lambda)$ ).<sup>[146]</sup>

Some of the ways of measuring these values involve the use of several set-ups, which have their pros and cons. Assuming a QLED emitted as a Lambertian source, then the use of a commercial luminance meter would be the easiest choice. However, this should only be used for characterizing the actual display performance and not that of the QLED emission. Therefore, a more exact way of measuring the EQE of QLEDs is by using a calibrated photodetector. For instance, a calibrated silicon photodiode, as used in this work. In order to avoid errors originating from the use of lenses and other accumulating items, the diode should be positioned at an intermittent close to the QLED. To avoid losing photons in any direction, the diode should have a bigger active area than that of the QLED. This

way, the coupling factor  $f$  is close to unity and can be neglected. Thus, every photon emitted from the device can be detected in a forward direction to the calibrated detector. With this set-up, the EQE can be directly calculated from the detector photocurrent.<sup>[146]</sup>

### 3.7.5 Transmission Electron Microscopy

The form and size of the synthesized nanoparticles can be analyzed via transmission electron microscopy (TEM). According to the Abbe's diffraction limit, the resolution limit for a typical light microscope lies at 300 nm. Therefore, light microscopy cannot be used for the analysis of nanostructures.

According to the de-Broglie law, the wavelength of an electron is defined by equation 19. Thus, by using high accelerating voltage, they exhibit small wavelengths, which are used to produce the resolution at transmission electron microscopes. The occurrent deflection and scattering phenomena from the accelerating electrons with the sample can be used to produce an image of the analyzed object with a very high resolution.<sup>[147]</sup>

$$\lambda = \frac{h}{p} = \frac{h}{\sqrt{2em_eU^*}} \quad (19)$$

Here,  $\lambda$  is the wavelength of the electrons,  $h$  the Planck's constant,  $p$  the momentum of the electron,  $e$  the elementary charge,  $m_e$  the reduced mass of the electron and  $U^*$  the accelerating voltage of the electrons.

Another type of electron microscopy is the scanning electron microscopy (SEM), which produces images by scanning the surface of a sample with a focused beam of electrons. This method is very effective for the detection of layers in QLEDs, which allows the determination of the thickness each layer has and an overview on their morphology.<sup>[148,149]</sup>

### 3.7.6 Atomic Force Microscopy

For the optimization of the layers in QLEDs in spite of their thickness and roughness, the analysis of each layer's surface is a critical point. To this end, atomic force microscopy (AFM) offers an effective way to analyze the surface in nanometer range of substrates. For this, an  $xy$ -surface is scanned with a cantilever, which detects the height differences

and can determine the roughness of the sample. A cantilever is a plate spring, which is fixed at one end of the device, while the other end supports a pointed tip. The tip can range in very few nanometers and its size should always be taken into account depending on the size limit and the quality the scan should have. As the instrument moves across the sample while the tip is in contact with the surface, the deflection of the cantilever is scanned, thus generating a three-dimensional image of the sample.<sup>[150,151]</sup>

While there are different scanning techniques, AFM uses a flexible cantilever in order to measure the force between the tip and the sample's surface, this can be seen in figure 22 a). The interactions between the tip and the sample can be described with the Lennard-Jones potential.<sup>[150]</sup> This includes a term for the local attractive or repulsive forces which generate the bending on the cantilever tip. In order to detect the bending of the cantilever, a laser beam is focused on the back of the cantilever and through reflexion of it, focused onto a detector. This way, the attractive or repulsive forces cause a deflection of the cantilever towards or away from the sample. As the cantilever deflects, the angle of the reflected laser beam changes and the spot falls on a different part of the photodetector as seen in figure 22 b).<sup>[150,151]</sup>

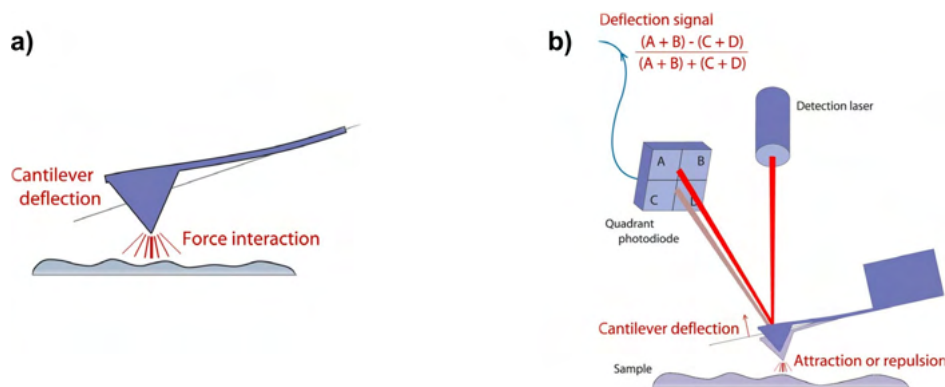


**Figure 22:** a) Working principle of an AFM. The cantilever scans the surface of the substrate while interacting with it in either attractive or repulsive interactions. b) Detection principle for an AFM. Here, a laser beam is focused on the back of the cantilever. While scanning the probe, the cantilever deflection is detected with a photodiode.<sup>[151]</sup>

### 3.7.7 X-ray Diffractometry

X-ray diffraction (XRD) is an effective method to determine the structure of crystalline solids. X-rays are normally directed to a sample under different angles. Rays are scattered when in contact with the atoms at each of the lattice planes. This way constructive

and destructive interference are obtained. Constructive interference can only occur if the scattered waves remain in phase. This means that the difference between the path lengths of two scattered waves is equal to an integer multiple of the wavelength. This condition is also known as the Bragg's condition, which leads to Bragg's law, expressed in the following equation:<sup>[152]</sup>

$$2 d \sin\theta = n \lambda \quad (20)$$

where  $d$  is the interplanar distance,  $\theta$  the scattering angle,  $n$  a positive integer and  $\lambda$  the wavelength of incident wave. Accordingly, a material's characteristic pattern is obtained. This is characterized by the interplanar distances in the crystal which are defined by the Miller indices. For a typical crystal lattice, if the wavelength of the incident wave is known, the interplanar distances of the structure can be calculated from the scattering angle with the following simplified equation 21.

$$d_{hkl} = \frac{\lambda}{2\sin\theta} \quad (21)$$

## 4 Objective

Aim of this thesis is the integration of CdSe/CdS quantum rods synthesized in a continuous flow reactor into polarized emissive quantum rod-based light-emitting diodes. For this, the synthesis of quantum rods using a continuous flow reactor shall be analyzed in scope of varying the properties of the quantum rods. The goal is to facilitate their integration into optical devices and to achieve high degrees of polarization. The advantage of using a reactor lies in its fast and easy screening of reaction parameters, as well as the high throughput of materials it can achieve. These advantages allow for an easy optimization of the reaction to analyze several properties and applications.

In order to achieve polarized emission in an active area, it is necessary to align QRs by applying an electrostatic potential. The alignment procedure shall be optimized in order to achieve high degrees of polarization on a substrate in a reproducible way. The aligned film is then transferred to an LED substrate and thus fabricating the PEQLED. Although several methods are known for alignment of quantum rods, these often integrate polymers which cannot be used for the fabrication of electroluminescent LEDs. Therefore, the alignment procedure without the use of polymers should be extensively investigated to achieve the aforementioned goal.

PEQLEDs offer a very interesting system, which will find application in the display industry, such as head-up displays and LCDs. To my best knowledge, little improvement has been reported on this system with DOPs ranging around 0.2. Thus, critical improvement on the fabrication of these devices is needed and shall be discussed in this work.



## 5 Results and Discussion

The production of polarized emissive quantum-rod based light-emitting diodes (PEQLEDs) is divided into three main procedures. First, the production of the CdSe/CdS quantum rods using a continuous flow reactor. For this work, the synthesized QRs emit in the red (600-630 nm). Second, the alignment of the quantum rods using an electric field on appropriate electrode substrates. The aligned nanoparticle film can then be transferred to a previously prepared ITO substrates. The last step is the fabrication of the PEQLED and its characterization.

### 5.1 Fabrication of CdSe Cores

Synthesis of CdSe cores for their subsequent coating with a CdS shell has been reported in extensive literature reports.<sup>[45,75,153–157]</sup> For this work, the adapted synthesis of Carbone *et al.*<sup>[76]</sup> into a continuous flow reactor was used. This work is based on previous works at Fraunhofer CAN by Dr. Tobias Jochum.<sup>[93]</sup> The main aspects analyzed here were the precise control of the nanoparticle size for the CdSe species. Moreover, the control of the emission wavelength by varying the selenium and cadmium ratios will also be discussed. The influence of the nucleation  $T_N$  and growth temperatures  $T_G$  will be discussed. These are crucial parameters which influence the crystal structure of the nanoparticles and therefore of great importance for the subsequent coating with a CdS shell.

#### 5.1.1 Influence of Nucleation and Growth Temperature

The synthesis of CdSe nanoparticles followed the procedure designed by Dr. Tobias Jochum<sup>[93]</sup> using a continuous flow reactor. Here, a cadmium precursor based on cadmium acetate dihydrate with ODPa and TOPO as ligands and a concentration of  $c = 68$  mM and a selenium precursor based on TOP-Se with a  $c = 680$  mM were used. These are pumped at defined volumetric flow rates to achieve the desired selenium:cadmium ratios and to assure a defined residence time. With the aim of producing high-quality CdSe/CdS quantum rods, the properties of the cores should exhibit the desired wurtzite structure, sharp absorption and emission bands and emit in the desired wavelength. For this work, quantum rods emitting in the red range of the visible spectrum (600-630 nm) were used.

Thus, the cores should be designed to allow the nanoparticles after being coated with CdS to emit in the desired range.

The first parameters to optimize the CdSe synthesis are the nucleation and growth temperatures. As mentioned in chapter 3.3, nanomaterial syntheses are divided into nucleation and growth. Using a reactor allows a geometric and time separation of both steps. While the nucleation takes place in the mixing chamber, growth occurs in the heated ovens.

First, the influence of the nucleation temperature  $T_N$  was analyzed. For this, three CdSe samples were prepared with the following parameters, listed in table 2.

**Table 2:** Reaction parameters used for the synthesis of three CdSe samples using different nucleation temperatures ( $T_N$ ).

| Sample | $T_N$ /<br>°C | $T_G$ /<br>°C | $\tau$ /<br>min. |
|--------|---------------|---------------|------------------|
| CdSe-1 | 350           | 280           | 15.7             |
| CdSe-2 | 375           | 280           | 15.7             |
| CdSe-3 | 390           | 280           | 15.7             |

The samples were analyzed via absorption and emission spectroscopy. The spectra are shown in the following figures 23 and 24.

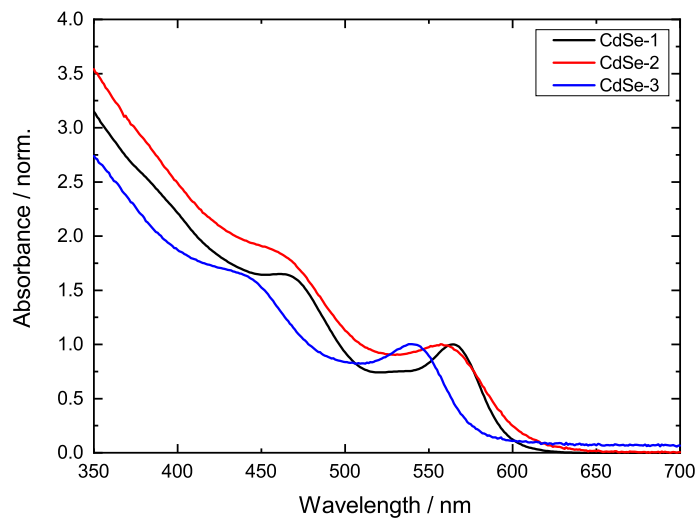


**Figure 23:** Absorbance spectra normalized at their first absorption maximum of CdSe samples at different nucleation temperatures for samples CdSe-1 ( $T_N = 350$  °C), CdSe-2 ( $T_N = 375$  °C) and CdSe-3 ( $T_N = 390$  °C).

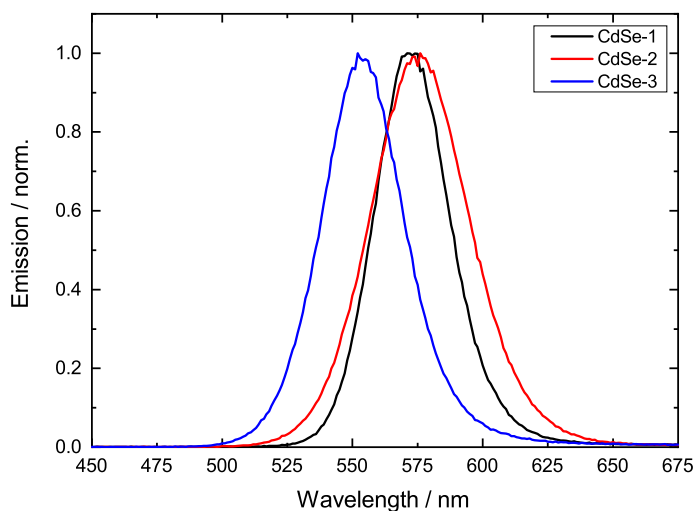


**Figure 24:** Emission spectra of CdSe samples at different nucleation temperatures for samples CdSe-1 ( $T_N = 350$  °C), CdSe-2 ( $T_N = 375$  °C) and CdSe-3 ( $T_N = 390$  °C) at an excitation of 350 nm.

As seen from figure 23 the absorption maximum from each sample blue shifts by increasing the nucleation temperature. While sample CdSe-1 exhibits an absorption maximum at 564 nm, CdSe-2 and CdSe-3 exhibit absorption maxima at 557 nm and 540 nm, respectively. By increasing the nucleation temperature, the amount of nuclei available for the reaction increase. This has a direct effect on the amount of monomers that can be used during the growth phase. If the reaction has more nuclei, the growth of more nuclei induces a reduction of the growth rate, thus shifting the absorption maxima of the nanoparticles to shorter wavelengths. The first absorption maximum broadens by increasing the nucleation temperature. This is also observed at the emission spectra in figure 24. The shift to shorter wavelengths also has a direct relationship to the nanoparticles' size, as explained in chapter 3.1.1. The nanoparticles' sizes were calculated using equation 8 from the absorption spectra. The CdSe samples showed diameters of 3.4 nm, 3.2 nm and 2.9 nm for CdSe-1, CdSe-2 and CdSe-3, respectively. This confirms the shrinking nanoparticle size by increasing the nucleation temperature in the reaction.

The emission from the CdSe samples also exhibit a blue shift by increasing the nucleation temperature. Also, the emission maxima exhibits the typical Stokes shift for nanoparticles. While the difference between samples CdSe-1 and CdSe-2 is negligible, sample CdSe-3 exhibits a blue shift of 22 nm in comparison to the previous samples. It is to be noted

that sample CdSe-2 shows a very broad band edge emission with an FWHM of 43 nm. This is due to a broad size distribution (polydisperse) of the sample.

Next, an XRD analysis of the three samples was performed. In order to coat the CdSe nanoparticles with a CdS elongated shell, a wurtzite crystal structure is desired. The diffractograms are shown in the following figure 25.

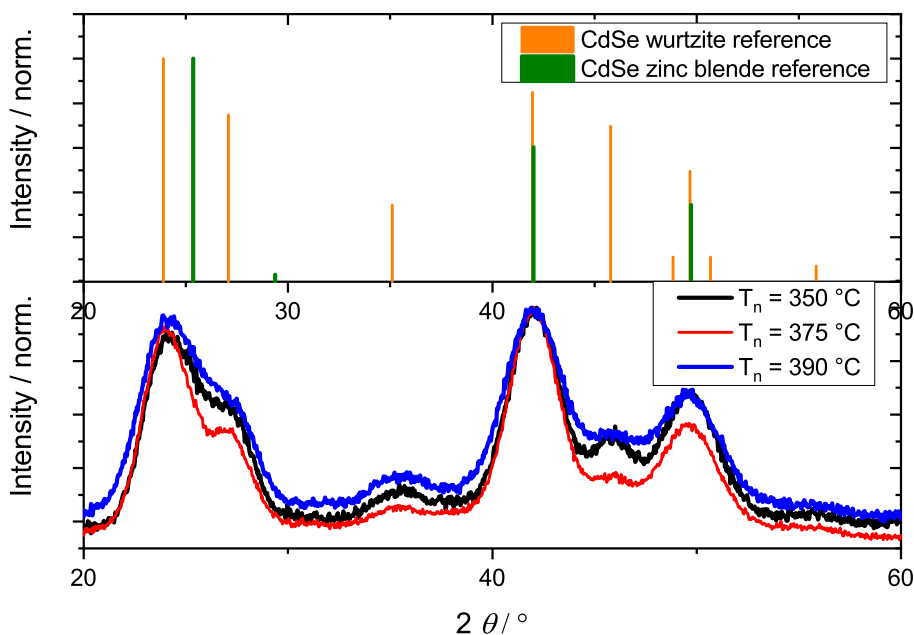


**Figure 25:** Up: Reference reflexes for CdSe in wurtzite and zinc blende. Down: X-ray diffractogram for CdSe nanoparticles with three different nucleation temperatures

As seen from the diffractograms, the samples exhibit broad reflexes typical of nanoparticles. The reference reflexes for bulk CdSe in zinc blende and wurtzite are also shown to facilitate the analysis. It can be observed that all three samples exhibit the typical reflexes for a wurtzite crystal structure. Since the diffractograms exhibit reflexes that are not possible for a zinc blende crystal structure, it is to assume that the nanoparticles crystallize mainly in the wurtzite crystal structure. However, a nucleation at 350 °C and 375 °C exhibit sharper reflexes at the typical wurtzite regions. Although it may be due to a better crystallization of the sample, it is also possible that the sharper reflexes come from the preparation of the sample for the XRD analysis.

Next, the influence of the growth temperature on the CdSe nanoparticle synthesis will be briefly analyzed. Typically an increase of the growth temperature induces a red shift

for the CdSe nanoparticles. However, the quality of the cores may be affected if the temperature is increased to very high temperatures. For this, growth temperatures of 280 °C, 300 °C and 320 °C were used. A nucleation temperature of 375 °C was used in order to guarantee a temperature difference between nucleation and growth. The reaction parameters for the three samples are summarized in the following table 3.

**Table 3:** Reaction parameters used for the synthesis of three CdSe samples using different growth temperatures ( $T_G$ ).

| Sample | $T_N$ /<br>°C | $T_G$ /<br>°C | $\tau$ /<br>min. |
|--------|---------------|---------------|------------------|
| CdSe-2 | 375           | 280           | 15.7             |
| CdSe-4 | 375           | 300           | 15.7             |
| CdSe-5 | 375           | 320           | 15.7             |

The samples were then analyzed for their opto-electronic properties. The absorption and emission spectra are shown in the following figures 26 and 27.

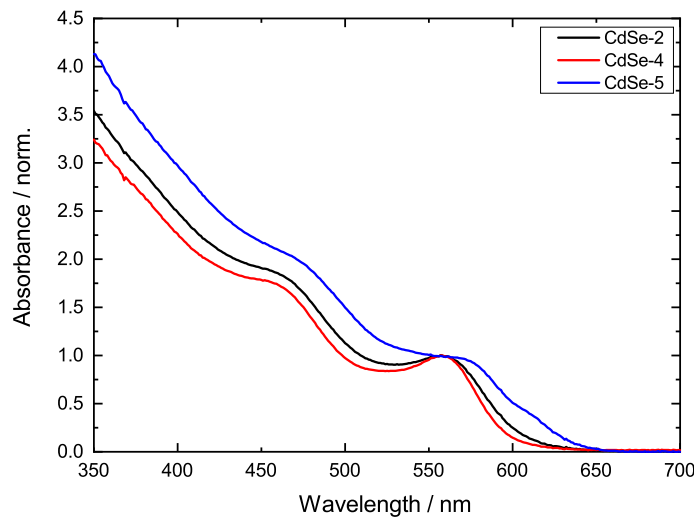


**Figure 26:** Absorbance spectra normalized at their first absorption maximum of CdSe samples at different growth temperatures for samples CdSe-2 ( $T_G = 280$  °C), CdSe-4 ( $T_G = 300$  °C) and CdSe-5 ( $T_G = 320$  °C).

As seen from the absorption spectra, an increase of the growth temperature from 280 °C to 300 °C shows almost no difference. While the sample CdSe-2 exhibits a broader first absorption maximum, the position for CdSe-2 and CdSe-4 is the same. This is not the case for the CdSe-5 sample. Using a growth temperature of 320 °C shifts the maximum

by around 10 nm. This is rather an approximation since the first absorption feature is very broad. A higher growth temperature may induce further nucleation and therefore difficult the separation of nucleation and growth, delivering a sample with low quality. The calculated nanoparticles' sizes (using equation 8) were 3.2 nm, 3.2 nm and 3.6 nm for CdSe-2, CdSe-4 and CdSe-5, respectively. As seen from the nanoparticles' sizes, a higher growth temperature, while maintaining the same growth time, slightly increases the median nanoparticle diameter.

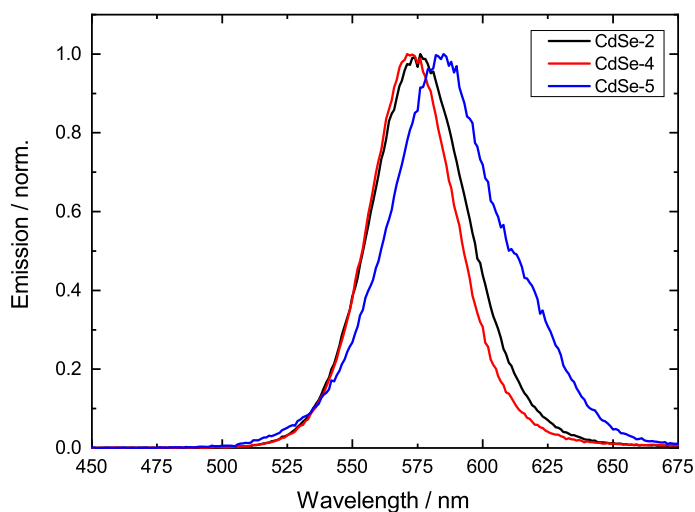


**Figure 27:** Emission spectra of CdSe samples at different growth temperatures for samples CdSe-2 ( $T_G = 280$  °C), CdSe-4 ( $T_G = 300$  °C) and CdSe-5 ( $T_G = 320$  °C) at an excitation of 350 nm.

The emission spectra shown in figure 27 exhibit the same trend as seen from the absorption spectra. A red shift can be observed by increasing the growth temperature to 320 °C. The band gap emission from sample CdSe-5 is very broad and exhibits a shoulder at around 620 nm. This feature may come from further nucleation steps by using a very high temperature, delivering many different species of CdSe.

The results presented above deliver important information for the synthesis of CdSe cores. While increasing the nucleation temperature exhibits a blue shift due to the creation of more nuclei during the synthesis, the increase in growth temperature delivers a red shift. It is to note that choosing very high temperatures for nucleation and growth may deliver nanoparticles with broad absorption and emission features and should be therefore

avoided. Another factor that affects the opto-electronic properties of the CdSe cores is the selenium to cadmium ratios. This will be discussed in the next chapter.

### 5.1.2 Influence of Selenium to Cadmium Ratio

The selenium to cadmium ratio has a direct influence on the synthesis of CdSe cores. This was investigated by using the same procedure with a continuous flow reactor and varying the selenium to cadmium ratios. The syntheses were designed so that the residence times were kept almost the same. While an identical residence time is desired, this is not completely possible since the flow rates that control the selenium and cadmium ratios also have a direct influence in the set residence time.

The parameters used for this analysis are summarized in the following table 4.

**Table 4:** Reaction parameters used for the synthesis of three CdSe samples with three different selenium to cadmium ratios.

| Sample | $T_N /$<br>°C | $T_G /$<br>°C | $\tau /$<br>min. | Se:Cd ratio |
|--------|---------------|---------------|------------------|-------------|
| CdSe-6 | 350           | 280           | 10               | 2           |
| CdSe-7 | 350           | 280           | 9.7              | 1.5         |
| CdSe-8 | 350           | 280           | 10.2             | 1           |

The three samples were analyzed for their opto-electronic properties using absorption and emission spectroscopy. Both spectras are shown in the following figures 28 and 29.

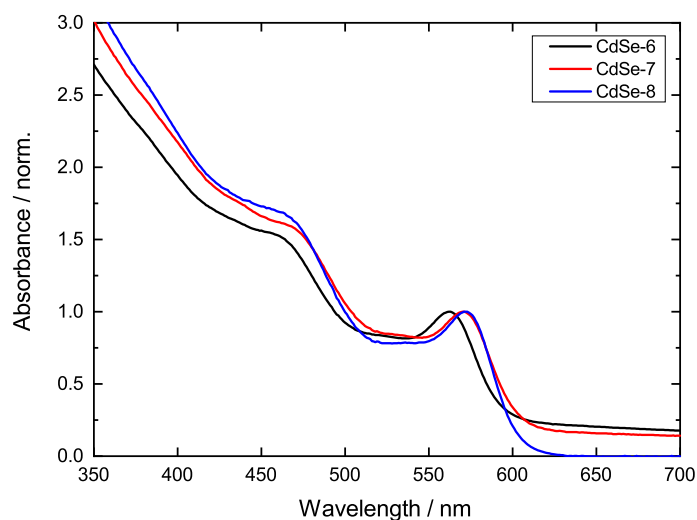


**Figure 28:** Absorbance spectra normalized at their first absorption maximum of CdSe samples with varying selenium to cadmium ratios.

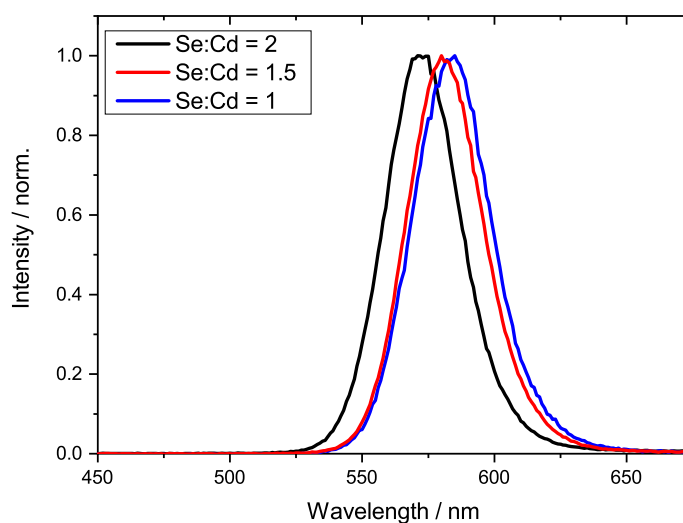


**Figure 29:** Emission spectra of CdSe samples with varying selenium to cadmium ratios at an excitation of 350 nm.

As seen from the absorbance spectra and emission spectra, increasing the selenium to cadmium ratio in the reaction leads to a blue shift of the absorption and emission maxima. The calculated nanoparticles' sizes for the three samples are 3.3 nm, 3.5 nm and 3.6 nm for CdSe-6, CdSe-7 and CdSe-8, respectively. Increasing the Se:Cd ratio comes from increasing the flow rate of the selenium precursor and reducing the cadmium precursor



one. Since the components of both precursors are different, this changes the reactivity of the reaction. The selenium precursor only includes TOP and selenium (as TOP-Se), while the cadmium precursor includes phosphonic acids as ligands. As reported in the literature, secondary phosphines count as the reactive species in nanoparticle reactions.<sup>[158]</sup> Thus, an increase in the amount of TOP increases the reactivity of the solution, inducing more nuclei and therefore a blue shift in the absorption and emission spectra. This trend can be very useful while designing precise syntheses for CdSe cores of any size, and is therefore important to take into account. Moreover, a huge increase in the selenium to cadmium ratios may lead to a defocussing of the reaction, as in the work of Dr. Tobias Jochum<sup>[93]</sup> and therefore should be avoided.

### 5.1.3 Size Control of CdSe Cores

Taking into account the factors described in the previous sections, it is possible to synthesize CdSe nanoparticles using a continuous flow reactor to produce species of any size. This would translate into adapting the reaction time, Se:Cd ratios and temperatures by adjusting the reactor parameters and set-up. The advantage of using a reactor in contrast to a classical hot injection is the possibility to easily adapt the set-up to meet the reaction criteria. For instance, the size control of CdSe cores using a reactor allows the synthesis of clusters with first absorption maxima at around 400 nm. Some of these examples will be briefly presented in this chapter.

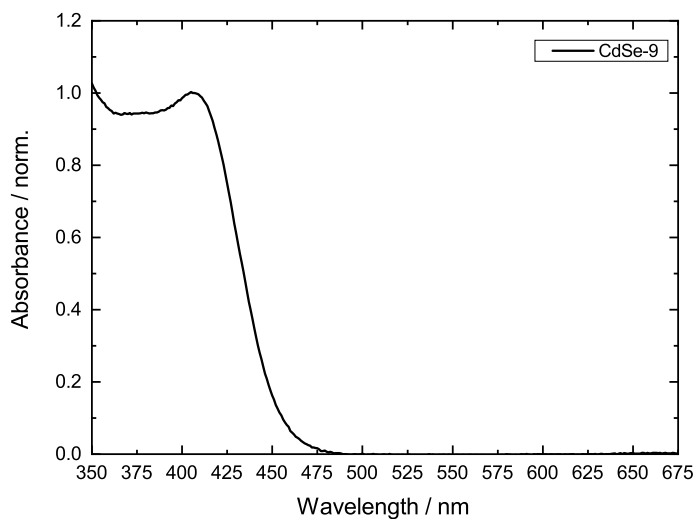
First, the synthesis of small CdSe species which find use for the synthesis of CdSe/CdS CS nanoparticles emitting in the blue or for the analysis of kinetic dynamics of magic size clusters<sup>[84]</sup> will be analyzed. The synthesis followed almost the same procedure as mentioned in the previous chapters. Additionally, a heat exchanger was placed between the mixing chamber and the ovens in order to rapidly cool the solution before allowing it to shortly grow for the desired time. The reaction parameters for this synthesis are summarized in the following table 5.

As can be observed from the parameters, a short residence time and a high Se:Cd ratio are needed. This is to guarantee a small size as seen from the influence of these parameters in the previous chapters. The growth temperature is also kept low in order to avoid a rapid growth of the nanoparticles. The CdSe species were then analyzed via absorption

**Table 5:** Reaction parameters used for the synthesis of very small CdSe species.

| Sample | $T_N$ /<br>°C | $T_G$ /<br>°C | $\tau$ /<br>min. | Se:Cd ratio |
|--------|---------------|---------------|------------------|-------------|
| CdSe-9 | 350           | 180           | 0.56             | 10.5        |

spectroscopy. Such small CdSe species exhibit no typical band gap emission due to their very small size. The absorption spectrum is shown in the following figure 30.

**Figure 30:** Absorbance spectrum normalized at their first absorption maximum of CdSe-9.

As seen, the CdSe species exhibits an absorption maximum at ca. 406 nm, which could be ascribed to one of the magic size nanoclusters of CdSe, mainly  $(\text{CdSe})_{33}$ .<sup>[84,159,160]</sup> This species exhibits typically an absorption maximum at 403 nm, which means the synthesized species are slightly bigger than the expected cluster. The calculated size for the sample was 1.6 nm. Nevertheless, this confirms the possibility of synthesizing rather small CdSe species using the reactor setting. Interestingly, an analysis of the CdSe-9 sample over time revealed the rapid growth of this species under ambient temperature. After purification, the nanoparticles grow and exhibit a slight red shift. However, if the sample is kept in the reaction solution, unpurified, it exhibits a blue shift, which reveals another magic size cluster species. The absorbance spectra are shown in figure 31.

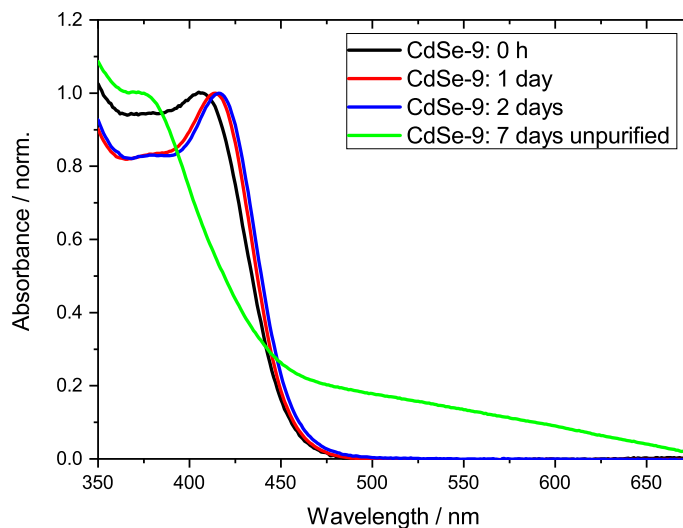


**Figure 31:** Absorbance spectra normalized at their first absorption maximum of the CdSe-9 sample measured at four different times.

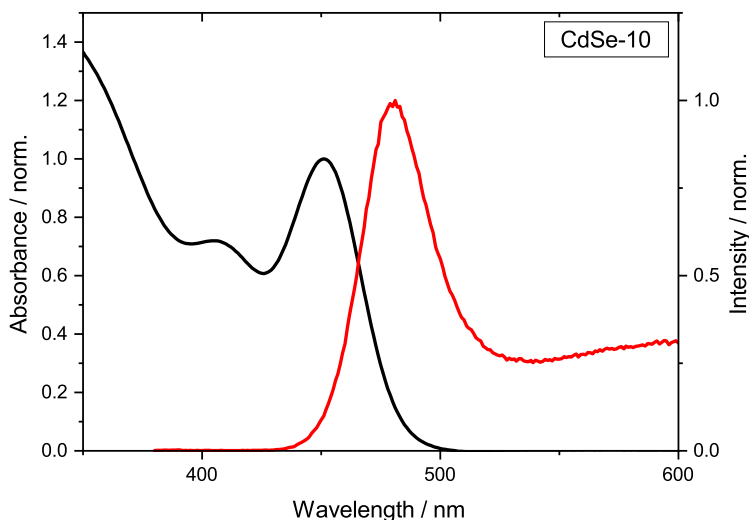
As can be seen from the absorbance spectra, the clusters grow and exhibit a slight red shift to maxima of 413 nm and 416 nm after one and two days, respectively. Keeping the sample unpurified and over a longer period of time, shows the existence of a species with an absorption maximum at ca. 377 nm. This could be ascribed to the magic size nanocluster  $(\text{CdSe})_{19}$  which has an absorption maximum at 380 nm. This feature can also be observed in the other spectra of the purified samples, revealing the presence of the species in the sample. After purification, it is highly possible that the very small species are removed due to their size. In order to further investigate this phenomenon, size selective precipitation would be recommended. This, however, will not be further discussed in this work since it does not contribute to the core of the topic.

With the focus on producing CdSe/CdS quantum rods of any size, cores needed for emission in the green are usually of a size of 1.9 to 2.0 nm. This is also possible by using the same set up as for the CdSe clusters by adding a heat exchanger between mixing chamber and ovens. In order to achieve a bigger size for the nanoparticles a higher growth temperature and a longer residence time are needed. The parameters used for this synthesis are summarized in the following table 6.

**Table 6:** Reaction parameters used for the synthesis of CdSe species for the synthesis of green emitting QRs.

| Sample  | $T_N$ /<br>°C | $T_G$ /<br>°C | $\tau$ /<br>min. | Se:Cd ratio |
|---------|---------------|---------------|------------------|-------------|
| CdSe-10 | 350           | 210           | 1.7              | 10.5        |

As can be seen from the parameters, these are adapted from the previous synthesis and adjusted to achieve a bigger size. The synthesized nanoparticles were analyzed via absorption and emission spectroscopy. Both spectra are shown in the following figure 32.

**Figure 32:** Absorbance spectrum normalized at their first absorption maximum of CdSe-10 and emission spectrum normalized at its maximum for the same sample.

The absorption spectrum exhibits a first absorption maximum at 451 nm, while the emission maximum, due to the Stokes shift, at 480 nm. The emission also exhibits a defect fluorescence starting from ca. 530 nm. The calculated size for the synthesized nanoparticles was of 1.96 nm, which is in the range needed for the synthesis of green emitting QRs. This also confirms the adaptability of the reactor for the desired CdSe species. Due to the very small size of the nanocrystals, the surface to volume ratio is very high. Thus, the amount of defects on the surface tends to be higher. This would explain the observable defect fluorescence from the sample.

Last, the main species used for this work, is the synthesis of CdSe cores which allow the production of CdSe/CdS QRs emitting in the red. Depending on the length of the

rod, cores emitting between 570 nm and 590 nm are needed. The synthesis followed the same procedure described in the previous chapters, without the use of a heat exchanger. A factor that was investigated was the influence of the nucleation temperature on the cores for the polarization properties after being coated with a CdS shell. Therefore, CdSe cores synthesized at two different  $T_N$  will be addressed. The nucleation temperature was analyzed with the aim of producing CdSe samples with a higher wurtzite crystal structure and therefore induce the strain needed for polarized emission as discussed in chapter 3.2. The parameters for the synthesis of the CdSe cores used for the QRs in this thesis are summarized in the following table 7.

**Table 7:** Reaction parameters used for the synthesis of CdSe cores used for the synthesis of red emitting QRs.

| Sample  | $T_N$ /<br>°C | $T_G$ /<br>°C | $\tau$ /<br>min. | Se:Cd ratio |
|---------|---------------|---------------|------------------|-------------|
| CdSe-6  | 350           | 280           | 10               | 2           |
| CdSe-11 | 350           | 290           | 10               | 1.5         |
| CdSe-12 | 350           | 290           | 10               | 1.5         |
| CdSe-13 | 375           | 290           | 15.6             | 2.3         |
| CdSe-14 | 375           | 290           | 15.6             | 2.3         |
| CdSe-15 | 375           | 300           | 15.6             | 2.3         |

As seen from the parameters above, the reactions involving a nucleation temperature at 350 °C quite differ from those with a  $T_N$  of 375 °C. A nucleation at lower temperature, as explained in chapter 5.1.1, leads to a red shift of the optical properties, thus to nanoparticles of a bigger size. In order to obtain cores in the same range of band edge emission, the residence time is reduced for the cores with  $T_N = 350$  °C. Thus, reducing the reaction time. The difference in the Se:Cd ratios comes due to the set-up used for the different reactions. The syntheses with a Se:Cd ratio of 1.5 used two ovens, while the one with Se:Cd = 2, four ovens. In order to adapt the volumetric flow rates in order to achieve the same residence time, a slight change in the Se:Cd ratios was done. As for the set-up for the cores synthesized with a  $T_N = 375$  °C, this was kept identical. The opto-electronic properties of the nanoparticles are shown in the following figure 33.

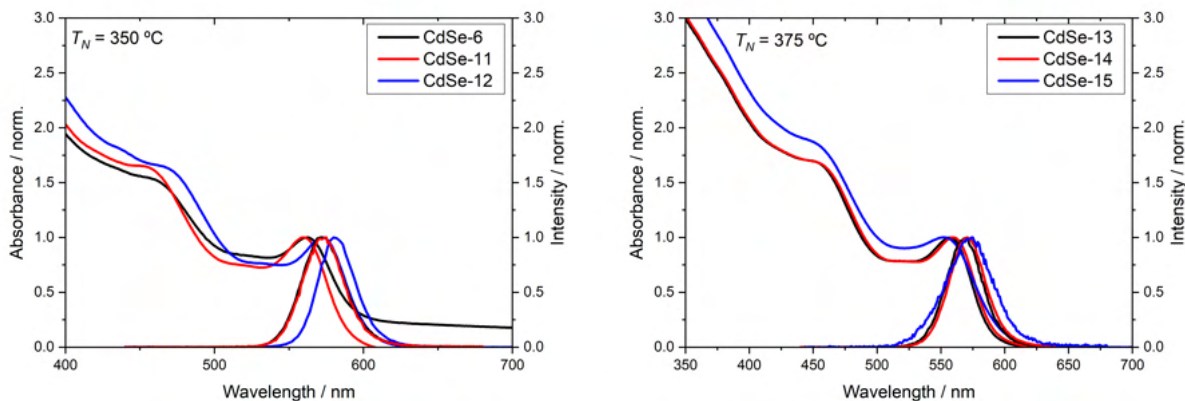


**Figure 33:** Absorbance and emissionspectrum normalized at their first excitonic transition for (left) CdSe cores synthesized with a  $T_N = 350$  °C and (right)  $T_N = 375$  °C.

As seen from the spectra above, using a nucleation temperature of  $T_N = 350$  delivers CdSe species with their first absorption maximum at 562 nm, 560 nm and 573 nm for samples CdSe-6, CdSe-11 and CdSe-12, respectively. While the two samples only differ by two nanometers, the third exhibits a difference of almost 13 nm, even with the same parameters as sample CdSe-11. This difference usually origins from impurities in the reactor pipes. As mentioned in chapter 3.3.3 using an ideal PFR relies on a constant volumetric flow in order to guarantee a reproducible reaction. While this is true for an ideal set-up, the reactivity of the precursors and the flow inside the set-up usually vary. If impurities such as CdSe residues stick on the titanium pipes, then the flow won't be ideal and will be rather laminar. This, added to the slower flow inside the reactor may increase the residence time, the homegeinity and thus lead to a red-shift and broadening of the absorption and emission features. Indeed, when comparing the FWHM values of the three samples, it is clear that sample CdSe-12 shows a rather broad FWHM with 34 nm in comparison to 30 nm and 31 nm for CdSe-6 and CdSe-11, respectively. The absorption maxima, emission maxima, calculated diameters and FWHM of the samples are summarized in table 8.

As for the CdSe species synthesized with  $T_N = 375$  °C, these all exhibit almost the exact absorption and emission maxima<sup>b</sup>, while increasing the growth temperature by 10 degrees only broadened the band gap emission of the synthesized nanoparticles. This means a more polydisperse sample was obtained.

<sup>b</sup>The summarized values are found in table 8

**Table 8:** Summarized values for the synthesized CdSe cores using two different nucleation temperatures for the production of red emitting QRs.

| Sample  | Absorption<br>maximum | Emission<br>maximum | FWHM<br>nm | Diameter<br>nm |
|---------|-----------------------|---------------------|------------|----------------|
| CdSe-6  | 562                   | 572                 | 30         | 3.3            |
| CdSe-11 | 560                   | 570                 | 31         | 3.3            |
| CdSe-12 | 573                   | 585                 | 34         | 3.6            |
| CdSe-13 | 560                   | 571                 | 33         | 3.3            |
| CdSe-14 | 560                   | 571                 | 33         | 3.3            |
| CdSe-15 | 553                   | 573                 | 43         | 3.1            |

The synthesized CdSe cores, as described in this section, can be used for the synthesis of various CdSe/CdS species. For that reason, a precise control of their size, while retaining good properties reflected in sharp emission bands, is of main interest. With the methods described here, it was possible to use the CdSe cores for the synthesis of quantum rods. For that, the purified cores were dissolved in TOP to achieve a concentration of  $c = 100 \mu M$ . The next chapter will focus on the synthesis of CdSe/CdS quantum rods for their integration in novel optical devices.

#### 5.1.4 Summary

The synthesis of CdSe nanoparticles using a continuous flow reactor was analyzed in order to design a proper control of the nanoparticles' size. With the aim of coating the cores with an elongated CdS shell, several species were investigated.

First, the influence of nucleation and growth temperatures was briefly addressed. The trends correlate with theoretical assumptions and with previous work. These two parameters allow the control of the nanoparticles' size while the optimization of these exhibit sharp absorption and emission features.

Next, the selenium to cadmium ratio was analyzed. This revealed that an increase in the Se:Cd ratio leads to a blue shift of the absorption and emission features. This is related to the reactivity of the solution which is changed by changing this parameter in the reactor.

Last, a brief overview on the different CdSe species that can be synthesized with the reactor set-up was given. It is possible to synthesize CdSe magic size clusters and CdSe species for the fabrication of CdSe/CdS heterstructures. This is possible by adapting the

reactor set-up and the reaction parameters. The CdSe cores synthesized for this work were also addressed.



## 5.2 Fabrication of CdSe/CdS Quantum Rods

The fabrication of CdSe/CdS quantum rods (QRs) follows a two step procedure as described by Carbone *et al.*<sup>[76]</sup> and was adapted and optimized for a continuous flow reactor in the works of Dr. Tobias Jochum.<sup>[93]</sup> The first step is the synthesis of the CdSe cores as described in the previous chapter. After purification of these, the cores are dispersed in TOP to achieve a concentration of  $c = 100 \mu\text{M}$  and stored in a sure-store flask. Opposed to the works of Dr. Tobias Jochum, the cadmium precursor for the syntheses used in this work was based on cadmium acetate. However, for the synthesis of blue and green emitting CdSe/CdS heterostructures a precursor based on cadmium oxide is recommended. The sulfur precursor ( $c = 2\text{M}$  in TOP) and the cores are pumped and mixed at room temperature. These are then mixed at  $100 \text{ }^\circ\text{C}$  with the cadmium precursor ( $c = 6\text{mM}$ ) and pumped to the ovens to slowly grow the CdS shell at  $320 \text{ }^\circ\text{C}$ . In contrast with the production of the CdSe cores, the volumetric flow rates can be adjusted to the desired Cd:Core and S:Cd ratios. All these parameters have a direct influence on the length, width and quantum yield of the synthesized quantum rods.

For this work, the production of several CdSe/CdS QRs emitting in the red (600-630 nm) with varying aspect ratios (ARs), or specifically, varying lengths and widths, was analyzed. The production of high quantities of the material is wished, since the optimization of the alignment procedure requires a high amount of the product of the same sample. In the following sections, some of the aspects that influence the properties of the synthesized QRs using a continuous flow reactor will be addressed. However, the main use of the reactor for the production of QRs in this work was the high throughput of the material, the easy screening of parameters to analyze their polarization properties on optical devices and the facilitated production of QRs which meet specific criteria for the fabrication of PEQLEDs.

### 5.2.1 Influence of Growth Temperature

The synthesis of CdSe/CdS QRs follows a heating up procedure in which the mixed precursors at  $100 \text{ }^\circ\text{C}$  are then quickly heated to a set growth temperature  $T_G$ . Typically, this temperature is set very high to guarantee the growth of a sufficient CdS shell for long

rods. This parameter will be addressed in this chapter. For this, two growth temperatures for four different samples were chosen to analyze the trend. Here, a CdSe sample was used for the synthesis of both QRs with a  $T_G$  of 280 °C and 320 °C. The samples and the parameters used for the synthesis are summarized in the following table 9.

**Table 9:** Reaction parameters used for the synthesis of three CdSe samples with three different selenium to cadmium ratios.

| Sample | $T_G$ /<br>°C | $\tau$ /<br>min. | S: Cd | Cd: CdSe | CdSe Sample |
|--------|---------------|------------------|-------|----------|-------------|
| QR-1   | 280           | 28               | 6.3   | 6314     | CdSe-1      |
| QR-2   | 280           | 28               | 6.3   | 6314     | CdSe-2      |
| QR-3   | 320           | 28               | 6.3   | 6314     | CdSe-1      |
| QR-4   | 320           | 28               | 6.3   | 6314     | CdSe-2      |

As seen from the parameters above, a high sulfur to cadmium ratio as well as a very high cadmium to CdSe ratio are needed. Indeed, the cadmium (set by the volumetric flow rate of the cadmium precursor) volumetric flow rate is set at high values. This is to adjust the flow rate for the high volume inside the ovens. Moreover, the synthesis of a CdS shell requires both precursors to build an elongated shell throughout the whole reaction, therefore enough of both materials is needed. The high sulfur ratio is needed, as reported in the initial synthesis reports,<sup>[39,76]</sup> to guarantee the building of an elongated shell. This enhances the growth of the shell along the  $c$ -axis and is therefore a requirement for the syntheses of all QRs. Furthermore, a growth time of 28 min. is required, in order to allow the CdS shell to be properly coated. The synthesized QRs were characterized via absorption and emission spectroscopy and their spectra are shown in the following figure 34.

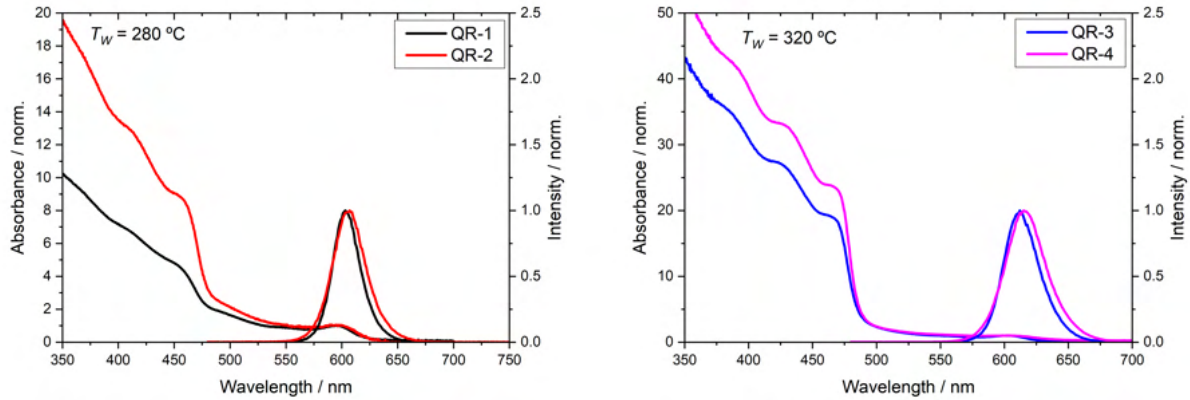


**Figure 34:** Absorbance and emission spectrum (excitation at 450 nm) normalized at their first excitonic transition for (left) CdSe/CdS QRs synthesized with a  $T_G = 280$  °C and (right)  $T_G = 320$  °C.

As seen from the absorption spectra, the CdSe/CdS QRs exhibit the typical features of such a heterostructure. After the first absorption maximum belonging to the CdSe cores (ca. 600 nm), the absorbance rapidly increases to exhibit the absorption maximum of the CdS shell at around 450 nm. The important values for the synthesized QRs are summarized in table 10. Increasing the growth temperature of the QR synthesis, shows an increase in the CdS features in the absorbance spectra. This means a higher amount of CdS is present. Furthermore, the emission maxima are red shifted. Following the quantum size effect and the confinement of this C/S system, a red-shift of the emission features should account to a wider and longer CdS shell (hence a weaker confinement). To confirm this, TEM images of the synthesized quantum rods were analyzed. The TEM images are shown in the following figure 35.

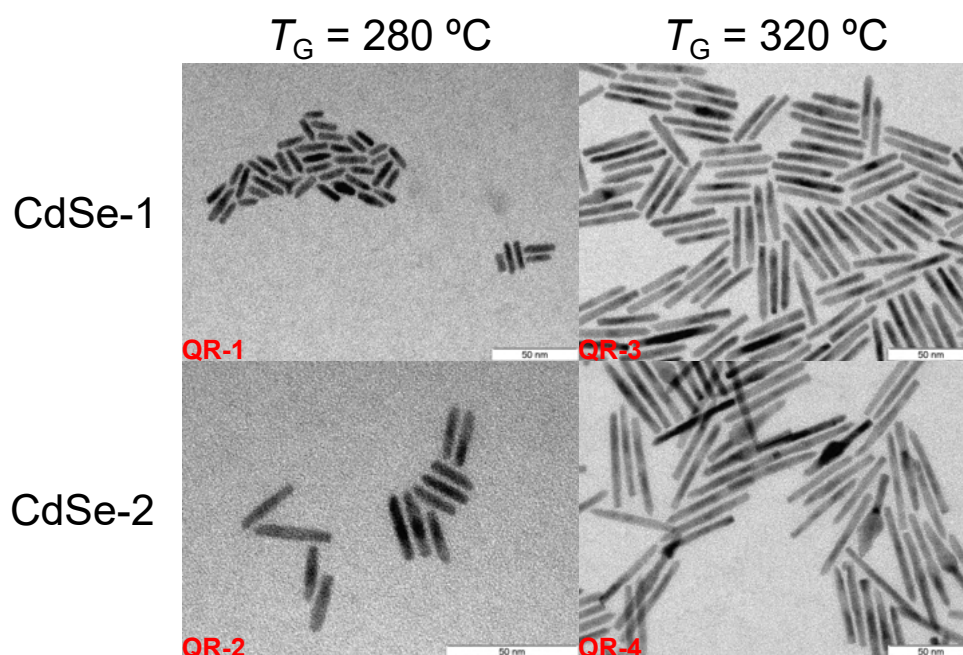


**Figure 35:** TEM images of the synthesized QRs with two growth temperatures: 280 °C and 320 °C for two different CdSe cores.

As seen from the TEM images, an increase of the growth temperature in the reaction leads to an increase of the deposited CdS material. This leads to longer quantum rods. This trend can also be observed in the absorbance spectra, as mentioned before. In table 9 the length and width of the synthesized quantum rods are summarized. Interestingly, the increase of the QR's length is not proportional with the increase of the QR's width. Due to the growth mechanism and the used ligands in the synthesis, as explained in chapter 3.3.1, the CdS is built predominantly along the *c*-axis. The width, however, still increases from QR-1 to QR-3 by 0.5 nm, while for the other two species by almost 1 nm. The increase in both width and length are also reflected in their optical properties with the increase of the CdS features and the observed red-shift of the maxima (at around 10 nm). The enhanced growth of the CdS shell due to an increased temperature is due to the increase in reactivity in the reaction and thus in the kinetics.

The quantum yield for the synthesized quantum rods remains pretty constant. This is reflected by comparing samples QR-1 and QR-3, where an increase in the rod's length does not imply a decrease in the quantum yield. This comes from the successful coating of the CdSe cores with a CdS shell. The slight increase in the width may lead to a marginal increase of the quantum yield. This is not true for samples QR-2 and QR-4, where an increase of the rod's length decreases the quantum yield. This may not directly come

**Table 10:** Summarized values for the synthesized CdSe/CdS quantum rods using two different growth temperatures.

| Sample | Absorption<br>maximum | Emission<br>maximum | FWHM /<br>nm | Length /<br>nm | Width /<br>nm | QY /<br>% |
|--------|-----------------------|---------------------|--------------|----------------|---------------|-----------|
| QR-1   | 594                   | 604                 | 28           | $15.9 \pm 2.4$ | $4.4 \pm 0.4$ | 70        |
| QR-2   | 595                   | 605                 | 34           | $24.5 \pm 2.5$ | $4.4 \pm 0.5$ | 75        |
| QR-3   | 602                   | 612                 | 32           | $40.8 \pm 4.5$ | $4.9 \pm 0.6$ | 71        |
| QR-4   | 605                   | 617                 | 37           | $57.8 \pm 4.0$ | $5.3 \pm 0.9$ | 63        |

from the quality of the rod but from the rather low monodispersity, as seen from the increase in the FWHM. Side nucleation while building CdS and tetrapods, is also possible by increasing the growth temperature and therefore could, in the worst case, lead to the decrease of the quantum yield. Additionally, the length of QR-4 is substantially larger than all the other samples. Coating a very large CdS shell also leads to the creation of defects in the crystal structure of the shell, thus, the quantum yield can also decrease the longer the shell.

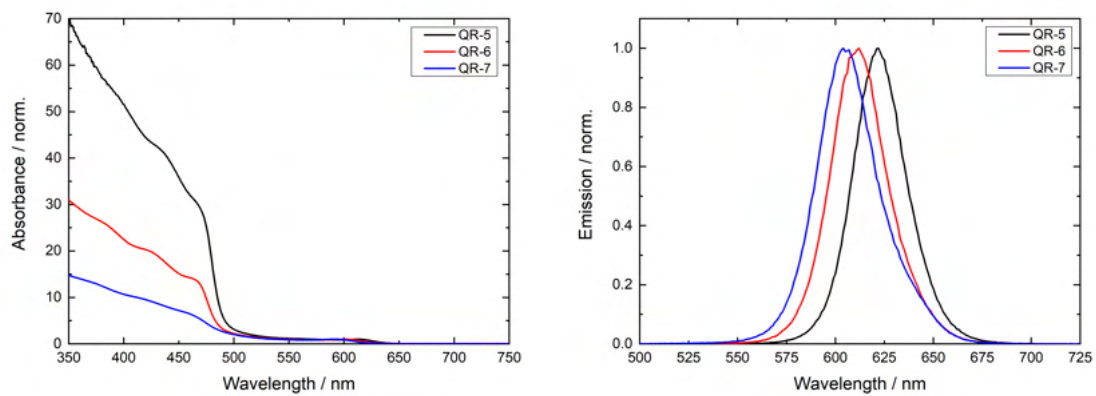
### 5.2.2 Adjusting the Quantum Rod Size with Volumetric Flow Rates

An easy way to adjust the quantum rod length is by changing the volumetric flow rate of the CdSe cores. This leads to an increased amount of CdSe cores in the reaction solution, thus a reduced amount of shell material per CdSe core is present. Since the volumetric flow rates of the CdSe cores are rather low, this has no direct influence in the residence time and thus guarantees the growth of a sufficient CdS shell. For this analysis, three samples with different volumetric flow rates for the CdSe cores in the reactor were synthesized. The trend was analyzed with two different growth temperatures to have a better overview on the shell growth. The synthesis followed the same procedure as mentioned in the previous chapter and used the same CdSe cores for the three QRs. The parameters used for the synthesis of the three samples are summarized in the following table 11.

As seen from the parameters, the slow volumetric flow rates for the CdSe cores have a marginal influence into the residence time. Since the coating of the CdS shell requires long reaction times, the difference into the three samples can be neglected. The samples were then analyzed via absorption and emission spectroscopy. Their spectra are shown in the following figure 36 for a  $T_G = 320$  °C and figure 37 for  $T_G = 290$  °C.

**Table 11:** Reaction parameters used for the synthesis of three CdSe/CdS QR samples with three different  $\dot{V}(\text{CdSe})$ 

| Sample | $T_G /$<br>°C | $\tau /$<br>min. | S:Cd | Cd:CdSe | $\dot{V}(\text{CdSe})$<br>mL/min |
|--------|---------------|------------------|------|---------|----------------------------------|
| QR-5   | 320           | 28               | 6.3  | 6597    | 0.05                             |
| QR-6   | 320           | 26               | 6.3  | 3298    | 0.1                              |
| QR-7   | 320           | 24               | 6.3  | 1649    | 0.2                              |
| QR-8   | 290           | 28               | 6.3  | 6597    | 0.05                             |
| QR-9   | 290           | 26               | 6.3  | 3298    | 0.1                              |
| QR-10  | 290           | 24               | 6.3  | 1649    | 0.2                              |

**Figure 36:** Absorbance and emission spectra (excitation at 450 nm) normalized at their first excitonic transition for CdSe/CdS QRs synthesized with a  $T_G = 320$  °C and different CdSe volumetric flow rates.

As seen from the absorbance spectra, an increase in the CdSe amount during the reaction, reduces the amount of CdS that is coated per nanoparticle. This can be seen at the typical absorption features of CdS around 450 nm, which clearly decrease from each sample. Increasing the CdSe amount in the solutions means that there is more material to be coated with CdS, therefore reducing the size of the shell. This is also a result from the change of the reaction time. The trend can also be observed in the blue shift of the band gap emission. This is true, since the synthesized nanoparticles should exhibit a shorter CdS shell, hence delivering smaller nanoparticles which emit at shorter wavelengths. Using another growth temperature should evidence the same trend.

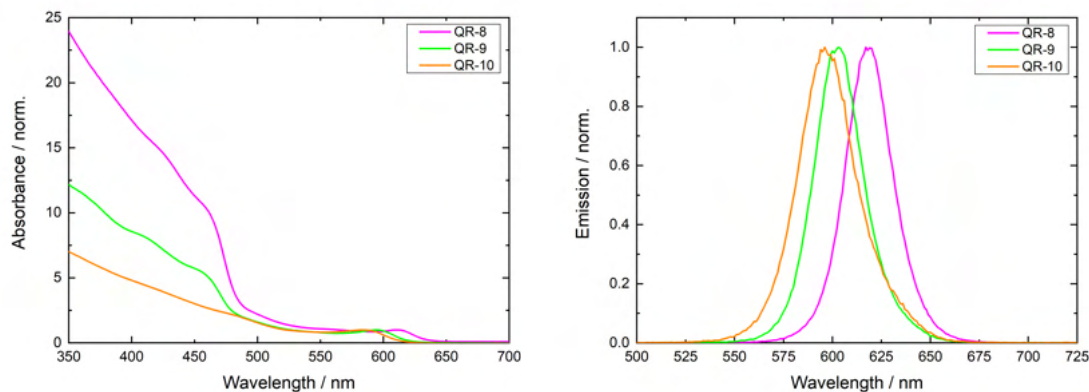


**Figure 37:** Absorbance and emission spectrum (excitation at 450 nm) normalized at their first excitonic transition for CdSe/CdS QRs synthesized with a  $T_G = 290$  °C and different CdSe volumetric flow rates.

As seen from the absorbance spectra, the trends are identical to the reaction using a higher growth temperature. Compared to the spectra before, however, the emission wavelengths are slightly blue-shifted. This can be accounted to the lower growth temperature and therefore the slower reaction, which delivers slightly smaller QRs. The relevant values for the synthesized nanoparticles are summarized in table 12. Unfortunately, for this screening experiment, no quantum yield measurements could be performed since some of the samples agglomerated before the measurement. Agglomeration of quantum rods usually occurs when the nanoparticles weren't sufficiently purified, maintaining organic residues of TOPO, which tend to make the solution viscous.

The QRs were analyzed via TEM to confirm the growth of the CdS shell and the influence of the CdSe amount during the reaction. These are shown in figure 38.

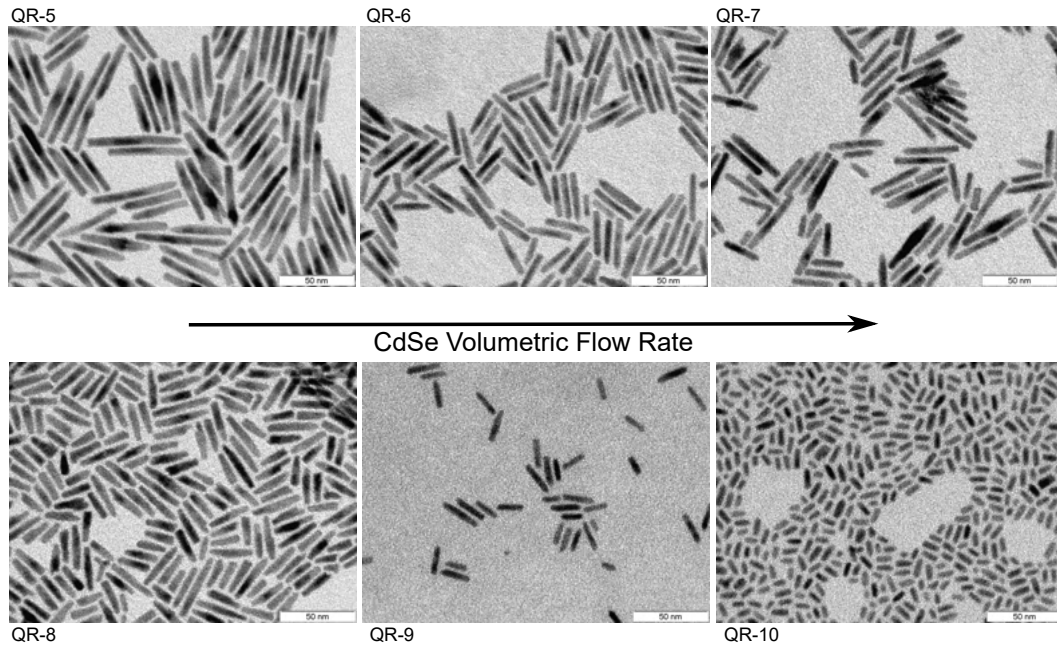


**Figure 38:** TEM images of the synthesized QRs with two growth temperatures: 290 °C and 320 °C with an increasing CdSe volumetric flow rate.

As seen from the micrographs, an increase in CdSe during the reaction slows the growth of the CdS shell. This is reflected in shorter QRs. While using a growth temperature of 320 °C increases the polydispersity, as seen in sample QR-7, this is not true for the synthesis with  $T_G = 290$  °C. This is also evident by looking at the FWHM of the band gap emission (see table 12). While a reaction with a higher growth temperature usually delivers wider FWHM, increasing the CdSe amount also affects the dispersity of the sample. This comes due to the increased reactivity of the solution by adding more CdSe "seeds", which leads to a faster reaction according to the heterogeneous nucleation at the seeds. If the reaction is faster, then an irregular growth is facilitated. The shrinking size is in both experiments evident, but the higher the growth temperature, the easier it is to still grow nanoparticles with long CdS shells. Moreover, this experiment revealed an increase in the QR width by increasing the growth temperature and by reducing the CdSe seeds in the reaction. All these factors must always be taken into account when designing a synthesis in order to achieve QRs emitting in the desired wavelength and exhibiting the desired length and width. This will be addressed in the next chapter with the syntheses of the QRs used in this work for the optimization of the alignment process and the PEQLED fabrication.



**Table 12:** Summarized values for the synthesized CdSe/CdS quantum rods using two different growth temperatures and with an increasing CdSe volumetric flow rate.

| Sample | Absorption<br>maximum | Emission<br>maximum | FWHM /<br>nm | Length /<br>nm | Width /<br>nm |
|--------|-----------------------|---------------------|--------------|----------------|---------------|
| QR-5   | 614                   | 622                 | 30           | $48.8 \pm 8.5$ | $6.5 \pm 0.8$ |
| QR-6   | 600                   | 612                 | 33           | $33.0 \pm 4.1$ | $5.4 \pm 0.7$ |
| QR-7   | 593                   | 605                 | 35           | $30.1 \pm 8.2$ | $5.1 \pm 0.4$ |
| QR-8   | 611                   | 618                 | 28           | $23.6 \pm 5.3$ | $5.4 \pm 0.6$ |
| QR-9   | 595                   | 603                 | 29           | $19.4 \pm 2.4$ | $4.6 \pm 0.6$ |
| QR-10  | 584                   | 596                 | 34           | $11.1 \pm 1.6$ | $4.3 \pm 0.6$ |

### 5.2.3 Design of Different Quantum Rod Species

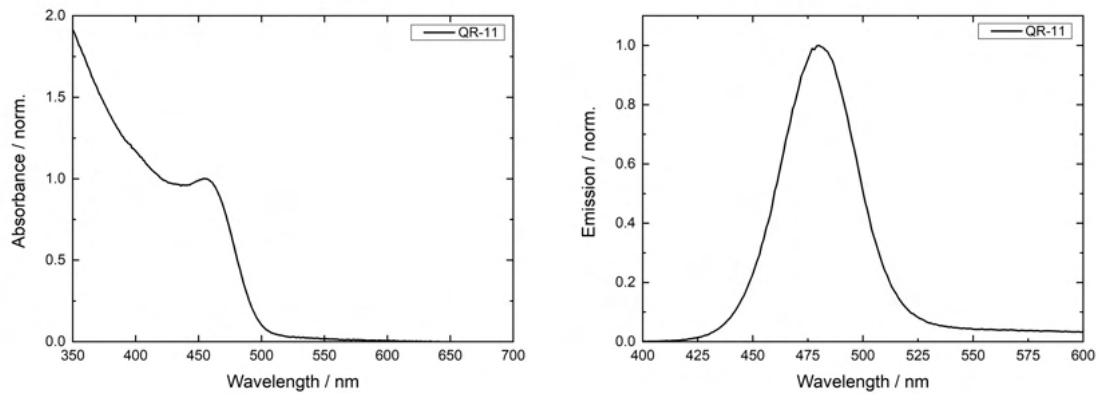
The synthesis of different CdSe/CdS heterostructures with a continuous flow reactor allows the precise control of their size, emission wavelength and yield. One of the main aspects in nanoparticle syntheses is the control of the nanoparticles size, thus the control of their emission wavelength, while achieving good properties. This is translated into control of the emission wavelength with high quantum yields and high long-term stability. This chapter will give an overview on how to design the syntheses for three CdSe/CdS species: blue emitting CdSe/CdS nanoparticles, green emitting QRs and red emitting QRs. As can be seen, these are also the colors of main interest for the fabrication of pixels in the display industry (see chapter 3.4) and are therefore relevant when fabricating optical devices. There are two aspects that have to be taken into account into the design of QRs emitting at different wavelengths: the size of the CdSe cores and the size of the CdS shell. Both will be discussed in the following sections.

First, the synthesis of CdSe/CdS emitting in the blue ( $\sim 475$  nm) using the reactor will be addressed. For this, the set-up was slightly modified by adding a heat exchanger after the oven in order to prevent further growth of the nanoparticles. CdSe clusters (as described in chapter 5.1.3) were used as the CdSe seeds for this reaction. These are dispersed in TOP to achieve a concentration of  $c = 100 \mu M$ , then pumped to be mixed with the cadmium and sulfur precursors. The cadmium precursor is based on cadmium oxide, instead of cadmium acetate. Syntheses using cadmium oxide often exhibit a blue shift as to those using cadmium acetate. The summarized parameters for this reaction are shown in the following table 13.

**Table 13:** Reaction parameters used for the synthesis of three CdSe/CdS nanoparticles emitting in the blue.

| Sample | $T_G$ /<br>°C | $\tau$ /<br>min. | S:Cd | Cd:CdSe | CdSe Sample |
|--------|---------------|------------------|------|---------|-------------|
| QR-11  | 230           | 0.5              | 6.3  | 5525    | CdSe-9      |

As mentioned in the previous chapters, a high sulfur to cadmium ratio is needed to guarantee the growth of a CdS shell. The residence time is kept very low in order to avoid the further growth of the nanoparticles and shift the emission wavelengths to the green. The nanoparticles were analyzed via absorption and emission spectroscopy and their spectra are shown in the following figure 39.

**Figure 39:** Absorbance and emission spectrum (excitation at 350 nm) normalized at their first excitonic transition for CdSe/CdS nanoparticles emitting in the blue (sample QR-11).

As seen from the absorbance spectrum, this exhibits a first absorption maximum at 456 nm. Since CdS shows features in the same wavelengths, it is not possible to confirm how much CdS was deposited on the material. The red-shift in comparison to the used CdSe cores, however, confirms the coating with a second nanomaterial. Furthermore, emission in the blue can be observed with a band gap transition at 480 nm. The significant red-shift of the absorption maximum in comparison to the used CdSe cores (50 nm) can be explained with the band gap alignment of this core/shell system. Since the used CdSe seeds are of a very small size, their band gap is rather big. This implies that the band edges of CdSe approach the band edges of CdS. Thus, a quasi type-II system is formed. This means that the wave function of the electron is delocalized over the core and shell, while the hole's wavefunction is confined inside the core (see chapter 3.1.2).

This results in a considerable red-shift of the absorption (and emission) maximum. The FWHM of the sample is rather broad (40 nm), however, this was expected for a synthesis with very short growth times and small CdSe seeds. The main values for the synthesized nanoparticles are summarized in table 14. Since the CdS shell is rather thin, the surface defects cannot be fully passivated, resulting in a low quantum yield of 32 %. This value is still very promising, since most of the CdSe/CdS heterostructures tend to emit in the green or red. Blue emitting species usually involve the coating with a ZnS shell. The nanoparticles were also analyzed via TEM. The micrographs are shown in the following figure 44.

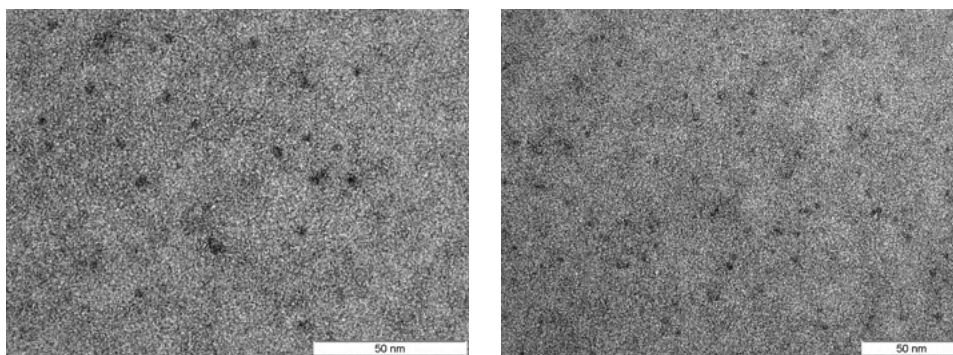


**Figure 40:** TEM images of the synthesized CdSe/CdS nanoparticles.

As seen from the micrographs, it is rather difficult to identify the CdSe/CdS species, since they are very small. Some of the nanoparticles could still be identified as quasi-spherical nanoparticles with a median size of  $2.8 \pm 0.7$  nm. This value should be taken with caution, since the analysis of the nanoparticles with a low contrast could lead to false information. In comparison to the used CdSe cores (1.6 nm), a growth of these is evident. This confirms the coating of a CdS shell, delivering blue emitting CdSe/CdS nanoparticles.

**Table 14:** Summarized values for the synthesized CdSe/CdS nanoparticles emitting in the blue

| Sample | Absorption maximum | Emission maximum | FWHM / nm | Diameter / nm | QY / % |
|--------|--------------------|------------------|-----------|---------------|--------|
| QR-11  | 456                | 480              | 40        | $2.8 \pm 0.7$ | 32     |

Next, the synthesis of green emitting QRs will be discussed. The synthesis follows the same procedure as mentioned in the previous chapters, without the use of a heat exchanger. The cadmium precursor can be based on cadmium acetate or cadmium oxide. For this

work, a cadmium acetate based precursor was used. The parameters for the synthesis are summarized in the following table 15.

**Table 15:** Reaction parameters used for the synthesis of CdSe/CdS nanoparticles emitting in the green.

| Sample | $T_G$ /<br>°C | $\tau$ /<br>min. | S:Cd | Cd:CdSe | CdSe Sample |
|--------|---------------|------------------|------|---------|-------------|
| QR-12  | 280           | 7.3              | 6.5  | 5069    | CdSe-10     |

The QRs were analyzed via absorption and emission spectroscopy, their normalized spectra are shown in the following figure 41.

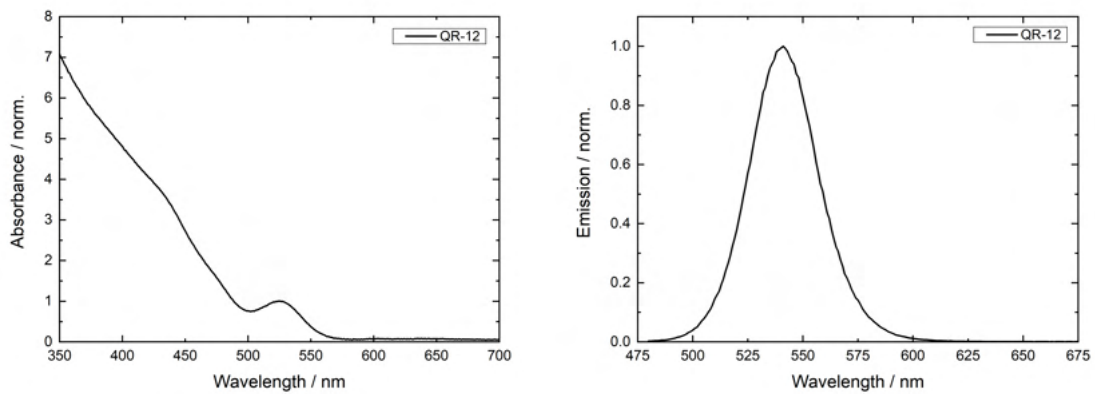


**Figure 41:** Absorbance and emission (excitation at 450 nm) spectrum normalized at their first excitonic transition for CdSe/CdS QRs emitting in the green (sample QR-12).

As seen from the absorption spectrum, the first absorption maximum exhibits a substantially large red shift in comparison to the used CdSe cores (451 nm). This can be explained with the delocalization of the electron wave function inside the core and throughout the CdS shell. Just as mentioned with the previous sample, this induces a red shift of the optical features, due to the nature of the quasi type-II system. Moreover, the increase in absorbance around 400-450 nm confirms the coating with a CdS shell. The band gap emission is rather broad, with an FWHM of 36 nm. The values for the synthesized QRs are summarized in table 16. This comes due to the polydispersity of the sample. However, the emission lies in the expected range for green-emitting chromophores. The QRs were analyzed via TEM with the micrographs shown in the following figure 44.

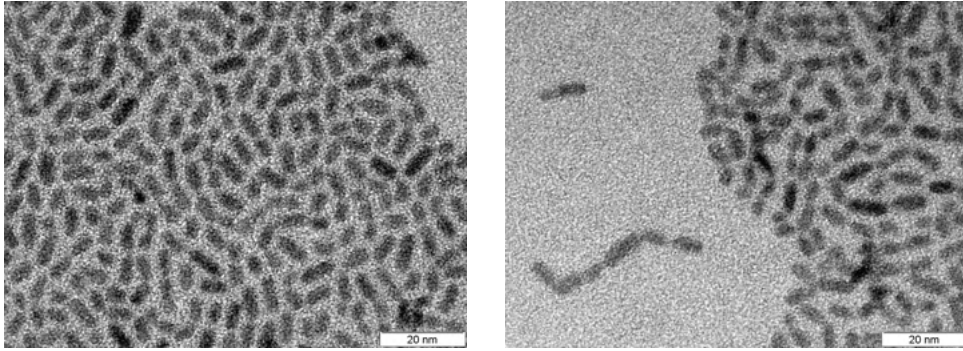


**Figure 42:** TEM images of the synthesized CdSe/CdS quantum rods.

As can be seen from the micrographs, the QRs show an elongated structure, as expected for the reaction. The increase in both length and width in comparison to the used CdSe is evident. This induces the described changes in the opto-electronic properties of the rods. Last, the QRs exhibit a high quantum yield of 71 %. This could be further increased by increasing the CdS shell, however, this would also shift the emission wavelegths into the red. To avoid this, the use of a CdO precursor would be recommended, in order to correct the emission wavelength to the desired range.

**Table 16:** Summarized values for the synthesized CdSe/CdS nanoparticles emitting in the green

| Sample | Absorption maximum | Emission maximum | FWHM / nm | Length / nm   | Width / %     | QY / % |
|--------|--------------------|------------------|-----------|---------------|---------------|--------|
| QR-12  | 526                | 541              | 36        | $8.5 \pm 0.9$ | $3.5 \pm 0.4$ | 71     |

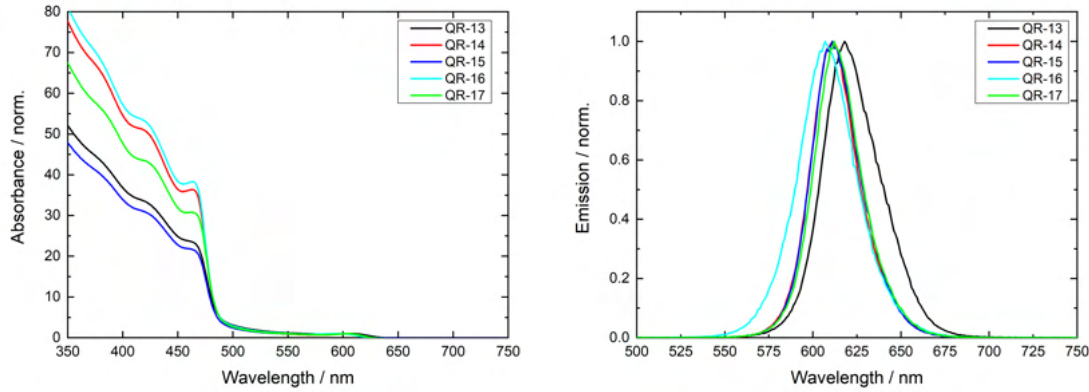
Last, the synthesis of red emitting QRs will be discussed. These QRs were used for the optimization of the alignment process and the fabrication of PEQLEDs. Therefore, an interesting aspect is the production of a high amount of material. The synthesis follows the same procedure as mentioned in the sections before. For this work, five QRs were used for the most optimization procedures. The parameters for their syntheses are summarized in the following table 17.

As can be seen from the parameters, a high growth temperature and a high Cd:CdSe ratios are chosen. This is to guarantee a long CdS shell. A long CdS shell is according to literature needed to exhibit good polarization properties from the rods. Since, as explained in chapter 3.2, the polarization properties derive from the strain in the core induced by CdS along the *c*-axis, a substantially long CdS shell is wished, in order to

**Table 17:** Reaction parameters used for the synthesis of CdSe/CdS nanoparticles emitting in the red.

| Sample | $T_G$ / °C | $\tau$ / min. | S:Cd | Cd:CdSe | CdSe Sample |
|--------|------------|---------------|------|---------|-------------|
| QR-13  | 320        | 28            | 6.3  | 9208    | CdSe-13     |
| QR-14  | 320        | 28            | 6.3  | 6597    | CdSe-14     |
| QR-15  | 320        | 28            | 6.3  | 9567    | CdSe-11     |
| QR-16  | 320        | 28            | 6.3  | 7921    | CdSe-15     |
| QR-17  | 320        | 28            | 6.3  | 6597    | CdSe-14     |

exploit the polarization properties as much as it is possible. Due to the reactor set-up, longer residence times and higher growth temperatures are not possible, hence these parameters were chosen to achieve QRs with a sufficiently long CdS shell. The synthesized QRs were analyzed via absorption and emission spectroscopy. The spectra are shown in the following figure 43.

**Figure 43:** Absorbance and emission (excitation at 450 nm) spectrum normalized at their first excitonic transition for CdSe/CdS QRs emitting in the red.

As seen from the absorbance spectra, the first absorption maximum characteristic of the CdSe cores shows a low absorbance in comparison to the CdS features (at 450 nm). This confirms the growth of a substantially large CdS shell. The most relevant values for the QRs are summarized in table 18. The emission range for all the QRs is very similar, with only QR-13 exhibiting a red-shifted emission. This comes from a higher Cd:CdSe ratio. As mentioned in the previous chapter, a higher Cd:CdSe ratio, this means a reduced amount of CdSe seeds, leads to a red shift of the emission properties since the nanoparticles are coated with more CdS. To confirm the length of the CdS shell, the QRs were analyzed via TEM.

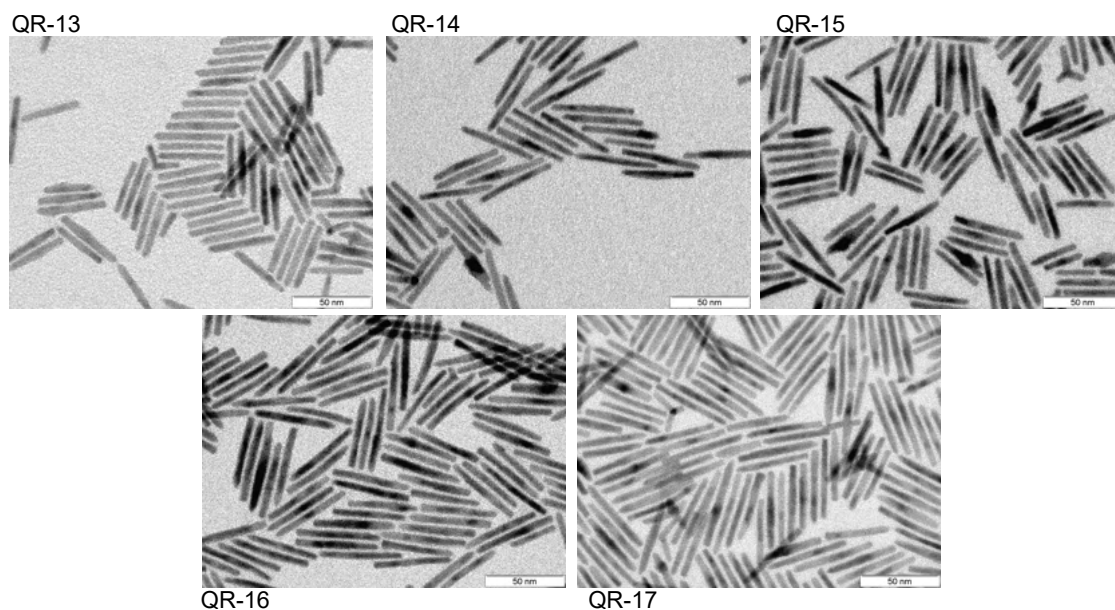


**Figure 44:** TEM images of the synthesized CdSe/CdS quantum rods.

The TEM reveal that the red-shift of the QR-13 sample is due to the wider CdS shell. This is true since a weaker confinement is therefore achieved when both the width and the length increase in size (see quantum size effect). The weaker confinement and the high amount of CdS in both directions induces a red shift compared to the other species. Additionally, the monodispersity of the QR-13 and QR-16 samples is rather low, reflected in their large FWHM. This has a direct influence to the quantum yield of the sample. As seen in table 18, the QRs exhibit a high quantum yield for all samples. However, the samples exhibiting a large FWHM also exhibit a lower QY. This is a direct influence of the polydisperse sample. Compared to spherical CS nanoparticles, the QY of QRs is still a bit low. This is due to the defects coming from the long CdS shell, which trap the charge carriers, inhibiting recombination. As mentioned previously, the aim of using a reactor is a high throughput of the materials. This was calculated for each sample after purification. Hence, the throughput stated in table 18 derives from the total amount of purified CdSe/CdS per milliliter (heptane or hexane) without counting the organic ligands per minute of the collected sample at the reactor outlet. As can be seen, the throughput is rather constant and relatively high, ranging between 4.8 to 5.4 mg/mL. Effectively, it is possible to synthesize 5 mg of CdSe/CdS quantum rods per minute using this set-up.

**Table 18:** Summarized values for the synthesized CdSe/CdS QRs emitting in the red

| Sample | Absorption maximum | Emission maximum | FWHM / nm | Length / nm    | Width / nm    | QY / % | Throughput / mg/min. |
|--------|--------------------|------------------|-----------|----------------|---------------|--------|----------------------|
| QR-13  | 609                | 617              | 37        | $40.4 \pm 3.5$ | $5.1 \pm 0.7$ | 62     | 5.4                  |
| QR-14  | 603                | 611              | 30        | $52.0 \pm 4.0$ | $4.9 \pm 0.6$ | 85     | 5.0                  |
| QR-15  | 602                | 611              | 31        | $39.9 \pm 5.0$ | $4.6 \pm 0.5$ | 80     | 5.3                  |
| QR-16  | 598                | 607              | 37        | $51.8 \pm 4.7$ | $4.8 \pm 0.6$ | 73     | 4.9                  |
| QR-17  | 604                | 612              | 30        | $50.1 \pm 4.0$ | $4.6 \pm 0.8$ | 79     | 4.8                  |

### 5.2.4 Summary

The successful synthesis of CdSe/CdS heterostructures was possible using a continuous flow reactor. The reactor allows a precise control of the nanoparticle's size, emission wavelength and aspect ratios. By choosing CdSe cores of different sizes, it is possible to synthesize CdSe/CdS as a quasi type-II core/shell system. This is due to the change in the band edge energies of the CdSe nanoparticles following the quantum size effect. As a result, CdSe/CdS nanoparticles emitting in the blue can be synthesized, exhibiting rather low quantum yields, though.

Furthermore, the influence of the growth temperature and the CdSe amount during the reaction was investigated. With these two parameters, it is possible to vary the quantum rods' length. By applying this knowledge, the design for different quantum rods with varying length is possible. It was demonstrated that quantum rods emitting in the green and in the red can be synthesized by using the analyzed parameters. The synthesized quantum rods exhibit high quantum yields and can be synthesized in large scale due to the high throughput of the reactor. The throughput of the reactor for the red emitting quantum rods lies at around 4.8 to 5.3 mg/mL.



### 5.3 Alignment of Quantum Rods with an Electrostatic Field Using Interdigitated Electrodes

In order to exploit the polarized emission of quantum rods, the ensemble must be aligned on a suitable substrate. In solution, the polarized emission of QRs cannot be observed, since they are statistically disordered, following Brownian motion. There are several factors that must be taken into account before designing an alignment procedure for the QRs for LED applications. First, the alignment procedure must be non-invasive. This means, the quantum rods should not be intrinsically modified or damaged. This would lead to a change in the opto-electronic properties of the quantum rod and thus hinder the optimization of the optical device (the PEQLED). Second, the procedure should avoid the use of polymers or additives which may hinder the charge carrier transport inside an LED. For instance, procedures such as described in chapter 3.2.1 which use polymers to align the QRs, should usually be avoided. The polymer residues would affect the electric transport, which is already challenging within the QLED stack. Last, the procedure should be performed on a substrate that allows the transfer of the aligned QR film to the designated QLED substrate. For these reasons, the alignment of QRs using an electrostatic field was chosen and optimized. This procedure can be combined with deposition methods such as drop-casting and dip coating, which allow the fabrication of an aligned QR film. The next chapters will discuss the optimization of this procedure to deliver aligned QR films with high degrees of polarization (DOP) for the use on PEQLEDs.

#### 5.3.1 Alignment on Interdigitated Electrodes by Drop-casting

The alignment of QRs using an electrostatic field was first investigated using interdigitated electrodes (IDEs). This procedure follows the works by Christoph Schloen<sup>[161]</sup> and Leonhard Niemann<sup>[162]</sup> at Fraunhofer IAP-CAN. For this, interdigitated electrodes fabricated using photolithography with an electrode width of 5  $\mu\text{m}$  and a distance of 10  $\mu\text{m}$  between electrodes with a total active area of 25  $\text{mm}^2$ , were used. A solution of QR-17 in *n*-heptane with a concentration of  $c = 18 \text{ mg/mL}$  was used for the following experiments. A voltage of 150 V using an alternating current (AC) with a square wave and 100 Hz was applied to the electrodes. Next, 10  $\mu\text{L}$  of the QR solution were drop casted on the

electrode substrate. During this, a slight vibration of the solution can be observed until the solution dries.

The aligned film was analyzed for their polarized emission. For this, the substrate was excited using a blue LED ( $\lambda = 451 \text{ nm}$ ) as described in chapter 3.7.3. The acquired images were then analyzed by calculating the DOP using equation 6 for each pixel in the acquired image. Since the CCD camera takes one acquisition every time the half wave plate moves by one degree, the experiment allows the calculation of the DOP for the whole substrate. The DOP can then be ascribed to a color scala to facilitate the analysis of the substrate. The DOP analysis is shown in the following figures 45 for substrate IDE-1.

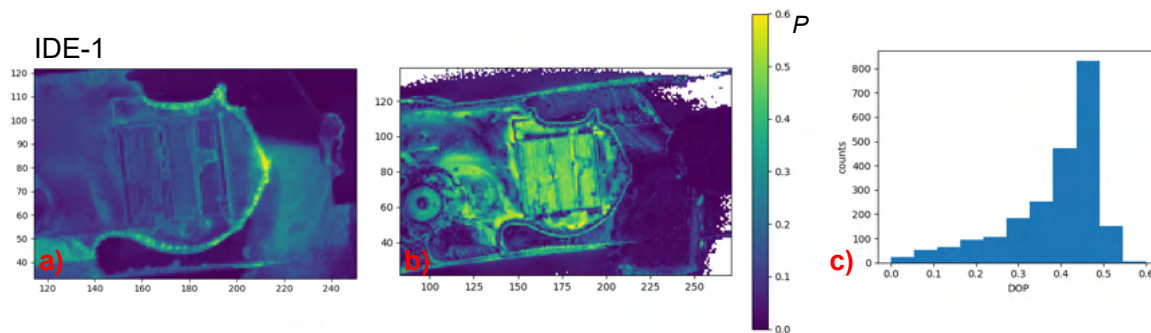


**Figure 45:** a) Acquisition of an IDE substrate after drop-casting of the QR-17 solution while applying an electrostatic field. The acquisition exhibits the IDE without calculating the DOP for each pixel. It depicts the general overview of the substrate. b) Acquisition of the IDE substrate after calculation of  $P$  for each pixel. The color bar shows blue for  $P = 0$  and yellow for  $P = 0.6$ , while the x and y axis show the position of each pixel in a typical coordinate diagramm. d) Histogramm of the DOP distribution inside the  $25 \text{ mm}^2$  active area of the IDE.

As can be seen from the acquisition, the QRs exhibit polarized emission. First, the active area inside the IDE, this means the area where the electrodes are intertwined, shows a higher intensity (figure 45 a) since the QR solution is directly drop casted over this area. It can also be seen that the solution "slides" in the direction of one of the electrodes (to the left) where the pin contacts are placed. This can be explained by the electrostatic potential that moves the solution to one direction (resembling electrochemical set-ups), but also if the substrate is placed on an uneven surface, the solution will wander to one of the sides. Additionally, the capillary forces draw the solution towards the contact pins, adding to the inhomogeneity of the deposited film. After calculating  $P$  for each pixel, it can be observed that the active area inside the IDE exhibits the higher DOP. Indeed, the highest value for  $P$  inside the active area was  $P = 0.57$ . It is also possible to observe

high DOP outside the active IDE area. This is due to the self-assembly of QRs during the drying procedure. The circular accumulations resemble the "coffee ring" effect. It is to be noted, that high degrees of polarization do not implicitly mean the quantum rods are perfectly aligned. The degree of polarization should therefore not be confused with the degree of alignment, which is not possible to calculate using this set-up. Moreover, the median value for  $P$  inside the active was calculated at  $P = 0.43$ . This can also be observed by looking at the DOP distribution in figure 45 c). The histogram shows the calculated DOP for each pixel and distributes it according to their counts. It is clear that while most of the DOP ranges at around 0.3 to 0.5, there are still many values under that number. This is due to the IDE geometry itself. Quantum rods align along the electric field (as described in chapter 3.2.1). While this is possible between the electrodes, the area above the electrodes does not have an electric field. This means these areas will only exhibit polarization from quantum rods by self-assembly. This has a direct influence in the median DOP and must always be taken into consideration while analyzing the results.

### 5.3.2 Frequency Dependence on Interdigitated Electrodes

The electrostatic procedure was further analyzed by adjusting the frequency  $f$  of the AC. In order to optimize the electrostatic procedure, two values can be screened: the voltage and the frequency. While the voltage is already set at the maximum allowed by the amplifier (150 V), a higher voltage also leads to the breaking of the electrodes due to the strong electric fields and the high possibility of defects inside the IDE. As mentioned before, the photolithography process limits the size of IDEs due to short circuits. These also hinder the use of a higher voltage. Therefore, only the influence of the frequency was investigated. The experiment uses an AC to guarantee the complete alignment of the quantum rods. A direct current (DC) would not only hinder the process, but set a preferred direction for the QRs, which would move them into the direction of one of the contact pins, therefore hindering the alignment inside the IDE using the electric field. This can be avoided by using an AC. For this, three IDEs were used and the QR-17 solution was aligned with the process described in the previous chapter. Here, three frequencies were analyzed: 100 Hz, 100 kHz and 1 MHz. The aligned films were then analyzed for their polarization with the methods described before.

First, the alignment with  $f = 100$  Hz was analyzed. This is shown in the following figure 46.

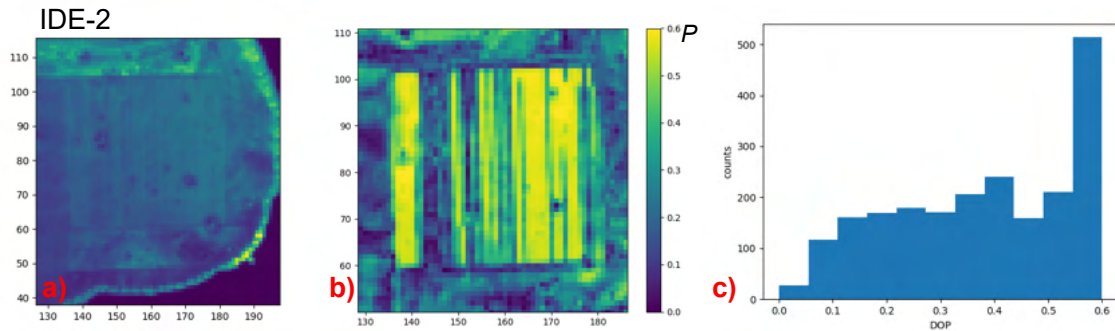


**Figure 46:** a) Acquisition of an IDE substrate after drop-casting of the QR-17 solution while applying an electrostatic field with  $f = 100$  Hz. The acquisition exhibits the IDE without calculating the DOP for each pixel. It depicts the general overview of the substrate. b) Acquisition of the IDE substrate after calculation of  $P$  for each pixel. The color bar shows blue for  $P = 0$  and yellow for  $P = 0.6$ , while the x and y axis show the position of each pixel in a typical coordinate diagram. c) Histogram of the DOP distribution inside the  $25 \text{ mm}^2$  active area of the IDE.

As can be seen from the acquisitions, the film covers the whole active area of the IDE, as seen in figure 46 a). After calculating  $P$ , it is clear that some areas exhibit very high polarization, while others very low values. One possible reason to explain this, is that while applying such a high voltage, some of the electrodes can break, therefore hindering the alignment through an electrostatic field. Indeed, some of the areas which show low values for  $P$  follow the pattern of a finger electrode. Additionally, the areas on top of the electrodes usually show no polarization. Nevertheless, the polarization from the substrate is still very high. While a high degree of polarization does not implicitly mean that the quantum rods are perfectly aligned, this property strongly depends on the alignment of the quantum rods in ensemble. The DOP distribution exhibits some interesting aspects. While the highest calculated value was  $P = 0.6$ , the median for the structure lies at  $P = 0.4$ . This is due to the low values that are found throughout the whole active IDE area. This means, using this set-up can achieve high DOP but it also shows inhomogeneities.

Next, the electrostatic alignment using a frequency of  $f = 100$  kHz was analyzed. The acquisitions are shown in the following figure 47.

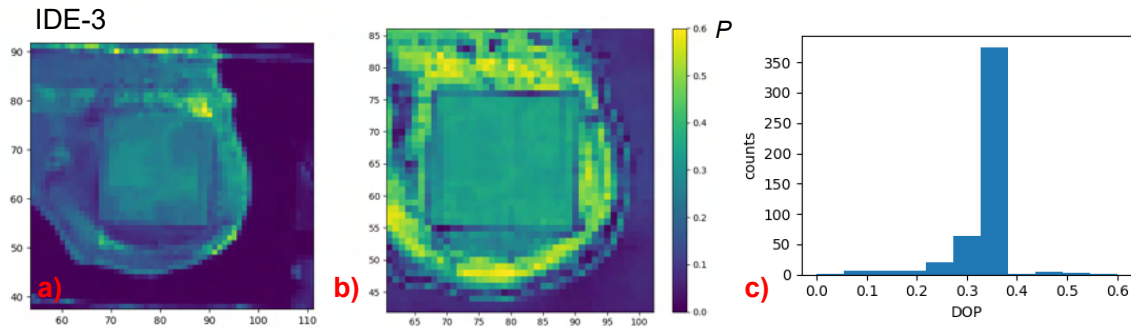


**Figure 47:** a) Acquisition of an IDE substrate after drop-casting of the QR-17 solution while applying an electrostatic field with  $f = 100$  kHz. The acquisition exhibits the IDE without calculating the DOP for each pixel. It depicts the general overview of the substrate. b) Acquisition of the IDE substrate after calculation of  $P$  for each pixel. The color bar shows blue for  $P = 0$  and yellow for  $P = 0.6$ , while the x and y axis show the position of each pixel in a typical coordinate diagramm. c) Histogramm of the DOP distribution inside the  $25 \text{ mm}^2$  active area of the IDE.

As seen from the acquisitions, the QR film covers the whole IDE active area. After calculating the values for  $P$ , it can be seen that the IDE active area shows a very homogenous film with very similar DOP. Interestingly, the area outside the IDE exhibits a ring with high values for  $P$ . This may come due to the drying process as described in the previous chapter. The self-assembly of QRs is visible in the outer area of the drying circle, by comparing figure 47 a) and b). The DOP distribution also shows a high homogeneity for the aligned film. Most of the calculated values range around 0.3. This is reflected in the median DOP of  $P_{\emptyset} = 0.33$  and a maximum value of  $P = 0.55$ .

To further investigate the effect of the frequency on the alignment procedure, a last IDE was analyzed with  $f = 1$  MHz. The results are shown in the following figure 48.

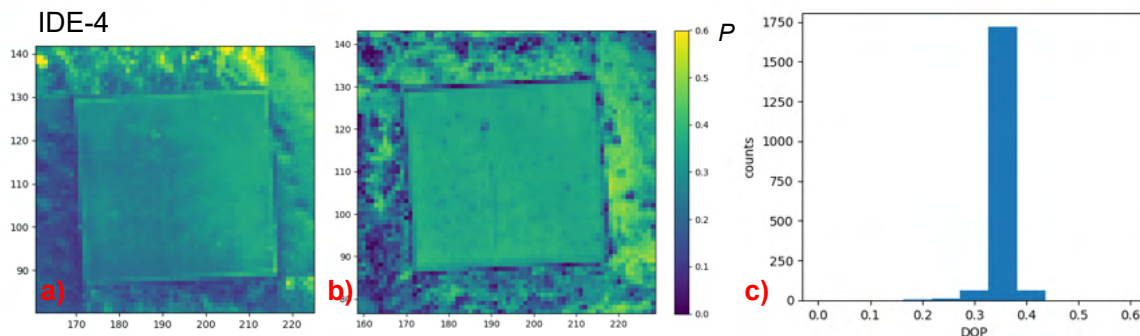


**Figure 48:** a) Acquisition of an IDE substrate after drop-casting of the QR-17 solution while applying an electrostatic field with  $f = 1$  MHz. The acquisition exhibits the IDE without calculating the DOP for each pixel. It depicts the general overview of the substrate. b) Acquisition of the IDE substrate after calculation of  $P$  for each pixel. The color bar shows blue for  $P = 0$  and yellow for  $P = 0.6$ , while the x and y axis show the position of each pixel in a typical coordinate diagramm. c) Histogramm of the DOP distribution inside the  $25 \text{ mm}^2$  active area of the IDE.

As can be seen, the active area inside the IDE exhibits a high homogeneity, which confirms that a high frequency delivers a homogeneous film. After calculating the DOP, this is also reflected on the median DOP with  $P_{\emptyset} = 0.36$ . While the maximum DOP is rather low with  $P = 0.4$  in comparison to the structures with a lower frequency, this is still an acceptable value. This is reflected in the DOP distribution, which shows a very homogenous distribution of the values.

It could be shown that increasing the frequency for the alignment procedure delivers a higher homogeneity in the deposited film. This is also reflected in the DOP distributions. However, it also affects the values for  $P$ . Using a low frequency at 100 Hz delivered the highest DOP, although it exhibited a rather low homogeneity. A low frequency may influence the alignment of the quantum rod, which should align in the direction of the electric field. If the movement of the quantum rod is slower than the change of amplitude during the electrostatic alignment, it may induce changes that affect the solution and the alignment. A high frequency means that the QRs are in a constant change of polarity, but are rather static, since their movement should not be as fast as the change of amplitude. If the frequency is lower, this may affect the induced dipole moment of the quantum rod and enhance its alignment along the electric field. This effect is clearly seen at the polarization values, which are summarized in table 19. Both the highest calculated DOP at the structure and the median DOP decrease by increasing the frequency.

**Table 19:** Summarized values for the alignment experiments using an electrostatic field on IDEs

| Sample | QR Sample | $P_{max.}$ | $P_{\emptyset}$ | $f /$<br>Hz | $V /$<br>V |
|--------|-----------|------------|-----------------|-------------|------------|
| IDE-2  | QR-17     | 0.6        | 0.4             | 100         | 150        |
| IDE-3  | QR-17     | 0.55       | 0.33            | 100000      | 150        |
| IDE-4  | QR-17     | 0.4        | 0.36            | 1000000     | 150        |

The electrostatic alignment using IDEs delivers high degrees of polarization and by adjusting the frequency also homogeneous films. However, the reproducibility of this set-up is rather difficult. Drop casting the QR solution usually delivers inhomogeneous films, since the procedure depends on many variables that cannot be controlled, such as drop size, dropping speed, among others. Moreover, the size of the active area is limited due to the photolithography process and the nature of the electrode. For these reasons, another

method was developed to align QRs using an electrostatic field. This will be discussed in the next chapter.

## 5.4 Alignment of Quantum Rods with an Electrostatic Field Using Fringe-Field Electrodes

The alignment of quantum rods with an electrostatic field can be performed on fringe-field electrodes (FFE). As described in chapter 3.2.1, these offer several advantages towards IDEs. Due to their geometry, it is impossible to produce short circuits. For this work, commercial silicon wafers passivated with a  $\text{SiO}_2$  layer of  $500 \text{ nm}$  were used. The silicon layer is used as the bottom contact (or bottom substrate) while the electrodes are fabricated with a titanium/gold layer using optical lithography on top of the  $\text{SiO}_2$  layer. Here,  $\text{SiO}_2$  works as an insulating layer to avoid short circuits. The geometry of the structures is schematically shown in the following figure 49.

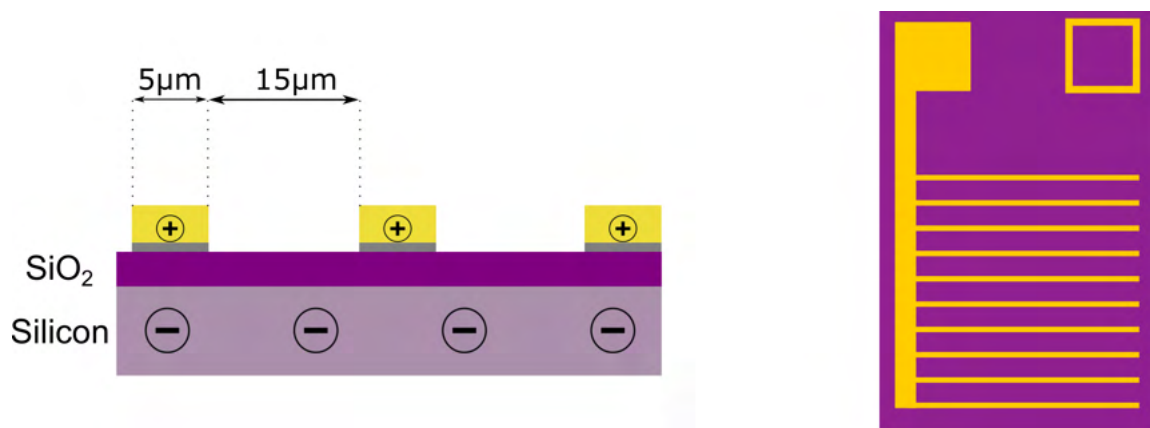


**Figure 49:** Left: Schematic illustration of the used FFE in this work. The bottom substrate is a silicon wafer, while the upper electrode structures are separated by an insulating  $\text{SiO}_2$  layer. A typical finger electrode with  $5 \text{ }\mu\text{m}$  width and an interdistance of  $15 \text{ }\mu\text{m}$ . Right: schematic illustration of the FFE design for the dip coating experiments.

As can be seen, the structure can vary its electrode width and interdistance. This factor would have a direct influence on the electric field of the structure. There are also some other considerations that have to be taken into account for the use of FFEs. In contrast to the use of IDEs, the deposition of QRs to the electrode can be performed by dip coating. For this, the electrode active area should be big enough to guarantee the deposition of a sufficient layer. Therefore, FFEs with an active area of  $2 \text{ cm}^2$  and  $1 \text{ cm}^2$  were used for this work. As can be noticed, the structures can be designed at any size (only limited by the

photolithography process), since any defects on the electrodes do not affect the working principle of the electrode. This factor will be addressed in the next chapter. Moreover, due to the dip coating process, other parameters have to be addressed. Dip coating is based on the immersion of a substrate into a solution followed by withdrawal of this while guaranteeing a homogeneous drying process. The step of interest here is the withdrawal while forming a thin film. For this, two forces come into play: draining and entraining forces. The first force works to draw the liquid away from the surface and back towards the bath. The latter works to retain fluid onto the substrate. Balancing both depends mainly on the withdrawal speed and the viscosity of the solution. To guarantee a successful dip coating experiment, the concentration of the solution should also be addressed.

Taking these considerations into account deliver the following design for the dip coating of FFE while applying an electrostatic potential. First, the finger electrodes on the FFE should be parallel to the meniscus of the QR solution during dip coating (see figure 49, right). This way, agglomerations on the top of the electrode can be avoided. Having the finger electrodes perpendicular to the meniscus facilitate the accumulation of QR agglomerates throughout the active area, as could be observed in previous experiments. This is due to the capillary forces throughout the finger electrodes and the electrostatic potential that is applied in the structure. The electric field on the side of the finger electrodes contributes to the QRs agglomeration which is dragged throughout the structure if the finger electrodes are perpendicular to the meniscus. Second, the withdrawal speed should always be adjusted to the QR solvent. Last, the concentration of the solution should not be too high. This is to avoid so called "stripes" on the structure.

To this end, in a typical dip coating procedure using QRs in *n*-heptane, the withdrawal speed was set at 45 mm/min while the concentration of the solution was kept at  $c = 2.5$  mg/mL.

#### 5.4.1 Variation of the Electrode Width and Interdistance

The design of the FFE was analyzed by varying the finger electrode width and the interdistance between them. This will be abbreviated with electrode width/electrode interdistance  $w/i$ . For instance, a substrate with finger electrodes with a width of 5  $\mu\text{m}$  and 15  $\mu\text{m}$  interdistance would be 5/15. The FFE were dip coated with QR-17 in *n*-heptane with



$c = 2.5$  mg/mL while applying 150 V with an AC (sine formed) and 100 Hz. Since a sine curve is intrinsically more "natural", this setting was chosen instead of a squared wave. The voltage was set at 150 V, since applying a higher voltage damages the insulating layer and breaks the finger electrodes, making the experiment impossible. Heptane is a typical solvent used for depositing nanoparticles, as known from several different systems such as gold nanoparticles and lead sulfide. The analyzed  $w/i$  were 4/8, 4/12, 5/15, 5/20 and 5/25 (in micrometers). Thinner electrodes are hindered by the photolithography process, therefore a limit of 4 micrometers was chosen.

First, the 4/8-FFE was analyzed. This was dip coated into the QR-17 solution, tempered for at least 30 s and withdrawn at 45 mm/min from the solution while applying a voltage as described before. The substrate was analyzed to its polarization using the previously described method (see chapter 3.7.3) and the acquisitions are shown in the following figure 50.

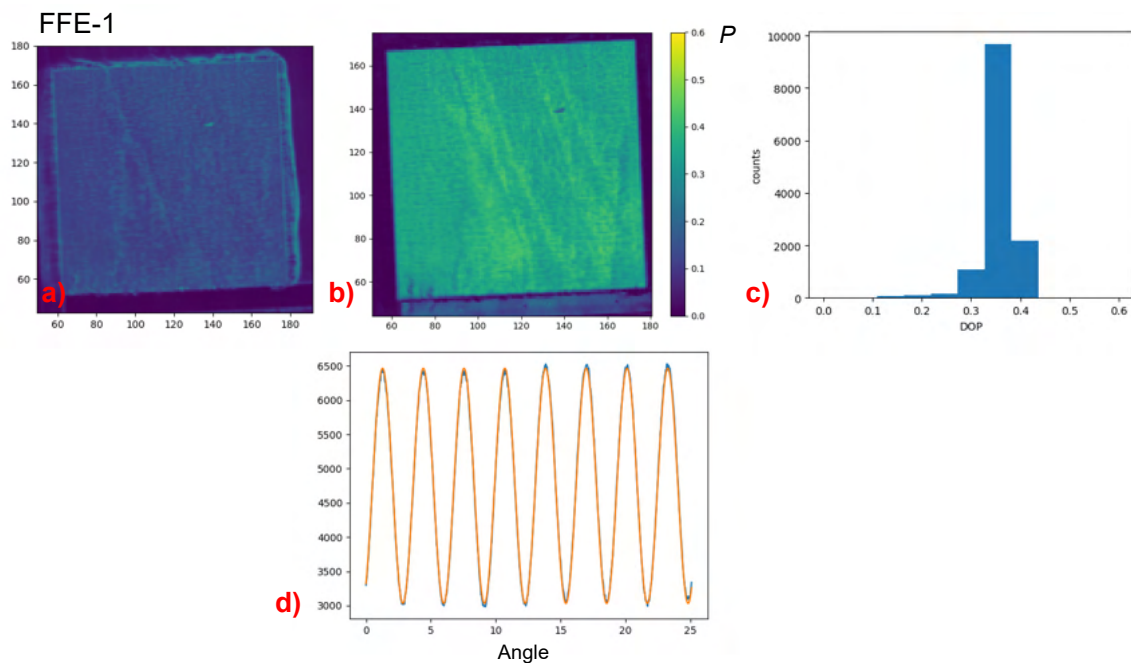


**Figure 50:** a) Acquisition of a 4/8-FFE substrate after dip coating of the QR-17 solution while applying an electrostatic field with  $f = 100$  Hz. The acquisition exhibits the FFE without calculating the DOP for each pixel. It depicts the general overview of the substrate. b) Acquisition of the 4/8-FFE substrate after calculation of  $P$  for each pixel. The color bar shows blue for  $P = 0$  and yellow for  $P = 0.6$ , while the x and y axis show the position of each pixel in a typical coordinate diagramm. c) Histogramm of the DOP distribution inside the  $1 \text{ cm}^2$  active area of the FFE. d) (Blue line) Intensity of the analyzed emission after going through a polarizer in dependence of the half-wave plate rotation. The angle is in radian. (Orange line) Fit of the intensity dependence to the angle, resembling a sine curve.

As seen from the acquisition, the FFE active area is completely coated with a QR film. This is true since the dip coating procedure allows the coating of the whole desired area. After calculating the DOP of the structure, it can be observed that a homogeneous film exhibiting similar values for  $P$  was formed. Some of the stripes that can be observed are a result of using dip coating instead of drop casting. These are usually induced by the evaporation process, when this is slower than expected. Thus, through capillary forces the solution concentrates at those stripes until the evaporation proceeds back to normal. Nevertheless, these do not show a hindrance in the overall deposition and alignment. The calculated median DOP was  $P_{\varnothing} = 0.36$  and the maximum value was of  $P = 0.44$ . The values for all the experiments are summarized in table 20. This can also be observed from the DOP distribution, which shows a very homogenous film. Thus, the median DOP is very near to the maximum DOP calculated in a single pixel. The intensity change by rotating the half-wave plate by one radian is also visible. This exhibits the nature of the polarized emission and demonstrates the validity of the experiment. This figure, although useful for the calculation of the DOP, will not be further shown in the following figures, since the aim of it is to calculate the DOP and this is shown in the other pictures.

Next, the 4/12-FFE was investigated. Here, the interdistance of the previous geometry was doubled. This is to analyze the influence of the interdistance to the overall alignment procedure. The acquisitions are shown in the following figure 51.

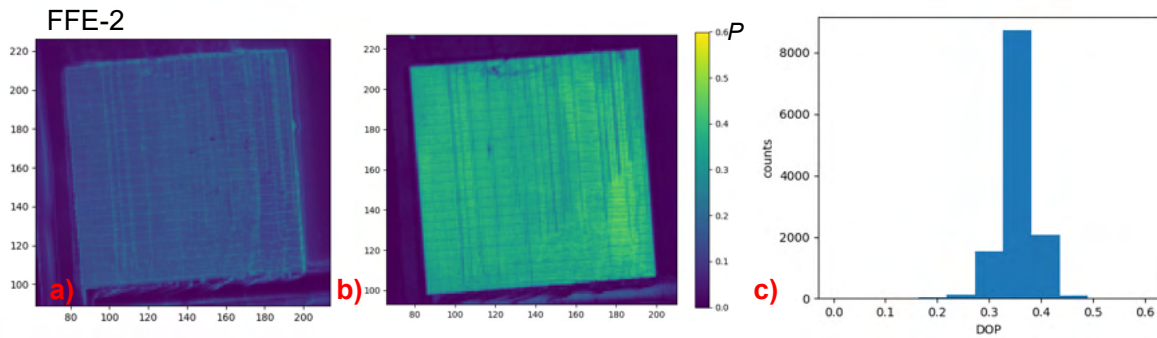


**Figure 51:** a) Acquisition of a 4/12-FFE substrate after dip coating of the QR-17 solution while applying an electrostatic field with  $f = 100$  Hz. The acquisition exhibits the FFE without calculating the DOP for each pixel. It depicts the general overview of the substrate. b) Acquisition of the 4/12-FFE substrate after calculation of  $P$  for each pixel. The color bar shows blue for  $P = 0$  and yellow for  $P = 0.6$ , while the x and y axis show the position of each pixel in a typical coordinate diagramm. c) Histogramm of the DOP distribution inside the  $1 \text{ cm}^2$  active area of the FFE.

As seen from the acquisitions, the deposited QR film shows a homogeneous film with only some observable stripes. These have no substantial influence to the quality of the film. After calculating the DOP of the substrate, the values slightly increase for each pixel. For instance, the maximum value for  $P$  was  $P = 0.47$ . However, the median DOP remains the same with  $P_{\emptyset} = 0.36$ . This can also be observed at the DOP distribution, which is pretty much identical to the previous structure. This means that doubling the interdistance between the electrodes, does not directly affect the alignment of quantum rods. This comes due to the different electric field lines that are responsible of the alignment using FFE. In IDEs, the electric field is perpendicular to the finger electrodes and depends on the distance between them as known from a parallel-plate capacitor. The electric field lines in an FFE are, as the name says, a fringe field, which varies according to figure 9 in chapter 3.2.1. These simulations can be found in the literature,<sup>[72]</sup> which use the Ericksen-Leslie equation coupled with the Laplace equation to numerically solve the motion of LC molecules. Performing simulations with FEMM deliver similar electric field lines. These are shown in the following figure 52 for 4/8- and 4/12-FFE.

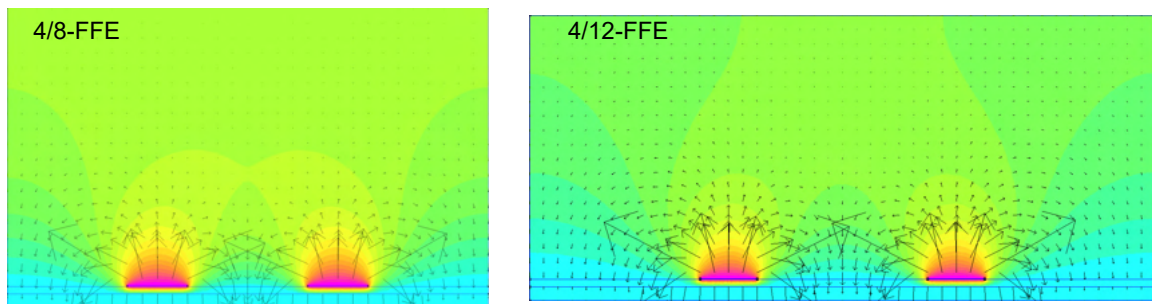


**Figure 52:** Simulation using FEMM for 4/8- and 4/12-FFE. The arrows show the direction of the electric field. The simulation was done with the specified materials and with 150 V. The color map depicts the voltage, with purple representing the highest voltage.

As seen from the simulations, the electric field lines are rather similar. According to the direction of the electric field lines, it can be assumed that most of the QRs are aligned at the interdistance between both electrodes where the field lines show a planar direction. It is to be noted, that these simulations only represent the direction of the possible electric field lines and does not take into account the drying process, the organic components in the solution and other factors that have an effect on the deposition (via dip coating) during the whole procedure. This simulation only helps to understand the difference between the two electrode geometries.

Next, the 5/15-FFE were analyzed. Here, the electrode width was increased, while the interdistance was set at thrice the electrode width. The structures were analyzed for their polarization after the alignment procedure. The acquisitions are shown in figure 53.

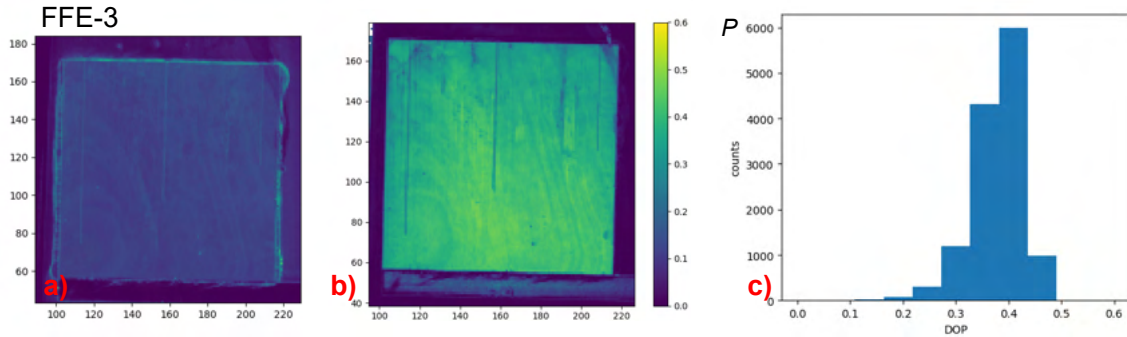


**Figure 53:** a) Acquisition of a 5/15-FFE substrate after dip coating of the QR-17 solution while applying an electrostatic field with  $f = 100$  Hz. The acquisition exhibits the FFE without calculating the DOP for each pixel. It depicts the general overview of the substrate. b) Acquisition of the 5/15-FFE substrate after calculation of  $P$  for each pixel. The color bar shows blue for  $P = 0$  and yellow for  $P = 0.6$ , while the x and y axis show the position of each pixel in a typical coordinate diagram. c) Histogramm of the DOP distribution inside the  $1 \text{ cm}^2$  active area of the FFE.

As seen from the acquisitions, the structures are coated with a homogeneous QR film (as seen from figure 53 a). After calculating the DOP, it can be observed that the median  $P$  value slightly increases in comparison to the 4/8- and 4/12-FFEs. Interestingly, the outer QR layer surrounding the FFE active area is quite thick as seen in figure 53 a). This layer does not exhibit polarization, though. This means the outer electric fields do not contribute to the alignment of the QRs. Looking at the DOP distribution, it can be seen that the alignment was rather homogeneous. The maximum  $P$  value found in a pixel was of  $P = 0.48$ , while the median was of  $P_{\emptyset} = 0.38$ .

Next, the 5/20-FFE structure was analyzed. This means the interdistance between electrodes is four times the width of the finger electrode. The acquisitions are shown in the following figure 48.

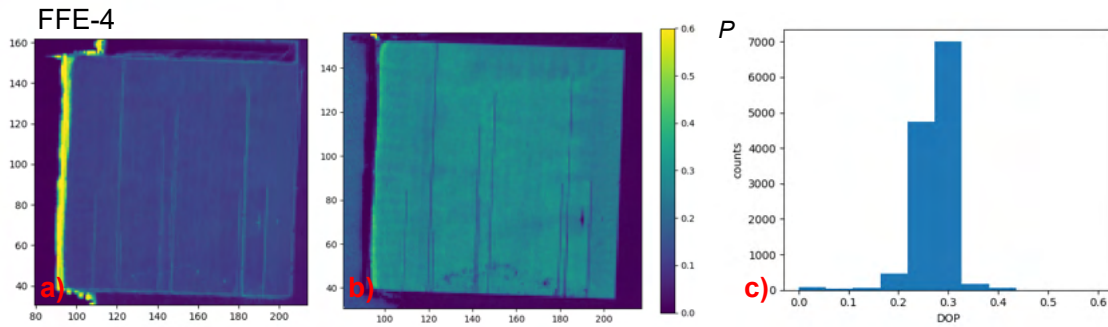


**Figure 54:** a) Acquisition of a 5/20-FFE substrate after dip coating of the QR-17 solution while applying an electrostatic field with  $f = 100$  Hz. The acquisition exhibits the FFE without calculating the DOP for each pixel. It depicts the general overview of the substrate. b) Acquisition of the 5/20-FFE substrate after calculation of  $P$  for each pixel. The color bar shows blue for  $P = 0$  and yellow for  $P = 0.6$ , while the x and y axis show the position of each pixel in a typical coordinate diagramm. c) Histogramm of the DOP distribution inside the  $1 \text{ cm}^2$  active area of the FFE.

As seen from the acquisitions, the substrate is completely coated with the QR film. Some of the finger electrodes exhibit a slightly higher intensity. After calculating the DOP of the film, it is clear that these stripes exhibit no polarization, which accounts for broken finger electrodes. This would mean that although the stripes show a high intensity, the emission is not polarized and therefore no alignment of quantum rods is to be expected in those regions. This is true since the breaking of an electrode would hinder the formation of an electric field. The maximum value for  $P$  found at one pixel was  $P = 0.42$  and the median was of  $P_{\emptyset} = 0.27$ , which are both slightly lower than from a 5/15 substrate. Following this pattern, a further increase in the interdistance should decrease the DOP of the structure even further. For this a 5/25-FFE was analyzed.

The acquisitions for the 5/25-FFE are shown in the following figure 55.

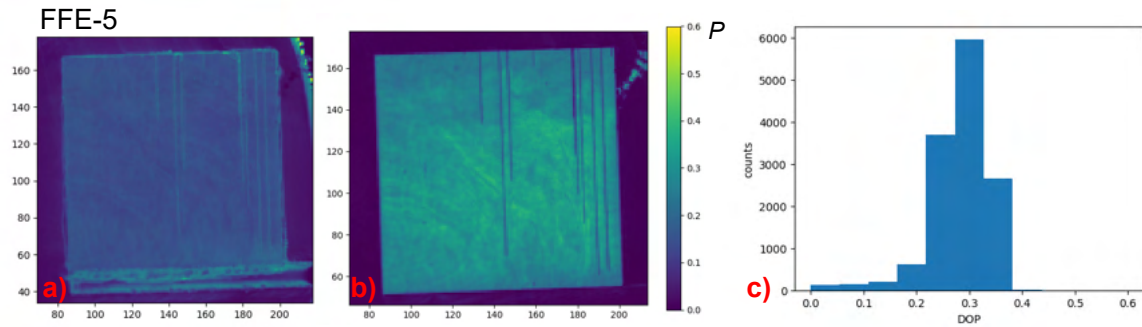


**Figure 55:** a) Acquisition of a 5/25-FFE substrate after dip coating of the QR-17 solution while applying an electrostatic field with  $f = 100$  Hz. The acquisition exhibits the FFE without calculating the DOP for each pixel. It depicts the general overview of the substrate. b) Acquisition of the 5/25-FFE substrate after calculation of  $P$  for each pixel. The color bar shows blue for  $P = 0$  and yellow for  $P = 0.6$ , while the x and y axis show the position of each pixel in a typical coordinate diagramm. c) Histogramm of the DOP distribution inside the  $1 \text{ cm}^2$  active area of the FFE.

As can be seen, the substrate shows a rather homogeneous QR film. Some stripes and inhomogeneities are still present which resemble drying effects due to the dip coating procedure. After calculating the DOP of the structure it is clear that the values for  $P$  are slightly lower than from the previous samples. This can be confirmed by looking at the maximum  $P$  value of  $P = 0.39$  and the median DOP of  $P_{\varnothing} = 0.28$ . Although the median DOP is almost identical, the maximum DOP is still lower. This could be explained by the increasing interdistance between the electrodes and the possible weakening of the electric field. Again, to get a better overview of the electric field lines for these structures, a simulation using FEMM was performed for the three different geometries. The results are shown in the following figure 56.

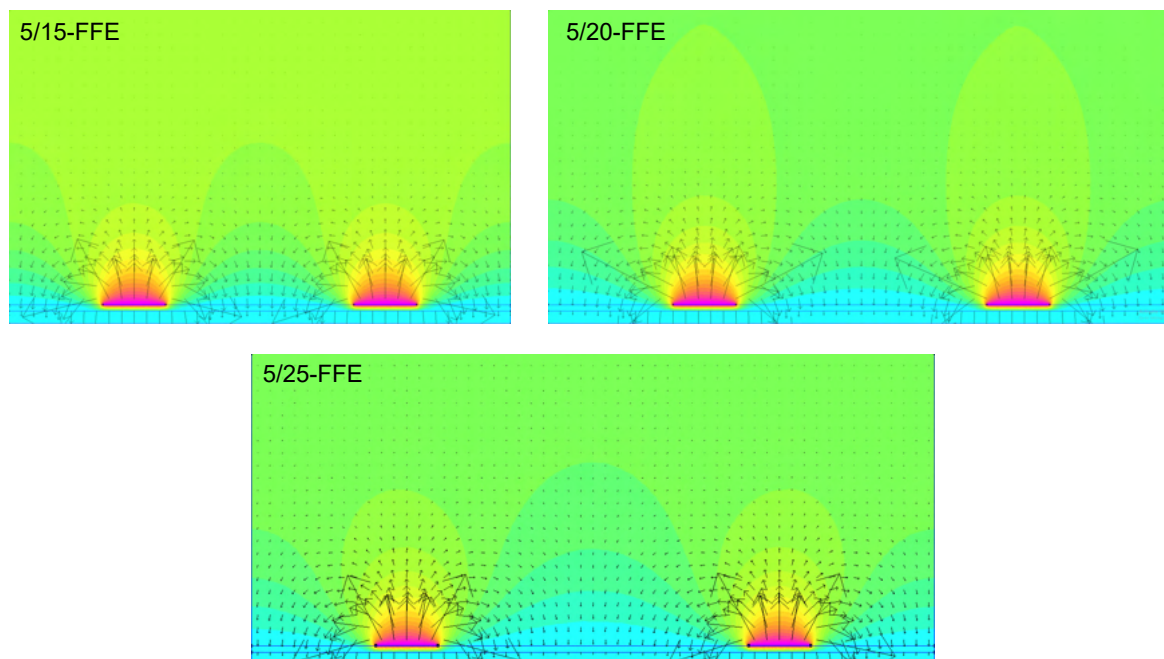


**Figure 56:** Simulation using FEMM for 5/15-, 5/20- and 5/25-FFEs. The arrows show the direction of the electric field. The simulation was done with the specified materials and with 150 V. The color map depicts the voltage, with purple representing the highest voltage.

The simulation shows the direction of the electric field vector lines (depicted as arrows) and the color scale the voltage. It can be seen that increasing the interdistance of the electrodes has a direct effect on the direction of the electric field during the experiment. While the 5/15-FFE shows a substantially high amount of electric field vectors parallel to the bottom substrate, these disappear if the distance is increased. This would affect the alignment of QRs in the middle area between the finger electrodes. The effect is slightly present by looking at the DOP of the three substrates. However, it does not have a significant effect on the overall polarization. This means that the electric field lines are not the only forces responsible of the QR alignment. Effects on the organic phase, the solution, the dip coating procedure and the drying process, all influence the alignment of quantum rods and therefore should be looked at in the following experiments. It is also to be noted that the simulation cannot take all parameters from the experiment into account and is rather an ideal scenario. Interestingly, the area immediately next to the finger electrode shows the strongest electric fields. Since these are fringe-field lines, this area should exhibit the least alignment.

To confirm this, microscopic images of an exemplaric 5/15-FFE were acquired. First, the acquisition was taken from the aligned substrate with the described settings showing the

finger electrode and the interdistance after coating. By using a wide-band (WB) filter, the QR layer can be irradiated with a wavelength below its band edge. This means, the QR film will emit following photoluminescence. This set-up is typical for fluorescence imaging and is helpful to analyze fluorophores. The microscope images are shown in the following figure 57.

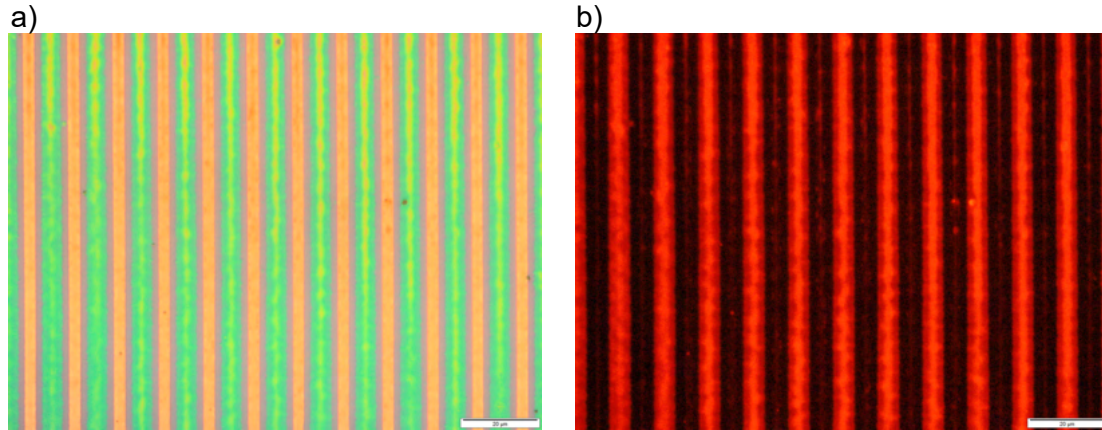


**Figure 57:** Microscopic images of a 5/15-FFE after the alignment procedure (with QR-17) with a) standard set-up and b) the use of a WB filter.

As seen from the microscopic images, there is indeed an area next to the finger electrode which shows no significant QR film. This shows the typical purple color of the used wafer. Furthermore, the area of the finger electrode shows no proper film. By looking at the same section with a WB filter, the red emission of the QRs is visible. The sections between the finger electrodes exhibit the highest emission, which would mean these are the regions with most of the material. While the microscopic image cannot fully confirm the presence of QRs on the finger electrodes and immediately next to them, it is highly probable that these regions still have a very thin QR layer. However, the use of an electric field has shown to enhance the deposition and furthermore align the substrates, as seen from the previous analysis. The summarized results for the FFEs are shown in the following table 20.

Comparing the maximum  $P$  values and the median DOP, the structures with a 5/15, 4/12 and 4/8 electrode width and interdistance exhibit the highest values. Moreover, there is no significant difference between the 4/8 and 5/15-FFE, which means both structures can be used for further optimization steps. This can be explained from the described



**Table 20:** Summarized values for the alignment experiments using an electrostatic field on FFEs with different electrode width and interdistance

| Sample | $w/i$ | $P_{max.}$ | $P_{\emptyset}$ | $f /$<br>Hz | $V /$<br>V |
|--------|-------|------------|-----------------|-------------|------------|
| FFE-1  | 4/8   | 0.44       | 0.36            | 100         | 150        |
| FFE-2  | 4/12  | 0.47       | 0.36            | 100         | 150        |
| FFE-3  | 5/15  | 0.48       | 0.38            | 100         | 150        |
| FFE-4  | 5/20  | 0.42       | 0.27            | 100         | 150        |
| FFE-5  | 5/25  | 0.39       | 0.28            | 100         | 150        |

effects of the electric field. For this reason, 4/8- and 5/15-FFE were used in the following experiments.

### 5.4.2 Influence of the Quantum Rod Solvent

The previous chapter discussed the influence of the geometry on the alignment procedure. While the geometry of the FFE has a direct effect on the electrostatic field, there are other factors involving the procedure that can affect the result. For instance, the dip coating procedure depends heavily on the solvent of the QR solution. Hence, the influence of the QR solvent will be addressed in this chapter.

In order to design the experiment, solvents in which QRs are soluble were chosen. For this, *n*-heptane, octane, toluene and chloroform were investigated. These solvents also exhibit different dielectric constants, thus, should have an influence in the process. Furthermore, due to their different evaporation rates (characterized with the solvent's vapor pressure), the withdrawal speed for each solvent should be adapted.

First, the alignment was investigated with *n*-heptane as the QR solvent. This solvent was already used in the previous experiments. Here, the QR-14 sample was used and 4/8-FFE with an active area of 2 cm<sup>2</sup> were used. The experiment followed the same procedure as described in the previous chapter. The substrate was immersed into the QR-14 solution in heptane while 150 V with an AC with  $f = 100$  Hz were applied. The FFE was analyzed for their polarization and homogeneity with the method mentioned in the previous chapters. The acquisitions are shown in the following figure 58.

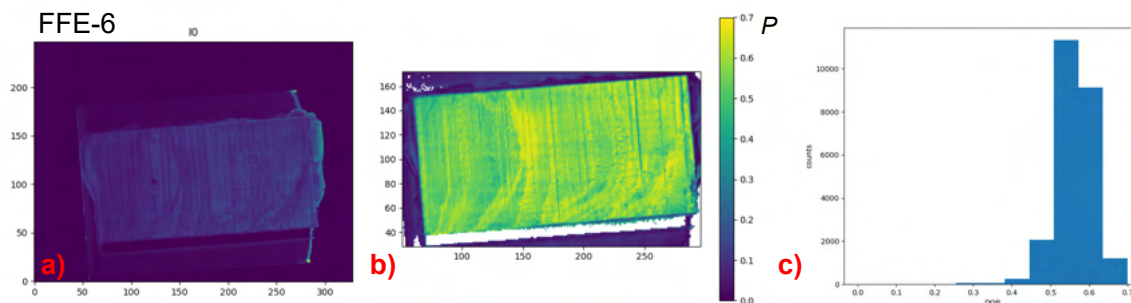


**Figure 58:** a) Acquisition of a 4/8-FFE substrate after dip coating of the QR-14 solution in heptane while applying an electrostatic field with  $f = 100$  Hz. The acquisition exhibits the FFE without calculating the DOP for each pixel ( $I_0$ ). It depicts the general overview of the substrate. b) Acquisition of the FFE substrate after calculation of  $P$  for each pixel. The color bar shows blue for  $P = 0$  and yellow for  $P = 0.7$ , while the x and y axis show the position of each pixel in a typical coordinate diagramm. c) Histogramm of the DOP distribution inside the  $2 \text{ cm}^2$  active area of the FFE.

As seen from the acquisitions, the QR film covers the whole FFE active area. Some stripes can be observed, which are typical for the drying process when using heptane. This could also be observed in the results of the previous chapter. This effect originates from the dip coating process itself, which allows the drying of some regions at a slightly uneven rate. Adjusting the withdrawal speed could not solve the problem. Hence, other external factors such as temperature and air flux during the experiment may have led to the formation of such stripes. Nevertheless, after calculating the DOP of the QR film a very high value for  $P$  was observed. For instance, the maximal value for  $P$  was  $P = 0.69$ , while the median was  $P_{\varnothing} = 0.56$ . It is to be noted that the color scala was adjusted to depict values above 0.6, in comparison to the experiments from the previous chapter. The DOP distribution confirms the homogeneity of the sample. The lower  $P$  values may origin from the drying process as mentioned before and therefore hinder the improvement of the median DOP.

Next, the alignment procedure was analyzed with octane as the solvent. This is an alkane whose boiling point and vapor pressure are much higher than heptane. Hence, the drying should be slower. For this, a withdrawal speed of  $20 \text{ mm/min.}$  was set. The experiment followed otherwise the same settings. The acquisitions are shown in the following figure 59.

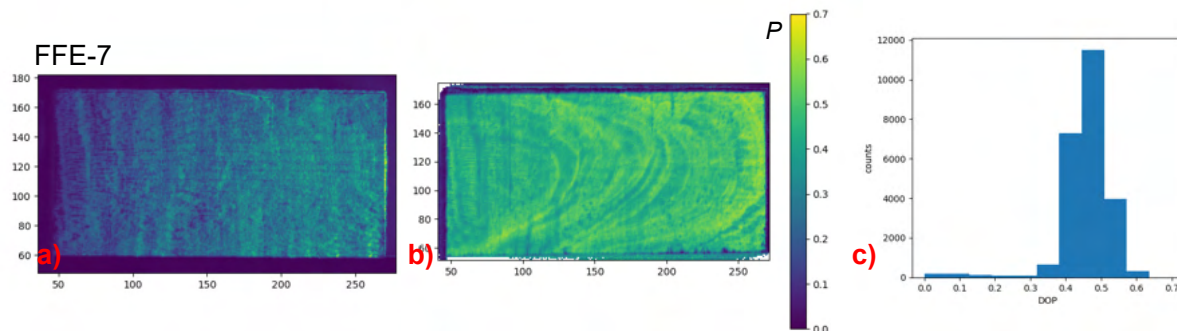


**Figure 59:** a) Acquisition of a 4/8-FFE substrate after dip coating of the QR-14 solution in octane while applying an electrostatic field with  $f = 100$  Hz. The acquisition exhibits the FFE without calculating the DOP for each pixel ( $I_0$ ). It depicts the general overview of the substrate. b) Acquisition of the FFE substrate after calculation of  $P$  for each pixel. The color bar shows blue for  $P = 0$  and yellow for  $P = 0.7$ , while the x and y axis show the position of each pixel in a typical coordinate diagramm. c) Histogramm of the DOP distribution inside the  $2 \text{ cm}^2$  active area of the FFE.

As seen from the acquisition, the QR film covers the active area homogeneously. However, some slight "holes" can be observed. The layer also shows some drying stripes. These originate from the slow drying process of the solvent. Since the substrate is withdrawn more slowly, the effects are more visible in comparison to the experiments using heptane. This is also clearly seen after calculating the DOP of the film. A semi-circular pattern can be observed, which suggests the irregular drying process while withdrawing the substrate from the solution. The calculated DOP are still high, with a maximum  $P$  value of  $P = 0.62$  and a median of  $P_{\emptyset} = 0.46$ . The DOP distribution is also broader than the substrate with heptane, meaning that the deposition and the alignment are slightly reduced by using octane. This should mainly come from the evaporation rate of octane, which is not ideal for a dip coating experiment.

Next, toluene was analyzed. This solvent is in comparison to heptane slightly more viscous, while it also exhibits a lower vapor pressure. Its dielectric constant is also higher than that of the alkanes (these are summarized in table 21). The withdrawal speed for this experiment was set at  $30 \text{ mm/min}$ . The acquisitions are shown in the following figure 60.

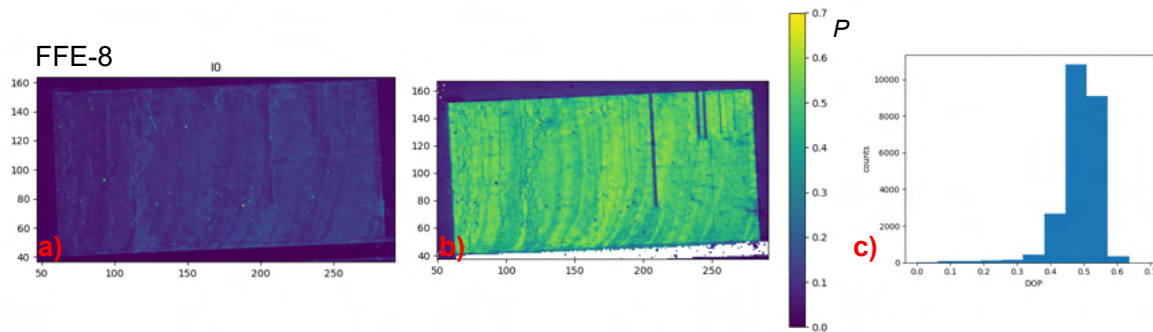


**Figure 60:** a) Acquisition of a 4/8-FFE substrate after dip coating of the QR-14 solution in toluene while applying an electrostatic field with  $f = 100$  Hz. The acquisition exhibits the FFE without calculating the DOP for each pixel ( $I_0$ ). It depicts the general overview of the substrate. b) Acquisition of the FFE substrate after calculation of  $P$  for each pixel. The color bar shows blue for  $P = 0$  and yellow for  $P = 0.7$ , while the x and y axis show the position of each pixel in a typical coordinate diagramm. c) Histogramm of the DOP distribution inside the  $2 \text{ cm}^2$  active area of the FFE.

As can be seen from the acquisitions, the QR film shows some evaporation stripes, as well as some dots, which could indicate either agglomerations or dust in the sample. The stripes resemble the ones from heptane and octane, being semi-circular. This results from the evaporation process while dip coating the structure. After calculating the DOP for the sample, it is clear that some of the finger electrodes broke during the alignment procedure, exhibiting lines without polarization, these can also be observed in the general overview of the sample (figure 60 a). Nonetheless, the DOP of the sample is still very high, with a maximal  $P$  value of  $P = 0.6$  and a median of  $P_{\varnothing} = 0.49$ . The median value is naturally affected by the breaking of some of the finger electrodes, as also seen from the DOP distribution. The distribution, however, shows that a rather homogeneous polarization throughout the sample is present.

Last, chloroform was analyzed. This solvent has a very similar viscosity to toluene and a very high vapor pressure. Its dielectric constant is also higher and it is to be noted that chloroform is a polar aprotic solvent, while alkanes are aprotic and non polar. For this experiment, a withdrawal speed of  $50 \text{ mm/min}$  was set. The acquisitions are shown in the following figure 61.

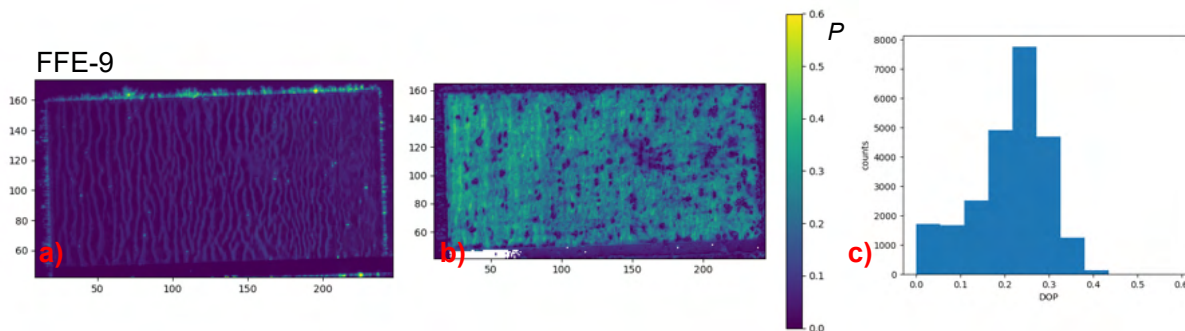


**Figure 61:** a) Acquisition of a 4/8-FFE substrate after dip coating of the QR-14 solution in chloroform while applying an electrostatic field with  $f = 100$  Hz. The acquisition exhibits the FFE without calculating the DOP for each pixel ( $I_0$ ). It depicts the general overview of the substrate. b) Acquisition of the FFE substrate after calculation of  $P$  for each pixel. The color bar shows blue for  $P = 0$  and yellow for  $P = 0.6$ , while the x and y axis show the position of each pixel in a typical coordinate diagramm. c) Histogramm of the DOP distribution inside the  $2 \text{ cm}^2$  active area of the FFE.

As seen from the acquisitions, the layer could not be deposited homogeneously. This is seen at the wavy stripes in figure 61 a). The rather unusual pattern exhibits stripes with a higher concentration of QRs. This is not ideal for the deposition of a homogeneous film. After calculating the DOP, it is also clear that some regions exhibit no polarization, being depicted as some holes. These areas are too big to be accounted for dust or other impurities, it is more a direct effect of the solvent. Being a polar aprotic solvent, the properties of chloroform may hinder the electrostatic alignment and the movement of the QRs. The polarity in the solvent may affect the induced polar moment in the QR and therefore hinder the alignment. Moreover, the nature of the solvent appears to be unsuitable for a deposition using dip coating, as seen from the unusual stripe pattern. Looking at the  $P$  values, these are also rather low in comparison to the other solvents. The maximum  $P$  value calculated at a pixel was of  $P = 0.45$  and a median of  $P_{\emptyset} = 0.21$ . This is no surprise since many areas exhibit very low polarized emission.

The  $P$  values as well as the dielectric constant  $\epsilon$  and the vapor pressure  $p_{vap}$  of the used solvents are summarized in table 21.

As can be seen from the values, the procedure delivers the highest DOP and median DOP using heptane as the QR solvent. For this reason, heptane was used in the following experiments.

**Table 21:** Summarized values for the alignment experiments using an electrostatic field on FFEs with different solvents. The dielectric constant and vapor pressure of the solvents are also listed.<sup>[163,164]</sup>

| Sample | Solvent    | $\epsilon$ | $p_{vap.}$<br>kPa | $P_{max.}$ | $P_{\emptyset}$ |
|--------|------------|------------|-------------------|------------|-----------------|
| FFE-6  | Heptane    | 1.92       | 48                | 0.69       | 0.56            |
| FFE-7  | Octane     | 1.94       | 14                | 0.62       | 0.46            |
| FFE-8  | Toluene    | 2.38       | 29                | 0.60       | 0.49            |
| FFE-9  | Chloroform | 4.81       | 210               | 0.45       | 0.21            |

### 5.4.3 Influence of Organic Additives

To guarantee a controlled and reproducible process, the QR solution was analyzed by adding organic additives which change the viscosity and change the organic mix inside the solution. Since the alignment process involves the movement of the QRs, the organic compounds must be taken into account. For instance, QRs usually exhibit ca. 20 % organic residues as seen from the thermogravimetric analysis of the samples. This organic percentage originates from the ligands that bind to the inorganic CdSe/CdS QRs. The organic ligands for the used QRs are ODPA and HPA. These influence the alignment procedure and also the electric transport. To make sure the QRs can be aligned in the organic solvent, additives were analyzed. The following additives were investigated and will be discussed in this chapter: 1-octadecene, nonanoic acid, 1-octanethiol and oleylamine. As can be seen, the selected additives all show different functional groups. Furthermore, they are all based on long chained alkanes and exhibit a polar end group (except for ODE).

First, the use of 1-octadecene (ODE) as an additive was investigated. ODE has a high boiling point and a very low vapor pressure (1.3 hPa at 20 °C), which would contribute to a slower evaporation rate during the dip coating experiment. Moreover, the synthesis of QRs usually uses ODE as a high boiling solvent. For the experiment, a 5/15-FFE was immersed into the QR-15 solution in heptane. To the solution, the effect of ODE was investigated by performing the alignment with 10  $\mu\text{L}$  (0.98 mmol/L), 20  $\mu\text{L}$  (1.97 mmol/L) and 40  $\mu\text{L}$  (3.95 mmol/L) added to the QR solution. The alignment proceeded with 150 V and 100 Hz (sine curve) with a withdrawal speed of 45 mm/min. The substrates were

then analyzed for their polarization properties. The acquisitions for the three structures with varying ODE parts are shown in the following figure 62.

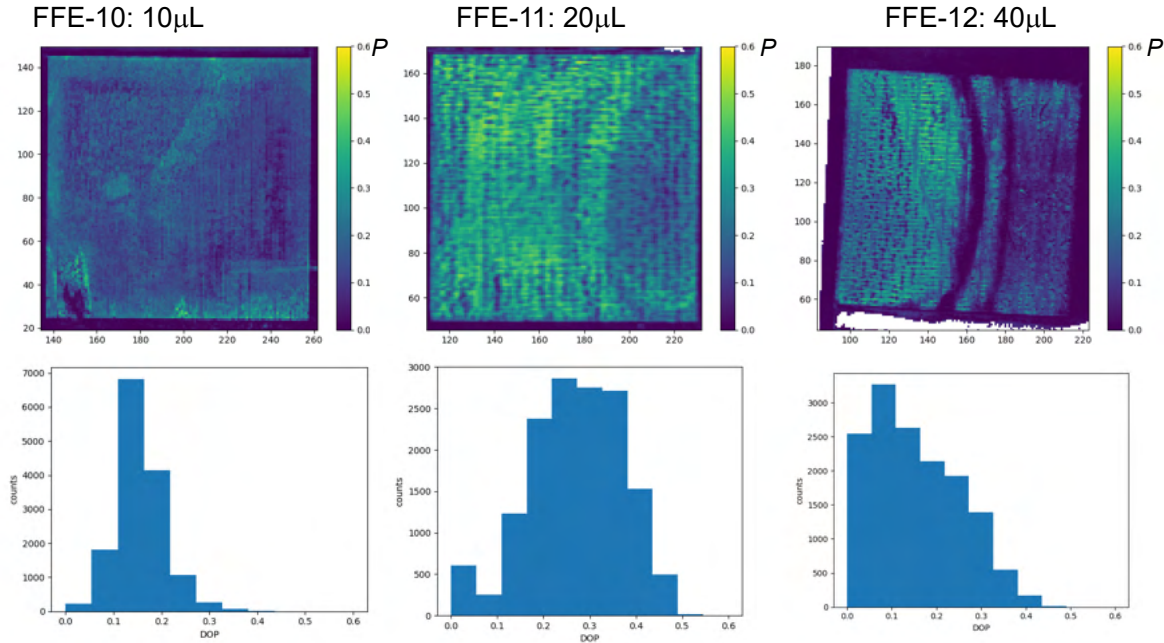


**Figure 62:** Acquisition of three 5/15-FFEs after dip coating into the QR-15 solution in heptane while applying an electrostatic field with  $f = 100$  Hz. (Up) The acquisitions of the three FFE substrates after calculation of  $P$  for each pixel. The color bar shows blue for  $P = 0$  and yellow for  $P = 0.6$ , while the x and y axis show the position of each pixel in a typical coordinate diagramm. (Down) Histogramm of the DOP distribution inside the  $1 \text{ cm}^2$  active area of the FFE for the three samples with varying ODE parts.

As can be seen from the acquisitions, the amount of ODE in the solution influences the overall deposition and the DOP in the substrate. For instance, adding  $10 \mu\text{L}$  ODE delivers a rather homogeneous film but with slightly low DOP. Increasing the amount guarantees an increase in the DOP as can be seen from the maximum  $P$  value and the median  $P$  value. These are summarized for the three structures in table 22. Moreover, FFE-11 shows some "holes" with no polarization. These resemble impurities in the solution like dust or agglomerations. It is possible that adding ODE to the solution makes some of the QRs agglomerate. Thus, the median DOP is decreased in the structure. FFE-12 exhibits a semi-circular pattern with no polarization. This origins from the slow drying of the solution by adding a high boiling solvent and a very low vapor pressure. If the solution does not dry at the same rate in which it is being withdrawn, then stripes will appear and damage the homogeneity of the film. While doing the experiment, it could be observed that while heptane easily evaporates at the set rate, ODE leaves a thin film

which is not easily removed, thus affecting the deposition of the QRs. For this reason, adding too much additives is not recommended. From the calculated  $P$  values, it is sure to say that adding 20  $\mu\text{L}$  of an additive does exhibit changes in the alignment procedure. To compare this effect, the same amounts of additives were investigated using the other compounds.

**Table 22:** Summarized values for the alignment experiments using an electrostatic field on FFEs with ODE as an additive.

| Sample | Additive | $\mu\text{L}$ | $P_{max.}$ | $P_{\emptyset}$ |
|--------|----------|---------------|------------|-----------------|
| FFE-10 | ODE      | 10            | 0.45       | 0.16            |
| FFE-11 | ODE      | 20            | 0.53       | 0.30            |
| FFE-12 | ODE      | 40            | 0.46       | 0.15            |

Next, nonanoic acid was analyzed. Nonanoic acid (pelargonic acid) has a high boiling point and a very low vapor pressure (0.04 hPa). It also includes a carboxylic acid group, while exhibiting a long alkane chain, working as a possible ligand for the quantum rods. The experiment followed the same procedure by adding 10  $\mu\text{L}$ , 20  $\mu\text{L}$  and 40  $\mu\text{L}$  of nonanoic acid to the solution. After the alignment procedure, the substrates were analyzed for their polarization. These are shown in figure 63.



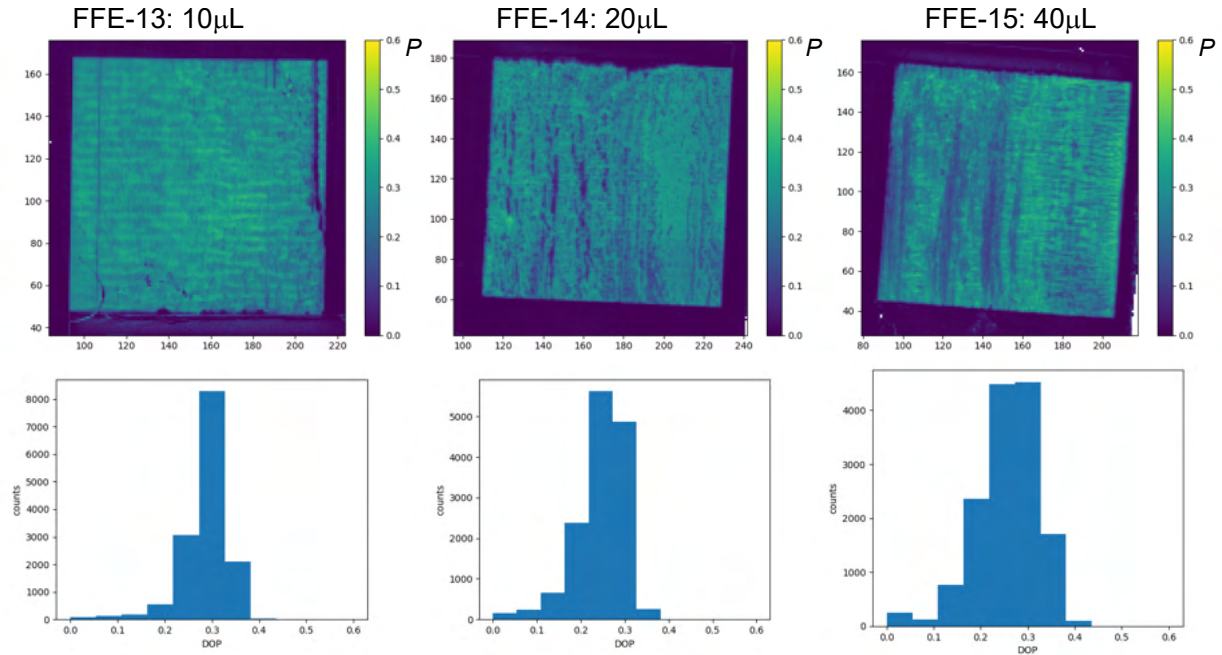


**Figure 63:** Acquisition of three 5/15-FFEs after dip coating into the QR-15 solution in heptane while applying an electrostatic field with  $f = 100$  Hz. (Up) The acquisitions of the three FFE substrates after calculation of  $P$  for each pixel. The color bar shows blue for  $P = 0$  and yellow for  $P = 0.6$ , while the x and y axis show the position of each pixel in a typical coordinate diagramm. (Down) Histogramm of the DOP distribution inside the  $1 \text{ cm}^2$  active area of the FFE for the three samples with varying nonanoic acid parts.

As can be seen from the acquisitions, adding nonanoic acid to the QR solution delivers a rather homogeneous film. Increasing the nonanoic acid part does not necessarily increase the DOP, as seen from the  $P$  values. These are summarized in table 23. The polarization is still lower than the one obtained by using ODE. This means nonanoic acid has a slight negative effect in the alignment procedure.

**Table 23:** Summarized values for the alignment experiments using an electrostatic field on FFEs with nonanoic acid as an additive.

| Sample | Additive      | $\mu\text{L}$ | $P_{max.}$ | $P_{\emptyset}$ |
|--------|---------------|---------------|------------|-----------------|
| FFE-13 | Nonanoic acid | 10            | 0.41       | 0.28            |
| FFE-14 | Nonanoic acid | 20            | 0.42       | 0.25            |
| FFE-15 | Nonanoic acid | 40            | 0.41       | 0.26            |

Next, 1-octanethiol was analyzed. Octanethiol is a typical ligand for nanoparticle synthesis and has a high boiling point as well as a low vapor pressure (0.3 hPa). The experiment followed the same procedure by adding 10  $\mu\text{L}$ , 20  $\mu\text{L}$  and 40  $\mu\text{L}$  of 1-octanethiol to the so-

lution. After the alignment procedure, the substrates were analyzed for their polarization. These are shown in figure 64.

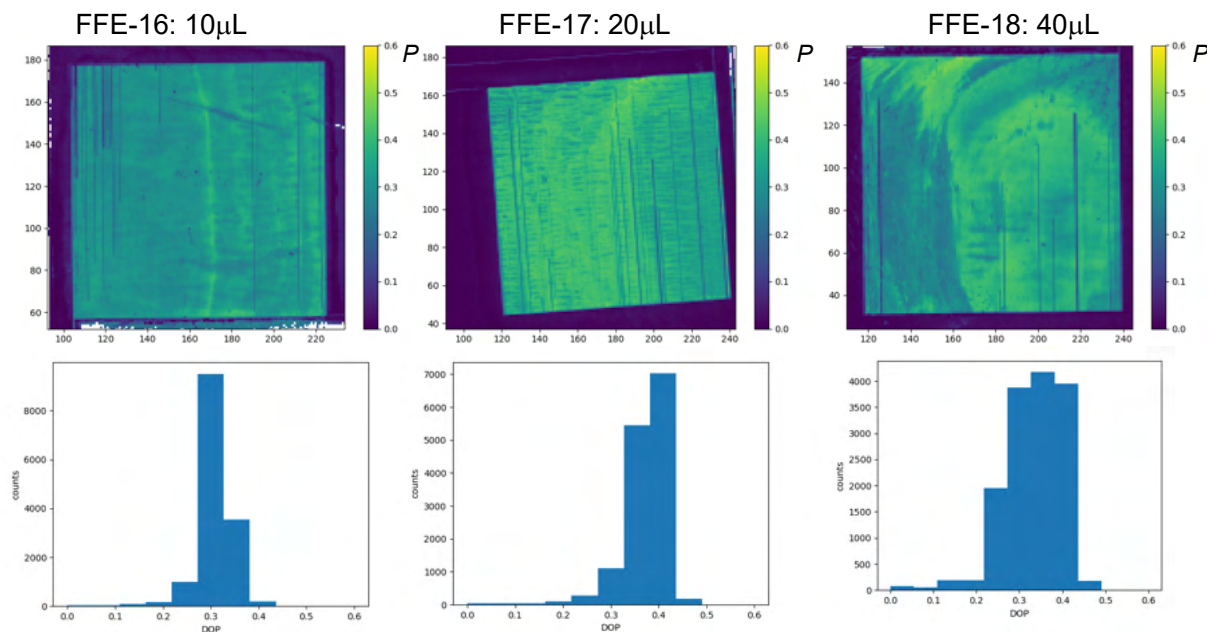


**Figure 64:** Acquisition of three 5/15-FFEs after dip coating into the QR-15 solution in heptane while applying an electrostatic field with  $f = 100$  Hz. (Up) The acquisitions of the three FFE substrates after calculation of  $P$  for each pixel. The color bar shows blue for  $P = 0$  and yellow for  $P = 0.6$ , while the x and y axis show the position of each pixel in a typical coordinate diagramm. (Down) Histogramm of the DOP distribution inside the  $1 \text{ cm}^2$  active area of the FFE for the three samples with varying octanethiol parts.

As can be seen from the acquisitions, adding octanethiol to the solution delivers homogeneous films. This can be confirmed by looking at the DOP distribution. While a low amount of octanethiol delivers slightly lower DOPs, the homogeneity is very high. Increasing the octanethiol amount too much leads to difficulties for the deposition. This can be observed at the stripes and uneven pattern from FFE-18. These are drying effects that affect the alignment procedure and therefore should be avoided. Using  $20 \mu\text{L}$  leads to higher DOP and accounts for a good homogeneity as seen from the median DOP. The values are summarized in table 24. The better deposition and higher DOP in comparison to the additives could be accounted to the nature of 1-octanethiol as a ligand. It may bind to the QRs and allow for a better mobility in solution while applying the electrostatic potential.

Last, oleylamine was analyzed. Oleylamine is also a typical ligand for nanoparticle synthesis. Being a liquid unsaturated fatty amine, it is an interesting compound with a

**Table 24:** Summarized values for the alignment experiments using an electrostatic field on FFEs with 1-octanethiol as an additive.

| Sample | Additive      | $\mu\text{L}$ | $P_{max.}$ | $P_{\emptyset}$ |
|--------|---------------|---------------|------------|-----------------|
| FFE-16 | 1-Octanethiol | 10            | 0.42       | 0.31            |
| FFE-17 | 1-Octanethiol | 20            | 0.48       | 0.37            |
| FFE-18 | 1-Octanethiol | 40            | 0.49       | 0.33            |

high boiling point and a vapour pressure of 1.3 hPa. The experiments quickly delivered a negative influence on the overall procedure. No polarization could be observed after adding just 10  $\mu\text{L}$  of oleylamine to the solution. Adding higher amounts delivered the same negative result. To exemplify this, the acquisitions after the alignment procedure by adding 10  $\mu\text{L}$  of oleylamin are shown in figure 65.

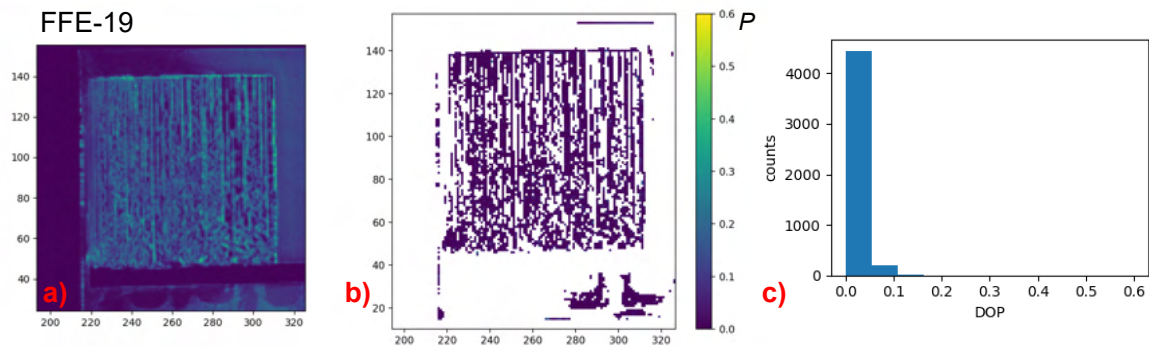


**Figure 65:** a) Acquisition of a 5/15-FFE substrate after dip coating of the QR-15 solution in heptane with oleylamine as an additive while applying an electrostatic field with  $f = 100$  Hz. The acquisition exhibits the FFE without calculating the DOP for each pixel ( $I_0$ ). It depicts the general overview of the substrate. b) Acquisition of the FFE substrate after calculation of  $P$  for each pixel. The color bar shows blue for  $P = 0$  and yellow for  $P = 0.6$ , while the x and y axis show the position of each pixel in a typical coordinate diagramm. c) Histogramm of the DOP distribution inside the  $1 \text{ cm}^2$  active area of the FFE.

As can be seen from the acquisitions, the quantum rod film could be deposited but shows many stripes and lines which account for no deposited material. This is clearer after calculating the DOP, which is very low. The DOP distributions also confirms this, exhibiting only DOP below 0.1. This suggests that oleylamine hinders the alignment procedure and should therefore be avoided.

In summary, adding additives mainly improves the homogeneity and has a direct influence on the alignment procedure, either inhibiting it or facilitating it. Moreover, it allows a more precise control of the procedure, allowing for reproducible results. Therefore, the use of ODE and 1-octanethiol as additives is highly recommended.

### 5.4.4 Influence of Frequency and Voltage

After optimizing the dip-coating procedure to be used for the effective alignment of quantum rods with an electrostatic field, the parameters involving the electrostatic alignment will be discussed. These are mainly the frequency and the voltage. These parameters have a direct effect on the electrostatic potential and should be addressed.

First, the influence of the frequency will be analyzed. Compared to the alignment using IDE substrates, this parameter also has an effect on the dip coating procedure. Increasing the frequency may lead to a vibrating solution which hinders the effectiveness of the QR deposition. The following experiments used 4/8-FFE and the QR-14 solution following the same settings for dip coating with a heptane solution. For this, the FFEs were immersed into the QR-14 solution in heptane while applying an AC (sine curve) and 150 V with a varying frequency. The following frequencies were analyzed:  $f = 1$  Hz, 10 Hz, 100 Hz, 500 Hz and 1000 Hz. The substrates were then analyzed for their polarization properties. First, the electrostatic alignment using a frequency of  $f = 1$  Hz was analyzed. The acquisitions are shown in the following figure 66.

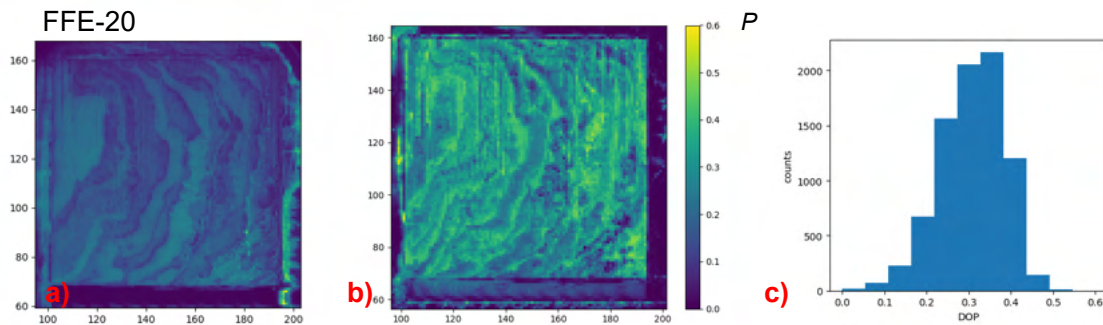


**Figure 66:** a) Acquisition of a 4/8-FFE substrate after dip coating of the QR-14 solution in heptane while applying an electrostatic field with  $f = 1$  Hz. The acquisition exhibits the FFE without calculating the DOP for each pixel ( $I_0$ ). It depicts the general overview of the substrate. b) Acquisition of the FFE substrate after calculation of  $P$  for each pixel. The color bar shows blue for  $P = 0$  and yellow for  $P = 0.6$ , while the x and y axis show the position of each pixel in a typical coordinate diagramm. c) Histogramm of the DOP distribution inside the  $1 \text{ cm}^2$  active area of the FFE.

As seen from the acquisitions, the QR film exhibits a rather inhomogeneous film. Drying lines due to the low frequency can be observed. Although the withdrawal speed for heptane was kept the same (45 mm/min.), the alignment appears to be hindered by changing the frequency in the experiment. After calculating the DOP of the substrate,

high  $P$  values can be observed with a maximum of  $P = 0.51$  but many regions still show low polarization. This means the alignment does not follow a homogeneous pattern. A low frequency resembles a DC the most, which allows the movement of QRs in the direction of the contact electrodes. This hinders the alignment overall and favors the uneven pattern of the film. This is confirmed by looking at the DOP distribution, having a very broad distribution leading to a median of  $P_{\emptyset} = 0.31$ . The values for all the experiments are summarized in table 25.

The influence of the frequency was further analyzed by increasing the frequency to  $f = 10$  Hz. The acquisitions are shown in the following figure 67.

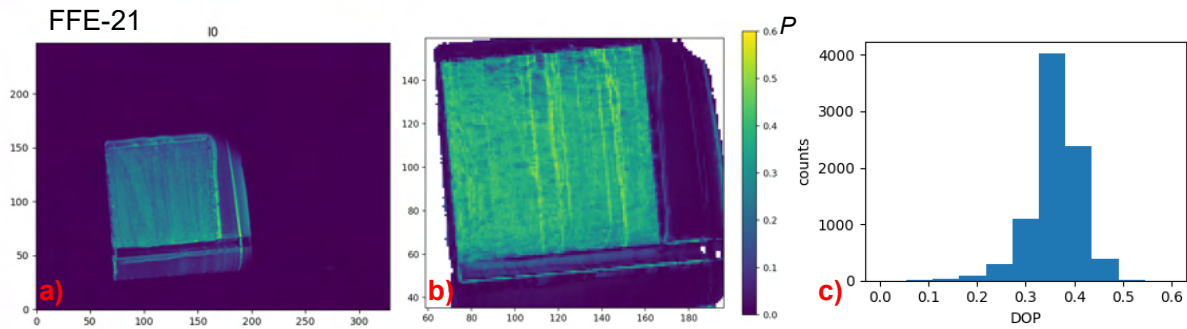


**Figure 67:** a) Acquisition of a 4/8-FFE substrate after dip coating of the QR-14 solution in heptane while applying an electrostatic field with  $f = 10$  Hz. The acquisition exhibits the FFE without calculating the DOP for each pixel ( $I_0$ ). It depicts the general overview of the substrate. b) Acquisition of the FFE substrate after calculation of  $P$  for each pixel. The color bar shows blue for  $P = 0$  and yellow for  $P = 0.6$ , while the x and y axis show the position of each pixel in a typical coordinate diagramm. c) Histogramm of the DOP distribution inside the  $1 \text{ cm}^2$  active area of the FFE.

As seen from the acquisitions, the homogeneity of the film is highly increased, as seen from figure 67 a). After calculating the DOP, it is clear that the polarization is also enhanced, meaning the alignment of the QRs is facilitated by applying a higher frequency. A higher rate also stabilized the vibration of the solution, which leads to a better deposition. The homogeneity can also be observed by looking at the DOP distribution. The highest  $P$  value was measured at  $P = 0.51$  and a median of  $P_{\emptyset} = 0.36$ . While the highest  $P$  value is the same as the previous structure, the median value is slightly increased.

Next, an increase of ten fold was analyzed with  $f = 100$  Hz. The acquisitions are shown in figure 68.

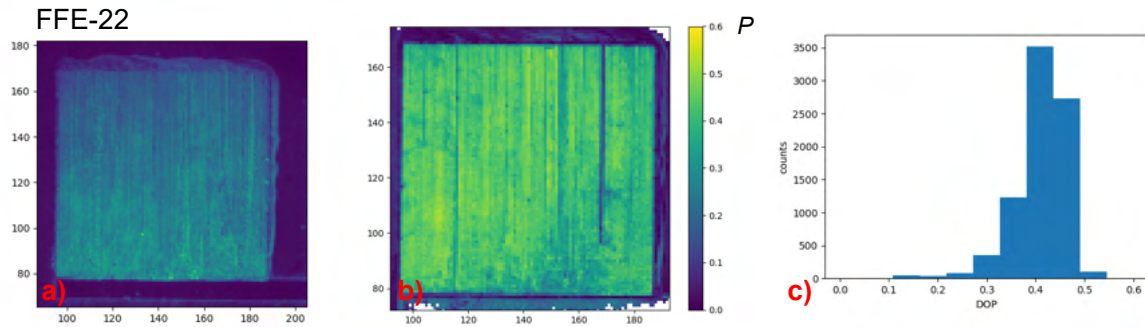


**Figure 68:** a) Acquisition of a 4/8-FFE substrate after dip coating of the QR-14 solution in heptane while applying an electrostatic field with  $f = 100$  Hz. The acquisition exhibits the FFE without calculating the DOP for each pixel ( $I_0$ ). It depicts the general overview of the substrate. b) Acquisition of the FFE substrate after calculation of  $P$  for each pixel. The color bar shows blue for  $P = 0$  and yellow for  $P = 0.6$ , while the x and y axis show the position of each pixel in a typical coordinate diagramm. c) Histogramm of the DOP distribution inside the  $1 \text{ cm}^2$  active area of the FFE.

As seen from the acquisitions, the homogeneity of the film is improved. Some finger electrodes appear to be broken, however, this does not heavily affect the alignment procedure. After calculating the DOP of the substrate, the maximum  $P$  value is increased to  $P = 0.52$ , while the median is increased to  $P_{\emptyset} = 0.41$ . This is confirmed by looking at the DOP distribution, which accounts for a homogeneous film with high  $P$  values.

Next, an increase of five fold with a  $f = 500$  Hz was analyzed. The acquisitions are shown in the following figure 69.

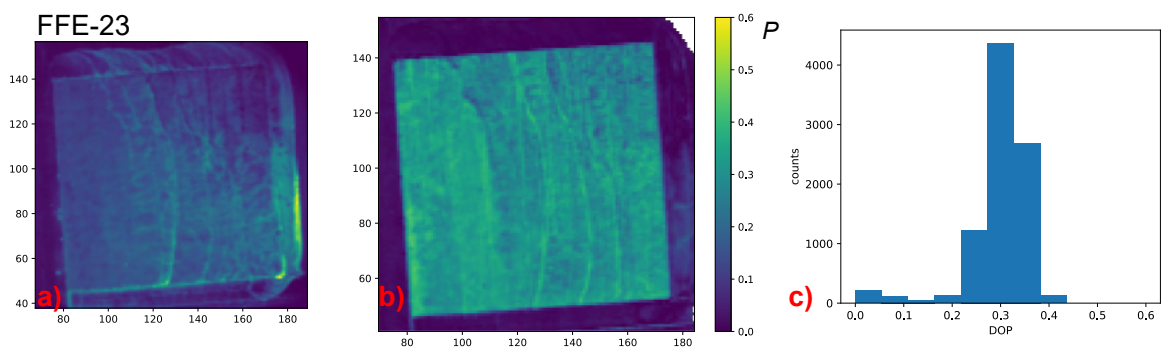


**Figure 69:** a) Acquisition of a 4/8-FFE substrate after dip coating of the QR-14 solution in heptane while applying an electrostatic field with  $f = 500$  Hz. The acquisition exhibits the FFE without calculating the DOP for each pixel ( $I_0$ ). It depicts the general overview of the substrate. b) Acquisition of the FFE substrate after calculation of  $P$  for each pixel. The color bar shows blue for  $P = 0$  and yellow for  $P = 0.6$ , while the x and y axis show the position of each pixel in a typical coordinate diagramm. c) Histogramm of the DOP distribution inside the  $1 \text{ cm}^2$  active area of the FFE.

As can be seen from the acquisitions, the QR film remains homogeneous and exhibits high DOP. Some drying stripes can be observed on the structure. This origin from the slight

vibration of the solution while dip coating. This effect can be observed when increasing the frequency. Thus, the frequency has a direct effect on the dip coating procedure and may hinder the alignment as well. This can also be observed by the increasing low  $P$  values in the DOP distribution. While the maximum  $P$  value decreases in comparison to the 100 Hz sample with  $P = 0.43$ , the median DOP also decreases with  $P_{\emptyset} = 0.30$ . To confirm this a further increase in the frequency was investigated.

Last, a frequency of  $f = 1000$  Hz was applied during the electrostatic alignment. The acquisitions are shown in the following figure 70.

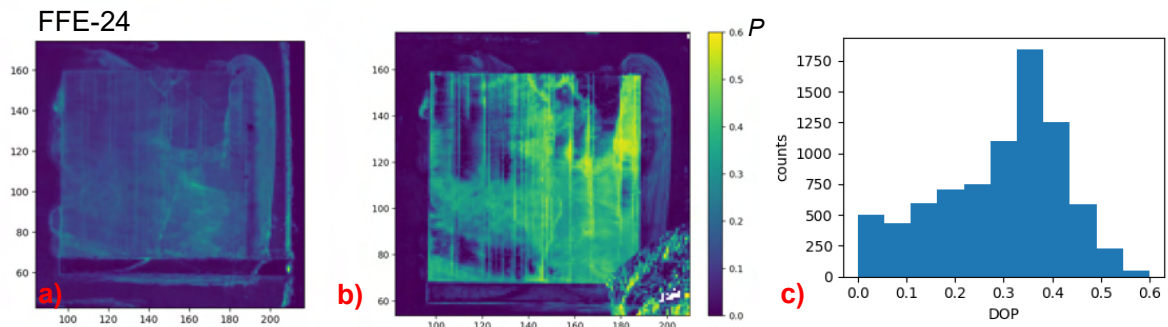


**Figure 70:** a) Acquisition of a 4/8-FFE substrate after dip coating of the QR-14 solution in heptane while applying an electrostatic field with  $f = 1000$  Hz. The acquisition exhibits the FFE without calculating the DOP for each pixel ( $I_0$ ). It depicts the general overview of the substrate. b) Acquisition of the FFE substrate after calculation of  $P$  for each pixel. The color bar shows blue for  $P = 0$  and yellow for  $P = 0.6$ , while the x and y axis show the position of each pixel in a typical coordinate diagramm. c) Histogramm of the DOP distribution inside the  $1 \text{ cm}^2$  active area of the FFE.

As seen, the deposition of the QR film is hindered by using a high frequency of 1 kHz. This could be observed during the dip-coating process, where the solution slightly resonated and vibrated on the surface of the FFE. Thus, the process cannot work properly. After calculating the DOP, it can be observed that the maximum  $P$  value could be increased by increasing the frequency as compared to the previous substrates (with  $P = 0.58$ ). However, due to the hindered deposition, the DOP distribution is severely affected. Therefore, a median DOP of  $P_{\emptyset} = 0.29$  was calculated, which is lower than from all the previous experiments.

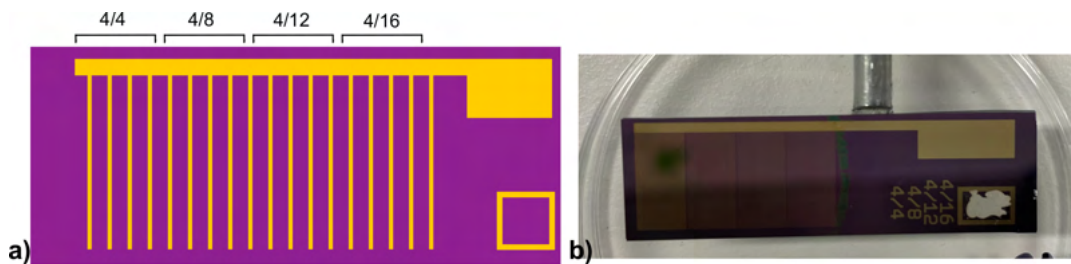
By looking at table 25, the maximum  $P$  value could be obtained by using the highest frequency (with  $f = 1000$  Hz). However, using such a high frequency affects the dip coating process and is not suitable for this deposition method. Therefore, using a lower frequency of 100 Hz allows for high DOP values and also a homogeneous deposition.

**Table 25:** Summarized values for the alignment experiments using an electrostatic field on FFEs with different frequencies.

| Sample | $P_{max.}$ | $P_{\emptyset}$ | $f /$<br>Hz | $V /$<br>V |
|--------|------------|-----------------|-------------|------------|
| FFE-20 | 0.51       | 0.31            | 1           | 150        |
| FFE-21 | 0.51       | 0.36            | 10          | 150        |
| FFE-22 | 0.52       | 0.41            | 100         | 150        |
| FFE-23 | 0.43       | 0.30            | 500         | 150        |
| FFE-24 | 0.58       | 0.29            | 1000        | 150        |

Therefore, the alignment process using dip coating and an electrostatic field should be performed with this set frequency.

Next, the influence of the voltage towards the alignment process will be discussed. Since the increase of a voltage directly affects the strength of the electric field, this was investigated by using substrates with varying electrode width and interdistance. This way, it is possible to analyze the effect of voltage on a changing geometry and therefore obtain the best suitable voltage for a suitable FFE. Since the increasing voltage may affect the insulating  $\text{SiO}_2$  layer (this can be observed at the simulations in figure 52, chapter 5.4.1), a wafer with  $1 \mu\text{m}$   $\text{SiO}_2$  insulating layer was used for the fabrication of the substrates. The influence of voltage was analyzed on FFE with the following  $w/i$ : 4/4, 4/8, 4/12 and 4/16; and with the following voltages: 50 V, 100 V, 150 V, 200 V, 250 V, 300 V, 350 V and 400 V. The geometries of the FFE are shown in the following figure 71. This orientation is the same as the orientation from the DOP acquisitions and helps identifying the  $w/i$  of the analyzed substrate.

**Figure 71:** a) Schematic illustration of the used FFE in this work. The bottom substrate is a silicon wafer, while the upper electrode structures are separated by a  $1 \mu\text{m}$  insulating  $\text{SiO}_2$  layer. The electrode width and interdistance ( $w/i$ ) from left to right are: 4/4, 4/8, 4/12, 4/16. b) Picture of the used FFE electrode to illustrate their geometry.



The voltage was analyzed by dip coating the FFE into the QR-16 solution and applying the desired voltage with a frequency of 100 Hz (sine curve) and withdrawing the substrate at 45 mm/min. The substrates were then analyzed for their polarization properties with the methods described previously. The acquisitions for all the applied voltages are shown in the following figure 72.

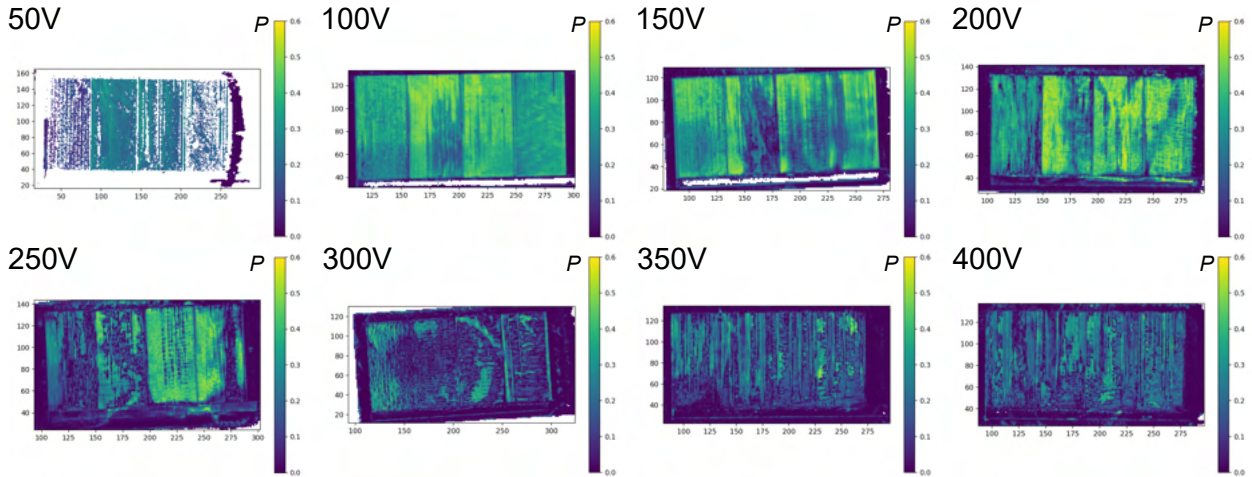


**Figure 72:** Acquisitions of the aligned QR films with QR-16 on FFE with varying geometry and applied voltage. The color bar shows the calculated DOP with blue being  $P = 0$  and yellow  $P = 0.6$ , while the x and y axis show the position of each pixel in a typical coordinate diagram.

The acquisitions show the FFE after calculating the DOP for each pixel and assigning it a color according to the calculated values. As can be seen, the increase of the voltage increases the DOP on the substrate. However, it is not a linear increase. First, the substrate with 50 V shows the lowest DOP. Varying the  $w/i$  has a direct effect on the alignment, as can be seen from the FFE. Having the same width as interdistance delivers very low DOP. Similar to the analysis made in chapter 5.4.1, the 4/8 FFE delivers a homogeneous film and DOP with a median of  $P = 0.28$ . The maximum was calculated at  $P = 0.41$ . Next, increasing the voltage to 100 V delivers an increase in both the median and the maximum DOP. As can be seen, some areas are not perfectly deposited, thus damaging the alignment process. However, it can be seen that the 4/8 and 4/12 FFEs deliver the highest  $P$  values. While the 4/16 FFE exhibits a very homogeneous film, the calculated DOP are not as high as the other electrodes. These results also correlate with the experiments in chapter 5.4.1. Increasing the voltage to the usually set 150 V shows rather similar results to the previous voltage. However, the 4/8 FFE shows several inhomogeneities, which do not correlate with the previous experiments throughout this

work. This may come due to impurities in the QR solution, or defects at the electrodes which could have led to the difficulties of the alignment. Setting a voltage of 200 V exhibits the highest DOP. However, the homogeneity of the film shows an increase in defects. This could be associated with the increase of the electric field that hinders the dip coating process, as observed with the change of frequencies. This time, the 4/8, 4/12 and 4/16 FFEs show very similar results. The highest DOP value was calculated at  $P = 0.59$ , confirming the influence of the applied voltage to the alignment process. A further increase in voltage does not deliver higher DOP, neither on the maximum calculated DOP, nor in the median DOP for any of the FFE. This can be easily observed at the deposited films, which show very inhomogeneous films and very low polarization. This could be ascribed to the strength of the electric field, which would increase the field perpendicular to the finger electrodes and hinder the alignment on the field lines as seen in the simulation in the previous chapters. Another possibility is that the increased voltage may affect the alignment process through the dip coating and the organic presence in the solution. Since the alignment process not only involves the inorganic QRs but also the ligands and the solvent, the increase of the electric field may affect these components. Thus, the deposition and alignment may be hindered. This effect was summarized in the following diagram, where the DOP is shown in dependence of the applied voltage as well as the frequency.

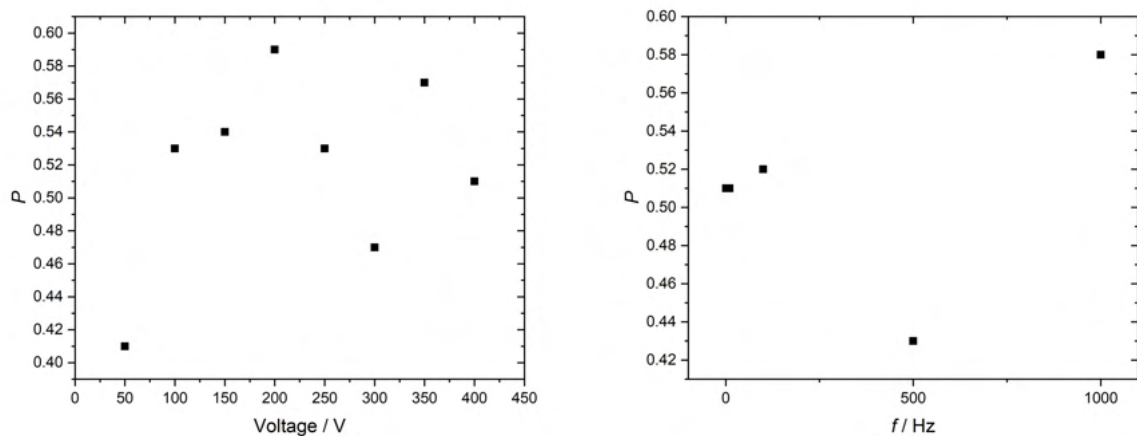


**Figure 73:** Left: Calculated maximum  $P$  values from the experiments against the voltage (in V). Right: calculated maximum  $P$  values from the experiments against the frequency (in Hz).

The experiments show very mixed results. While an increase in the applied voltage could increase the maximum DOP in the substrate it does not show any linear trend and as seen from the experiments before it also hinders the deposition of the film. Furthermore, while an increase of up to 200 V shows a rapid increase in the DOP, this process involves many factors and parameters which should always be taken into account. On the other hand, an increase in the frequency delivers high DOP. While the experiment with 500 Hz does not follow the trend, the increasing frequency shows a slight increase in the calculated maximum  $P$  values. However, as discussed in this chapter, an increase in the applied frequency also hinders the median DOP and the deposition of the film due to the vibrating solution during dip coating. As of these results, applying 150 V and 200 V with  $f = 100$  Hz delivers the highest median DOP as well as a high maximum DOP.

#### 5.4.5 Influence of the Quantum Rod Sample

Throughout this work, several QR samples with different characteristics were analyzed and aligned with an electrostatic field. The results from the experiments delivered similar trends but different DOP. While several samples exhibit very similar characteristics such as length and width, the alignment process involves several external factors such as those analyzed in the previous chapters. As a way to analyze the trends and sources of the different results, a screening of some QR samples with different length and width were analyzed. As described in chapter 3.2, the polarized emission in QRs originates from the split of the exciton fine structure due to the strain at the core. For this reason, the maximum DOP obtained from several samples with different length  $l$  and width  $w$  were analyzed by using the same alignment procedure. It is important to note, that the same samples were used for the length and width analysis. For instance, the sample with a length of 11 nm exhibits a width of 4.5 nm. While a varying length with a fixed width would be preferred (and vice versa), synthetically, this is very difficult to achieve. Hence, a big range in the QR length (40 nm) could be analyzed, while a very small range in the QR width was investigated (0.6 nm). The diagrams are shown in the following figure 74.

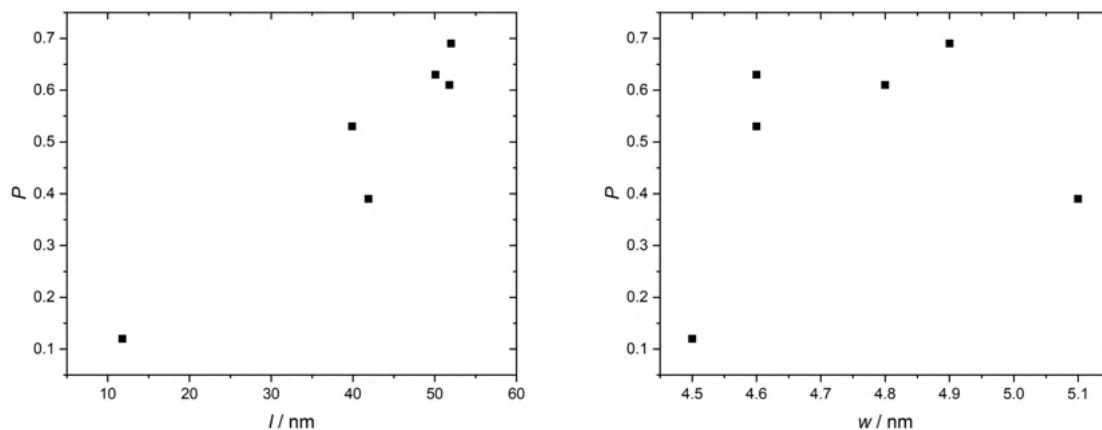


**Figure 74:** Calculated maximum  $P$  value in dependence of the QR length (left) and width (right).

The diagrams exhibit some clear trends. First, the length of the QR sample appears to have a direct influence in the obtained DOP by using the described alignment procedure. This correlates with some theoretical reports as described in chapter 3.2, whereas an increased length usually increases the polarization of the sample. Although a linear trend was not fully observed, a clear increase in the DOP is present. Furthermore, a relationship between the polarized emission and the QR width was also observed. While the difference in width for the analyzed samples is not very high, an increase in the width increases the calculated DOP severely. This could be ascribed to the increased strain at the cores, since the energetic separation of the excitonic levels should increase by applying a higher strength on this axis.

While these results offer an overview of the acquired results, it should be noted that the alignment procedure involves several external parameters such as the applied voltage, frequency and also the use of organic additives and ligands. However, it is sure to say that the polarized emission strongly depends on the QR's length and width. Since the alignment procedure can be optimized and delivers reproducible results, the inner property of polarized emission originates from the characteristics of the quantum rod and these can differentiate from sample to sample.

### 5.4.6 Summary

The alignment procedure using fringe field electrodes by dip coating in a quantum rod solution was optimized and established. Several factors were investigated that have a direct effect on either the electric field during the alignment or on the dip coating of the QR sample.

First, the electrode width and interdistance was investigated. This has a direct effect on the electric field and thus influences the effectivity of the alignment using an electrostatic field. From the analyzed structures, FFE with 4/8, 4/12, 5/15  $w/i$  delivered the best results. This could be confirmed with simulations showing the electric field lines.

Moreover, the solvents and the use of organic additives was analyzed. Using heptane as the QR solvent and adding octanethiol and 1-octadecene in very small concentrations allowed the alignment procedure to be reproducible and deliver high DOP.

Next, the influence of the frequency and voltage was analyzed. While an increase in both parameters usually increases the maximum DOP, the homogeneity strongly decreases by increasing both parameters. Therefore, the use of 150-200 V and 100-Hz is the recommended setting.

Last, a correlation of the quantum rod sample and the calculated DOP using this method was shown. An increase in both width and length delivers an increase in DOP, which correlates with the theory of the polarized emission.

## 5.5 Fabrication of PEQLEDs

The fabrication of PEQLEDs is based on the described process using stacked layers in chapter 3.4. For this work, two stacks were analyzed and discussed. The first QLED stack is the conventional stack. While this offers a fast fabrication using liquid solutions, some difficulties may arise for the fabrication of the PEQLED. One of the main steps for the fabrication of these devices is the transfer of the aligned QR film onto the QLED stack. This will be addressed in the following chapters. For the use in display technologies and due to the controlled fabrication of many of the involved layers, an inverted stack was also analyzed.

The QLED fabrication involves the following steps:

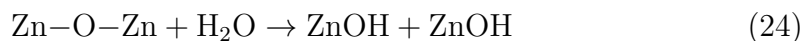
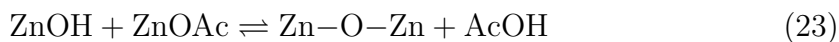
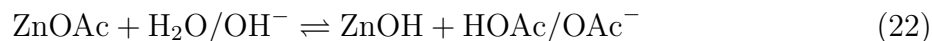
1. Fabrication of structured indium-tin oxide
2. Synthesis of ZnO nanoparticles
3. Transfer of the aligned QR film
4. Deposition of the remaining ETL, HTL, HIL either via spin coating or PVD

The fabrication of structured indium-tin oxide is achieved by photolithography and is described in chapter 8.3.5. This has the advantage of a quick design of the desired active area in the PEQLED. The required zinc oxide nanoparticles were synthesized and will be discussed in the following chapter. While ZnO is commercially available, it has been shown in previous works at Fraunhofer CAN and at Fraunhofer IAP that the use of synthesized ZnO nanoparticles always delivers improved results. Last, depending on the stacking, the remaining layers were deposited either via spin coating or using PVD.

### 5.5.1 Synthesis of ZnO Nanoparticles

The synthesis of ZnO nanoparticles followed an adapted method reported by Mashford *et al.*<sup>[110]</sup> Here, the synthesis was upscaled as described in chapter 8.5.1. This follows the condensation of zinc acetate in the presence of water and an organic base (in this case tetramethylammonium hydroxide). This delivers ZnO nanoparticles through a sol-gel

method with the following steps.<sup>c[110,165]</sup>



Here, the oxides can be formed by either hydrolysis (equation 22), condensation (equation 23) or by dissolution to ZnO in equation 24.<sup>[165]</sup> Following this procedure, ZnO nanoparticles were synthesized and analyzed. The synthesized ZnO nanoparticles used in this work were characterized via absorption spectroscopy, XRD, TEM and the deposited spin coated layers via AFM.

First, the absorbance of the sample ZnO-1 is shown in the following figure 75.

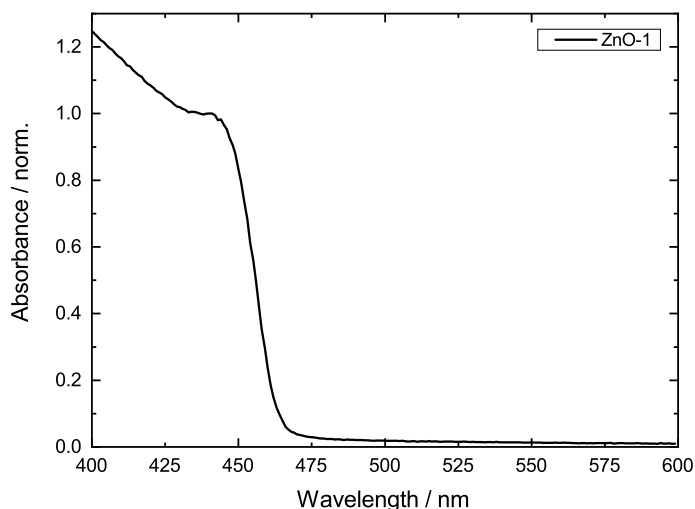


**Figure 75:** Absorbance spectrum of the synthesized ZnO nanoparticles.

The absorbance spectrum exhibits a broad absorption maximum at 445 nm. Although this feature is red shifted in comparison to small ZnO nanoparticles, which show band gap absorption between 340 and 400 nm, the presence of ZnO can be confirmed using other methods. For instance, the nanoparticles were characterized via XRD to confirm the successful synthesis of the nanoparticles, this is shown in the following figure 76.

---

<sup>c</sup>AcO<sup>-</sup> = CH<sub>3</sub>COO<sup>-</sup>

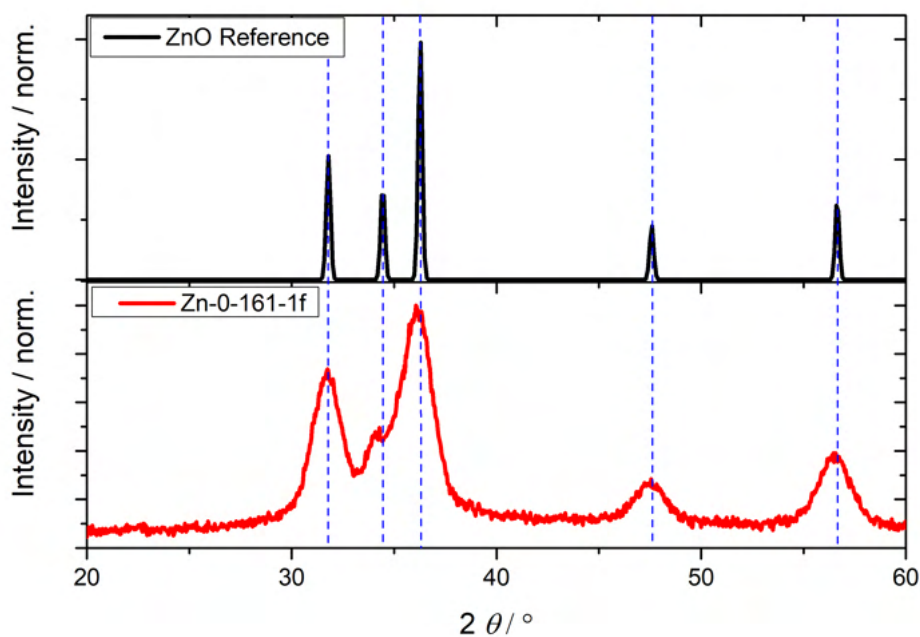


**Figure 76:** XRD for the synthesized ZnO nanoparticles. (Up) Reference reflexes for bulk ZnO crystallized in the wurtzite crystal structure.<sup>[166,167]</sup> (Down) Reflexes of the synthesized ZnO-1 (Log-Nr: Zn-0-161-1f) sample.

The X-ray diffractogram shows that the particles prepared with the described synthesis are wurtzite ZnO with the visible (100), (002), (101), (102) and (110) reflexes. These are broad due to the small crystalline size of the nanoparticles. To calculate the nanoparticles' size, these were analyzed via TEM. The micrographs are shown in the following figure 77.

ZnO-1

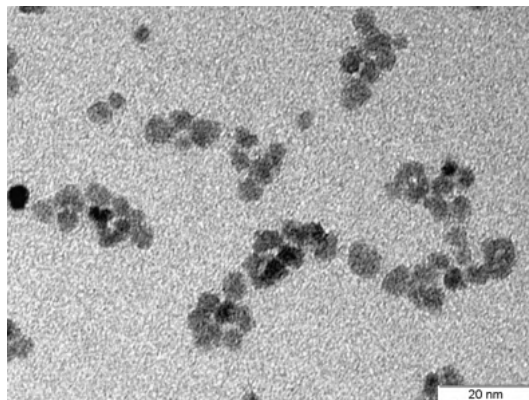
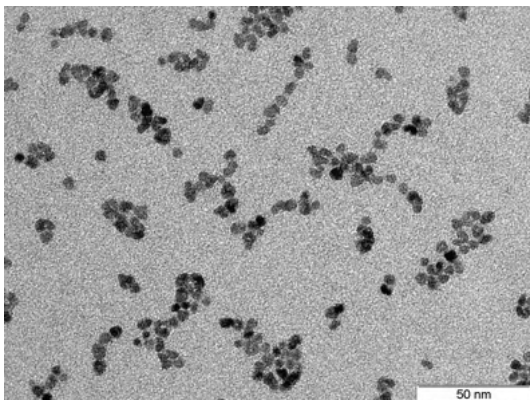


**Figure 77:** TEM images of the synthesized ZnO nanoparticles with (left) 50 nm and (right) 20 nm scale bar.



The micrographs show quasi-spherical ZnO nanoparticles with a median size of  $4.1 \pm 0.8$  nm. According to the literature,<sup>[110,165]</sup> the expected nanoparticle size for this synthesis ranges between 4 - 5 nm. Therefore, it can be confirmed that the nanoparticle synthesis was successful.

For the fabrication of a QLED using ZnO as the ETL, a layer of 25 nm to 75 nm is required.<sup>[115,116,168]</sup> For this work, following the works by Ekaterina Salikhova<sup>[169]</sup> from Fraunhofer CAN and Dr. Yohan Kim<sup>[115]</sup> from Fraunhofer IAP, a 40 nm ZnO layer was used. The deposition of the ZnO layer follows a simple spin coating followed by a baking step. The first step guarantees a homogeneous layer with the desired thickness, while the latter removes any remaining impurities in the ZnO solution.

For the deposition, a solution of ZnO nanoparticles (ZnO-1) in 1-propanol with a concentration of  $c = 15$  mg/mL was spin coated at 2000 rpm for 30 s. This step is repeated twice in order to guarantee a 40 nm thick layer. This can be confirmed with AFM measurements, shown in the following figure 78.

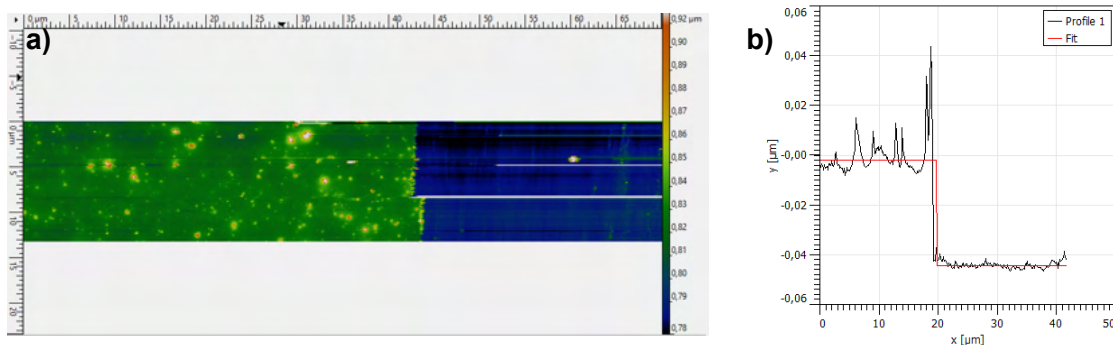


**Figure 78:** (a) AFM measurement analyzed with Gwyddion exhibiting the spin coated layer (green) and by measurement through a scratch the height of the layer. (b) Height profile analyzed with Gwyddion confirming the 40 nm thick layer.

The AFM analysis shows a layer thickness of  $40.9 \pm 5.2$  nm. Furthermore, the baking step was investigated by looking at the impurities in the ZnO solution. Although the solution is purified and filtered with a PTFE filter, some organic impurities may remain in the solution. These can be analyzed with a thermogravimetric analysis (TGA). The TGA is shown in the following figure 79.

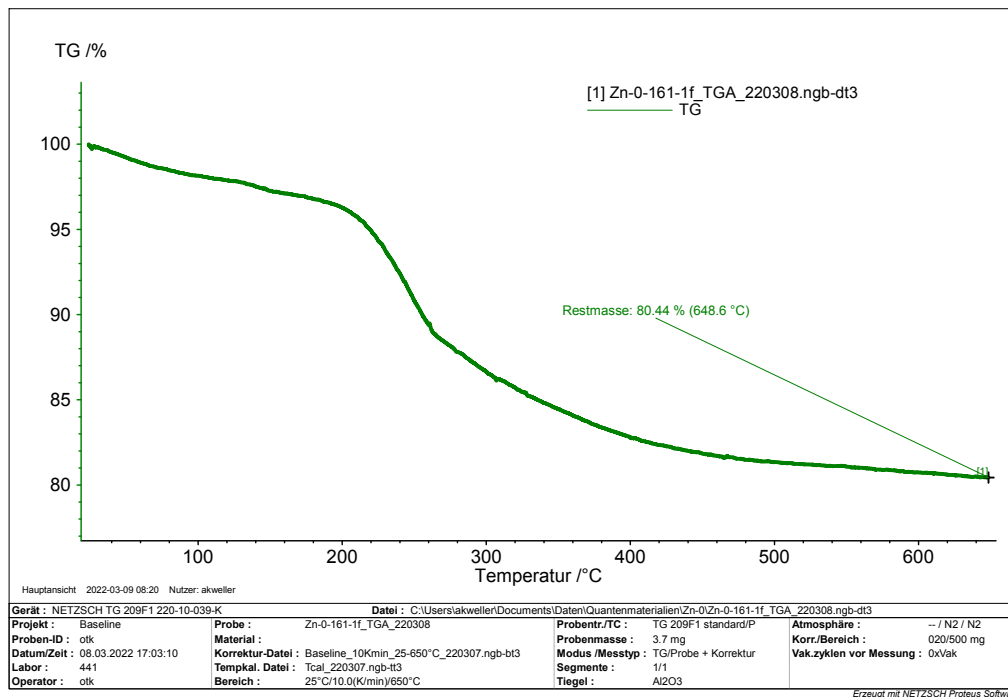


**Figure 79:** TGA of the synthesized ZnO nanoparticles following 10 K steps from 20 to 650 °C.

As can be seen from the TGA, the solution contains impurities which evaporate at around 220 °C. This could be ascribed to tetramethylammonium acetate residues in the solution. For this reason, a baking step at 300 °C is recommended.

### 5.5.2 Transfer of Aligned Quantum Rod Films to LED Substrates

The fabrication of PEQLEDs requires the transfer of the aligned QR film dip coated on the electrode to a prepared QLED substrate. Depending on the stack, this step is on the ITO/PEDOT:PSS/PVK coated substrate (for the conventional stack) or on the ITO/ZnO coated substrate. In this chapter the method of choice to transfer the aligned QR film will be described.

The transfer of aligned quantum rods used a thermal release tape (Teltec), which is typical for semiconductors. The thermal release tape has one side coated with the adhesive, while the other side is protected with a plastic layer. The adhesive is heat sensitive and decomposes at 120 °C. Thus, it is possible to completely eliminate the adhesive from the transferred structure. The transfer principle is schematically illustrated in figure 80.

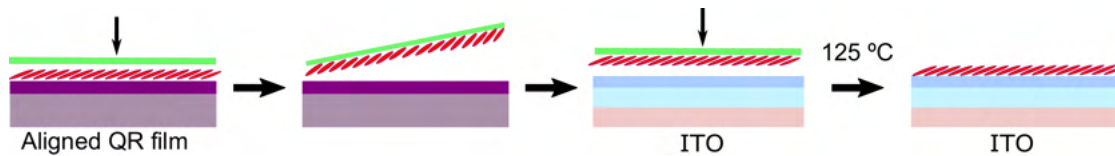


**Figure 80:** Schematical illustration of the transfer process using a thermal release tape (green). The first step involves pressing the adhesive side of the tape onto the aligned QR film. The tape is then rapidly extracted, taking the QRs. This film is then pressed gently onto the QLED substrate. To evaporate the adhesive, the substrate is heated to 125 °C. The plastic is taken out and the QR film is deposited onto the QLED substrate.

First, the thermal release tape is pressed with the adhesive side onto the aligned QR film. This way, the adhesive can bind to the QR layer. After gently pressing on the substrate, the tape is rapidly removed in the direction of the finger electrodes. This way, the transfer of the QRs is enhanced. A rapid removal helps taking a homogeneous layer. The transferred layer can be observed by the red coloring on the tape. Next, the adhesive side, which includes the QR film, is pressed onto the active area of the QLED substrate. After gently pressing the tape with the transferred film onto the QLED substrate, it is heated to 125 °C. It can be observed that the adhesive evaporates and the protecting plastic layer can be removed from the substrate. The QR film remains on the QLED substrate and can then be further prepared to deliver a PEQLED.

### 5.5.3 PEQLEDs with Conventional Stack

The fabrication of PEQLEDs using a conventional stack used an established method at Fraunhofer CAN.<sup>[161,162,169]</sup> For this, ITO was patterned using photolithography to deliver a 1 x 1 cm<sup>2</sup> active area. Next, the HIL and HTL are deposited via spin coating. In this work, PEDOT:PSS and PVK are used as the HIL and HTL, respectively. For this, the ITO substrate is thoroughly washed and cleaned for at least 30 minutes in a plasma cleaner. This step is essential, since the ITO surface must be functionalized with oxygen plasma to allow an aqueous solution of PEDOT:PSS to be deposited. As reported by Ekaterina Salikhova, spin coating the PEDOT:PSS solution at 3000 rpm delivers a layer with a thickness of 33 nm.<sup>[169]</sup> Next, the PVK layer in chlorobenzene is spin coated at 4000 rpm to deliver a layer of 17 nm. In the literature, layers between 7 and 35 nm can be used for the fabrication of QLEDs with a conventional stack.<sup>[106,126]</sup> The next step involves the transfer of the aligned QR film to the QLED stack as described in the previous chapter.

The synthesized ZnO nanoparticles are then spin coated as described in chapter 5.5.1. It must be noted, that the polymeric compounds used as HIL and HTL may decompose by using a very high baking temperature after the ZnO deposition. Therefore, this step was held at a temperature of 145 °C for 30 min. Last, an aluminum layer is deposited via PVD.

PEQLEDs fabricated this way were analyzed for their opto-electronic properties and polarization. Main goal of this work remains a high polarization. For this, FFE substrates with aligned QR films exhibiting high polarization were used. Here, the FFE will be shown with its polarization analysis and compared with the polarization coming from the electroluminescence of the PEQLED. Three PEQLEDs fabricated this way will be presented in this chapter. The three PEQLEDs were fabricated using the same FFE after extracting several layers from the substrate. Moreover, since the used FFE has an aligned area of 2 cm<sup>2</sup> and the PEQLED one of 1 cm<sup>2</sup>, the substrate can be used for the fabrication of several devices. Furthermore, the opto-electronic properties of the devices were analyzed via I-V measurements and emission spectra from the electroluminescence. Since the active area of this PEQLED is 1 cm<sup>2</sup>, EQE and luminance calculations could not be performed. This is due to the smaller size of the calibrated Si-photodiode used for the measurements. If the photodiode is smaller than the QLED, the method described in chapter 3.7.4 cannot be used.

The first PEQLED (PEQLED-1) was fabricated using FFE-8 (see chapter 5.4.2) after extracting 3 layers using a thermal release tape. Usually, the first layer contains a high amount of non aligned QRs and a high amount of dirt. Therefore, the layers beneath, usually exhibit higher polarization since they are closer to the electric field lines responsible for the alignment in an FFE. The polarization analysis of the FFE-8 and of PEQLED-1 is shown in the following figure 81. For this, the PEQLED was turned on by applying 3 mA which exhibited 6.02 V during the polarization measurement.

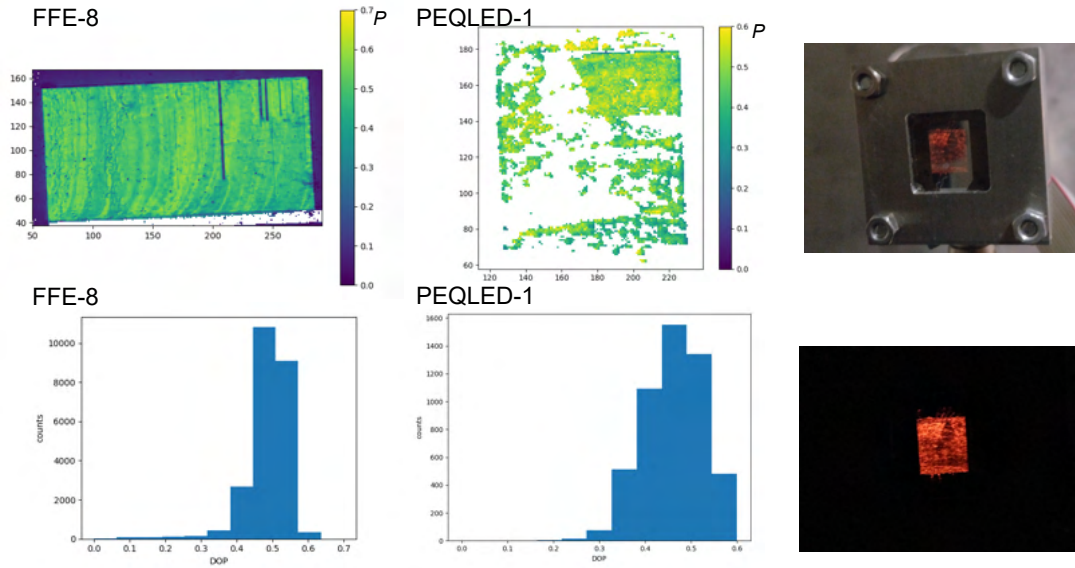


**Figure 81:** (Left) Acquisitions of the FFE-8 exhibiting the calculated DOP for each pixel with a color bar. Yellow shows a  $P = 0.7$  while blue  $P = 0.0$ . The histogram of the DOP distribution is also shown below. (Center) Acquisitions of the PEQLED-1 exhibiting the calculated DOP for each pixel with a color bar. Yellow shows a  $P = 0.6$  while blue  $P = 0.0$ . The white areas are areas where no intensity could be measured. The DOP distribution is shown below. (Right) Photographic images of the PEQLED exhibiting electroluminescence in the red under (up) ambient light and (down) without illumination by applying 3 mA and 6.02 V.

The fabricated PEQLED showed polarization from the aligned FFE. As can be seen from the acquisitions and the photographic images, some areas in the PEQLED exhibit no emission, hence these areas are marked as white holes in the acquisitions. This has its origin since some areas show no intensity that can be used to calculate a DOP. By looking at the transfer method, it is no surprise that some of the areas in the PEQLED exhibit no emission. Any dust or inhomogeneity during the transfer process would lead to areas without QRs. After comparing the PEQLED with its original FFE structure, many areas exhibit high DOP. However, the  $P$  values are lower than from the FFE. For instance, the median DOP of the FFE was of  $P_{\emptyset} = 0.49$ , while from the emissive areas of the PEQLED range at  $P_{\emptyset} = 0.43$ . Taking into account that many areas of the PEQLED exhibit no emission, the real DOP should be lower. However, this could not be calculated accordingly. Both for the FFE and the PEQLED showed a maximum  $P$  value of  $P = 0.6$ . This means that most of the aligned QRs could be transferred to the substrate.

Further analysis of the opto-electronic properties investigated the I-V characteristics of the diode and its electroluminescence spectrum (EL spectrum). With the I-V curve it is possible to calculate the threshold voltage ( $V_{th}$ ). This is the voltage needed to create a

conducting path along the diode and is characteristic for each device. As in reality the diode is never "off", the threshold voltage can be determined from the voltage needed for the diode to conduct exponentially. Hence, by finding the tangent and extrapolating the curve, the threshold voltage can be determined.<sup>[170,171]</sup> The I-V measurement and the EL spectrum are shown in the following figure 82.

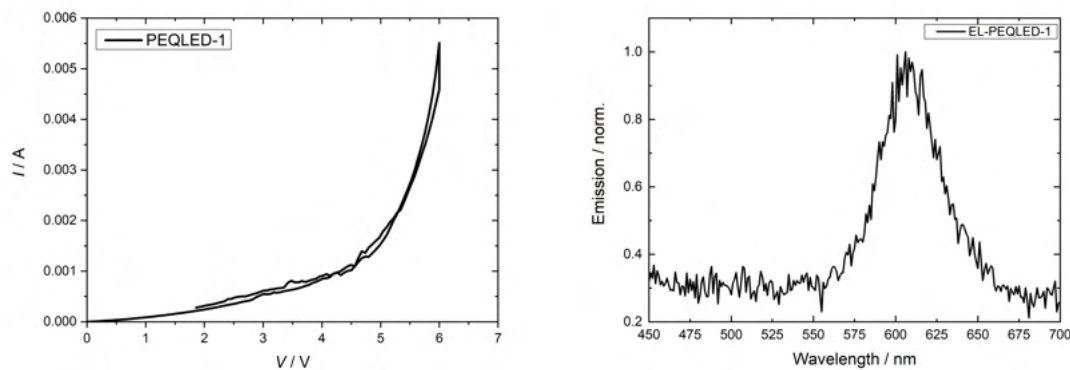


**Figure 82:** (Left) I-V measurement of the PEQLED-1 showing a characteristic diode curve. (Right) EL spectrum of the PEQLED after applying 20 mA to the device.

As seen from the I-V curve, the diode shows a slight hysteresis which originates from changes at the materials through the applied voltage and current. For instance, a high voltage can induce changes in the materials. A threshold voltage of 4.2 V was determined. This high voltage originates from the unbalance of the charge carrier transport throughout the layers. As explained in chapter 3.4, this unbalance can originate from the difficulty in the transport of either holes or electrons throughout the different materials. Usually the holes exhibit the most difficulties in transport, therefore the need of an HIL and HTL. Moreover, the inhomogeneities in the QR layer also account for an unbalance in the charge carrier transport and may induce a short circuit. The EL spectrum measured at 20 mA shows a very weak intensity, which could be also observed at the acquisitions in figure 81. This may originate from the charge carrier unbalance and the inhomogeneity of the EML as well as defects induced by the spin coating processes. Moreover, as mentioned in the previous chapters, the ZnO could still have impurities such as tetramethylammonium acetate. This would inhibit the charge carrier transport and thus affect the electroluminescence. Interestingly, the EL maximum is blue shifted from the photoluminescence of the QR solution (EL: 608 nm, PL: 611 nm). A shift can originate from the applied

electric field into the device, which "tilts" the energy levels from the materials and therefore induce a minimal change in the energetic levels, which changes the band gap energy required for the photon emission. This effect is known as the quantum confined Stark effect and can either induce a red or blue shift.<sup>[172–174]</sup> The red shift is typically attributed to the change in the energy states by applying an electric field. For instance the electron states shift to lower energies and the hole to higher energies. The blue shift, on the other hand, originates from the free carrier screening effect in the quantum confined Stark effect. This occurs when the carrier density increases in the "tilted" quantum well by the electric field, thus the suppressed quantum confined Stark effect brings an increase of the exciton binding energy by the wave function confinement. This leads ultimately to a minimal blue-shifted EL peak.<sup>[175–177]</sup>

Using the same FFE, a second PEQLED was fabricated using the conventional stack. For this, the fourth stamp (this means after extracting the layer for PEQLED-1), was used for the transfer of the aligned QR film. The PEQLED was then analyzed for its polarization by applying 4 mA and having 4.61 V during the measurement. It is to be noted that the PEQLED turned off once during the measurement, thus the measurement had to be repeated.

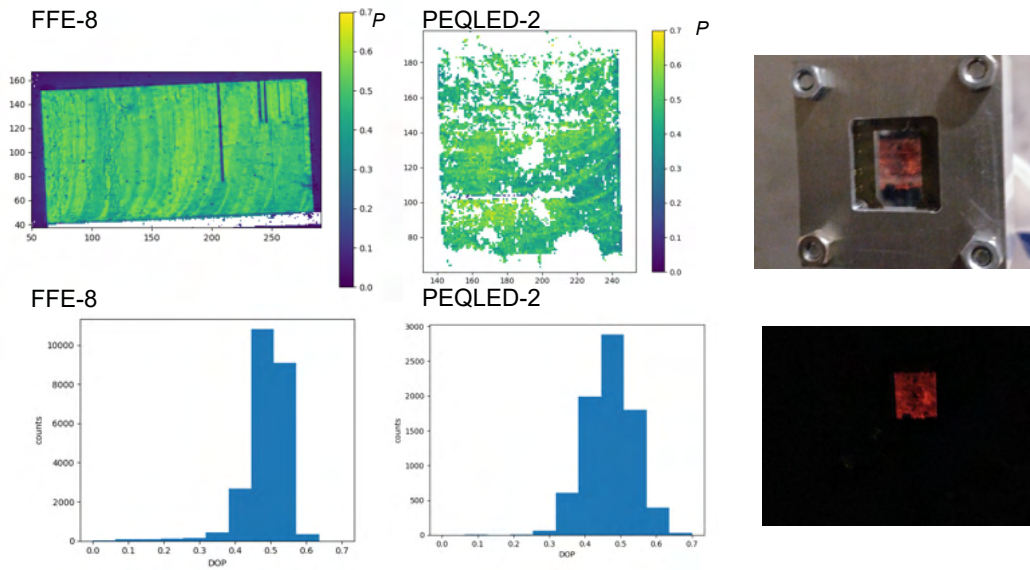


**Figure 83:** (Left) Acquisitions of the FFE-8 exhibiting the calculated DOP for each pixel with a color bar. Yellow shows a  $P = 0.7$  while blue  $P = 0.0$ . The histogram of the DOP distribution is also shown below. (Center) Acquisitions of the PEQLED-2 exhibiting the calculated DOP for each pixel with a color bar. Yellow shows a  $P = 0.7$  while blue  $P = 0.0$ . The white areas are areas where no intensity could be measured. The DOP distribution is shown below. (Right) Photographic images of the PEQLED exhibiting electroluminescence in the red under (up) ambient light and (down) without illumination by applying 6 mA and 5.1 V.

The fabricated PEQLED showed high polarization as seen from the FFE that was used. This confirms the effectiveness of the transfer method. While some areas exhibit no emission, the polarization of the substrate is still very high. The PEQLED exhibits a maximum DOP of  $P = 0.64$ , which is higher than from the analyzed FFE. This comes due to the extraction of previous layers with the thermal release tape. The layers at the top are in contact during the alignment process with the weakest electric fields, thus, the layers closer to the electrodes and the bottom substrate will exhibit a higher DOP. These layers cannot be measured from the FFE since the analysis can only measure the layer that is at the top. The homogeneity, however, decreases due to the transfer method.

The PEQLED was further analyzed for its opto-electronic properties. Unfortunately, the PEQLED exhibited a short circuit after the I-V measurement and could not exhibit electroluminescence again. Therefore, the EL spectrum could not be acquired. The I-V curve is shown in figure 84.



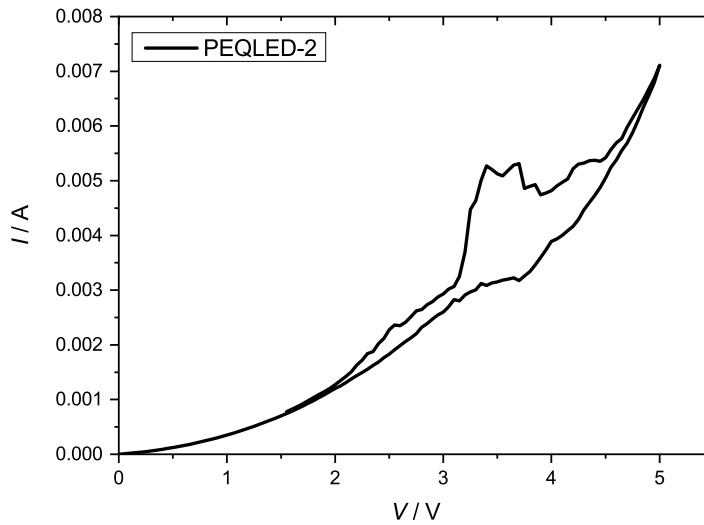


**Figure 84:** I-V measurement of the PEQLED-2 showing its characteristic diode curve.

As seen from the I-V curve, the irregular increase in current points to an irregular film deposition. Increasing both current and voltage induces changes in the layers of the PEQLED, whose irregularities lead to the jumps. Indeed, the inhomogeneity of the EML may also induce irregularities inside the layers and led to a short circuit. Therefore, it was not possible to measure the EL of the sample. The threshold voltage was determined at 2.0 V, which is lower than the previous PEQLED. This may arise from the spin coating of the HIL, HTL and ETL, in which the step may have led to a better deposited film. Thus, the required voltage to create the conducting path is lower. It must be noted, that the curve does not show an exponential increase and may therefore need a higher current to operate appropriately.

Last, a third PEQLED using the fifth stamp from FFE-8 was fabricated with a conventional stack. The PEQLED was analyzed for its polarization and opto-electronic properties. The polarization analysis is shown in the following figure 85 by analyzing the PEQLED while applying a current of 1 mA and having a voltage of 4.8 V.

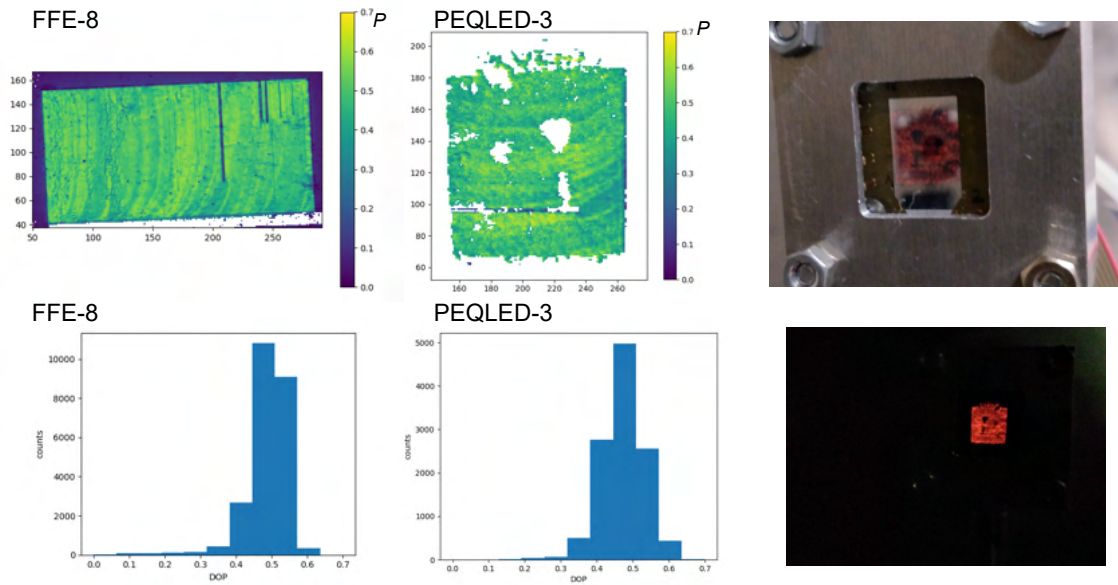


**Figure 85:** (Left) Acquisitions of the FFE-8 exhibiting the calculated DOP for each pixel with a color bar. Yellow shows a  $P = 0.7$  while blue  $P = 0.0$ . The histogram of the DOP distribution is also shown below. (Center) Acquisitions of the PEQLED-3 exhibiting the calculated DOP for each pixel with a color bar. Yellow shows a  $P = 0.7$  while blue  $P = 0.0$ . The white areas are areas where no intensity could be measured. The DOP distribution is shown below. (Right) Photographic images of the PEQLED exhibiting electroluminescence in the red under (up) ambient light and (down) without illumination by applying 1 mA and 4.8 V.

As can be seen from the acquisition, the PEQLED shows a high polarization and improved homogeneity. The device has fewer defects originated from the transfer of the aligned film. As can be seen, the maximum DOP is also higher than from the FFE. This is due to the same reason as explained before. The DOP distribution is also high, as can be observed from the histogram. The opto-electronic properties of the device were analyzed with I-V measurements and from the EL spectrum. These are shown in the following figure 86.

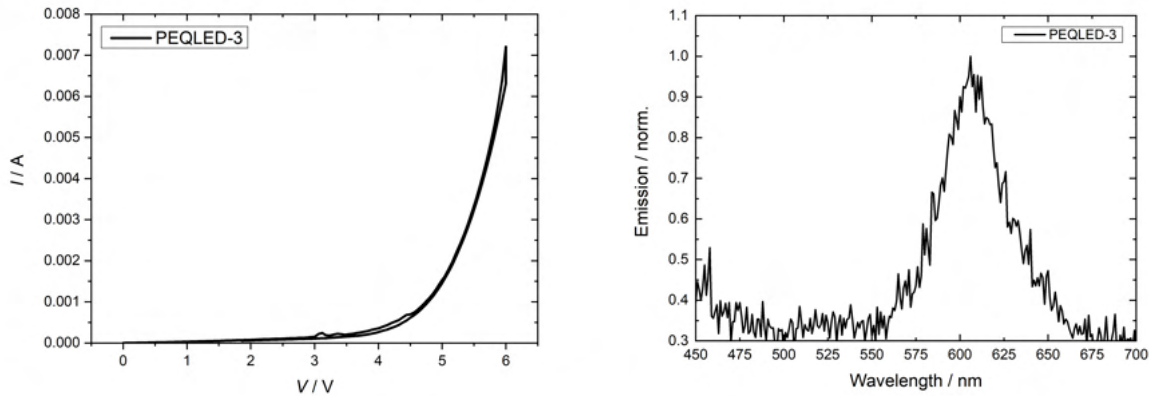


**Figure 86:** (Left) I-V measurement of the PEQLED-3 showing a characteristic diode curve. (Right) EL spectrum of the PEQLED after applying 20 mA to the device.

The I-V measurement shows a characteristic diode behavior with a determined threshold voltage of 4.0 V. In comparison to the previous PEQLEDs, the measurement shows no hysteresis, which accounts for the high stability of the materials. This also indicates an improvement in the homogeneity of the layers. However, due to the high voltage originated from the low current, the charge carrier unbalance and the high resistance inside the device lead to a low electroluminescence. This can be observed from the acquired EL spectrum. Furthermore, the emission maximum (606 nm) is also blue shifted from the photoluminescence of the QRs in solution.

The analyzed PEQLEDs with the main values for polarization and their opto-electronic properties are summarized in the following table 26.

**Table 26:** Summarized values for the PEQLEDs with a conventional stack.

| Sample   | $P_{max.}$ | $P_{\emptyset}$ | EL maximum<br>nm | PL maximum<br>nm | $V_{th}$<br>V |
|----------|------------|-----------------|------------------|------------------|---------------|
| PEQLED-1 | 0.6        | 0.43            | 608              | 611              | 4.2           |
| PEQLED-2 | 0.64       | 0.49            | -                | 611              | 2.0           |
| PEQLED-3 | 0.64       | 0.50            | 606              | 611              | 4.0           |

From the extracted values, it can be seen that the PEQLEDs fabricated with a conventional stack exhibit the same high DOP as from the aligned substrate. Their maximum DOP is also increased by removing the first QR layers from the FFE. However, the homogeneity of the EML is low and exhibits several non emitting areas. This originates

from the transfer process, which should be optimized in future works. Nevertheless, the polarization properties of the fabricated PEQLEDs exhibit much higher values than those reported in the literature (at around 0.23, this work 0.43 and above).<sup>[24,26,130]</sup> This confirms the effectiveness of the method. On the other hand, the opto-electronic properties of the devices exhibit the typical diode characteristics. However, only PEQLED-3 exhibited a fast exponential increase in current with fewer voltage changes. This means the charge carrier mobility inside the device is enhanced in comparison to the two other devices. This is true by looking at the I-V measurements and the homogeneity of the EML. QLEDs also exhibit high voltages for small currents due to the stacks, the polymeric materials and the intrinsic characteristics of the nanoparticles. This includes the ligands binding at the nanoparticle which hinder the charge carrier injection, increasing the resistance inside the device. While many of the layers could be improved, the improvement in the transfer method to deliver a homogeneous thin QR film should be addressed in future works.

Last, the use of conventional QLEDs, although exhibiting high polarization, has some drawbacks in spite of their opto-electronic performance. Some of these are the EL quenching due to the use of organic charge transport layers. This originates by Auger recombination with charged carriers, as well as from the strong electric field and the own device degradation in organic materials (see chapter 3.4). i-QLEDs offer an alternative, which can be adapted to the driving concept of displays and uses alternative materials that can also be easily deposited with PVD. These will be discussed in the following chapter.

#### 5.5.4 PEQLEDs with Inverted Stack

The fabrication of PEQLEDs using an inverted stack used a modified method reported at Fraunhofer IAP.<sup>[115]</sup> For this, ITO was patterned using photolithography to deliver a 0.5 x 0.5 cm<sup>2</sup> optical active area. This active area was chosen in order to fully characterize the QLEDs with a calibrated Si diode (of a 1 cm<sup>2</sup> active area) using the method described in chapter 3.7.4. Next, the synthesized ZnO nanoparticles were spin coated for the fabrication of the ETL delivering layers with a thickness of 40 nm (see chapter 5.5.1). Here, the substrate can be heated to 300 °C to remove any remaining impurities in the solution. Then, the aligned QR film was transferred using the method described in chapter 5.5.2. The HTL and HIL were then deposited using a PVD with a calibrated QCM to read out

the film thicknesses. Here, 50 nm of CBP and 10 nm of MoO<sub>3</sub> were used as HTL and HIL, respectively. It is to be noted that i-QLEDs can also be prepared with TCTA as the HTL, however, in this work no electroluminescent PEQLEDs could be fabricated this way. Last, a 100 nm aluminum layer is deposited using PVD.

PEQLEDs fabricated this way were analyzed for their polarization and opto-electronic properties. For this, FFE substrates with a aligned QR films from QR-16 were used. Here, the polarization analysis of the FFE will be shown and compared with the polarization originating from the electroluminescence of the PEQLED. Three PEQLEDs were fabricated and discussed in this chapter. Two PEQLEDs were fabricated with the same FFE after extracting the first and second layer of the aligned QR film.

The first PEQLED (PEQLED-4) was fabricated with the first stamp of FFE-25. The polarization analysis of the FFE-25 and PEQLED-4 is shown in the following figure 87. For this, the PEQLED was turned on by applying 3 mA.

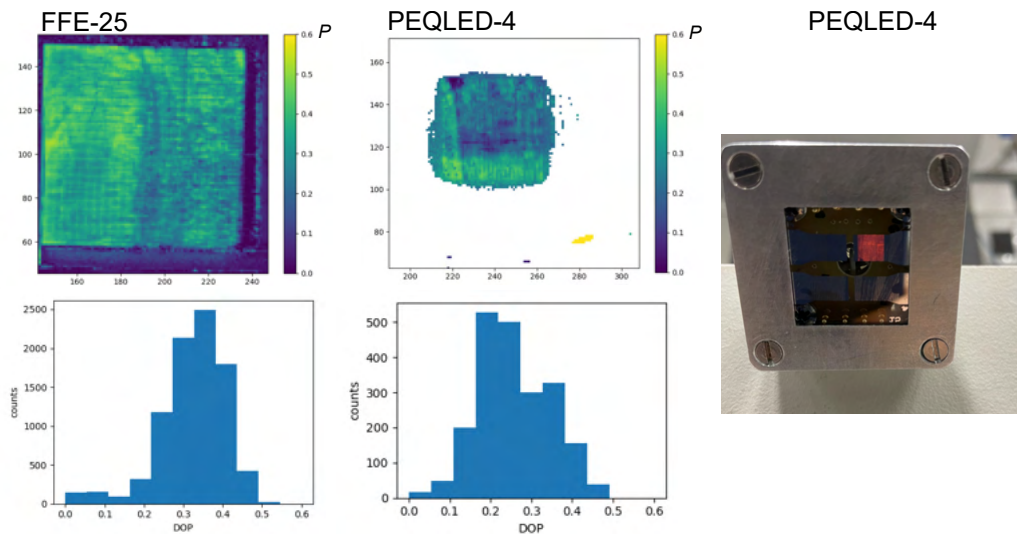


**Figure 87:** (Left) Acquisitions of the FFE-25 exhibiting the calculated DOP for each pixel with a color bar. Yellow shows a  $P = 0.6$  while blue  $P = 0.0$ . The histogram of the DOP distribution is also shown below. (Center) Acquisitions of the PEQLED-4 exhibiting the calculated DOP for each pixel with a color bar. Yellow shows a  $P = 0.6$  while blue  $P = 0.0$ . The white areas are areas where no intensity could be measured. The DOP distribution is shown below. (Right) Photographic images of the PEQLED exhibiting electroluminescence in the red under ambient light while applying 3 mA.

The fabricated PEQLED exhibits electroluminescence with polarization similar to the FFE. The FFE shows a homogeneous layer with a maximum DOP of  $P = 0.52$  and a median of  $P_{\varnothing} = 0.33$ . These properties are transferred with a slight decrease to the PEQLED. Due to the transfer process, not all the QRs could be extracted and therefore the

polarization is slightly decreased. Dust, impurities and movements during the stamping process can all lead to the decrease of polarization from the FFE to the PEQLED. This can be observed from the maximum  $P$  value for the PEQLED with  $P = 0.49$  and a median of  $P_{\varnothing} = 0.26$ . These are summarized in table 27.

The opto-electronic properties of the PEQLED were analyzed via I-V-L measurements using an integrating sphere and a calibrated Si photodiode. The relevant spectra are shown in the following figure 88.

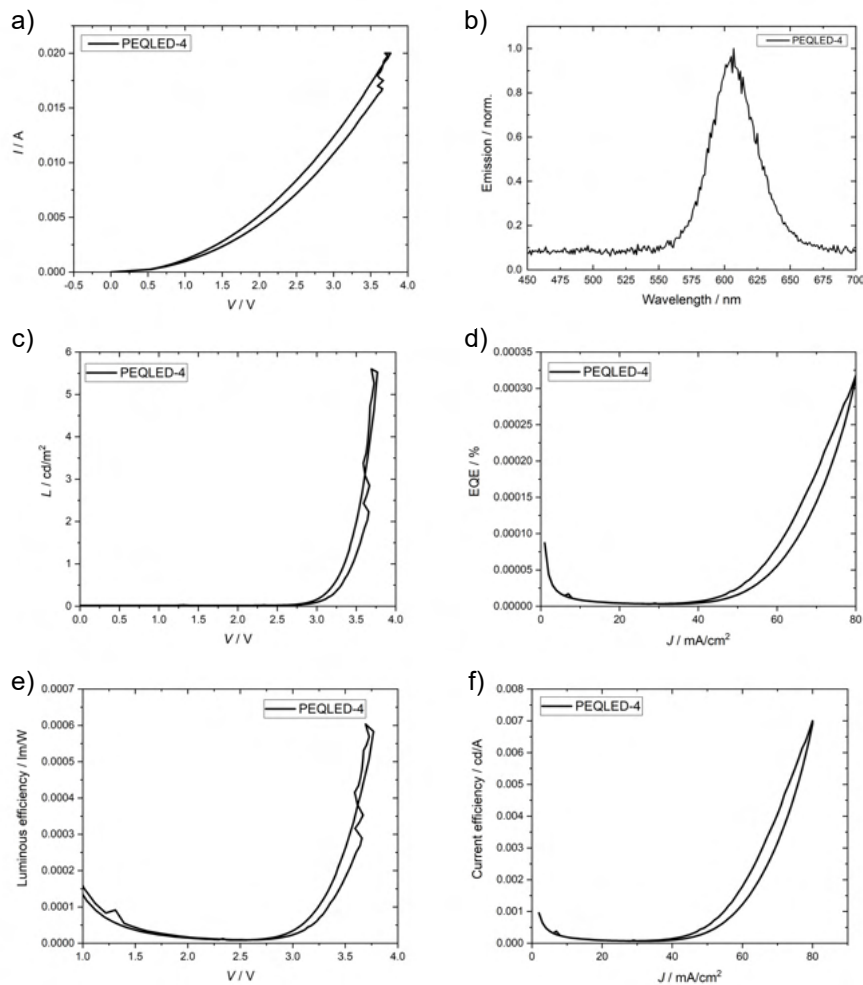


**Figure 88:** a) I-V measurement of the PEQLED-4 measuring from 0 to 3.5 V, exhibiting the characteristic diode curve. b) Normalized EL spectrum of PEQLED-4 by applying 20 mA and using an integrating sphere. c) Luminance against voltage of the PEQLED, exhibiting a maximum luminance of 5.6 cd/m<sup>2</sup>. d) External quantum efficiency against the current density. e) Luminous efficiency (luminosity) against the voltage. f) Luminous current efficiency ( $\eta_L$ ) against the current density.

The PEQLED exhibits a characteristic diode curve with a threshold voltage of 1.06 V. This is in comparison to the PEQLEDs with a conventional stack, much lower. However,

the measurements did not cover a range of higher voltages, therefore the results could be misleading. The measurements did not go above a voltage of 3.5 V in order to protect the LED from having a short circuit. Since the PEQLEDs often exhibit areas with no EL, it is always highly probable that after applying higher voltages, the device can have a short circuit and be damaged in the process. This could be observed, for example, with PEQLED-2.

Furthermore, the EL spectrum exhibits a low intensity while having an EL maximum at 607 nm. This is the same as the photoluminescence maximum of the QRs in solution. This means no quantum confined Stark effect can be observed. The calculated luminance of the device can be seen against the applied voltage in figure 88 c). It can be observed that the luminance highly increases after applying a voltage of 3.0 V. The maximum luminance was  $5.6 \text{ cd/m}^2$ , which is very low. This could be traced to the nature of the device, where the EML is transferred using a thermal release tape. Thus, many areas could have missing QRs and hinder the photon emission. Furthermore, impurities during the spin coating and transfer process (which does not take place in a clean room) may always provide defects in the device. However, a measurement at higher voltages would probably lead to higher luminance and thus allow for the determination of the maximum luminance. Unfortunately, this could not be measured in this work. The low luminance also correlates with the very low EQE, with values under 0 %. The device performance can be observed from figure 88 e) and f). Here, the low luminous efficiency at high voltages account for the many defects and charge carrier unbalance, which hinder the device performance. Furthermore, the current efficiency shows a high increase and no saturation. All these diagrams point that the device could have been used at higher voltages to exhibit its peak performance.

Next, PEQLED-5 was fabricated with the second stamp of FFE-25. The polarization analysis for FFE-25 and PEQLED-5 are shown in the following figure 89. For this, the PEQLED was turned on by applying 10 mA.

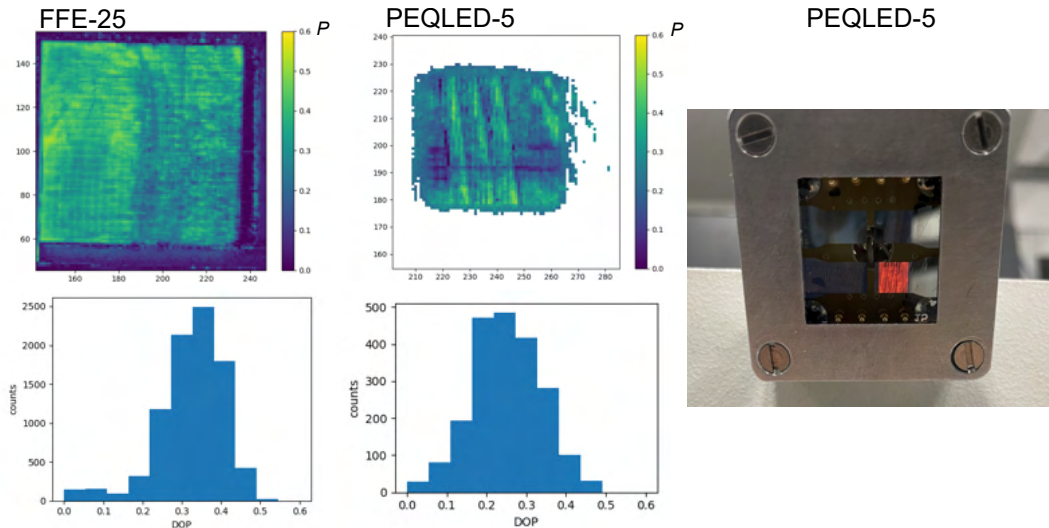


**Figure 89:** (Left) Acquisitions of the FFE-25 exhibiting the calculated DOP for each pixel with a color bar. Yellow shows a  $P = 0.6$  while blue  $P = 0.0$ . The histogram of the DOP distribution is also shown below. (Center) Acquisitions of the PEQLED-5 exhibiting the calculated DOP for each pixel with a color bar. Yellow shows a  $P = 0.6$  while blue  $P = 0.0$ . The white areas are areas where no intensity could be measured. The DOP distribution is shown below. (Right) Photographic image of the PEQLED exhibiting electroluminescence in the red under ambient light while applying 10 mA.

As seen from the acquisitions, the PEQLED exhibits electroluminescence and polarized emission. The PEQLED exhibits some stripes with high polarization followed by some lower polarization. These stripes originated from the transfer method while removing the thermal release tape from the FFE. An uneven pull of the tape leads to some areas extracting more of the aligned film than others, therefore leading to the formation of stripes. Nevertheless, the maximum  $P$  value of the PEQLED remained at  $P = 0.49$  and the median at  $P_{\emptyset} = 0.25$ . These values are very similar to those of the previous PEQLED, which confirms the fabrication method and the effectiveness of the transfer method.

Next, the PEQLED was characterized via I-V-L measurements with the same procedure as described before. The relevant spectra are shown in the following figure 90.



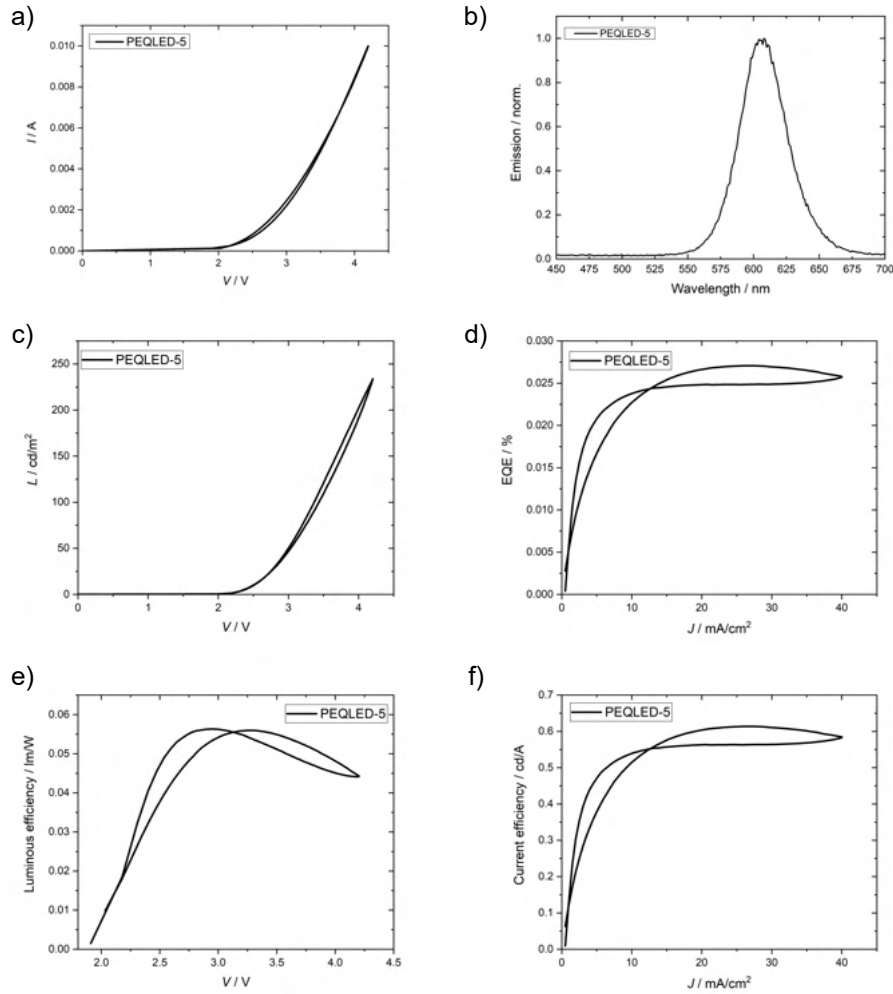


**Figure 90:** a) I-V measurement of the PEQLED-5, exhibiting the characteristic diode curve. b) Normalized EL spectrum of PEQLED-5 by applying 3 mA and using an integrating sphere. c) Luminance against voltage of the PEQLED, exhibiting a maximum luminance of  $234 \text{ cd/m}^2$ . d) External quantum efficiency against the current density. e) Luminous efficiency (luminosity) against the voltage. f) Luminous current efficiency ( $\eta_L$ ) against the current density.

The PEQLED exhibits a characteristic diode curve with a threshold voltage of 2.5 V. This is higher than the previous PEQLED, however, the electroluminescence of the device is enhanced. While the EL maximum remains the same as the photoluminescence of the QR sample, the luminance analysis reveals an enhanced performance. For instance, the luminance of the device is substantially higher than from the previous PEQLED, exhibiting luminance of  $L = 234 \text{ cd/m}^2$  at 4 V. This is almost 42 times higher than the previous device. Furthermore, the EQE shows a saturation by increasing the current density. This is characteristic of QLEDs, which means the performance could be measured adequately. The EQE of the device is still very low at 0.03 % with a current density

of  $J = 27 \text{ mA/cm}^2$ . Looking further at the luminous efficiency, this correlates with the threshold voltage, exhibiting values after the QLED is switched "on". The curve saturates and exhibits a maximum efficiency at 2.92 V with 0.06 lm/W. Last, the current efficiency exhibits the same saturation by driving the device at  $27 \text{ mA/cm}^2$  with an efficiency of 0.6 cd/A. The analysis reveals all in all an improved performance, which originates from the better deposition of the EML and possibly of the spin coated ZnO layer. This allows for a better charge carrier transport and therefore an enhanced recombination of charge carriers that allows for an enhanced performance.

Last, PEQLED-6 was analyzed. This device was fabricated from the first stamp of FFE-26, which will also be shown in the polarization analysis. The polarization analysis for both FFE-26 and PEQLED-6 are shown in the following figure 91.

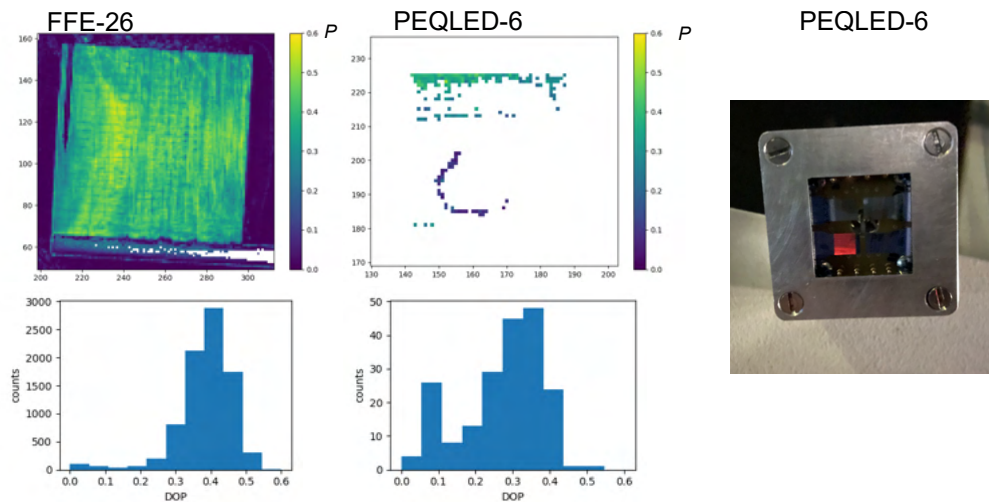


**Figure 91:** (Left) Acquisitions of the FFE-26 exhibiting the calculated DOP for each pixel with a color bar. Yellow shows a  $P = 0.6$  while blue  $P = 0.0$ . The histogram of the DOP distribution is also shown below. (Center) Acquisitions of the PEQLED-6 exhibiting the calculated DOP for each pixel with a color bar. Yellow shows a  $P = 0.6$  while blue  $P = 0.0$ . The white areas are areas where no intensity could be measured. The DOP distribution is shown below. (Right) Photographic image of the PEQLED exhibiting electroluminescence in the red under ambient light while applying 30 mA.

As can be seen from the acquisitions, FFE-26 shows a homogeneous film with a maximum DOP of  $P = 0.57$  and a median of  $P_{\emptyset} = 0.40$ . Unfortunately, the polarization could not be fully transferred to the PEQLED. While the device still exhibits electroluminescence, the DOP is almost vanished. This is probably to a problem from the transfer method. For instance, if the stamp is pressed hardly and moved while transferring it to the QLED stack, then the QRs can move inside the adhesive paste and disrupt the alignment they had before. Also, it is possible that the uppermost layer of the FFE could have contained

a high amount of non aligned QRs. While the DOP analysis exhibits high polarization, the layer responsible for this DOP could have been more inside the device and not from the uppermost layer. While some devices using the second and third stamps from FFE-26 were made, these did not show electroluminescence. Nevertheless, by looking at the DOP distribution from the PEQLED-6, it can be seen that some of the values from FFE-26 can be found again in the device. Naturally, the counts in PEQLED-6 are very low, since they only account for the small regions exhibiting polarization in the analysis.

The opto-electronic properties of the device were analyzed next. The I-V-L measurements are shown with the relevant spectra in figure 92.

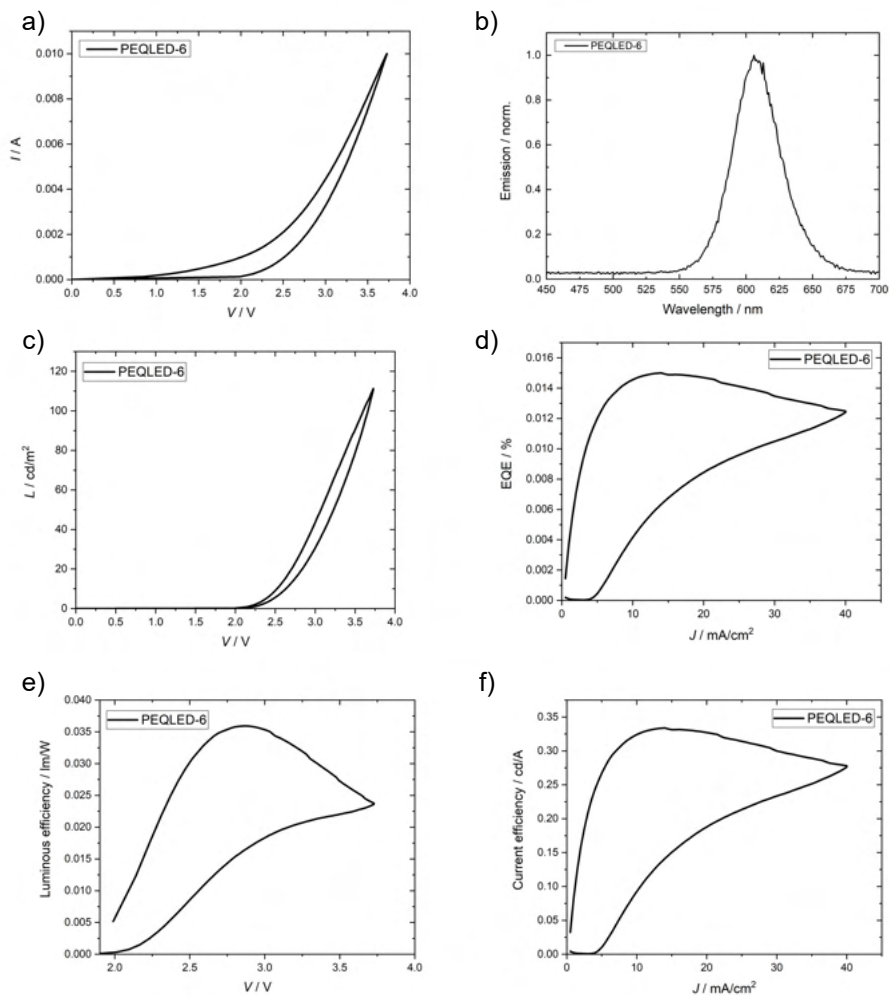


**Figure 92:** a) I-V measurement of the PEQLED-6, exhibiting the characteristic diode curve. b) Normalized EL spectrum of PEQLED-6 by applying 10 mA and using an integrating sphere. c) Luminance against voltage of the PEQLED, exhibiting a maximum luminance of  $111 \text{ cd/m}^2$ . d) External quantum efficiency against the current density. e) Luminous efficiency (luminosity) against the voltage. f) Luminous current efficiency ( $\eta_L$ ) against the current density.

The PEQLED exhibits its characteristic diode curve with a threshold voltage of 2.0 V, which is similar to the previous device. The EL maximum remains at 607 nm, showing no shift from the photoluminescence of the QR solution. The luminance of the device shows the typical increase in dependence of the voltage. The increase starts once the threshold voltage is achieved. The maximum luminance was determined at 111 cd/m<sup>2</sup> at 3.7 V. This is lower than the previous PEQLED and could originate from impurities during the transfer process as well as a charge carrier unbalance as explained previously. Furthermore, the EQE remains low and saturates after reaching 10 mA/cm<sup>2</sup>. The EQE of the device was 0.015 % at 14 ma/cm<sup>2</sup>. However, the curves show a very irregular trend, similar to a hysteresis. This could be attributed to a change in the materials due to the current flow over time. Hence, the stability of the device is not very high. This can also be observed from the the other graphs exhibiting the device performance. This means the performance is very fragile and sensible to changes, which can occur from any change in the materials inside the QLED stack. The luminous efficiency showed a maximum at 0.034 lm/W at 2.8 V. On the other hand, the current efficiency was determined at 0.33 cd/A at 13.0 mA/cm<sup>2</sup>.

In order to give an overview on how the performances of QLEDs with polarized emission are in comparison to i-QLEDs fabricated with this method, a QLED with a spin coated QR-16 EML was fabricated. For this, the QR-16 solution with  $c = 15$  mg/mL in *n*-heptane was spin coated at 3000 rpm after the ZnO deposition. The remaining steps were performed identically as the PEQLEDs. The QLED (i-QLED-1) exhibited no polarization, but was characterized for its opto-electronic properties. This is useful to identify the origin of the low performance in the PEQLEDs. The opto-electronic characterization of i-QLED-1 is shown in the following figure 93 with it most relevant graphs.

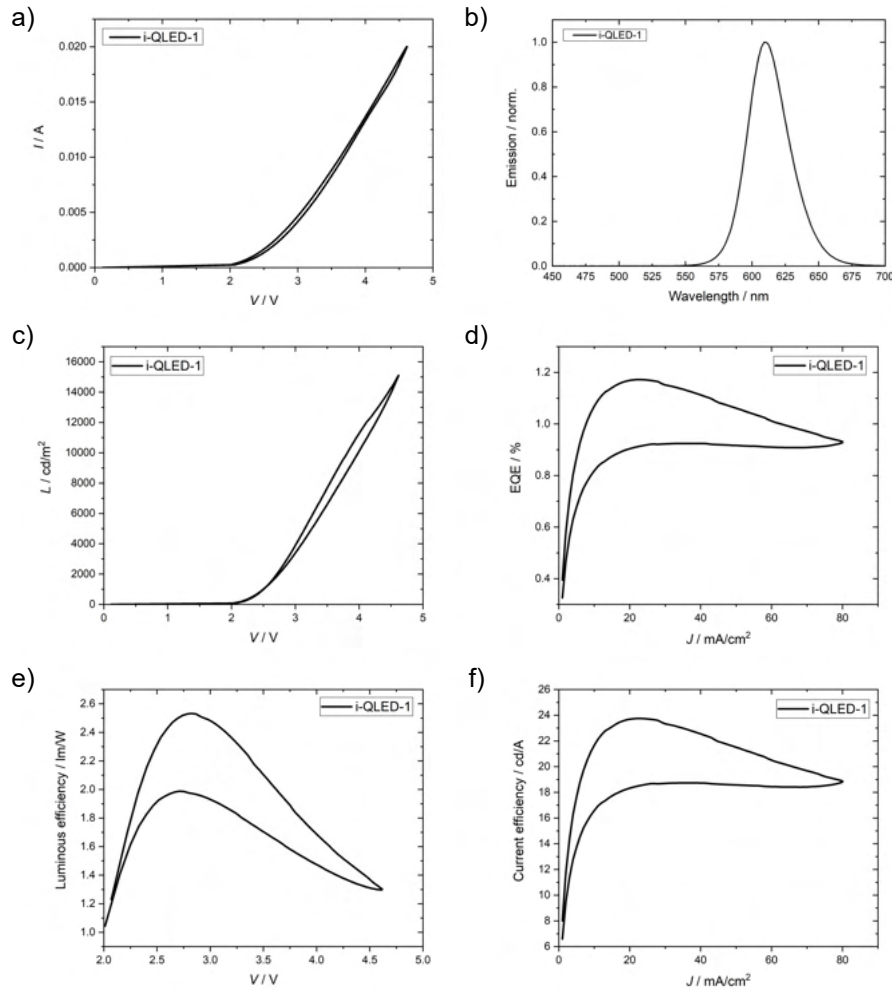


**Figure 93:** a) I-V measurement of the i-QLED-1, exhibiting the characteristic diode curve. b) Normalized EL spectrum of i-QLED-1 by applying 3 mA and using an integrating sphere. c) Luminance against voltage of the i-QLED, exhibiting a maximum luminance of 15111  $\text{cd}/\text{m}^2$ . d) External quantum efficiency against the current density. e) Luminous efficiency (luminosity) against the voltage. f) Current efficiency ( $\eta_L$ ) against the current density.

The i-QLED exhibits a characteristic diode curve with a threshold voltage of 2.1 V. This is very similar as the PEQLEDs and confirms the nature of the device. The device exhibits a red shift compared to the photoluminescence of the QR solution. As previously explained, this originates from the quantum confined Stark effect by applying an electric field. The effect is more notorious since the EML is homogeneously dispersed and contacted throughout the device. Unlike the PEQLEDs, which exhibit many areas without QRs, the i-QLED exhibited a homogeneous emissive layer. The luminance of the device is much higher in the analyzed range, exhibiting a maximum luminance of  $L = 15111 \text{ cd}/\text{m}^2$ . This value is relatively high for inverted QLEDs and confirms the successful fabrication. The EQE has a maximum value of 1.17 % at 23  $\text{mA}/\text{cm}^2$ , which is a relative low value for

QLEDs based on quantum rods (literature: EQE = 10 %).<sup>[26]</sup> The luminosity of the device had a maximum of 2.53 lm/W at 2.8 V. Last, the current efficiency had a maximum of 23.8 cd/A at 24 mA/cm<sup>2</sup>. It can also be observed that the stability of the device is also very low by looking at the change of performance throughout the measurement. These values, together with those of the PEQLEDs, are summarized in table 27. Comparing all the values, it is clear that the PEQLEDs lose a lot of performance due to the transfer of the aligned QR film. Since all the other layers were fabricated the same way, only the spin coated ZnO layer, which could account for human errors, and the EML could lead to any performance difference. Since the transfer of the QR layer involves the use of a thermal release tape and the transfer of a very thin film, this leads to many defects and impurities in the device. A possibility to optimize the transfer would be layer-by-layer transfer by using several stamps of the same FFE and aligning them on the QLED stack to transfer it on a precise area. This is just one option to further optimize the process in further works. Nonetheless, it was possible to demonstrate the fabrication of working PEQLEDs by using an established method, which would deliver i-QLEDs with high luminance.

**Table 27:** Summarized values for the PEQLEDs and the i-QLED (as reference) with an inverted stack: the maximum degree of polarization  $P_{max}$ , the median DOP  $P_{\emptyset}$ , the maxima for the EL (device) and PL (QRs), the threshold voltage  $V_{th}$ , the maximum luminous efficiency (luminosity)  $\eta_{P,max}$ , the external quantum efficiency and the current efficiency  $\eta_L$

| Sample   | $P_{max}$ | $P_{\emptyset}$ | EL max.<br>nm | PL max.<br>nm | $V_{th}$<br>V | $\eta_{P,max}$<br>lm/W | $L_{max}$<br>lm | EQE<br>% | $\eta_L$<br>cd/A |
|----------|-----------|-----------------|---------------|---------------|---------------|------------------------|-----------------|----------|------------------|
| PEQLED-4 | 0.49      | 0.26            | 607           | 607           | 1.06          | 0.006                  | 5.6             | 0.0003   | 0.07             |
| PEQLED-5 | 0.49      | 0.25            | 607           | 607           | 2.5           | 0.05                   | 234             | 0.027    | 0.6              |
| PEQLED-6 | 0.52      | -               | 607           | 607           | 2.0           | 0.03                   | 111             | 0.015    | 0.33             |
| i-QLED-1 | -         | -               | 610           | 607           | 2.1           | 2.53                   | 15111           | 1.17     | 23.8             |

### 5.5.5 Summary

The fabrication of polarized emissive quantum-rod based light-emitting diodes was analyzed and optimized for a conventional and inverted stack. The procedure involves the use of synthesized ZnO nanoparticles, which usually exhibit enhanced properties than commercially available materials.

For the fabrication of PEQLEDs, the process involved the transfer of the aligned QR film by using a thermal release tape. Although this method induces changes in the homogeneity of the EML, it allows for the extraction of the aligned QR film without losing much of the polarization. This way, it is possible to easily and quickly transfer aligned QRs to a designated substrate.

First, PEQLEDs were fabricated using a conventional stack. The PEQLEDs exhibited high polarization, which originated from the aligned FFE. Hence, the transfer was successful and did not account for much loss of polarization. The opto-electronic properties of the device, on the other hand, exhibit typical diode curves and electroluminescence with blue shifts in comparison to the photoluminescence of the QR solution. Further characterization was not possible due to the large active area of these devices.

PEQLEDs with an inverted stack were fabricated and fully characterized for their polarization and opto-electronic properties. The PEQLEDs exhibited a slight decrease in their median DOP, while the maximum DOP found remained high. The loss originates from the transfer method. The opto-electronic properties exhibit low EQE and luminance. However, most of the loss originates from the EML and therefore the transfer method is, yet again, responsible of most of the performance loss.

The established method presented in this work, could show the fabrication of PEQLEDs both in a conventional and inverted stack with higher DOP than those, to my best knowledge, found in the literature. Hence, by improving the transfer method, it should be possible to fabricate PEQLEDs with high DOP and enhanced device performance.

## 6 Outlook

The established production of CdSe/CdS quantum rods is of main interest for industry projects, which motivated the optimization of the synthetic route. Several aspects like the precise control of the quantum rod length, emission wavelength, while exhibiting high quantum yields, were discussed in this work. An aspect of main interest, is the precise control of the polarization properties of the quantum rod. While it could be shown that some aspects like the length and width influence the DOP of the QR sample, the precise control of this property remains challenging. For this, work remains on the analysis of which synthetic parameters could influence the fabrication of QRs with high DOP. This would help the production of QRs aimed for the fabrication of polarized emitters. To analyze this, several analysis methods could come into play. For instance single particle polarization spectroscopy and polarized excitation spectroscopy are methods that would allow the fast and easy characterization of the quantum rods.<sup>[56]</sup>

Furthermore, a step that requires improvements is the transfer of aligned QRs to the LED substrate. The use of thermal release tape showed throughout this work the easiest, fastest and most efficient way of transferring aligned films. While most of the performance issues and decrease in DOP originate from this step, it still showed its feasibility. A precise extraction using a set force or a controlled transfer with a set pressure would facilitate the optimization of the process. On the other hand, other materials like PDMS could offer an alternative for either the fabrication of color converters with polarized emission or for electroluminescent PEQLEDs (see figure 94 b). Indeed, the fabrication of color converters with polarized emission is also an attractive field where several industry partners have shown interest.



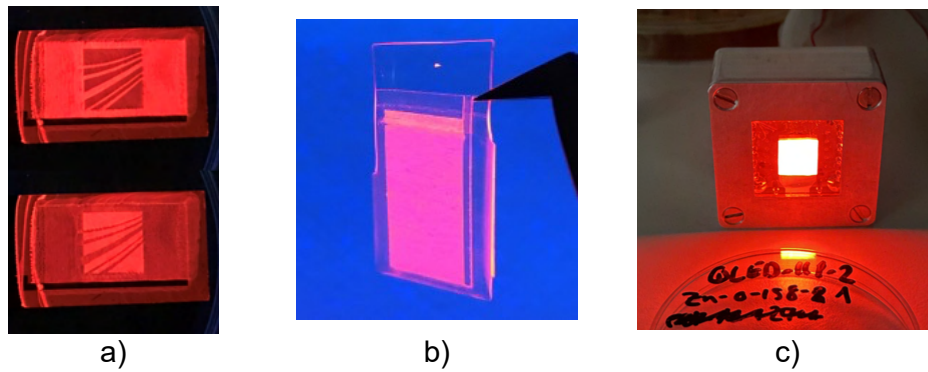


**Figure 94:** a) Polarized emission from aligned QRs on an FFE with the Fraunhofer logo through (up) a polarizer in the parallel and (down) perpendicular position. b) PDMS with an aligned QR film, which offers the possibility of fabricating color converters with polarized emission. c) InP-based QLED using the inverted stack fabricated with the method described in this work.

Last, the optimization of PEQLEDs by analyzing its stacking, the materials used as ETL, HTL and HIL, not only helps the improvement in performance of the PEQLED, but also for electroluminescent QLEDs. Furthermore, the advances made on cadmium-based electroluminescent QLEDs can be used for the fabrication of cadmium-free systems such as InP-based QLEDs. For instance, the method described in this work not only produces cadmium-based QLEDs and PEQLEDs, but can be used for the fabrication of an InP-based QLED, as seen in figure 94 c).

## 7 Summary

### 7.1 English

Aim of this thesis was establishing a fabrication process for polarized emissive quantum rod-based LEDs with high DOP. This process was split into three main areas: the production of CdSe/CdS quantum rods with a continuous flow reactor, the alignment of QRs using an electrostatic field and the fabrication of PEQLEDs with a conventional and inverted stack.

The successful production of CdSe/CdS quantum rods with enhanced properties was possible using a continuous flow reactor. The process involves a two step procedure with the production of the CdSe cores and its subsequent coating with an elongated CdS shell. The parameters responsible for the precise control of the CdSe species were analyzed and presented. The use of a reactor allows the production of all CdSe species: from CdSe clusters to CdSe cores emitting in the red. Its subsequent coating with an elongated CdS shell was presented and discussed. It was possible to synthesize CdSe/CdS heterostructures emitting in the blue, green and red, with varying lengths and width by adjusting some few parameters in the reactor. The fabricated QRs were used for the subsequent steps in this thesis, exhibiting the necessary polarized emission and high quantum yield.

The second step involved the optimization of an alignment process for QRs in solution. Here, the use of IDEs and FFEs was presented and discussed. While the use of IDEs delivers high DOP, it involved drop casting the QR solution, which is not a reproducible procedure. The use of FFE was analyzed and optimized, discussing several parameters which influence the result of the experiment. By using dip coating and different settings (mainly 100 Hz and 150 V), it was possible to deliver QR films exhibiting very high DOP of up to  $P = 0.69$  and a median of  $P_{\emptyset} = 0.56$ . This confirms the effectiveness of the procedure.

Last, the fabrication of PEQLEDs was possible by transferring the aligned QR film using a thermal release tape onto the desired QLED stack. The use of conventional and inverted stacks was analyzed and discussed. Most of the PEQLEDs exhibited similar DOP as from the used aligned QR films, which confirms the effectiveness of the process. While

the performance of both devices still needs improvement, it was possible to fabricate PEQLEDs which exhibit much higher DOP than reported in the literature (with  $P_{max.} = 0.64$  and  $P_{\emptyset} = 0.49$ ) with a conventional stack and (with  $P_{max.} = 0.52$  and  $P_{\emptyset} = 0.26$ ) with an inverted stack.

## 7.2 Deutsch

Ziel dieser Arbeit war die Etablierung eines Herstellungsprozesses für polarisiert emittierende LEDs basierend auf Nanostäbchen mit hohen Polarisationsgraden. Der Prozess wurde in drei Abschnitten unterteilt: die Herstellung der CdSe/CdS Nanostäbchen mit einem kontinuierlichen Flussreaktor, die Ausrichtung von Nanostäbchen in einem elektrischen Feld und die Herstellung des PEQLEDs mit einem konventionellen und inversen *stack*.

Die erfolgreiche Produktion der CdSe/CdS Nanostäbchen war mit Hilfe eines kontinuierlichen Flussreaktors möglich. Zunächst erfolgt die Produktion der CdSe Kerne mit der anschließenden Passivierung mit einer elongierten CdS Schale. Die erforderlichen Parameter für die gezielte Synthese mehrerer CdSe Spezies wurden analysiert und dargestellt. Mit Hilfe eines Reaktors war die Produktion von allen CdSe Spezies möglich: von CdSe Clustern zu CdSe Kernen, die im roten Bereich des visuellen Spektrums emittieren. Die anschließende Passivierung mit einer elongierten CdS Schale wurde präsentiert und diskutiert. Es war möglich derartigen CdSe/CdS Spezies zu synthetisieren, die im blauen, grünen und rotem Bereich des visuellen Spektrums emittieren und deren Breite und Länge variieren. Dieses wurde durch die genaue Steuerung weniger Parameter im Reaktor bewirkt. Die so hergestellten Nanostäbchen wurden in den nächsten Versuchen in dieser Arbeit verwendet und zeigten dabei die erforderliche polarisierte Emission und hohe Quantenausbeuten.

Der zweite Schritt war die Optimierung der Ausrichtung von Nanostäbchen in Lösung. Dafür wurden IDEs und FFEs analysiert und diskutiert. Die Verwendung von IDEs zeigte hohe Polarisationsgrade, jedoch beruht der Prozess auf *drop casting*, welcher wenig reproduzierbar ist. Die Verwendung von FFE wurde analysiert und optimiert. Dazu wurden unterschiedlichen Parameter untersucht, die das Ergebnis des Versuches stark beeinflussten. Mit Hilfe von *dip coating* und unterschiedlichen Einstellungen (meistens

100 Hz und 150 V) war es möglich QR Filme mit sehr hohen Polarisationsgraden bis  $P_{max.} = 0.69$  und  $P_{\emptyset} = 0.56$  herzustellen.

Im dritten Schritt wurde die erfolgreiche Darstellung von PEQLEDs durch die Anwendung eines *thermal release tape* gezeigt, welches den Transfer des ausgerichteten Filmes ermöglichte. Der konventionelle und inverse *stack* wurden analysiert und diskutiert. Die meisten PEQLEDs zeigten ähnlichen Polarisationsgrade wie die verwendeten ausgerichteten Filme (aus den FFE), was die Effektivität des Prozesses bestätigt. Obwohl die Leistung der PEQLEDs noch weiterer Verbesserungen bedarf, war es möglich PEQLEDs herzustellen, die höhere Polarisationsgrade als die in der Literatur erwähnten Devices zeigten. Die hergestellten PEQLEDs zeigten Polarisationsgrade bei  $P_{max.} = 0.64$  und  $P_{\emptyset} = 0.49$  für Devices mit einem konventionellen *stack* und mit  $P_{max.} = 0.52$  und  $P_{\emptyset} = 0.26$  für einen inversen *stack*.

## 8 Experimental

### 8.1 Preparation of Precursors for the Reactor

For the use in a continuous flow reactor, precursors must be in the liquid phase, avoid high viscous substances and avoid any agglomerations. These would lead to false flow rates, hinder the flow and therefore the reaction. The materials should also avoid a reaction with the components inside the reactor. The precursors needed for the reactor are as followed: a selenium, a cadmium (cores), cadmium (shell) and a sulfur precursor. Their synthetic approach will be described in the following sections. The following reactions were performed under Schlenk-technique standards under nitrogen atmosphere.

**Chemicals and solvents:** Unless otherwise stated, all the used reagents were acquired from commercial sources and used without further purification.

#### 8.1.1 Preparation of the Selenium Precursor

**Materials and Apparatus:** *Materials:* 1-octadecene (ODE, Merck), selenium (Alfa Aesar), tri-*n*-octylphosphine (TOP, Cytec).

**Reaction:** (In a glovebox) In a typical reaction, 66.5 g (0.84 mol) selenium shots were dissolved in 600 mL (1.35 mol) TOP and stirred for at least 18 hours until a clear yellow solution was obtained. The solution was then taken out of the glovebox. 600 mL ODE were placed under vacuum for at least one hour. The solution was subsequently placed under nitrogen atmosphere. This procedure was repeated at least three times. Afterwards, the TOP-Se solution was transferred to the ODE solution with a cannula and stirred until a homogeneous solution was obtained. The solution was then transferred to a sure-store flask and kept under nitrogen atmosphere.

#### 8.1.2 Preparation of the Cadmium Precursor for the Cores

**Cadmium precursor based on cadmium acetate**

**Materials and Apparatus:** *Materials:* cadmium acetate dihydrate ( $\text{Cd}(\text{AcO}^-)_2 \cdot 2\text{H}_2\text{O}^{\text{d}}$ , Alfa Aesar), octadecylphosphonic acid (ODPA, min. 97 %, PCI), liquid trioctylphos-

---

<sup>d</sup>AcO<sup>-</sup> = CH<sub>3</sub>COO<sup>-</sup>

phine oxide (TOPO, mixture of four trialkylphosphine oxides, Cytop 503, Cytec), tri-*n*-octylphosphine (TOP, Cytec).

**Reaction:** In a glovebox, 20.2 g (75.8 mmol)  $\text{Cd}(\text{AcO}^-)_2 \cdot 2\text{H}_2\text{O}$  and 450 mL TOP were dissolved and stirred for at least 18 hours until a clear solution was obtained. Slight traces of water can be observed. The solution was then taken out of the glovebox. In a three-necked reaction flask, 46 g (137.5 mmol) ODPAs were mixed with 666 mL (1.5 mol) TOP. The solution was stirred and placed under vacuum at room temperature for at least 10 min. The solution was subsequently placed under nitrogen atmosphere. This procedure was repeated three times to assure an oxygen-free atmosphere. Under nitrogen atmosphere, the solution was heated to 110 °C and stirred at 500 rpm. After achieving the desired temperature, the cadmium in TOP solution was transferred to the reaction solution containing ODPAs and TOPO. During this step a significant amount of condensed water is obtained. The water and other condensates are removed using vacuum and freezing them in a cold trap. After the cadmium solution is transferred, the cold trap is removed and the turbid white solution is heated at 90 °C under vacuum until a pressure of at least  $8 \cdot 10^{-2}$  mbar is obtained. After reaching the desired pressure, the solution was placed under nitrogen atmosphere and heated to 210 °C. The solution was stirred at this temperature until the solution is clear with no trace of agglomerates. The solution is then cooled down to 140 °C and placed under vacuum. After reaching a pressure of around  $5 \cdot 10^{-1}$  mbar, the solution is placed under nitrogen atmosphere, then heated again to 210 °C. Subsequently, the solution is cooled down to at least 50 °C and transferred to a sure-store flask and kept under nitrogen.

### 8.1.3 Preparation of the Sulfur Precursor

**Materials and Apparatus:** *Materials:* sulfur (99.998 %, Sigma Aldrich), tri-*n*-octylphosphine (TOP, Cytec).

**Reaction:** (In a glovebox) 77 g (2.4 mol) sulfur were dissolved in 1.2 L TOP to obtain a clear solution. The solution was taken out of the glovebox and then transferred to a sure-store flask, being kept under nitrogen atmosphere.

### 8.1.4 Preparation of the Cadmium Precursor for the Quantum Rods

#### Cadmium precursor based on cadmium acetate

**Materials and Apparatus:** *Materials:* cadmium acetate dihydrate ( $\text{Cd}(\text{AcO}^-)_2 \cdot 2\text{H}_2\text{O}$ , Alfa Aesar), *n*-hexylphosphonic acid (HPA, > 99 %, PCI), octadecylphosphonic acid (ODPA, min. 97 %, PCI), liquid trioctylphosphine oxide (TOPO, mixture of four tri-alkylphosphine oxides, Cytop 503, Cytec), tri-*n*-octylphosphine (TOP, Cytec).

**Reaction:** In a glovebox, 20.62 g (78 mmol)  $\text{Cd}(\text{AcO}^-)_2 \cdot 2\text{H}_2\text{O}$  and 450 mL TOP were dissolved and stirred for at least 18 hours until a clear solution was obtained. Slight traces of water can be observed. The solution was then taken out of the glovebox. In a three-necked reaction flask, 48.4 g (145 mmol) ODPA and 13.8 g (83 mmol) HPA were mixed with 688 mL (1.5 mol) TOP. The solution was stirred and placed under vacuum at room temperature for at least 10 min. The solution was subsequently placed under nitrogen atmosphere. This procedure was repeated three times to assure an oxygen-free atmosphere. Under nitrogen atmosphere, the solution was heated to 110 °C and stirred at 500 rpm. After achieving the desired temperature, the cadmium in TOP solution was transferred to the reaction solution containing ODPA, HPA and TOPO. During this step a significant amount of condensed water is obtained. The water and other condensates are removed using vacuum and freezing them in a cold trap. After the cadmium solution is transferred, the cold trap is removed and the turbid white solution is heated at 90 °C under vacuum until a pressure of at least  $8 \cdot 10^{-2}$  mbar is obtained. After reaching the desired pressure, the solution was placed under nitrogen atmosphere and heated to 210 °C. The solution was stirred at this temperature until the solution is clear with no trace of agglomerates. The solution is then cooled down to 140 °C and placed under vacuum. After reaching a pressure of around  $5 \cdot 10^{-1}$  mbar, the solution is placed under nitrogen atmosphere, then heated again to 210 °C. Subsequently, the solution is cooled down to at least 50 °C and transferred to a sure-store flask and kept under nitrogen.

#### Cadmium precursor based on cadmium oxide

**Materials and Apparatus:** *Materials:* cadmium oxide ( $\text{CdO}$ , > 99.99 %, Alfa Aesar), *n*-hexylphosphonic acid (HPA, > 99 %, PCI), octadecylphosphonic acid (ODPA,

min. 97 %, PCI), liquid trioctylphosphine oxide (TOPO, mixture of four trialkylphosphine oxides, Cytop 503, Cytec), tri-*n*-octylphosphine (TOP, Cytec).

**Reaction:** In the glovebox, 9.9 g (77 mmol) CdO were placed in a reaction flask. Separately, 400 mL TOP (0.9 mmol) were placed in a reaction flask. Both flasks were taken out of the glovebox. In a three bottle neck flask, 48.4 g (145 mmol) ODPa and 13.8 g (83 mmol) HPA were mixed with 738 mL (1.7 mol) TOPO and placed under nitrogen atmosphere. The CdO was then added to the reaction solution and stirred at 500 rpm. The solution was placed at 120 °C under vacuum until a pressure of  $2.7 \cdot 10^{-1}$  was reached. The flask was heated on the sides with a hot air gun. The flask was placed under nitrogen atmosphere from time to time to assure an oxygen-free atmosphere. During this reaction, water and other impurities are obtained. These are removed with vacuum and frozen with a cold trap. After at least 1 hour, the reaction was placed under nitrogen and heated to 300 °C. After a considerable amount of gas is produced, the CdO completely dissolves in the reaction solution. After complete dissolution of the cadmium oxide, the solution is cooled down to 120 °C and then placed under vacuum until a pressure of at least  $8 \cdot 10^{-2}$  mbar is reached. Then, the solution is placed under nitrogen atmosphere and heated again to 300 °C. After stirring at this temperature for at least 30 min., the solution is cooled down to 100 °C. At this temperature the TOP is transferred to the reaction solution and stirred to obtain a clear solution. The precursor is then transferred to a storage flask and kept under nitrogen atmosphere.

## 8.2 General Synthesis of CdSe Cores and CdSe/CdS Core/Shell Nanoparticles Using a Reactor

The general synthesis of CdSe cores and CdSe/CdS heterostructures in a reactor follows the same procedure for both species. Following the schematic in chapter 3.3.4 (figure 13) the main settings that should be taken into account are as followed. The nucleation temperature ( $T_N$ , in the mixing chamber) and the growth temperature ( $T_G$ , in the ovens) can be set using a touch screen temperature controller. The volumetric flow rate ( $\dot{V}$ ) of each precursor (selenium, sulfur, cadmium (core), cadmium (shell)) can be set using a touch display panel on the HPLC pumps.



**Materials and Apparatus:** *Materials:* cadmium (core) precursor, cadmium (shell) precursor, ethanol (dried with molecular sieve, VWR), methanol (dried with molecular sieve, Th. Geyer), *n*-heptane (Merck), *n*-hexane (Honeywell), 1-octadecene (ODE, Alfa Aesar), purified CdSe cores (dissolved in TOP to  $c = 100$   $\mu\text{M}$ , Cytec), sulfur precursor, selenium precursor, toluene (Honeywell). *Apparatus:* 1/16" titanium tubes (for the ovens and connection), titanium mixing chips, stainless steel mixing chambers, HPLC pump (Knauer), Advanti J-E Centrifuge (Beckman Coulter), Cary 5000 UV-Vis Spectrometer (Varian), Cary Eclipse Spectrofluorimeter (Varian), JOEL 1011 transmission electron microscope.

**Reaction:** The precursor solutions are connected to the reactor under nitrogen atmosphere. All components are then verified and any leakage is cleared. For this, ODE is pumped at a controlled rate (usually around 1 mL/min.). The volumetric rate is then verified by measuring the solution at the outlet. Once the rate and pressure at the pumps is verified and under standard conditions, the mixing chamber and the ovens are heated at the desired temperatures. After the desired temperatures are reached, the ODE is then switched to the precursors and the desired flow rates are set for each solution. In order to assure a pure product at the outlet, the solutions are pumped for at least four times the expected residence times (for the reaction) before collecting the product. Once the desired amount of product is collected, the precursors are switched back to ODE, the temperature is set back to ambient temperature and the flow rates are adjusted to assure the cleaning of the reactor. If needed, ODE can be switched to toluene (at max. 120 °C) to clean the tubes from any nanoparticle residue.

**Purification: (CdSe Cores)** In a typical reaction, the reaction solution was purified by adding 90 mL ethanol and 90 mL methanol. The solution was centrifuged at 5000 g for 10 min. at 15 °C. The supernatant was disposed and the precipitate dissolved in 20 mL toluene. 20 mL methanol were then added to the solution. Afterwards, the solution was centrifuged at 5000 g for 10 min. at 15 °C. The supernatant was disposed and the precipitate dissolved in 10 mL *n*-hexane. After adding 10 mL ethanol, the solution was centrifuged at 5000 g for 10 min. at 15 °C. The supernatant was disposed and the precipitate was dissolved in 10 mL *n*-hexane.

**Purification: (CdSe/CdS Heterostructures)** In a typical reaction, the reaction solution was purified by adding 100 mL methanol. The solution was then centrifuged at 5000 g for 10 min. at 15 °C. The supernatant was disposed and the precipitate dissolved in 30 mL toluene. After adding 30 mL methanol, the solution was centrifuged at 5000 g for 10 min. at 15 °C. The supernatant was disposed and the precipitate dissolved in 10 mL either *n*-hexane or *n*-heptane.

### 8.3 Fabrication of Substrates via Photolithography

For this work, different substrates were fabricated using photolithography. First, electrodes were fabricated for the electrostatic alignment of quantum rods. These are interdigitated electrodes (IDEs) and fringe-field electrodes (FFE). Moreover, ITO substrates were also prepared for the fabrication of QLEDs. This will also be described here as it also involves the use of photolithography. The preparation of the chromium mask for photolithography will be addressed as well.

#### 8.3.1 Fabrication of a Chromium Mask

**Materials and Apparatus:** *Materials:* Acetone (Honeywell), chromium blank mask (Nanofilm, 4x4x0.060 SL LRC 10M 1518 5K, Soda Lime, 2.8 OD, 53000 Å photoresist thickness), AZ 726 MIF (Microchemicals), chrome etch n.1 (perchloric acid: (HClO<sub>4</sub>) and ceric ammonium nitrate ((NH<sub>4</sub>)<sub>2</sub>[Ce(NO<sub>3</sub>)<sub>6</sub>], Technic). *Apparatus:* ML3 Microwriter (Durham Magneto Optics).

**Procedure:** The blank soda-lime glass photomask precoated with thick chromium and 530 nm thick AZ 1518 positive photoresist layer was exposed with 90 J/s/cm<sup>2</sup> in the Microwriter using a pre-designed mask. After exposure, the resist was developed for 30 s in AZ 726 MIF and then washed with distilled water and dried in a flow of nitrogen. The chromium layer was then etched with chrome etch solution for 60 s, then washed with distilled water and dried in a flow of nitrogen. To remove the photoresist, the mask was submerged in acetone, then in fresh acetone and finally washed with distilled water and dried in a flow of nitrogen.

### 8.3.2 Preparation of Substrates for Photolithography

Interdigitated electrodes use a glass substrate as the starting material. In order to avoid any impurities which may hinder their performance, these undergo a so called RCA cleaning (RCA: Radio Corporation of America).<sup>[178–180]</sup>

**Materials and Apparatus:** *Materials:* Acetone (Honeywell), ammonia (25 %, Sigma Aldrich), hydrogen peroxide (30 %, stabilized, Chemsolute), 2-propanol (Honeywell).

**Procedure:** In a typical reaction, 375 mL distilled water were mixed with 65 mL ammonia and heated to 70 °C while stirring. After reaching that temperature 65 mL of hydrogen peroxide were added to the solution. After 1 min. the solution started bubbling vigorously. Then the substrate were added and submerged for at least 15 min. The substrates are subsequently washed with distilled water and dried in a flow of nitrogen.

### 8.3.3 Fabrication of Interdigitated Electrodes

Glass substrates previously handled with the RCA clean were cut with a diamond scribe to the desired size, if needed.

**Materials and Apparatus:** *Materials:* Acetone (Honeywell), AZ nLOF 2020 (Microchemicals), AZ 726 MIF (Microchemicals), gold, hydrogen peroxide (30 %, stabilized, Chemsolute), iodine (Grüssing), 2-Propanol (Honeywell), potassium iodide (Chemsolute), technistrip NI555 (Microchemicals), titanium (slugs, Alfa Aesar), triammonium citrate (VWR). *Apparatus:* PVD evaporation unit (Univex 350 G, Oerlikon Leybold), Mask aligner (MJB-3 UV400, Karl Suss), spin coater (Labspin 6 Süss Microtec).

**Procedure:** The glass substrates were placed inside the PVD evaporation chamber and evacuated over night. After reaching a pressure of at least  $8.0 \cdot 10^{-6}$  mbar, a layer of 10 nm titanium, followed by 40 nm gold were coated on the substrates. The substrates were taken out of the evaporation chambered subsequently heated at 100 °C on a hot plate for at least 5 min. Then, the substrates were placed on a spin-coater and coated with AZ nLOF with a ramp of 5 s to 4000 rpm and a dwell time of 60 s. The coated substrate was then soft-baked at 110 °C for 60 s on a hot plate. Afterwards, the substrate is aligned on a mask aligner using a pre-designed chromium mask, and exposed to UV light for 12 s. The substrates are then baked (PEB) at 110 °C for 60 s and then developed with AZ 726

MIF for 30 s. To assure any remaining photoresist is removed, the substrates are quickly washed under fresh AZ 726 MIF developer and then washed with distilled water and dried under nitrogen flow.

To etch the non-coated gold, a solution of 10 vol-% 2-propanol and H<sub>2</sub>O:KI:I<sub>2</sub> in a ratio of 400:4:1 was prepared. The substrates are placed in the etching solution while frequently moving for 90 s, then washed with distilled water and dried under a nitrogen flow. The photoresist is then removed by submerging the substrates in Technistrip NI555 at 65 °C for at least 20 min. Then, the substrates are washed with distilled water and dried under nitrogen flow. If needed, the substrates can be further cleansed with acetone, followed by 2-propanol and water. To etch the titanium, a solution of 5 mass % triammonium citrate in hydrogen peroxide (30 %) was prepared. Then, the substrated were submerged to the stirring etch solution at 35 1C for 3 min. Finally, the substrates were washed with distilled water.

### 8.3.4 Fabrication of Fringe-Field Electrodes

**Materials and Apparatus:** *Materials:* Acetone (Honeywell), AZ nLOF 2020 (Microchemicals), AZ 726 MIF (Microchemicals), gold, hydrogen peroxide (30 %, stabilized, Chemsolute), iodine (Sigma Aldrich), 2-Propanol (Honeywell), potassium iodide (Sigma Aldrich), silicon wafers (Siegert Wafer, 500 nm SiO<sub>2</sub>, 725 ± 25 μm, P/Bor <100>), technistrip NI555 (Microchemicals), titanium (slugs, Alfa Aesar), triammonium citrate (Sigma Aldrich). *Apparatus:* spin coater (Labspin 6 Süss Microtec) PVD evaporation unit (Univex 350 G, Oerlikon Leybold), ML3 Microwriter (Durham Magneto Optics).

**Procedure:** The wafer was cut into a 10x10 cm (or 9x9 cm) rectangle and then placed inside the PVD evaporation chamber and evacuated over night. After reaching a pressure of at least  $8.0 \cdot 10^{-6}$  mbar, a layer of 10 nm titanium, followed by 40 nm gold were coated on the substrates. The substrates were taken out of the evaporation chambered subsequently heated at 100 °C on a hot plate for at least 5 min. Then, the substrates were placed on a spin-coater and coated with AZ nLOF with a ramp of 5 s to 4000 rpm and a dwell time of 60 s. The coated substrate was then soft-baked at 110 °C for 60 s on a hot plate. Afterwards, the substrate is placed inside the Microwriter and exposed with a dosis of 400 mJ/cm<sup>2</sup>. The substrates are then baked (PEB) at 110 °C for 60 s and then

developed with AZ 726 MIF for 30 s. To assure any remaining photoresist is removed, the substrates are quickly washed under fresh AZ 726 MIF developer and then washed with distilled water and dried under nitrogen flow.

To etch the non-coated gold, a solution of 10 vol-% 2-propanol and  $\text{H}_2\text{O}:\text{KI}:\text{I}_2$  in a ratio of 400:4:1 was prepared. The substrates are placed in the etching solution while frequently moving for 90 s, then washed with distilled water and dried under a nitrogen flow. The photoresist is then removed by submerging the substrates in Technistrip NI555 at 65 °C for at least 20 min. Then, the substrates are washed with distilled water and dried under nitrogen flow. If needed, the substrates can be further cleansed with acetone, followed by 2-propanol and water. To etch the titanium, a solution of 5 mass % triammonium citrate in hydrogen peroxide (30 %) was prepared. Then, the substrated were submerged to the stirring etch solution at 35 1C for 3 min. Finally, the substrates were washed with distilled water, dried with nitrogen flow and cut to the desired size using a diamond scribe.

### 8.3.5 Fabrication of Structured Indium-tin Oxide Substrates

**Materials and Apparatus:** *Materials:* Aceton (Honeywell), AZ 351B (Microchemicals), AZ ECI 3012 (Microchemicals), dish soap (Kiehl Spühl-Blitz), hydrochloric acid (Sigma Aldrich, 37 %), indium tin oxide (ITO, Ossila, 25x25 mm, unpatterned), nitric acid (Sigma Aldrich, 65 %), 2-propanol (Honeywell), water (demin.). *Apparatus:* Spin coater (Labspin 6, Süss MicroTec), mask aligner (MJB-3 UV400, Karl Suss), plasma cleaner (Harrick Plasma).

**Procedure:** The ITO substrate was cleaned by immersion of the substrate in acetone, then followed by 2-propanol and distilled water. The substrate was dried using a nitrogen flow. Then, the ITO was cleaned using a plasma cleaner for at least 2 min. The AZ ECI 3012 photoresist was spincoated at 3000 rpm for 60 s then soft baked for 90 s at 90 °C. The substrate was then placed and aligned at the mask aligner. It was exposed for 8 s. Then it was baked for 90 s at 110 °C. A solution o demin. water and AZ 351B Developer with 4:1 ratios was prepared. The substrates were then immersed into this solution for 60 s, then washed with distilled water and dried in a nitrogen flow. The substrates were then analyzed for beads remaining at the edges, if so, these were removed with a kimwipe soaked in acetone. Then the substrates were quickly washed in the developer solution.

The substrates were then hard-baked at 150 °C for 5 minutes. A solution of 54 mL hydrochloric acid, 7.5 mL nitric acid and 38.5 mL distilled water was prepared for the etching of ITO. 3 drops of dish soap were added to facilitate the procedure. The substrates were then immersed into the etch solution at 35 °C (max. of 45 °C) for 90 s. Then the substrates were washed in distilled water and dried in a nitrogen flow. To remove the photoresist, the substrates were immersed in acetone and placed in ultra sonic bath for at least 10 min. Then they were washed with fresh acetone, then distilled water and dried in a nitrogen flow.

## 8.4 Alignment of Quantum Rods

**Materials and Apparatus:** *Materials:* chloroform (Honeywell), *n*-heptane (Merck), nonanoic acid (Sigma Aldrich), octane (Sigma Aldrich), 1-octadecene (ODE, Alfa Aesar), 1-octanethiol (Merck, 90 %), oleylamine (cis-1-amino-9-octadecene, Julius Hoesch, 90 %), toluene (Honeywell), PTFE filter (0.2  $\mu\text{m}$ ), quantum rod solution. *Apparatus:* Dip coater (KSV DC/D/LM), high voltage amplifier (Trek Model 2205), oscilloscope (Rigol, DS1102E), function/arbitrary waveform generator (Rigol, DG1022), half wave plate (Thorlabs), CCD camera (Luca S 658M OEM Housing, Andor Technology), rotor (Thorlabs).

**Drop casting for IDEs:** The alignment of quantum rods using an electric field on IDEs was performed by drop casting the solution onto the IDE's active area.

**Procedure:** The quantum rod solution was filtered with a PTFE filter to remove agglomerations and any impurities. The IDE is then contacted with gold pin contacts and a voltage (usually 150 V) is applied with the desired settings (see 5.3.1) using a function generator, an oscilloscope to read-out the applied voltage, and an amplifier to achieve the desired voltage. While applying the electrostatic potential, 10  $\mu\text{L}$  of the quantum rod solution (usually at 18 mg/mL) was drop casted on the IDE active area. After the solution dried, the voltage was turned off and the sample removed.

**Dipcoating for FFE:** The alignment of quantum rods with using an electric field on FFEs was performed by dip coating of the substrate in the quantum rod solution.

**Procedure:** The quantum rod solution was filtered with a PTFE filter to remove agglomerations and any impurities. The FFE is then contacted with a self made PCB structure, which is connected to amplifier. The desired voltage (see 5.4 for specific information) and settings were set with the function generator, read-out with the oscilloscope. While applying the electrostatic potential, the structure was submerged into the quantum rod solution (usually at 2.5 mg/mL). After short tempering (around 30 s), the substrate was withdrawn at 45 mm/min and dried under ambient conditions. After the solution was completely dry, the voltage was turned off and the sample removed.

**Analysis:** (See chapter 3.7.3 for a detailed explanation) The structure was placed with a two sided adhesive tape and irradiated with blue light from a commercial LED ( $\lambda = 451$  nm). The emission was filtered with a long pass filter, a polarizer and a half wave plate (which is connected to a rotor) and an acquisition was taken by a CCD camera after moving the half wave plate by one degree.

## 8.5 Fabrication of Polarized Emissive Light-emitting Diodes

The fabrication of polarized emissive light-emitting diodes followed the classic and inverted stack. For this, ZnO nanoparticles were used as the ETL. The remaining materials were varied depending on the stack.

### 8.5.1 Synthesis of ZnO Nanoparticles for the ETL

The synthesis of ZnO nanoparticles followed an upscaled procedure from Mashford *et al.*<sup>[110]</sup>

**Materials and Apparatus:** ethanol (dried with molecular sieve, Honeywell), *n*-hexane (Honeywell), methanol (Chemsolute), 1-propanol (Sigma Aldrich), PTFE filter (5  $\mu\text{m}$  and 0.2  $\mu\text{m}$ ), tetramethylammonium hydroxide pentahydrate (TMAH, Sigma Aldrich), zinc acetate dihydrate (Scharlau). *Apparatus:* Advanti J-E Centrifuge (Beckman Coulter), Cary 5000 UV-Vis Spectrometer (Varian), Cary Eclipse Spectrofluorimeter (Varian), JOEL 1011 transmission electron microscope.

**Procedure:** In a 250 mL three necked reaction flask, 1.2 g (5.5 mmol) zinc acetate dihydrate were dissolved with 75 mL ethanol ( $c = 60$  mM) and placed under inert gas. If

needed, more ethanol can be added to completely dissolve the zinc acetate. A solution of 1.8 g (10 mmol) TMAH and 8 mL methanol was prepared. The zinc solution was heated to 60 °C and stirred for one hour. After complete dissolution of the salt, the solution was cooled to 40 °C. Then, 1 mL of the TMAH-MeOH solution were injected to the stirring solution. This injection was repeated in 15 s intervals. After complete injection of the TMAH-MeOH solution, the reaction was cooled and stored in a refrigerator.

**Purification:** 10 mL of the stock solution were placed in two separate centrifuge tubes, which were weighted before use. 30 mL *n*-hexane were added to the stock solution. A white precipitate can be observed. The solution was centrifuged at 5000 g for 10 min. at 20 °C. The supernatant was disposed and the centrifuge was filled with 10 mL of the stock solution. The procedure was repeated at least 5 times to guarantee enough of the product. The precipitate was then dried at air conditions and weighted. The white precipitate was then dissolved in 1-propanol to deliver a solution with  $c = 30$  mg/mL. The solution was placed under a ultrasonic bath for several hours. The solution (turbulent) was filtered with a 5  $\mu\text{m}$  PTFE filter and then with a 0.2  $\mu\text{m}$  PTFE filter to remove any remaining impurities. The colorless clear solution was then analyzed via thermogravimetric analysis to obtain the real concentration, usually of 15 mg/mL.

### 8.5.2 Fabrication of the Light-emitting Diodes

**Materials and Apparatus:** Acetone (Honeywell), aluminum (Alfa Aesar), 4,4'-Bis(N-carbazolyl)-1,1-biphenyl (CBP, Ossila, sublimed), chlorobenzene (Honeywell), molybdenum trioxide ( $\text{MoO}_3$ , Alfa Aesar), PEDOT:PSS (1.3 % aqueous solution), 1-propanol (VWR), 2-propanol (Sigma Aldrich), poly(9-vinylcarbazol) (PVK, Sigma Aldrich), TCTA (Ossila, sublimed), thermal release tape (Teltec), distilled water, zinc oxide (synthesized).

#### Conventional Stack

**Procedure:** The ITO substrate was cleaned with acetone, then 2-propanol and washed with distilled water, then dried in a nitrogen flow. The substrate was then cleaned with a plasma cleaner for at least 30 minutes. PEDOT:PSS was filtered using a PTFE filter (5  $\mu\text{m}$ ). Then, 200  $\mu\text{L}$  of the solution were spin coated onto the substrate at 3000 rpm for 60 s. The substrate was then baked at 150 °C for at least 30 min. The substrate was



then placed inside a glovebox. There, 75  $\mu\text{L}$  of a 0.1 % PVK solution (in chlorobenzene) were spin coated onto the substrate at 4000 rpm for 30 s. Then it was baked at 145  $^{\circ}\text{C}$  for 30 min. Outside of the glovebox, the aligned substrate, preferably recently aligned, was cleaned with a nitrogen flow. This is to remove any dust that may hinder the transfer of the aligned film. Using a thermal release tape, the tape was placed on the aligned substrate, pressed gently and then removed rapidly from a direction parallel to the direction of the finger electrodes. The tape was then placed on the active area of the ITO substrate. The substrate was heated to 125  $^{\circ}\text{C}$ . The thermal release tape was evaporated this way. The remaining stamp was removed and the substrate cleaned under a nitrogen flow. Next, 75  $\mu\text{L}$  of a ZnO solution (in 1-propanol,  $c = 15 \text{ mg/mL}$ ) was spincoated to the ITO substrate at 2000 rpm for 30 s. The solution can be either drop casted during spin coating or before the spin coating. The ZnO solution was spincoated twice to guarantee the desired thickness. The substrate was then baked at 145  $^{\circ}\text{C}$  for 30 min. and cleaned with a nitrogen flow to remove any dust. The substrate was then placed in the PVD chamber and a 100 nm aluminum layer was deposited.

### **Inverted Stack**

**Procedure:** The ITO substrate was cleaned with acetone, then 2-propanol and washed with distilled water, then dried in a nitrogen flow. The substrate was then cleaned with a plasma cleaner for at least 30 minutes. 75  $\mu\text{L}$  of a ZnO solution (in 1-propanol,  $c = 15 \text{ mg/mL}$ ) was spincoated to the ITO substrate at 2000 rpm for 30 s. The solution can be either drop casted during spin coating or before the spin coating. The ZnO solution was spincoated twice to guarantee the desired thickness. The substrate was then baked at 300  $^{\circ}\text{C}$  for 90 min. to remove any remaining impurities. Separately, the aligned substrate, preferably recently aligned, was cleaned with a nitrogen flow. This is to remove any dust that may hinder the transfer of the aligned film. Using a thermal release tape, the tape was placed on the aligned substrate, pressed gently and then removed rapidly from a direction parallel to the direction of the finger electrodes. The tape was then placed on the active area of the ITO substrate. The substrate was heated to 125  $^{\circ}\text{C}$ . The thermal release tape was evaporated this way. The remaining stamp was removed and the substrate cleaned under a nitrogen flow. The substrate was then placed inside the PVD chamber and under

vacuum. A 50 nm layer of either CBP or TCTA was deposited, followed by 10 nm MoO<sub>3</sub> and 100 nm aluminum.

**Analysis:** The QLED was analyzed for their emission and luminance. *Emission:* The QLED was contacted using a self-made contact box with a nitrogen atmosphere. Using a Keithly source meter, an integrating sphere a current is applied and the emission measured with a spectrofluorimeter. *Luminance-I-V:* Luminance, EQE and I-V measurements were performed by using a calibrated Si-photodiode (Thorlabs) while applying a current with the method described in chapter 3.7.4. The current and voltage of the QLED and the calibrated Si-photodiode were measured with two Keithley source meters.

## 9 Acknowledgments

Foremost I would like to thank Dr. Jan Niehaus for offering me this challenging but interesting topic and allowing me to do my Ph. D. thesis at Fraunhofer IAP-CAN. I would also like to thank Prof. Dr. Alf Mews for taking the role as supervisor for this project. Both their input and expertise were always helpful and allowed me to complete this incredible project.

I would also like to thank all the Fraunhofer CAN team, which gave me immense support in either theoretical or practical questions. A special thanks goes to the whole Quantum Materials team: Öznur Tokmak for all the quantum yield, TGA measurements and all her support in any matter; Sonja Krohn for her friendly support in countless discussions during both our projects; Sören Becker for all his input in many theoretical questions; Tobias Jochum for all the support starting already during my nano science lab course followed by my Master's thesis, without his engagement and input I would not have come this far; Christian Dörner for her help with all the TGA measurements; Maria Lohse for all her support with any practical question or with the order of any weird chemicals we needed; Carsten Ott for his support with any technical question regarding the glove-box, the reactor and anything related to the laboratory work and with the Fraunhofer server. Here, I would like to dedicate some extra special words to Dr. Hendrik Schlicke. His supervision throughout my whole Ph. D. with any theoretical and practical questions, added to the immense amount of meetings and discussions we had allowed me to successfully complete this project. His expertise and support will always be appreciated added to his always friendly and supportive words.

Many thanks go to all the HiWis at Fraunhofer who helped me with measurements and purification steps: Cem Güzel and Leonhard Niemann. The pre-works done by Leonhard were also very important for my whole project. Moreover, I would like to thank my lab students Ekaterina Salikhova, who now works as a Ph. D. student at CAN, Daniel Lengle, now Ph. D. with Prof. Mews, and my Bachelor student Christoph Tioka.

I would now like to thank all the AK Mews for their complete support and very interesting discussions during all the seminar talks. A special thanks goes to Dr. Christian Strelow who contributed a lot in the polarization measurements and allowed us to use his

equipment for a very long time. Also many thanks to Jan Flügge who was always ready to let us borrow some small parts for any new experiments I designed.

All of the team at the University of Hamburg, specially at the Institute of Physical Chemistry, contributed to the completion of this work. Special thanks go to Stefan Werner for all the TEM measurements he performed. Many thanks go to the *Werkstatt*, which did uncountable works needed for this project.

Throughout my whole studies, many of my friends gave me their full support. Therefore, I would like to thank my university friends and my close friends in Europe and in Mexico. Also having a balanced work-life is very important, therefore I thank all of these friends who either just had a nice talk during lunch or accompanied me at any festival during holidays.

Last and most importantly, I would like to thank my family, specially my beloved mom Maricela. Without her nothing of this would have been possible. She allowed me, supported me and gave me the chance to study abroad. It is thanks to her that I could have this opportunity and she will always have my full admiration, love and gratitude. ¡Gracias ma, te quiero, te admiro y te agradezco mucho!

## References

- [1] A. Ekimov, A.A.Onushchenko, *Jetp Lett.* **1981**, *34*, 345–349.
- [2] A. L. Efros, *Sov. Phys. Semicond. USSR* **1982**, *16*, 772–775.
- [3] Y. E. Panfil, M. Oded, U. Banin, *Angew. Chemie - Int. Ed.* **2018**, *57*, 4274–4295.
- [4] O. Chen, H. Wei, A. Maurice, M. Bawendi, P. Reiss, *MRS Bull.* **2013**, *38*, 696–702.
- [5] D. Vollath, *Nanomaterials*, 2nd ed., Wiley-VCH, Weinheim, **2013**.
- [6] A. P. Alivisatos, *J. Phys. Chem.* **1996**, *100*, 13226–13239.
- [7] X. Li, Z. Lu, T. Wang, *Nano Res.* **2021**, *14*, 1233–1243.
- [8] J.-S. Lim, *Asian J. Innov. Policy* **2019**, *8*, 274–287.
- [9] Y. P. Rakovich, F. Jäckel, J. F. Donegan, A. L. Rogach, *J. Mater. Chem.* **2012**, *22*, 20831–20839.
- [10] H. Weller, *Angew. Chem.* **1993**, *105*, 43–55.
- [11] J. Bang, J. Park, J. H. Lee, N. Won, J. Nam, J. Lim, B. Y. Chang, H. J. Lee, B. Chon, J. Shin, J. B. Park, J. H. Choi, K. Cho, S. M. Park, T. Joo, S. Kim, *Chem. Mater.* **2010**, *22*, 233–240.
- [12] R. Bhadoria, H. S. Chaudhary, *Int. J. Drug Deliv.* **2011**, *3*, 571–585.
- [13] N. Heydari, S. M. B. Ghorashi, W. H. a. P. Park in *Quantum-dot based Light. Diodes*, IntechOpen, London, **2017**, p. 13.
- [14] Y. Shirasaki, G. J. Supran, M. G. Bawendi, V. Bulović, *Nat. Photonics* **2013**, *7*, 13–23.
- [15] Samsung, Samsung Website, **2022**.
- [16] TCL, TCL Website, **2022**.
- [17] U. Resch-Genger, M. Grabolle, S. Cavaliere-Jaricot, R. Nitschke, T. Nann, *Nat. Methods* **2008**, *5*, 763–775.
- [18] P. Palomaki, *IEEE Spectr.* **2022**, 52–53.
- [19] S. Kim, J. A. Kim, T. Kim, H. Chung, S. Park, S. M. Choi, H. M. Kim, D. Y. Chung, E. Jang, *Chem. Mater.* **2020**, *32*, 5200–5207.

- [20] Y. H. Won, O. Cho, T. Kim, D. Y. Chung, T. Kim, H. Chung, H. Jang, J. Lee, D. Kim, E. Jang, *Nature* **2019**, *575*, 634–638.
- [21] J. Skirnewska, T. D. Wilkinson, *Adv. Mater.* **2022**, DOI 10.1002/adma.202110463.
- [22] W. D. Kim, D. Kim, D. E. Yoon, H. Lee, J. Lim, W. K. Bae, D. C. Lee, *Chem. Mater.* **2019**, *31*, 3066–3082.
- [23] S. Vezzoli, M. Manceau, G. Leménager, Q. Glorieux, E. Giacobino, L. Carbone, M. De Vittorio, A. Bramati, *ACS Nano* **2015**, *9*, 7992–8003.
- [24] R. A. Hikmet, P. T. Chin, D. V. Talapin, H. Weller, *Adv. Mater.* **2005**, *17*, 1436–1439.
- [25] A. Rizzo, C. Nobile, M. Mazzeo, M. De Giorgi, A. Fiore, L. Carbone, R. Cingolani, L. Manna, G. Gigli, *ACS Nano* **2009**, *3*, 1506–1512.
- [26] S. Rhee, D. Jung, D. Kim, D. C. Lee, C. Lee, J. Roh, *Small* **2021**, *17*, 1–8.
- [27] H. Schlicke, C. Schloen, T. Jochum, S. Becker, H. Weller, J. S. Niehaus, *Proc. Int. Disp. Work.* **2019**, *2*, 774–776.
- [28] M. N. Us, A. John, L. Elmo, M. N. Us, ( 12 ) United States Patent, **2005**.
- [29] G. Schmid, *Nanoparticles: from theory to application*, 2nd ed., Wiley-VCH, Weinheim, **2010**.
- [30] P. Atkins, J. De Paula, *Physical Chemistry, Vol. 99*, **2006**, p. 830.
- [31] N. Ashcroft, N. Mermin, *Solid state physics*, Saunders College, Philadelphia, **1976**.
- [32] E. Riedel, C. Janiak, *Anorganische Chemie*, 8th ed., Walter de Gruyter, Berlin, **2011**.
- [33] A. L. Rogach, *Semiconductor Nanocrystal Quantum Dots*, **2008**, pp. 1–4.
- [34] A. L. Efros, M. Rosen, *Annu. Rev. Mater. Sci.* **2000**, *30*, 475–521.
- [35] D. Ferreira, J. Sousa, R. Maronesi, J. Bettini, M. Schiavon, A. Teixeira, A. Silva, *J. Chem. Phys.* **2017**, *147*.
- [36] P. Reiss, M. Protière, L. Li, *Small* **2009**, *5*, 154–168.
- [37] J. C. Lindon, G. E. Tranter, D. W. Koppenaal, *Encyclopedia of Spectroscopy and Spectrometry*, 3rd ed., Elsevier Ltd., London, **2017**.

- [38] H. D. G. Yong S.Cho, V. R. W. Amarakoon, *Ceram. Nanopowders* **2004**.
- [39] D. V. Talapin, R. Koeppel, S. Götzinger, A. Kornowski, J. M. Lupton, A. L. Rogach, O. Benson, J. Feldmann, H. Weller, *Nano Lett.* **2003**, *3*, 1677–1681.
- [40] G. Zaiats, D. Yanover, R. Vaxenburg, J. Tilchin, A. Sashchiuk, E. Lifshitz, *Materials (Basel)*. **2014**, *7*, 7243–7275.
- [41] D. Dorfs, A. Eychmüller in *Semicond. Nanocrystal Quantum Dots Synth. Assem. Spectrosc. Appl.* **2008**.
- [42] L. Carbone, P. Cozzoli, *Nano Today* **2010**, 449–493.
- [43] J. Y. Kim, O. Voznyy, D. Zhitomirsky, E. H. Sargent, *Adv. Mater.* **2013**, *25*, 4986–5010.
- [44] J. Singh, *Physics of Semiconductors and Their Heterostructures*, McGraw-Hill, New York, **1993**.
- [45] M. G. Bawendi, O. Chen, J. Zhao, V. P. Chauhan, *Nat. Mater.* **2013**, *12*, 445–451.
- [46] K. H. Lee, J. H. Lee, W. S. Song, H. Ko, C. Lee, J. H. Lee, H. Yang, *ACS Nano* **2013**, *7*, 7295–7302.
- [47] B. Mahler, P. Spinicelli, S. Buil, X. Quelin, J. P. Hermier, B. Dubertret, *Nat. Mater.* **2008**, *7*, 659–664.
- [48] Y. Chen, J. Vela, H. Htoon, J. L. Casson, D. J. Werder, D. A. Bussian, V. I. Klimov, J. A. Hollingsworth, *J. Am. Chem. Soc.* **2008**, *130*, 5026–5027.
- [49] J. Hu, L. S. Li, W. Yang, L. Manna, L. W. Wang, A. P. Alivisatos, *Science (80-)*. **2001**, *292*, 2060–2063.
- [50] X. Chen, A. Nazzal, D. Goorskey, M. Xiao, Z. A. Peng, X. Peng, *Phys. Rev. B - Condens. Matter Mater. Phys.* **2001**, *64*, 2453041–2453044.
- [51] J. Planelles, F. Rajadell, J. I. Climente, *J. Phys. Chem. C* **2016**, *120*, 27724–27730.
- [52] I. Hadar, G. B. Hitin, A. Sitt, A. Faust, U. Banin, *J. Phys. Chem. Lett.* **2013**, *4*, 502–507.
- [53] S. A. Blanton, R. L. Leheny, M. A. Hines, P. Guyot-Sionnest, *Phys. Rev. Lett.* **1997**, *79*, 865–868.

- [54] C. Grivas, C. Li, P. Andreakou, P. Wang, M. Ding, G. Brambilla, L. Manna, P. Lagoudakis, *Nat. Commun.* **2013**, *4*, DOI 10.1038/ncomms3376.
- [55] Y. U. Staechelin, M. Deffner, S. Krohn, C. Castillo Delgadillo, J. S. Niehaus, H. Lange, *J. Chem. Phys.* **2022**, *156*, DOI 10.1063/5.0079619.
- [56] B. T. Diroll, T. Dadosh, A. Koschitzky, Y. E. Goldman, C. B. Murray, *J. Phys. Chem. C* **2013**, *117*, 23928–23937.
- [57] A. L. Efros, M. Rosen, M. Kuno, M. Nirmal, D. Norris, M. Bawendi, *Phys. Rev. B - Condens. Matter Mater. Phys.* **1996**, *54*, 4843–4856.
- [58] A. Shabaev, A. L. Efros, *Nano Lett.* **2004**, *4*, 1821–1825.
- [59] B. T. Diroll, A. Koschitzky, C. B. Murray, *J. Phys. Chem. Lett.* **2014**, *5*, 85–91.
- [60] S. H. Lohmann, P. Harder, F. Bourier, C. Strelow, A. Mews, T. Kipp, *J. Phys. Chem. C* **2019**, *123*, 5099–5109.
- [61] J. L. Baker, A. Widmer-Cooper, M. F. Toney, P. L. Geissler, A. P. Alivisatos, *Nano Lett.* **2010**, *10*, 195–201.
- [62] L. S. Li, A. P. Alivisatos, *Adv. Mater.* **2003**, *15*, 408–411.
- [63] M. Hasegawa, Y. Hirayama, S. Dertinger, *Appl. Phys. Lett.* **2015**, *106*, DOI 10.1063/1.4907548.
- [64] Z. Hu, M. D. Fischbein, C. Querner, M. Drndić, *Nano Lett.* **2006**, *6*, 2585–2591.
- [65] K. M. Ryan, A. Mastroianni, K. A. Stancil, H. Liu, A. P. Alivisatos, *Nano Lett.* **2006**, *6*, 1479–1482.
- [66] A. K. Srivastava, W. Zhang, J. Schneider, J. E. Halpert, A. L. Rogach, *Adv. Sci.* **2019**, *6*, 1–20.
- [67] M. Mohammadimasoudi, Z. Hens, K. Neyts, *RSC Adv.* **2016**, *6*, 55736–55744.
- [68] M. Mohammadimasoudi, L. Penninck, T. Aubert, R. Gomes, Z. Hens, F. Strubbe, K. Neyts, *Opt. Mater. Express* **2013**, *3*, 2045.
- [69] S. Gupta, Q. Zhang, T. Emrick, T. P. Russell, *Nano Lett.* **2006**, *6*, 2066–2069.
- [70] S. Kaur, G. Murali, R. Manda, Y. C. Chae, M. Yun, J. H. Lee, S. H. Lee, *Adv. Opt. Mater.* **2018**, *6*, 1–5.



- [71] G. S. Lee, J. H. Lee, D. H. Song, J. C. Kim, T. H. Yoon, D. L. Park, S. S. Hwang, D. H. Kim, S. I. Park, *Appl. Opt.* **2008**, *47*, 3041–3047.
- [72] T. H. Choi, S. W. Oh, Y. J. Park, Y. Choi, T. H. Yoon, *Sci. Rep.* **2016**, *6*, 1–9.
- [73] C. D. M. Donegá, *Chem. Soc. Rev.* **2011**, *40*, 1512–1546.
- [74] J. Park, J. Joo, S. G. Kwon, Y. Jang, *Angew. Chem.* **2007**, *119*, 4714–4745.
- [75] C. Murray, C. Kagan, M. Bawendi, *Annu. Rev. Mater. Sci.* **2000**, *30*, 545–610.
- [76] L. Carbone, C. Nobile, M. De Giorgi, F. Della Sala, G. Morello, P. Pompa, M. Hytch, E. Snoeck, A. Fiore, I. R. Franchini, M. Nadasan, A. F. Silvestre, L. Chiodo, S. Kudera, R. Cingolani, R. Krahne, L. Manna, *Nano Lett.* **2007**, *7*, 2942–2950.
- [77] I. Coropceanu, A. Rossinelli, J. R. Caram, F. S. Freyria, M. G. Bawendi, *ACS Nano* **2016**, *10*, 3295–3301.
- [78] A. Hinsch, S. H. Lohmann, C. Strelow, T. Kipp, C. Würth, D. Geißler, A. Kornowski, C. Wolter, H. Weller, U. Resch-Genger, A. Mews, *J. Phys. Chem. C* **2019**, *123*, 24338–24346.
- [79] Z. A. Peng, X. Peng, *J. Am. Chem. Soc.* **2001**, *123*, 1389–1395.
- [80] D. V. Talapin, J. H. Nelson, E. V. Shevchenko, S. Aloni, B. Sadtlir, A. P. Alivisatos, *Nano Lett.* **2007**, *7*, 2951–2959.
- [81] S. Marre, K. F. Jensen, *Chem. Soc. Rev.* **2010**, *39*, 1183–1202.
- [82] S. Marre, J. Park, J. Rempel, J. Guan, M. G. Bawendi, K. F. Jensen, *Adv. Mater.* **2008**, *20*, 4830–4834.
- [83] J. Baek, Y. Shen, I. Lignos, M. G. Bawendi, K. F. Jensen, *Angew. Chemie - Int. Ed.* **2018**, *57*, 10915–10918.
- [84] C. Palencia, R. Seher, J. Krohn, F. Thiel, F. Lehmkuhler, H. Weller, *Nanoscale* **2020**, *12*, 22928–22934.
- [85] B. K. Yen, N. E. Stott, K. F. Jensen, M. G. Bawendi, *Adv. Mater.* **2003**, *15*, 1858–1862.
- [86] J. B. Edel, R. Fortt, J. C. DeMello, A. J. DeMello, *Chem. Commun.* **2002**, *2*, 1136–1137.

- [87] H. Nakamura, Y. Yamaguchi, M. Miyazaki, H. Maeda, M. Uehara, P. Mulvaney, *Chem. Commun.* **2002**, *23*, 2844–2845.
- [88] E. M. Chan, A. P. Alivisatos, R. A. Mathies, *Micro Total Anal. Syst. - Proc. MicroTAS 2005 Conf. 9th Int. Conf. Miniaturized Syst. Chem. Life Sci.* **2005**, *1*, 921–923.
- [89] B. Nauman, *Handbook of Chemical Reactor Design, Optimization and Scaleup*, McGraw-Hill, New York, **2002**.
- [90] J. Hagen, *Chemiereaktoren, Grundlagen, Auslegung und Simulation*, 2nd ed., Wiley-VCH, Weinheim, **2017**.
- [91] J.-S. Niehaus, Dissertation: Aufbau und Charakterisierung einer mikroreaktionstechnischen Anlage zur Produktion von Nanopartikeln, University of Hamburg, **2012**.
- [92] D. Ness, Dissertation: Erweiterung und Optimierung der kontinuierlichen Synthese von Kern/Schale/Schale Halbleiter-Nanopartikeln durch mikrofluidische Hochtemperatur-Komponenten, **2013**.
- [93] T. Jochum, Dissertation: Entwicklung einer automatisierten Syntheseroute zur Darstellung von CdSe/CdS-Nanostäbchen sowie neuartigen elongierten Mischkristallstäbchen für die Displayindustrie, **2016**.
- [94] E. Fitzer, W. Fritz, G. Emig, *Technische Chemie, Vol. 4*, 4th ed., Springer-Lehrbuch, **2016**, pp. 1–23.
- [95] H. S. Fogler, *Essentials of Chemical Reaction Engineering*, Prentice Hall, Upper Saddle River, **2011**.
- [96] J. Lee, V. C. Sundar, J. R. Heine, M. G. Bawendi, K. F. Jensen, *Adv. Mater.* **2000**, *12*, 1102–1105.
- [97] V. Wood, V. Bulović, *Nano Rev.* **2010**, *1*, 5202.
- [98] H. Moon, C. Lee, W. Lee, J. Kim, H. Chae, *Adv. Mater.* **2019**, *31*, 1–14.
- [99] H. Göbel, *Einführung in die Halbleiter-Schaltungstechnik*, 6th ed., Springer Vieweg, Berlin, **2019**.
- [100] D. Bozyigit, O. Yarema, V. Wood, *Adv. Funct. Mater.* **2013**, *23*, 3024–3029.

- [101] H. Kim, C. M. Gilmore, A. Piqué, J. S. Horwitz, H. Mattoussi, H. Murata, Z. H. Kafafi, D. B. Chrisey, *J. Appl. Phys.* **1999**, *86*, 6451–6461.
- [102] L. Qian, Y. Zheng, J. Xue, P. H. Holloway, *Nat. Photonics* **2011**, *5*, 543–548.
- [103] W. D. Kim, D. Kim, D. E. Yoon, H. Lee, J. Lim, W. K. Bae, D. C. Lee, *Chem. Mater.* **2019**, *31*, 3066–3082.
- [104] J. Zhao, J. Zhang, C. Jiang, J. Bohnenberger, T. Basché, A. Mews, *J. Appl. Phys.* **2004**, *96*, 3206–3210.
- [105] S. Wang, S. Yang, C. Yang, Z. Li, J. Wang, W. Ge, *J. Phys. Chem. B* **2000**, *104*, 11853–11858.
- [106] P. C. Chiu, S. H. Yang, *Nanoscale Adv.* **2020**, *2*, 401–407.
- [107] Z. L. Wang, *J. Phys. Condens. Matter* **2004**, *16*, DOI 10.1088/0953-8984/16/25/R01.
- [108] J. Pan, J. Chen, Q. Huang, Q. Khan, X. Liu, Z. Tao, W. Lei, F. Xu, Z. Zhang, *RSC Adv.* **2015**, *5*, 82192–82198.
- [109] D. P. Singh, *Sci. Adv. Mater.* **2010**, *2*, 245–272.
- [110] A. J. Morfa, G. Beane, B. Mashford, B. Singh, E. Della Gaspera, A. Martucci, P. Mulvaney, *J. Phys. Chem. C* **2010**, *114*, 19815–19821.
- [111] H. M. Kim, J. Jang, *Dig. Tech. Pap. - SID Int. Symp.* **2014**, *45*, 67–70.
- [112] I. Cho, H. Jung, B. G. Jeong, J. H. Chang, Y. Kim, K. Char, D. C. Lee, C. Lee, J. Cho, W. K. Bae, *ACS Nano* **2017**, *11*, 684–692.
- [113] N. Van Den Brande, A. Gujral, C. Huang, K. Bagchi, H. Hofstetter, L. Yu, M. D. Ediger, *Cryst. Growth Des.* **2018**, *18*, 5800–5807.
- [114] W. K. Bae, Y. S. Park, J. Lim, D. Lee, L. A. Padilha, H. McDaniel, I. Robel, C. Lee, J. M. Pietryga, V. I. Klimov, *Nat. Commun.* **2013**, *4*, 1–8.
- [115] Y. Kim, Dissertation: Design of High Performance Indium Phosphide-based Quantum Dot Light Emitting Diodes, **2018**.
- [116] Q. Zeng, Z. Xu, C. Zheng, Y. Liu, W. Chen, T. Guo, F. Li, C. Xiang, Y. Yang, W. Cao, X. Xie, X. Yan, L. Qian, P. H. Holloway, *ACS Appl. Mater. Interfaces* **2018**, *10*, 8258–8264.

- [117] B. Zhang, Y. Luo, C. Mai, L. Mu, M. Li, J. Wang, W. Xu, J. Peng, *Nanomaterials* **2021**, *11*, DOI 10.3390/nano11051246.
- [118] S. Kar, N. F. Jamaludin, N. Yantara, S. G. Mhaisalkar, W. L. Leong, *Recent advancements and perspectives on light management and high performance in perovskite light-emitting diodes*, Vol. 10, **2021**, pp. 2103–2143.
- [119] J. Yun, J. Kim, B. J. Jung, G. Kim, J. Kwak, *RSC Adv.* **2019**, *9*, 16252–16257.
- [120] C. Pu, X. Dai, Y. Shu, M. Zhu, Y. Deng, Y. Jin, X. Peng, *Nat. Commun.* **2020**, *11*, 1–10.
- [121] M. A. Baldo, D. F. O. an dY. You, A. Shoustikov, S. Sibley, M. E. Thompson, S. R. Forrest, *Nature* **1998**, *395*, 151.
- [122] G. Gu, D. Z. Garbuzov, P. E. Burrows, S. Venkatesh, S. R. Forrest, *Opt. Lett.* **1997**, *22*, 396–398.
- [123] V. Wood, M. J. Panzer, J. E. Halpert, J. M. Caruge, M. G. Bawendi, V. Bulović, *ACS Nano* **2009**, *3*, 3581–3586.
- [124] H. Huang, A. Dorn, G. P. Nair, V. Bulović, M. G. Bawendi, *Nano Lett.* **2007**, *7*, 3781–3786.
- [125] S. Nam, N. Oh, Y. Zhai, M. Shim, *ACS Nano* **2015**, *9*, 878–885.
- [126] P. Rastogi, F. Palazon, M. Prato, F. Di Stasio, R. Krahne, *ACS Appl. Mater. Interfaces* **2018**, *10*, 5665–5672.
- [127] A. Castelli, F. Meinardi, M. Pasini, F. Galeotti, V. Pinchetti, M. Lorenzon, L. Manna, I. Moreels, U. Giovanella, S. Brovelli, *Nano Lett.* **2015**, *15*, 5455–5464.
- [128] Y. A. Z. Hang, F. E. Z. Hang, H. O. W. Ang, L. E. I. W. Ang, F. A. W. Ang, Q. I. L. In, H. U. S. Hen, L. I. N. S. O. N. G. L. I, *Opt. Express* **2019**, *27*, 7935–7944.
- [129] J. R. Lakowicz, *Principles of Fluorescence Spectroscopy*, 3rd ed., Springer, **2006**.
- [130] A. Rizzo, C. Nobile, M. Mazzeo, M. De Giorgi, A. Fiore, L. Carbone, R. Cingolani, L. Manna, G. Gigli, *ACS Nano* **2009**, *3*, 1506–1512.
- [131] M. Farehanim, U. Hashim, N. Soin, A. Azman, S. Norhafizah, M. Fatin, R. Ayub, *Adv. Mater. Res.* **2015**, *1109*, 118–122.

- [132] A. Biswas, I. S. Bayer, A. S. Biris, T. Wang, E. Dervishi, F. Faupel, *Adv. Colloid Interface Sci.* **2012**, *170*, 2–27.
- [133] G. Rius, A. Baldi, B. Ziaie, M. Atashbar, Z in *Handb. Nanotechnol.* Springer-Verlag, Berlin, **2017**, Chapter 3, pp. 51–86.
- [134] H. J. Levinson, *Princ. Lithogr.* **2010**, 1–6.
- [135] C. A. Mack, *Field Guide to Optical Lithography*, 6th ed., SPIE - International Society for Optical Engineering, Bellingham, **2006**.
- [136] C. Koch, T. Rinke, J, *Fotolithografie Grundlagen der Mikrostrukturierung*, 2nd ed., MicroChemicals GmbH, Friedrichshafen, **2020**.
- [137] M. D. Mattox, *Handbook of Physical Vapor Deposition (PVD) Processing*, 2nd ed., Elsevier Inc., Burlington, **2010**.
- [138] D. M. Dobkin, M. K. Zuraw, *Principles of Chemical Vapor Deposition*, **2003**.
- [139] W. Gottwald, K. Heinrich, *UV/VIS-Spektroskopie für Anwender*, Wiley-VCH, Weinheim, **1998**.
- [140] W. W. Yu, L. Qu, W. Guo, X. Peng, *Chem. Mater.* **2004**, *16*, 560.
- [141] J. Jasieniak, L. Smith, J. Van Embden, P. Mulvaney, M. Califano, *J. Phys. Chem. C* **2009**, *113*, 19468–19474.
- [142] J. R. Lakowicz in *Princ. Fluoresc. Spectrosc.* Springer, **1999**, pp. 25–61.
- [143] V. Balzani, P. Ceroni, A. Juris, *Photochemistry and Photophysics: Concepts, Research, Applications*, Wiley-VCH, Weinheim, **2015**.
- [144] A. P. Demchenko in *Introd. to Fluoresc. Sens.* Springer, Dordrecht, Netherlands, **2009**, pp. 1–26.
- [145] W. Demtröder, *Experimentalphysik*, 7th ed., Springer-Lehrbuch, Berlin, **2017**.
- [146] S. R. Forrest, D. D. Bradley, M. E. Thompson, *Adv. Mater.* **2003**, *15*, 1043–1048.
- [147] D. E. Newbury, D. B. Williams, *Acta Mater.* **2000**, *48*, 323–346.
- [148] J. Goldstein, D. E. Newbury, D. C. Joy, C. E. Lyman, P. Echlin, E. Lifshin, L. Sawyer, J. R. Michael, *Scanning Electron Microscopy and X-ray Microanalysis*, **2003**.

- [149] D. McMullan, *Scanning* **1995**, *17*, 175–185.
- [150] F. J. Giessibl, *Rev. Mod. Phys.* **2003**, *75*, 949–983.
- [151] JPK Instruments AG, *The NanoWizard AFM Handbook*, 2nd ed., Berlin, **2005**, p. 40.
- [152] L. Spiess, G. Teichert, R. Schwarzer, *Moderne Röntgenbeugung: Röntgendiffraktometrie für Materialwissenschaftler, Physiker und Chemiker*, 2nd ed., Wiesbaden, **2009**, pp. 240–257.
- [153] J. Lim, B. G. Jeong, M. Park, J. K. Kim, J. M. Pietryga, Y. S. Park, V. I. Klimov, C. Lee, D. C. Lee, W. K. Bae, *Adv. Mater.* **2014**, *26*, 8034–8040.
- [154] I. Mekis, D. V. Talapin, A. Kornowski, M. Haase, H. Weller, *J. Phys. Chem. B* **2003**, *107*, 7454–7462.
- [155] S. Christodoulou, G. Vaccaro, V. Pinchetti, F. De Donato, J. Q. Grim, A. Casu, A. Genovese, G. Vicidomini, A. Diaspro, S. Brovelli, L. Manna, I. Moreels, *J. Mater. Chem. C* **2014**, *2*, 3439–3447.
- [156] K. Boldt, N. Kirkwood, G. A. Beane, P. Mulvaney, *Chem. Mater.* **2013**, *25*, 4731–4738.
- [157] Y. Yin, A. P. Alivisatos, *Nature* **2005**, *437*, 664–670.
- [158] C. M. Evans, M. E. Evans, T. D. Krauss, *J. Am. Chem. Soc.* **2010**, *132*, 10973–10975.
- [159] V. Singh, Priyanka, P. V. More, E. Hemmer, Y. K. Mishra, P. K. Khanna, *Mater. Adv.* **2021**, *2*, 1204–1228.
- [160] Z. A. Peng, X. Peng, *J. Am. Chem. Soc.* **2002**, *124*, 3343–3353.
- [161] C. Schloen, Master’s Thesis: Polarised LED Based on Electrostatically Aligned CdSe/CdS Quantum Rods, **2019**.
- [162] L. Niemann, Bachelor Thesis: Optimization Approaches for Polarized LEDs Based on CdSe/CdS Quantum Dot-in-Rods and Characterization of LEDs Based on CdSe/CdS Giant-Shell Quantum Rods, **2019**.
- [163] C. Reichardt, *Solvents and Solvent Effects in Organic Chemistry*, 3rd ed., Wiley-VCH, Weinheim, **2003**.

- [164] R. Beckert, *Organikum*, 24th ed., Wiley VCH, Weinheim, **2015**, p. 774.
- [165] E. A. Meulenkamp, *J. Phys. Chem. B* **1998**, *5647*, 5566–5572.
- [166] H. Morkoç, Ü. Özgür in *Zinc Oxide Fundam. Mater. Device Technol.* Wiley-VCH, Weinheim, **2009**, pp. 1–76.
- [167] H. Swanson, R. Fuyat, *Standard X-ray diffraction patterns*, 2nd ed., National Bureau of Standards, Washington D.C., **1967**.
- [168] X. Li, Q. Lin, J. Song, H. Shen, H. Zhang, L. S. Li, X. Li, Z. Du, *Adv. Opt. Mater.* **2020**, *8*, 1–9.
- [169] E. Salikhova, Masterarbeit: Ausarbeitung und Optimierung eines reproduzierbaren Herstellungsverfahrens für giant shell quantum dot- basierte Leuchtdioden (GSQLEDs) sowie Charakterisierung ihrer optoelektronischen Eigenschaften, **2020**.
- [170] P. E. Allen, D. R. Holberg, *CMOS Analog Circuit Design*, 2nd ed., Oxford University Press, **2002**.
- [171] W.-K. Chen, *The Electrical Engineering Handbook*, Elsevier Academic Press, London, **2004**.
- [172] L. Zhang, B. Lv, H. Yang, R. Xu, X. Wang, M. Xiao, Y. Cui, J. Zhang, *Nanoscale* **2019**, *11*, 12619–12625.
- [173] D. Campi, C. Alibert, *Appl. Phys. Lett.* **1989**, *55*, 454–456.
- [174] N. Susa, T. Nakahara, *Electron. Lett.* **1992**, *28*, 941–943.
- [175] S. Riyopoulos, *Nanoscale Res. Lett.* **2009**, *4*, 993–1003.
- [176] C. Lu, L. Wang, J. Lu, R. Li, L. Liu, D. Li, N. Liu, L. Li, W. Cao, W. Yang, W. Chen, W. Du, C. T. Lee, X. Hu, *J. Appl. Phys.* **2013**, *113*, DOI 10.1063/1.4772683.
- [177] W. Lv, L. Wang, L. Wang, Y. Xing, D. Yang, Z. Hao, Y. Luo, *Appl. Phys. Express* **2014**, *7*, DOI 10.7567/APEX.7.025203.
- [178] Fridman, *INRF Appl. note* **1960**, *2*, 2–4.
- [179] W. Kern, *Proc. - Electrochem. Soc.* **1990**, *90*, 3–19.
- [180] W. Kern, C. A. Deckert, *Thin Film Processes*, (Eds.: W. Kern, J. L. Vossen), Academic Press, New York, **1978**.

- [181] S. Aldrich, Sigma-Aldrich Online Database, **2022**.
- [182] Ossila, Ossila Products, **2022**.
- [183] Microchemicals, SDS Microchemicals (Merck), **2022**.
- [184] TECHNIC, SDS Technistrip NI555, **2022**.
- [185] Chemsolute, SDS Wasserstoffperoxid, **2022**.
- [186] GESTIS, GESTIS-Stoffdatenbank, **2022**.



## A Appendices

### A.1 Safety

#### A.1.1 Chemicals Used

The following table 28 lists the chemicals used in this work with their GHS symbols as well as hazardous and precautionary statements.<sup>[181–185]</sup> Table 30 lists the used samples and their corresponding Log-nr.

**Table 28:** Used chemicals and their GHS symbols as well as their hazardous and precautionary statements.

| Substance         | GHS        | Hazardous statements                  | Precautionary statements  |
|-------------------|------------|---------------------------------------|---|
| Acetone           | 02, 07     | 225, 319, 336                         | 210, 280,<br>304+340+312,<br>305+351+338,<br>337+313,<br>403+235  |
| Aluminum          | 02, 07     | 228, 261                              | 210, 370+378,<br>402+404  |
| Ammonia           | 05, 06, 09 | 221, 280, 314,<br>331, 410,<br>EUH071 | 210, 260, 273,<br>280,<br>303+361+353+315,<br>304+340+315,<br>305+351+338+315,<br>377, 381, 403,<br>405 |
| AZ 351B Developer | 05, 08     | 290, 318, 360fd                       | 201, 280,<br>305+351+338,<br>308+313, 313   |

**Table 28:** Used chemicals and their GHS symbols as well as their hazardous and precautionary statements.

| Substance                        | GHS        | Hazardous statements                | Precautionary statements                     |
|----------------------------------|------------|-------------------------------------|--|
| AZ 726 MIF Developer             | 05, 06, 08 | 290, 302, 311, 314, 371, 373        | 380, 302+352, 305+351+338, 308+310           |
| AZ ECI 3012                      | 02, 05, 07 | 226, 318, 335                       | 210, 280, 305+351+338, 313                   |
| AZ nLOF 2020                     | 02, 07     | 226, 336                            | 210  |
| Cadmium acetate dihydrate        | 06, 08, 09 | 301, 312, 330, 340, 350, 371, 410   | 201, 202, 273, 280, 301+352+312, 304+340+310 |
| Cadmium oxide                    | 06, 08, 09 | 301, 330, 341, 350, 361fd, 372, 410 | 201, 260, 280, 304+340+310, 308+313          |
| Cadmium selenide                 | 06, 08, 09 | 301+331, 312, 350, 373, 410         | 201, 261, 273, 301+310+330, 308+313, 403+233 |
| CBP                              | 05, 07     | 315, 318, 335                       | 290, 305+351+338                             |
| Cadmium selenide/cadmium sulfide | 07, 08, 09 | 302, 341, 350, 361, 372, 410        | 201, 273, 301+312+330, 308+313, 501          |

**Table 28:** Used chemicals and their GHS symbols as well as their hazardous and precautionary statements.

| Substance        | GHS            | Hazardous statements                    | Precautionary statements  |
|------------------|----------------|---|---|
| Chlorobenzene    | 02, 07, 09     | 226, 315, 332, 411                      | 260, 262, 273, 403  |
| Chloroform       | 06, 08         | 302, 315, 319, 331, 336, 351, 361d, 372 | 201, 202, 235, 260, 264, 270, 271, 280, 281, 301+330+331, 302+352, 304+340, 305+351+338, 308+313, 310, 311, 314, 332+313, 337+313, 362, 403+233, 405, 501 |
| Chromium etchant | 03, 05, 07, 09 | 272, 290, 314, 317, 411                 | 210, 220, 273, 280, 303+361+353, 305+351+338  |
| Ethanol          | 02, 07         | 225, 319                                | 210, 305+351+338, 370+378, 403+235  |
| Gold             | -              | -                                       | -   |

**Table 28:** Used chemicals and their GHS symbols as well as their hazardous and precautionary statements.

| Substance                 | GHS            | Hazardous statements                     | Precautionary statements   |
|---------------------------|----------------|--|--|
| Heptane                   | 05, 07, 08, 09 | 225, 304, 361f,<br>373, 315, 336,<br>411 | 210, 240, 273,<br>301+310, 331,<br>302+352,<br>403+235           |
| Hexadecylphosphonic acid  | -              | -  | -  |
| Hexane                    | 05, 07, 08, 09 | 225, 304, 361f,<br>373, 315, 336,<br>411 | 210, 240, 273,<br>301+310, 331,<br>302+352,<br>403+235           |
| Hydrochloric acid<br>37 % | 05, 07         | 314                                      | 280,<br>303+361+353,<br>305+351+338                              |
| Hydrogen peroxide         | 05, 07         | 302+332                                  | 280, 302+352,<br>305+351+338,<br>310                             |
| Indium tin oxide          | -              | -  |  |
| Iodine                    | 07, 08, 09     | 312+332, 315,<br>319, 335, 372,<br>400   | 273, 303+352,<br>305+351+338,<br>314                             |
| Methanol                  | 05, 06, 08     | 301+311+331,<br>370                      | 210, 280,<br>302+352+312,<br>304+340+311,<br>370+378,<br>403+235 |

**Table 28:** Used chemicals and their GHS symbols as well as their hazardous and precautionary statements.

| Substance                | GHS            | Hazardous statements          | Precautionary statements                                     |
|--------------------------|----------------|-------------------------------|--|
| Molybdenum trioxide      | 07, 08         | 319, 335, 351                 | 305+351+338,<br>308+313                                      |
| Nitric acid              | 03, 05, 06     | 272, 290, 314,<br>331, EUH071 | 221, 280,<br>303+361+353,<br>304+340,<br>305+351+338,<br>310 |
| Nonanoic acid            | 07             | 315, 319, 412                 | -  |
| 1-Octadecene             | 08             | 304, EUH066                   | 301+310, 331   |
| Octadecylphosphonic acid | 07             | 315, 319                      | 264, 280,<br>302+352,<br>305+351+338,<br>332+313,<br>337+313 |
| n-Octane                 | 02, 07, 08, 09 | 225, 304, 315,<br>336, 410    | 210, 233, 272,<br>301+310,<br>303+361+353,<br>331            |
| 1-Octanethiol            | 07             | 315, 317, 319,<br>335         | 261, 264, 280,<br>304+340+312,<br>333+313,<br>337+313        |

**Table 28:** Used chemicals and their GHS symbols as well as their hazardous and precautionary statements.

| Substance        | GHS            | Hazardous statements            | Precautionary statements   |
|------------------|----------------|---------------------------------|--|
| Oleylamine       | 05, 07, 08, 09 | 302, 304, 314,<br>335, 373, 410 | 260, 280,<br>301+310,<br>303+361+353,<br>304+340+310,<br>305+351+338 |
| PEDOT:PSS        | 05             | 314                             | 280,<br>303+361+353,<br>304+340+310,<br>305+351+338,<br>363, 405     |
| PVK              | -              | -                               | -  |
| Potassium iodide | 08             | 372                             | 314  |
| 1-Propanol       | 03, 05, 07     | 225, 318, 336                   | 210, 233, 240,<br>241, 280   |
| 2-Propanol       | 03, 07         | 225, 319, 336                   | 210, 240,<br>305+351+338,<br>403+233                                 |
| Selenium         | 06, 08         | 373, 413,<br>301+331            | 301+310, 264,<br>304+340, 311,<br>403+233, 260,<br>273               |
| Silicon wafer    | -              | -                               | -  |
| Soap (dish)      | 07             | 319                             | 280,<br>305+351+338  |

**Table 28:** Used chemicals and their GHS symbols as well as their hazardous and precautionary statements.

| Substance  | GHS            | Hazardous statements             | Precautionary statements                                      |
|--|----------------|----------------------------------|---|
| Sulfur   | 07             | 315                              | -   |
| TCTA   | 07             | 315, 319, 335                    | 302+352,<br>305+351+338,<br>312, 337+313                      |
| Technistrip N155                                 | 07             | 302, 312                         | -   |
| Tetramethylammonium<br>hydroxide<br>pentahydrate | 05, 06, 08, 09 | 300+310, 314,<br>370, 372, 411   | 260, 273, 280,<br>303+361+353,<br>304+340+310,<br>305+351+338 |
| Titanium   | 03             | 228                              | 210, 370+378  |
| Toluene  | 02, 07, 08     | 225, 304, 315,<br>336, 361d, 373 | 210, 260, 280,<br>301+310,<br>370+378,<br>403+235             |
| Tri-n-octylphosphine                             | 05             | 314                              | 280,<br>305+351+338,<br>310                                   |
| Tri-n-octylphosphine<br>oxide                    | 05             | 315, 318                         | 264, 290,<br>302+352,<br>305+351+338,<br>310, 332+313,<br>362 |
| Triammonium citrate                              | -              | -                                | -   |

**Table 28:** Used chemicals and their GHS symbols as well as their hazardous and precautionary statements.

| Substance              | GHS        | Hazardous statements | Precautionary statements                |
|------------------------|------------|----------------------|---|
| Zinc acetate dihydrate | 05, 07, 09 | 302, 318, 410        | 280,<br>301+312+330,<br>305+351+338+310 |
| Zinc oxide             | 09         | 410                  | 272, 391, 501                           |

### A.1.2 KMR Substances

**Table 29:** Used KMR substances of categories 1A and 1B<sup>[186]</sup>

| CAS Number | IUPAC name                | Experiment and Amount Used           | Category |
|------------|---------------------------|--------------------------------------|----------|
| 1306-24-7  | Cadmium selenide          | Synthesis, device fabrication, <5 g  | 1A       |
| 1306-19-0  | Cadmium oxide             | Synthesis precursor, <30 g           | 1B       |
| 5743-04-4  | Cadmium acetate dihydrate | Synthesis precursors, >100 g         | 1B       |
| 1306-23-6  | Cadmium sulfide           | Synthesis, device fabrication, <10 g | 1B       |



**Table 30:** List of Samples and Corresponding Log-Nr.

| <b>Sample</b> | <b>Log-Nr.</b>          | <b>Sample</b> | <b>Log-Nr.</b>          |
|---------------|-------------------------|---------------|-------------------------|
| CdSe-1        | Cd-0-428-1              | PEQLED-5      | QLED-118-1-Stru-177-1-2 |
| CdSe-2        | Cd-0-428-4              | PEQLED-6      | QLED-118-1-Stru-177-2   |
| CdSe-3        | Cd-0-428-7              | IDE-1         | Stru-100-1              |
| CdSe-4        | Cd-0-428-5              | IDE-2         | Stru-100-2              |
| CdSe-5        | Cd-0-428-6              | IDE-3         | Stru-100-5              |
| CdSe-6        | Cd-0-348-1              | IDE-4         | Stru-101-2              |
| CdSe-7        | Cd-0-348-2              | FFE-1         | Stru-151-1              |
| CdSe-8        | Cd-0-348-3              | FFE-2         | Stru-151-3              |
| CdSe-9        | Cd-0-229-1              | FFE-3         | Stru-151-2              |
| CdSe-10       | Cd-0-352-1              | FFE-4         | Stru-151-4              |
| CdSe-11       | Cd-0-280-1              | FFE-5         | Stru-151-5              |
| CdSe-12       | Cd-0-135-1              | FFE-6         | Stru-077-2              |
| CdSe-13       | Cd-0-164-1              | FFE-7         | Stru-079-2              |
| CdSe-14       | Cd-0-194-1              | FFE-8         | Stru-079-6              |
| CdSe-15       | Cd-0-282-1              | FFE-9         | Stru-079-3              |
| QR-1          | Cd-1-060-1              | FFE-10        | Stru-148-1              |
| QR-2          | Cd-1-060-5              | FFE-11        | Stru-148-2              |
| QR-3          | Cd-1-060-2              | FFE-12        | Stru-148-3              |
| QR-4          | Cd-1-060-6              | FFE-13        | Stru-147-1              |
| QR-5          | Cd-1-043-1              | FFE-14        | Stru-147-2              |
| QR-6          | Cd-1-043-4              | FFE-15        | Stru-147-3              |
| QR-7          | Cd-1-043-5              | FFE-16        | Stru-147-5              |
| QR-8          | Cd-1-043-2              | FFE-17        | Stru-147-6              |
| QR-9          | Cd-1-043-6              | FFE-18        | Stru-147-7              |
| QR-10         | Cd-1-043-7              | FFE-19        | Stru-147-11             |
| QR-11         | Cd-1-047-3              | FFE-20        | Stru-068-4              |
| QR-12         | Cd-1-056-2              | FFE-21        | Stru-068-10             |
| QR-13         | Cd-1-038-3              | FFE-22        | Stru-065-9F             |
| QR-14         | Cd-1-044-1              | FFE-23        | Stru-067-11F            |
| QR-15         | Cd-1-048-1              | FFE-24        | Stru-069-1h             |
| QR-16         | Cd-1-050-1              | FFE-25        | Stru-177-1              |
| QR-17         | Cd-1-0-51-1             | FFE-26        | Stru-177-2              |
| PEQLED-1      | QLED-066                | QLED-1        | QLED-118-6              |
| PEQLED-2      | QLED-067                | ZnO-1         | Zn-0-161-1f             |
| PEQLED-3      | QLED-068                |               |                         |
| PEQLED-4      | QLED-118-1-Stru-177-1-1 |               |                         |

## A.2 Curriculum Vitae

# Christian Castillo Delgadillo



## Professional Experience

- |                      |   |
|----------------------|---|
| 02.2019 -<br>03.2022 | <b>Research assistant</b> at <b>Fraunhofer IAP-CAN</b> (Center for Applied Nanotechnology, Hamburg)<br>Production and analysis of semiconductor nanomaterials in a continuous flow reactor and their implementation in novel devices: LEDs and sensors<br>Research and development for industry partners and for third party projects<br>Organization and supervision of laboratory courses for students, as well as for bachelor and master's thesis |
| 10.2016 -<br>04.2018 | <b>Chemistry tutor</b> at the University of Hamburg for students of biochemistry and nano sciences (organic and inorganic chemistry)  |

## Education

- 2019–2022 **Doctorate (Chemistry), University of Hamburg**, Institute of Physical Chemistry in cooperation with Fraunhofer IAP-CAN  
Focus: Synthesis of semiconductor nanomaterials in batch as well as in a reactor, production of opto-electronic devices  
**Thesis:** Fabrication of polarized emissive light-emitting diodes based on CdSe/CdS quantum rods synthesized in a continuous flow
- 2016–2018 **Master of Science (Chemistry), University of Hamburg** (Final grade: 1.5)  
Focus: Nanochemistry, nanoelectronics and nanosensoric, energy: materials for energy storage  
Master's thesis at **Fraunhofer IAP-CAN** with the title: Green synthesis and characterization of zinc-based giant-shell nanoparticles
- 2017 **Foreign research residence** (Final grade: 1.0)  
Research project at the University of Oslo (Norway) at the Faculty of Chemistry – Biomolecules and soft matter  
Focus: Production of polymeric nanoparticles, analysis via SAXS and DLS. Title of the project: Structural characterization of nanocrystalline micelles formed by self-assembly of polymers in solution
- 2013–2016 **Bachelor of Science (Chemistry), University of Hamburg** (Final grade: 2.4)  
Title of the thesis: Production of gold nanoparticle based chemiresistors via contact printing
- 2011–2013 **Abitur**, boarding school **Sächsisches Landesgymnasium Sankt Afra zu Meissen** for highly gifted students  
Scholarship supported by the German School in Mexico City

## Scientific Expertise

|                   |   |
|-------------------|---|
| <b>Synthetic</b>  | wet-chemical, colloidal, electrochemical, inorganic, organic syntheses, under inert gas atmosphere as well as in gloveboxes. Purification and characterization of these   |
| <b>Devices</b>    | Photolithography, physical vapor deposition (PVD) for inorganic and organic materials, etching  |
| <b>Analytical</b> | Atomic force, scanning electron, transmission electron, optical microscopy. Thermogravimetric analysis, dynamic light scattering, small-angle x-ray scattering. Photoluminescence-, UV-vis-, infra-red spectroscopy |
| <b>Electrical</b> | IV-, luminance and sensitivity measurements for optical devices   |

## Publications and Conference Presentations

|        |   |
|--------|---|
| 2022   | Y. U. Staechlin, M. Deffner, S. Krohn, <u>C. Castillo Delgadillo</u> , J. S. Niehaus, H. Lange, <i>J. Chem. Phys.</i> <b>2022</b> , 156 |
| Oral   | Bunsentagung 2019, Jena   |
| Poster | Nanax 2019, Hamburg   |
| Oral   | NanoGE 2020, online   |
| Oral   | E-MRS Spring Meeting, online  |
| Oral   | Nanotech 2021, online   |

## Skills

|           |   |
|-----------|---|
| Languages | <b>German</b> – fluent, <b>English</b> – fluent, <b>Spanish</b> – native, <b>French</b> – basic, <b>Italian</b> – basic   |
| Computer  | Microsoft Office (Word, Power Point, Excel, Outlook), Klayout, CAD (FreeCAD), Adobe (Photoshop), Origin, Inkscape, Blender (basics), Gimp, Comsol (basics), Python (basics) |
| Other     | Certificate of competence §5 <i>Chemikalienverbotsverordnung</i>  |

### A.3 Erklärung

Hiermit versichere ich an Eides statt, die vorliegende Dissertation selbst verfasst und keine anderen als die angegebenen Hilfsmittel benutzt zu haben. Die eingereichte schriftliche Fassung entspricht der auf dem elektronischen Speichermedium. Ich versichere, dass diese Dissertation nicht in einem früheren Promotionsverfahren eingereicht wurde.

A handwritten signature in black ink, appearing to be 'S. P. ...', written over a horizontal line.

Hamburg, June 1, 2022